



UNIVERSITY OF MESSINA
DEPARTMENT OF ENGINEERING
DOCTORAL PROGRAM IN
“CHEMISTRY AND ENGINEERING OF MATERIALS AND
CONSTRUCTIONS

Application of advanced nanomaterials in gas and electrochemical sensors

Doctoral Thesis of:

Kaveh Moulae

Supervisor:

Prof. Giovanni Neri

The Chair of the Doctoral Program:

Prof. Giovanni Neri

(Academic Year 2018-2019) XXXIV Cycle



UNIVERSITÀ DEGLI STUDI DI MESSINA

DIPARTIMENTO DI INGEGNERIA

CORSO DI DOTTORATO IN:

“CHIMICA E INGEGNERIA DEI MATERIALI E DELLE
COSTRUZIONI”

Applicazione di nanomateriali in sensori elettrochimici e di gas avanzati

Tesi di dottorato di:

Kaveh Moulae

Relatore:

Prof. Giovanni Neri

Coordinatore del corso di dottorato:

Prof. Giovanni Neri

(A.A. 2018-2019) XXXIV Ciclo

Acknowledgments

I would like to thank Professor Giovanni Neri, my supervisor, for giving me the freedom to chase what, at times, must have seemed like totally demented ideas. You welcomed me with open arms and always encouraged me to read, to test, and never dissuaded me when I wanted to test some crazy idea. Your mentoring, always forthcoming, often extended outside of “bench” science. You probably have more faith in me and my abilities than I do myself. Thank you, from the bottom of my heart as you were an inspiration and a role model for both career advancement and personal attitude.

I also want to thank Dr. Salvatore Gianluca Leonardi for his sound scientific advice, and also for being accessible to answer my questions whenever these arose.

Lastly, I would like to thank my friends and family. Your support and love has been a joy in the good times, and has carried me through the bad.

Lab. Sensori members, past and present including Gianluca, Lavavya, Roberto, Angelo, Simona and Viviana. Thank you for your support, your friendship, and, above all, the laughter we shared.

Thank God for old houses and the gardeners. A man and a woman, my parents, are largely responsible for my being here writing this. Such faith, such patience, such love. Thank you. You are always in my heart and in my mind.

And the last paragraph, again, for Giovanni, Ali and Goli. You’ve made me a better human being. What else can anyone ask for?

Overview of the research activities

In this Ph.D. thesis, the main objective was to focus on improving the performance of sensing strategies for certain gases and (bio)chemical substances. Generally speaking, the research activities were divided into two main sections namely, electrochemical sensing studies (section 2.1) and gas sensing studies (section 2.2). In the former studies, the main attention was paid to the performance of the sensors for analytes in the *aqueous phase* using electroanalytical sensing strategies while in the latter ones getting deeper insight into the *gas phase* reactions and sensing performance of conductometric gas sensors, either qualitatively (mechanistic studies) or quantitatively were the core of studies.

Electrochemical sensing analyses of this thesis encompasses the outputs and results of three separate research activities as follows:

Study the effect of shell thickness (NiO in this case) on the electrochemical sensing detection of glucose using carbon nanotube/NiO core/shell nanostructure. The results were discussed and interpreted from both qualitative (*sensing mechanism*) and quantitative (improvement of *sensitivity*) points of view.

Another core/shell nanostructure, i.e. carbon nanotube/Al₂O₃ was taken as a sensing material in this study; however, the focus was to improve the *selectivity* of the proposed electrochemical sensing platform for dihydroxy benzene isomers, i.e. catechol, hydroquinone, and resorcinol.

In the last part of electrochemical sensing studies, CuO nanostructure was used to develop a non-enzymatic glucose sensor. Although the synthesis of sensing material was quite simple, cost-effective, and straightforward, the proposed electrochemical sensor was yet sensitive towards glucose detection mainly due to the electrocatalytic role of CuO.

In the gas sensing studies, on the other hand, analytes of interest were analyzed in the gas phase where the sensing phenomena were quite different from the electrochemical sensors mentioned above. The research activities in this part include four main topics as follows:

As in a conductometric gas sensor surface phenomena are of great importance, the carbon nanotube/NiO core/shell structures with different thicknesses of NiO shell were the subject of a study in which ethanol and acetone were analyzed as target gases. The effect of the shell thickness on the final performance of this gas sensor was clearly revealed and discussed in this study.

The copper-metal oxide framework was the next sensing material whose gas sensing behavior towards NO₂ was studied. The effect of operating temperature on the performance of this gas sensor was interesting and well discussed where it showed improved performance at lower temperatures (ca. 40 °C) for NO₂ detection and, on the contrary, at higher operating temperatures (ca. 200 °C) for acetone detection.

As detection of hydrogen is of great importance from industrial point of view, the next activity was devoted to designing a gas sensor for hydrogen monitoring. In this activity, the gas sensing behavior of WO₃ was deeply investigated and, based on the quantitative results obtained the possible sensing mechanism was modelled and presented. I was actively involved in the sensing measurements and sensing modelling studies were undertaken by our colleagues from the University of Catania.

My last activity in the gas sensing analyses section was to develop a gas sensor for NO₂ based on carbon dots as the sensing material. Carbon dots were prepared from a cheap and easily available natural precursor, i.e., olive solid waste, by a simple pyrolysis process combined with a chemical oxidation step. This low-cost gas sensor could successfully detect NO₂ even at very low concentrations.

A more detailed discussion on each topic mentioned above can be found in the following sections of this thesis.

Table of contents

Overview of the research activities	iv
--	-----------

Table of contents

1 Introduction	1
1.1 An introduction on electrochemistry	1
1.2 Electroanalytical methods (used in this thesis).....	4
1.2.1 Chronoamperometry.....	4
1.2.2 Voltammetric methods	6
1.2.2.1 Different types of current in voltammetry	7
1.2.2.2 Key-points in a voltammetric analysis	8
1.2.2.3 Cyclic voltammetry (CV).....	9
1.2.2.4 Differential pulse voltammetry (DPV).....	10
1.2.2.5 Square wave voltammetry (SWV).....	12
1.3 Conductometric gas sensors	14
1.3.1 An introduction on chemoresistive gas sensors.....	14
1.4 Analytical figures of merit	17
2 Experimental activities, Results and Discussions	21
2.1 Electrochemical sensing analyses	21
2.1.1 Tuning the NiO Thin Film Morphology on Carbon Nanotubes; Effect of shell thickness on electrochemical detection of glucose.....	21
2.1.1.1 Introduction	21
2.1.1.2 Electrode preparation	22
2.1.1.3 Result and discussion.....	23
2.1.1.3.1 Transmission electron microscopy analyses (TEM)	23
2.1.1.3.2 Electrochemical behavior of glucose at CNT/NiO modified electrode.....	24
2.1.1.3.3 Effect of NiO thickness on glucose oxidation	25
2.1.1.3.4 KOH effect	27
2.1.1.3.5 Scan rate effect	28
2.1.1.3.6 Amperometric application of CNT/NiO electrode for glucose sensing	30
2.1.1.3.7 Conclusions	33
2.1.2 CNT-Al ₂ O ₃ core-shell nanostructures; effect of Al ₂ O ₃ thickness on the electrochemical detection of dihydroxybenzene isomers	38
2.1.2.1 Introduction	39

2.1.2.2	Experimental	40
2.1.2.3	Results and discussion	41
2.1.2.3.1	Structural characterizations	41
2.1.2.3.2	Electrochemical behavior of modified electrodes towards DHB isomers	45
2.1.2.3.3	Sensing mechanism on modified electrodes	49
2.1.2.3.4	Scan rate effect study	51
2.1.2.3.5	Effect of the pH	51
2.1.2.3.6	Electrochemical measurement of DHB isomers.....	52
2.1.2.3.7	Applicability in real sample analysis and recovery tests	56
2.1.2.3.8	Repeatability, reproducibility and long-term stability of the electrodes	57
2.1.2.4	Conclusions	57
2.1.3	One-step microwave-assisted synthesis and characterization of novel CuO nanodisks for non-enzymatic glucose sensing.....	62
2.1.3.1	Introduction	62
2.1.3.2	Experimental	64
	Electrochemical tests	65
2.1.3.3	Results and discussion	66
2.1.3.3.1	Structural characterizations of CuO nanodisks	66
2.1.3.3.2	Electrochemical characteristics of modified CuO/SPCE	68
2.1.3.3.3	Effect of scan rate	70
2.1.3.3.4	Amperometric analyses	71
2.1.3.3.5	Selectivity, stability and real sample analyses	74
2.1.3.4	Conclusion.....	75
2.2	Gas sensing analyses	80
2.2.1	Evaluation of NiO-SCCNTs core-shell structure; new insight into shell thickness effect on gas sensing properties	80
2.2.1.1	Introduction	81
2.2.1.2	Experimental	82
2.2.1.3	Results and discussion	83
2.2.1.3.1	Structural characterization.....	83
2.2.1.3.2	Electrical characteristics.....	88
2.2.1.3.3	Gas sensing tests.....	89
2.2.1.4	Conclusion.....	94
2.2.2	Modulation of gas selectivity towards acetone and NO ₂ using Cu-MOF based gas sensor 101	
2.2.2.1	Experimental	103

2.2.2.2	Results and discussion	105
2.2.2.2.1	TG-DTA analysis.....	105
2.2.2.2.2	SEM and TEM studies.....	106
2.2.2.2.3	Powder XRD analysis	107
2.2.2.2.4	XPS analysis	109
2.2.2.2.5	Electrical tests	110
2.2.2.2.6	Acetone sensing tests	111
2.2.2.2.7	NO ₂ sensing tests	113
2.2.2.2.8	Temperature-dependent dual selectivity for detecting acetone and NO ₂ ..	117
2.2.2.3	Conclusions	118
2.2.3	H ₂ detection mechanism in chemoresistive sensor based on low-cost synthesized WO ₃ nanorods.....	122
2.2.3.1	Introduction	123
2.2.3.2	Material and methods	124
2.2.3.3	Results and discussion	125
2.2.3.3.1	Structural and electrical properties of WO ₃ nanorods.....	125
2.2.3.3.2	H ₂ sensing results	126
2.2.3.3.3	H ₂ sensing kinetics.....	129
2.2.3.3.4	Modelling of WO ₃ -H ₂ interaction	133
2.2.3.4	Conclusion.....	134
2.2.4	Carbon-dots conductometric sensor for high performance gas sensing	138
2.2.4.1	Introduction	139
2.2.4.2	Experimental Section	140
2.2.4.3	Results and discussion	142
2.2.4.3.1	Structural characterization.....	142
2.2.4.3.2	Electrical and gas sensing properties	145
2.2.4.4	Conclusion.....	151
3	<i>Final remarks and outlooks.....</i>	156
4	<i>Appendixes</i>	158
4.1	Appendix A: List of tables.....	158
4.2	Appendix B: List of figures.....	159
4.3	Appendix C: list of publications and conference presentations.....	167

1 Introduction

1.1 An introduction on electrochemistry

Electrochemistry is an area of chemistry that studies the interrelation of electrical and chemical effects [1] while electroanalytical chemistry is the use of electrochemical techniques to characterize a sample. Although most electrochemical methods are based on three types of analytical signals, namely *potential*, *current* and *charge*, but a wide range of electrochemical methods have been developed using these three parameters [2]. As the simplest classification, various electrochemical methods can be divided into two major groups as follows:

1- **Bulk methods**: Here the quantity measured is based on the phenomena that occur inside the solution. For example, in the conductometric method, the conductivity of a solution is measured, which is proportional to the concentration of the total ions dissolved in the bulk of a solution.

2- **Boundary methods** (or Interfacial methods): In these techniques, the desired signal originates from the interface of solution-electrode. As an example, measuring the pH of a solution with a pH meter is actually based on an interfacial phenomenon. .

It is worth noting that the variety of boundary methods is much greater than bulk methods and they can generally be divided into two categories of **static methods** and **dynamic methods**, each of which in turn includes a large number of sub-methods. The most important characteristic of a static system is the absence of electrochemical reactions and consequently the absence of current flow through the system ($i = 0$). Therefore, the concentration of species remains constant during the measurement. Unlike static methods, in dynamic methods, electric current flows in the system ($i \neq 0$) and therefore the concentrations of the species participating in the electrochemical reaction are changed. Figure 1-1 shows some of the most important examples of these boundary methods.

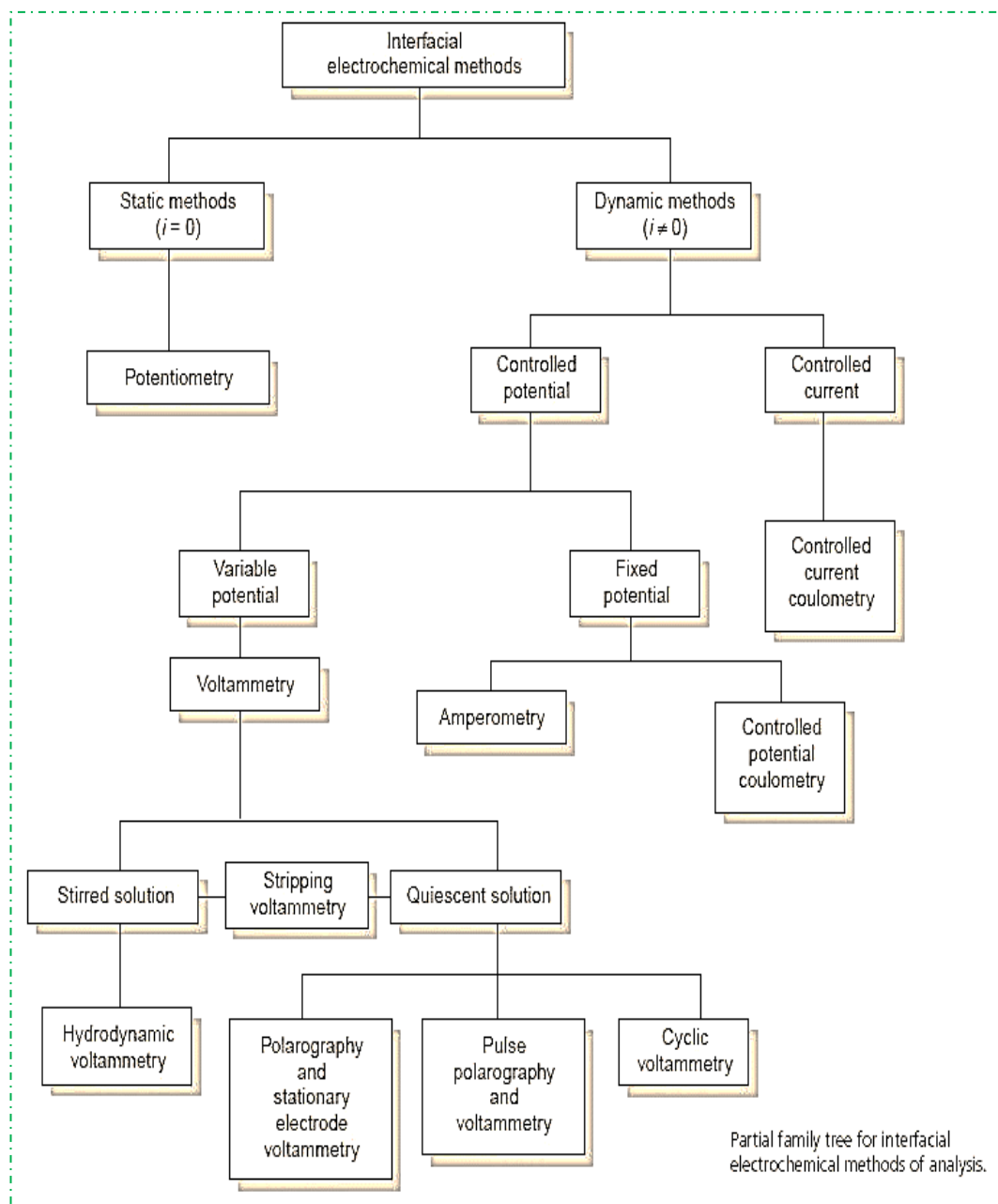


Figure 1-1. Schematic view of common interfacial electrochemical methods [2].

An electrochemical cell in its simplest form consists of two electrodes. The first is an electrode that is sensitive to the concentration (or, better to say, is sensitive to the activity) of the species and is called the working electrode. The second electrode is used to complete the circuit or create a constant potential, and is called the reference electrode. It is worth noting that this two-electrode system is usually suitable for static methods in which there is no current passage ($i = 0$).

In dynamic methods where current passes through the system during analysis ($i \neq 0$), the two-electrode system mentioned above is not very suitable because as the current passes through the reference electrode, its potential changes and it no longer has a constant value (this is not the case for micro or nano electrodes). Therefore, in dynamic methods, current should be prevented from passing through the reference electrode. For this purpose, three-electrode cells are usually used in dynamic methods. Here, one of the electrodes where the oxidation-reduction reaction of interest takes place is the working electrode, the other electrode that is used to complete the electrical circuit is called auxiliary or counter electrode, and the third electrode that is used to determine the potential of the working electrode at any given time is called reference electrode. Since in three-electrode cells the current flows only between the working and counter electrodes, a considerable current does not pass through the reference electrode and its potential remains constant. Two- and three-electrode configurations can be seen in Figure 1-2.

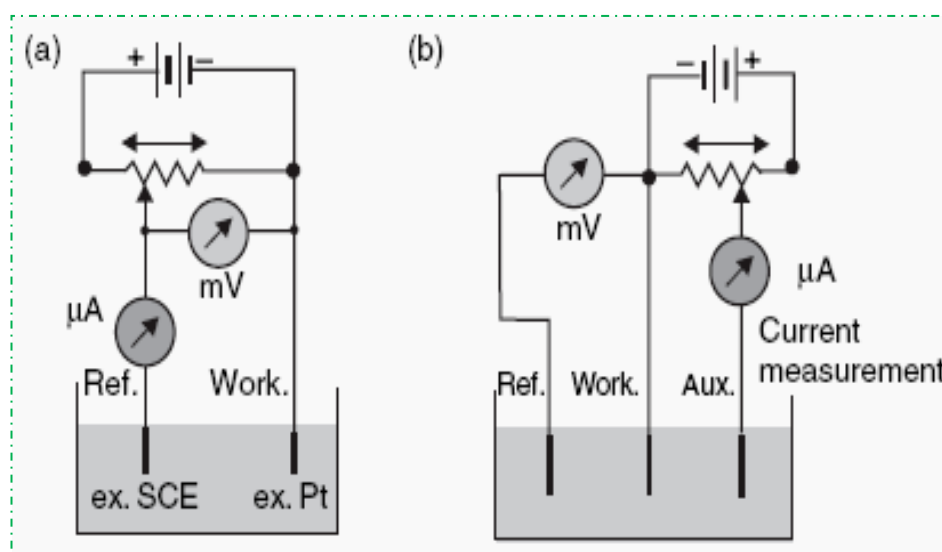


Figure 1-2. Schematic view of a two-electrode (a) and three-electrode (b) system: Here Aux. Auxiliary electrode, Ref. Reference electrode and Work are work electrodes [3].

1.2 Electroanalytical methods (used in this thesis)

1.2.1 Chronoamperometry

Chronoamperometry is a potential step technique, which generates a current-time graph at a constant potential applied to the working electrode [4]. This method involves tracking current changes due to the applying of potential step(s) to the working electrode over time. The potential step(s) are usually selected in such a way that the resulting current is of a diffuse nature. To perform this method, a three-electrode system including working, reference and auxiliary electrodes is used and a potential step is applied to the working electrode with the help of a potentiostat. To better understand this method, it is assumed that in the electrode reaction described by the following equation (1-1) and at the beginning of the experiment there is only oxidizing species (O) in the solution:



Here the potential step (as shown in Figure 1-3a) is applied to the working electrode. Usually E_1 is selected in such a way that O is not reduced. At the time the potential is applied to the working electrode, it is instantly changed to the new potential E_2 so that the reduction rate of O is controlled by diffusion. The current-time relationship in this analysis can be understood using the concentration-time sections shown in Figure 1-3b. Given that the surface concentration of species O at the applied potential of E_2 will be zero, a concentration gradient will be established in the vicinity of the electrode surface. The area where the solution is depleted of type O is known as the diffusion layer, which is given by its thickness, δ . At the beginning of the of the potential step E_2 , the concentration gradient is steep and the diffusion layer is thin, but over time, the diffusion layer gradually expands and its thickness increases, resulting in a decrease in the concentration gradient and consequently an exponential decrease in the current.

It is noteworthy that in this method, the immobility of the electrode and the solution causes that the flux of the electrolyzed compound towards the working electrode gradually decreases due to the increase in the thickness of the diffusion layer, which appears as a decrease in current. As long as the measured current intensity due to the

application of the E_2 potential step is a diffusing current, the changes in current over time can be described by the Cottrell equation.

$$i(t) = nFAC^* \left(\frac{D}{\pi t}\right)^{1/2} \quad (1-2)$$

i = Current

n = number of transferred electrons

F = faraday constant

A = electrode surface area

c^* = bulk concentration

D = diffusion constant

t = time

The Cottrell equation shows the relationship between the current intensity resulting from the applying of a potential step (E_2) at any given moment and the concentration of the species under study, C^* . In most cases, with the help of data obtained from the chronoamperometric method and by plotting the variation of $i-t^{-1/2}$, which appears as a straight line with a slope of $nFAC^*D^{1/2}\pi^{-1/2}$, the diffusion coefficient (D) of the species can be determined. Chronoamperometry can also be used to calculate the electrode area or to detect the mechanism of electrode reactions [5].

Figure (1-3) shows the potential-time change diagram (potential step applied to the working electrode), the changes of concentration sections in the vicinity of the working electrode over time, as well as the current-time response resulting from the application of the potential step of section (a).

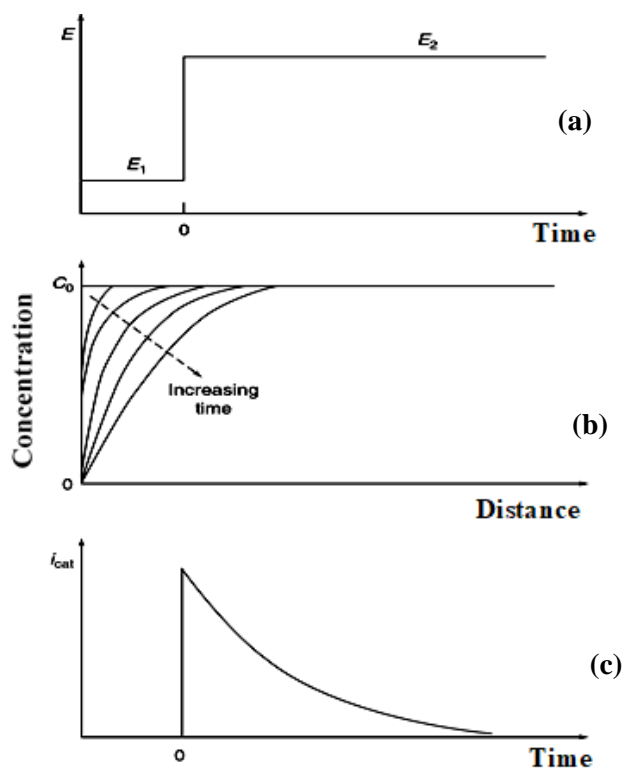


Figure 1-3. a) potential-time change diagram, b) concentration section changes with time and c) corresponding current-time response

1.2.2 Voltammetric methods

In voltammetric methods, a time-dependent potential is often applied to the working electrode, and the resulting current variations are followed as a function of the applied potential. The resulting diagram shows the changes in current according to potential and is called a voltammogram.

Historically, the oldest voltammetry method is polarography, which was introduced in the 1920s by a scientist named Jaroslav Heyrovský who won the 1959 Nobel Prize in Chemistry. A wide range of voltammetric methods have been developed since then. After the first cyclic voltammetry studies by Randles-Sevcik in the early 1950s, hydrodynamic voltammetric methods rapidly growth in the 1950s and 1960s [6]. In the same years, other very successful methods such as alternating current (ac) voltammetry and pulse voltammetry emerged [7]. After the introduction of microelectrodes in the 1970s and 1980s, another development in voltammetric methods occurred [8]. Electrode surface modification with the help of organic or

inorganic modifiers has greatly expanded the scope and capabilities of voltammetric methods and made it a powerful analytical method. With the help of electrode modification, many analyses that were not possible using unmodified electrodes (bare electrode) (for example, due to high overvoltage) could be performed successfully [9]. Plotting the current curves with respect to the applied potential to the system, can provide valuable quantitative and/or qualitative information about the electrochemical system under-study.

1.2.2.1 Different types of current in voltammetry

The current measured in voltammetric methods has two main sources, which are:

1. *Faradic current*: The origin of this type of current is the electron transfer processes at the electrode-solution boundary (interface). Moreover, the Faradic current itself can have two important sources. The first is the faradic current that arises from the electron transfer of the desired species (analyte) and we try to amplify this current as much as possible. The second source is the faradic current that results from the electron transfer of other species in the system (interferences) and we try to reduce its share in the total flow as much as possible.

2. *Non-faradic current*: To produce this current, no electron transfer reaction occurs on the electrode surface and for this reason it is called non-faradic current. The main source of non-faradic current generation is the formation of electrical double layers (similar to a capacitor), due to the application of potential, near the electrode surface. This electrical double layer is created due to the applying a potential to the electrode and consequently the accumulation of charges on the surface of the electrode where ions in solution that have opposite charge with respect to the surface of the electrode move toward the charged electrode and accumulate near its surface. The creation of this electrical double layer is the main source of non-faradic current. It should be noted that by reducing the share of non-faradic current (capacitive current) in the total current, the sensitivity and, consequently, the detection limit of the method can be improved.

1.2.2.2 *Key-points in a voltammetric analysis*

1. In a three-electrode configuration, the working, auxiliary and reference electrodes should be placed as close as possible to each other. For this purpose, the working electrode is usually placed between the reference and auxiliary electrodes so that it has the shortest possible distance from the reference electrode. This reduces the ohmic drop due to the resistance of the solution as much as possible and reduces the measurement error of the working electrode potential.
2. Electrochemical cells usually have an inlet and outlet for blowing inert gas into the solution inside the cell, in order to remove the oxygen from the solution. It should be noted that this inert gas should be as pure as possible. Nitrogen gas is often used as an inert gas due to its high purity, availability and low price.
3. The amount of solution required in electrochemical methods is often between 5 to 20 ml, although in special cases, electrochemical cells with a capacity of a few microliters or a few liters are also designed and used.
4. The concentration range of the analyte used in DC voltammetric methods is usually, not always, between 0.1-5 mM because at concentrations higher than 5 mM, large currents cause a significant ohmic drop, which is one of the effective sources of the error in voltammetric analyses. On the other hand, for concentrations lower than 0.1 mM, due to the decrease in the share of Faradaic current from the analyte in the total current, the share of background current in the total current will be dominant and this brings about error in measurements of analyte concentration. It is worth noting that in some voltammetric methods, such as the differential pulse or square wave voltammetry methods, the detection limit of the measurements can be reduced to concentrations of 10^{-7} M or even lower by increasing the ratio of faradic current to background current.
5. In a voltammetric analysis, usually a high concentration (often more than 0.1 M) of the supporting electrolyte (backup electrolyte) is added to the solution in order to first reduce the resistance of the solution (and therefore the ohmic drop). Additionally this supporting electrolyte will help to minimize the share of current due to analyte migration in the total current. It should be noted that,

firstly, the supporting electrolyte must be of high purity (because it is added to the solution with a much higher concentration than the analyte and then presence of even small amounts of impurities in it, will have a significant effect). Secondly, this supporting electrolyte, after dissolution, should produce ions that are not oxidized or reduced easily. This provides a wider potential window for analysis.

6. In the absence of constant temperature conditions in the laboratory, sometimes it is necessary to place the electrochemical cell inside a thermostatic bath, because in some cases voltammetric responses are affected by temperature [10].

1.2.2.3 Cyclic voltammetry (CV)

Among all voltammetric methods, cyclic voltammetry is the most widely used method, which is mainly used to acquire both quantitative and qualitative information. In recent years, a variety of potential scanning methods (such as cyclic voltammetry) have been used to study various systems. Understanding the mathematical equations governing these methods, it has become possible to measure many important kinetic parameters. Due to the high capability of the cyclic voltammetry method in investigating the mechanism of electrochemical reactions, this method is often used as the first and most useful method used to obtain mechanistic information about the electrochemical systems. For this purpose, we first perform potential sweeping in a wide range of potentials and obtain the resulting voltammograms. In these scans, several peaks may appear, which depending on their location, how they are created and decay, how they change with respect to the changes in potential scan speed, and how they change due to successive potential cycles, useful mechanical information can be provided.

Figure (1-4) shows a potential-time profile applied to an electrode in cyclic voltammetry as well as the response of a reversible redox couple during a potential cycle. For example, if we assume that there is only oxidant species (O) in the environment, a negative direction is chosen for potential sweep in the first half cycle. As the applied potential gets closer to the formal potential (E°) of the redox pair, the cathodic current increases until cathodic peak is formed (at E_p^c). By passing through the potential region in which the reduction process takes place (at least $90/n$ mV after

the E_{p^c}), the direction of the potential scan is reversed. During reverse potential sweep, the reducing molecules (R), produced in the previous half cycle, are re-oxidized to form the anodic peak [11].

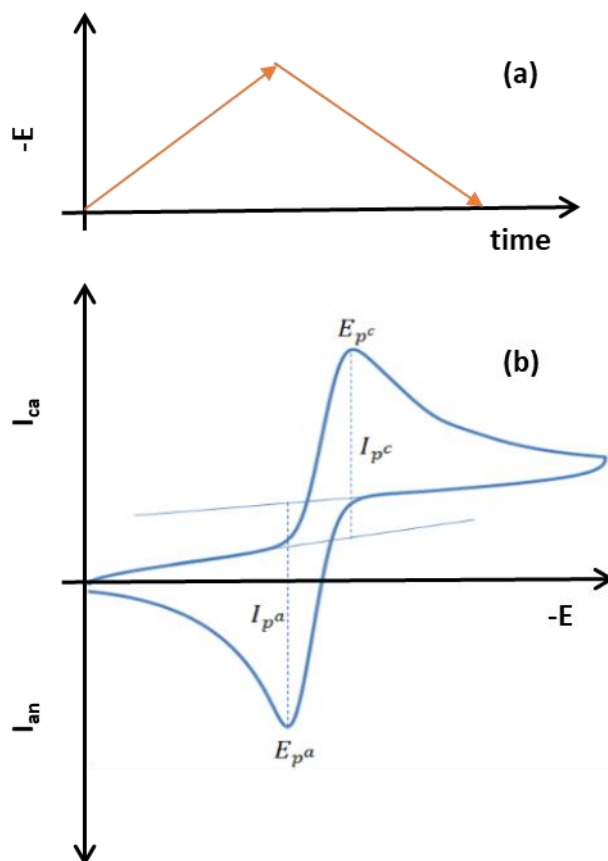


Figure 1-4. Potential-time excitation profile in a cyclic voltammetry analysis (a) and the resulting voltammogram for a reversible electrochemical reaction (b)

In the cyclic voltammetry method, to investigate the reaction mechanism, the potential scan range, potential scan direction, potential scan speed and number of potential cycle can be changed and useful information about the mechanism of the electrode process can be obtained from their effect on the resulting voltammograms [12].

1.2.2.4 Differential pulse voltammetry (DPV)

Although the cyclic voltammetry method has unique capabilities in the field of qualitative examination of electrochemical systems, it has not been very successful in terms of quantitative measurements as compared to other analytical methods such as

spectroscopic methods. Therefore, in the 1960s, due to some inherent disadvantages such as low analysis speed, low sensitivity and poor detection limit, pulse voltammetry methods gradually replaced potential linear scanning methods. Differential pulse voltammetry and square wave voltammetry were two of the most successful methods of pulse voltammetry [13]. One of the main reasons for the success of the differential pulse voltammetry method in chemical analysis is related to the successful minimization of capacitive current in this method. To remove the capacitive current in this method, the current is sampled (at least) twice during the applying each pulse. The first sampling of the current is done just before the applying the potential pulse (i_1 in figure 1-5a) and the second sampling of the current just before the end of each pulse (i_2 in figure 1-5a). The final current is reported as the difference between these two measured currents. Another result of dual current sampling is that the voltammogram obtained in the differential pulse voltammetry method appears as a peak (figure 1-5b). Due to the successful elimination of background current in the differential pulse voltammetry method and the consequent increase in the signal-to-noise ratio, the detection limits obtained for reversible redox systems can be reduced even to a concentration of 10^{-8} M.

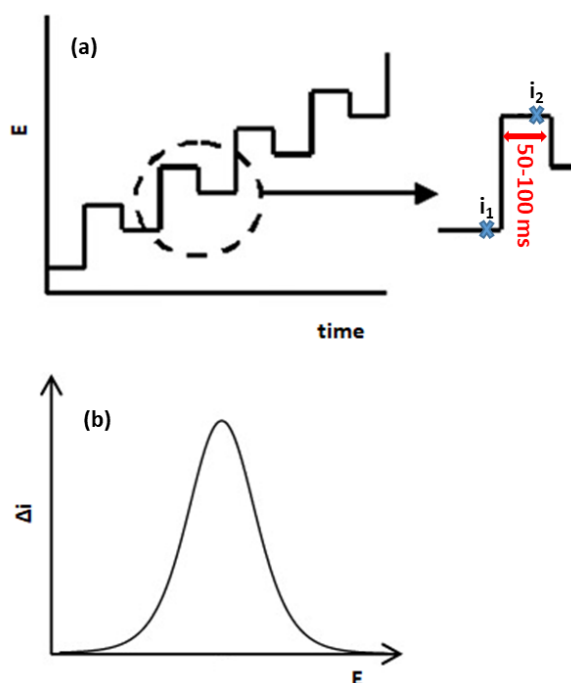


Figure 1-5. Differential pulse voltammetry. (a) The profile of potential waveform applied to the electrode over time and (b) the resulting voltammogram

1.2.2.5 Square wave voltammetry (SWV)

Square wave voltammetry was first introduced by Krauss and Ramali [1]. This method is often performed on a stationary electrode such as carbon paste, gold and glassy carbon electrodes etc. Figure 1-6 shows that, in a typical SWV, how the applied potential changes with time as well as the final response of a SWV analysis. As this figure shows, in the square wave voltammetry method, no time is given to the system to recover the diffusion layer again while applying successive potential pulses. It simply means that potential pulses are applied to the work electrode without time interval in between. Therefore, it can be said that the applied pulse profile in the SWV method is somehow similar to the differential pulse voltammetry method, except that in the SWV method no time is applied for pre-electrolysis (the time before applying a new potential pulse to the electrode to partially regenerate the diffusion layer) [14].

Figure 1-6 shows the most important parameters in a square wave voltammetric analysis. Pulse width (t_p), pulse height (ΔE_p) and potential step height (ΔE_s) are among these parameters. Frequency (f) is another alternative to show the pulse width, which is defined as the number of potential cycles per second and is expressed as $f = 1/2t_p$. Using the above definitions, the potential scan rate in a square wave voltammetric analysis can be calculated using the equation $V = \Delta E_s / 2t_p$ (where V stands for potential scan rate). It is worth noting that in the square wave voltammetry method, only frequency parameter can be varied widely. Considering the above data, it can be known that the square wave voltammetry method is a very fast method. For example, if we consider that pulse width (t_p) is 5 milliseconds and the potential step is 10 millivolts, we can scan a potential range of one volt in one second. This very high speed of the SWV makes it a very suitable choice for use in chromatographic methods as a detector.

Figure 1-6(a) clearly shows that in the square wave voltammetry method, the current is sampled twice per each potential cycle (shown by solid and hollow dots in the figure). The first current measurement is made at the end of the forward pulse and the second sampling of the current is performed at the end of the backward pulse of a potential cycle. Figure 1-6(b) shows the sampled currents variation over time and the current sampling locations (dark spots). As the applied pulse potential approaches the

reduction potential of the target species, the rate of analyte electrolysis increases sharply, and consequently the currents due to the reduction and oxidation of the analyte (in the opposite direction) begin to increase. As shown in the figure, the forward pulses accelerate the reduction of the oxidizing form and amplify the resulting cathodic currents, while the backward pulses cause the species produced in the forward (reducing) pulses to be re-oxidized

Figure 1-6(c) shows that by deduction of the forward currents from the backward currents, a peak shape net current, at about the formal reduction potential of the redox couple, is obtained, which is very similar to the differential pulse voltammetry method [15, 16].

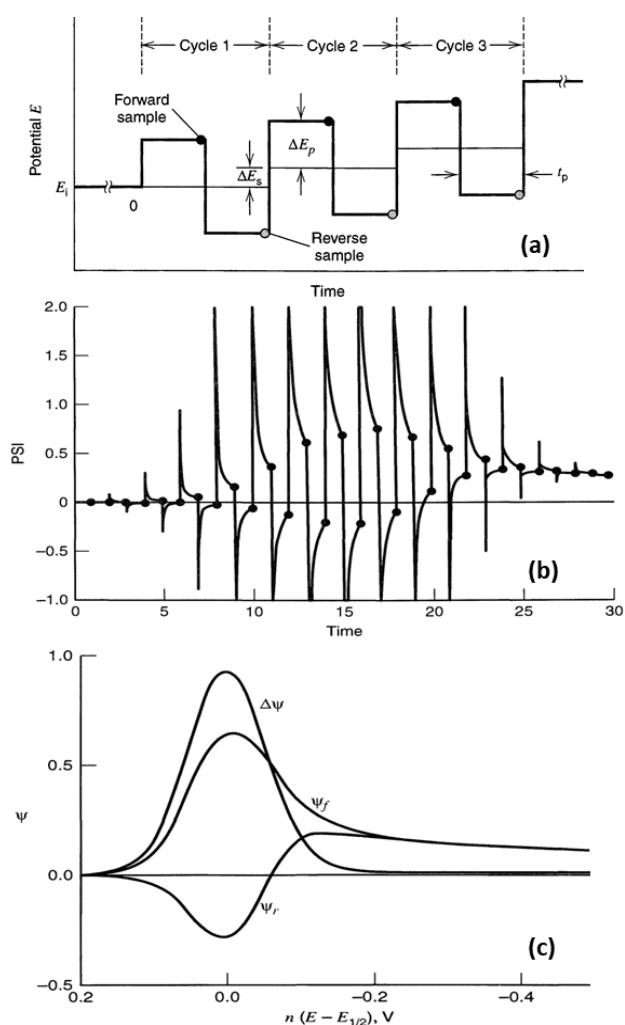


Figure 1-6. Square wave voltammetric analysis. Profile of potential waveform applied to the electrode over time (a) Current profile obtained over time (b) and normalized acquired voltammogram (c) [1].

The main advantage of the square wave voltammetry method over the cyclic voltammetry method is the ability of this method to reduce undesirable background effects, and consequently providing a more precise insight of the electrochemical systems under study. For this reason, useful quantitative information can be obtained for very low analyte concentrations using the square wave voltammetry method (compared to the cyclic voltammetry method).

1.3 Conductometric gas sensors

1.3.1 *An introduction on chemoresistive gas sensors*

Nanostructured metal oxides semiconductors (MOSs) gas sensors have attracted significant interest over the last few decades since they usually offer the advantages such as low cost, ease of fabrication, high sensor response and short response/recovery times [17]. According to the sensing properties of the metal oxides, MOSs can be typically divided into two main categories namely *n-type* metal oxides and *p-type* metal oxides. Usually, the resistances of an n-type metal oxides decrease after exposure to the reducing gases such as H₂, H₂S, CO, CH₄, NH₃ where oxidising gases such as NO₂, NO, O₃, SO₂, etc. increase the resistance of an n-type MOS. P-type metal oxides exhibit the opposite behaviour in the presence of reducing/oxidising gases [18].

Chemo-resistive metal oxide gas sensors, i.e. the gas sensing platform used in my thesis, rely on changes of electrical conductivity of the sensing material due to a change in the surrounding atmosphere. The main methods to deposit the sensing materials onto a gas sensing substrate are mostly divided into two main groups namely thin film deposition, e.g. using chemical vapour deposition method, and thick film deposition, e.g. drop casting method. More specifically,

- Thick films (thickness more than 1 μm) are easy to deposit through relatively cheaper, easier and faster techniques
- Thin film depositions (thicknesses between 5 nm and 1 μm) results in the more homogeneous sensing films, but usually these techniques are more expensive and require complex systems for the deposition.

As thick film deposition methods are typically faster and more simple, this method was used throughout my thesis, see figure 1-7.

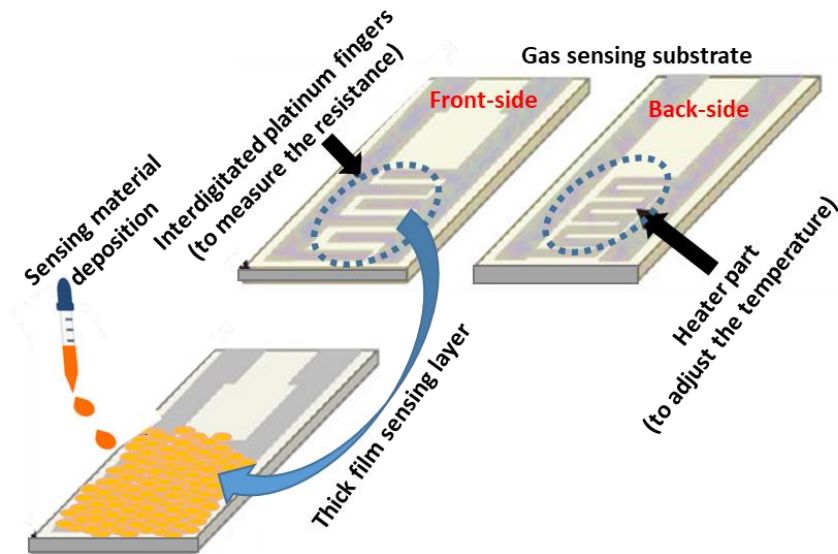


Figure 1-7. A typical thick film gas sensor preparation procedure by drop casting method using a gas sensing substrate with platinum interdigitated electrodes onto the front side and platinum heater part onto the backside.

An electrical heater is usually present on the backside of the ceramic substrate to ensure that the sensing material works at the optimal temperature.

Gas detection is broadly assumed to be related to the reactions between ionosorbed surface oxygen and the target gas [19]. There is a shift in the equilibrium state of the surface oxygen reaction in the presence of a target gas. The resulting change in the state and/or amount of the chemisorbed oxygen is emerged as a change in the sensing material conductivity. For example, when a reducing gas, e.g. H_2 , CO , ethanol, acetone, etc., comes into contact with the sensing material surface, it changes the density of the ionosorbed oxygen. This is manifested as a change in the sensor resistance which will be used as an analytical signal to quantify the concentration of the target gas [20].

The usual operating temperature of metal oxide gas sensors is from 150 to 500 °C. Operational temperature is the most important parameter influencing the performance of a chemoresistive gas sensor. To avoid long term variations in metal oxide based gas sensors function, the operating temperature should be low enough in order to prevent

significant bulk change of the sensing material and high enough so that gas reactions occur with acceptable response and recovery time.

Figure 1-8 illustrates a schematic diagram of a typical chemoresistive gas sensing setup. Herein, different gas needed for running the gas sensing setup are supplied either from certified bottles with known concentration of the desired gases (more common) or from different permeation tubes.

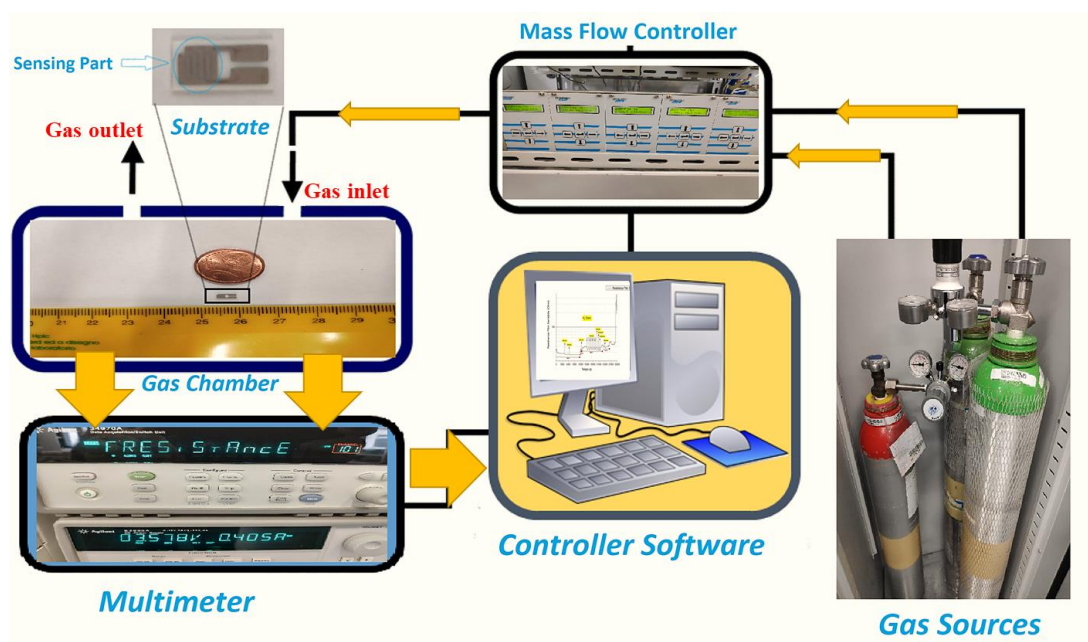


Figure 1-8. Schematic view of our in-house built gas sensing setup

These gases are mixed in the next step using mass flow controllers (MFC) to produce desired concentrations. These gas streams are later directed into a gas chamber in which gases are exposed to the sensing materials (deposited onto a gas sensing substrate). This contact between sensing material and gases inside the gas chamber brings about a variation in conductivity of the sensing material, which is then recorded using a multimeter and used as the sensing signal.

Usually two main gas mixtures is used in the chemoresistive gas sensors. First, a mixture of 20% oxygen and 80% of nitrogen which is used as a reference mixture. When the sensing material is exposed to this gas stream the recorded resistance is called baseline resistance (or reference resistance). In the next step, sensing material is exposed to another gas stream containing oxygen, nitrogen and target gas (whose concentration is going to be determined) and the new resistance is recorded as target

resistance. Depending on the gas sensing material, *p-type or n-type*, and type of target gas, *reducing or oxidizing gas*, a variation in resistance is observed. Ideally, this variation is related to the concentration of the target gas and is used to plot a calibration curve.

This operating simplicity together with low cost, miniaturization ability and compatibility to integrate with electronic devices, make MOS chemoresistive gas sensors a valuable option in real field applications. However, despite the aforementioned advantages, some limitations including low selectivity (the capability to discriminate among different gases) and low long-term stability are the main remaining challenges to be addressed.

Playing role in different fields like automotive industry, bio medics, homeland security, and breath analysis, developing gas sensors are of great importance in order to fulfil upcoming demands to develop more reliable gas sensors. In fact, by choosing specific type, size and shape of the material it is possible to improve the sensing performance of a gas sensor.

1.4 Analytical figures of merit

Chemists, to assay and eventually to compare different measurement methods, mainly use figures of merit. The most important figures of merit used in this thesis are linear dynamic range, sensitivity, selectivity and detection limit. They are briefly introduced as follows,

Linear dynamic range: Concentration range over which a *linear* change in the instrumental response (signal) is observed along with variation in the analyte concentration.

Sensitivity: Analytical sensitivity is defined as the variation in response (signal) magnitude due to the variation in the amount of analyte and is mostly reported as the change in signal per unit change of analyte. The sensitivity of a technique is correctly reported as the slope of the calibration curve and, provided the plot is linear, can be measured at any point on it.

Selectivity: Selectivity is an index that shows the ability of a method to determine particular analytes in mixtures or matrices without interfering from other components of similar properties. An analytical method is selective if its signal is a function of the amount of analyte present in the sample. In an ideal situation where the signal is *only* related to the analyte concentration, the method is called specific, which is rare to achieve.

Limit of detection: is defined as the minimum (smallest) detectable amount of analyte with a *certain level of confidence* (reliably detected). As a general rule, detection limit of an analyte shows the concentration which generates a signal *significantly* different from the 'blank' noise (commonly signal to noise ratio ≥ 3).

References

1. Bard A.J. and Faulkner L. R., *Electrochemical Methods: Fundamentals and Applications, 2nd Edition*. 2001: John Wiley and Sons Ltd.
2. Harvey D., *Modern Analytical Chemistry, 1st Edition*. 2000: McGraw-Hill Companies, Inc.
3. Rouessac F. and Rouessac A., *Chemical Analysis: Modern Instrumentation Methods and Techniques, 2nd Edition*. 2007: John Wiley & Sons, Inc.
4. Wang J. and Zeng H., *Recent advances in electrochemical techniques for characterizing surface properties of minerals*. Advances in Colloid and Interface Science, 2021. 288: p. 102346.
5. Ngamchuea K., Eloul S., Tschulik K., and Compton R.G., *Planar diffusion to macro disc electrodes—what electrode size is required for the Cottrell and Randles-Sevcik equations to apply quantitatively?* Journal of Solid State Electrochemistry, 2014. 18(12): p. 3251-3257.
6. Compton R. G. and Banks C. E., *Understanding Voltammetry, 3rd Edition*. 2018: world scientific publishing europe Ltd.
7. Batchelor-McAuley C., Kätelhön E., Barnes E.O., Compton R.G., Laborda E., and Molina A., *Recent Advances in Voltammetry*. ChemistryOpen, 2015. 4(3): p. 224-260.
8. Rees N.V. and Compton R.G., *Hydrodynamic microelectrode voltammetry*. Russian Journal of Electrochemistry, 2008. 44(4): p. 368.
9. Chillawar R.R., Tadi K.K., and Motghare R.V., *Voltammetric techniques at chemically modified electrodes*. Journal of Analytical Chemistry, 2015. 70(4): p. 399-418.
10. Bond A.M., *Broadening Electrochemical Horizons, 1st Edition*. 2002: Oxford university press.
11. Skoog A.D., West D.M., Holler F.J. , and CrouchS.R., *Fundamental of analytical chemistry, 9th Edition*. 2014: Brooks/Cole.
12. Scholz Fritz, *Electroanalytical Methods: Guide to Experiments and Applications, 2nd Edition*. 2010: Springer, Berlin, Heidelberg.
13. Labib M., Sargent E.H., and Kelley S.O., *Electrochemical Methods for the Analysis of Clinically Relevant Biomolecules*. Chemical Reviews, 2016. 116(16): p. 9001-9090.
14. Brett C.M.A. and Brett A.M.O., *Electrochemistry: Principles, Methods, and Applications*. 1994: Oxford University Press.
15. Mirceski V., Gulaboski R., Lovric M., Bogeski I., Kappl R., and Hoth M., *Square-Wave Voltammetry: A Review on the Recent Progress*. Electroanalysis, 2013. 25(11): p. 2411-2422.
16. Chen A. and Shah B., *Electrochemical sensing and biosensing based on square wave voltammetry*. Analytical Methods, 2013. 5(9): p. 2158-2173.
17. Dey A., *Semiconductor metal oxide gas sensors: A review*. Materials Science and Engineering: B, 2018. 229: p. 206-217.
18. Yang S., Lei G., Xu H., Lan Z., Wang Z., and Gu H., *Metal Oxide Based Heterojunctions for Gas Sensors: A Review*. Nanomaterials, 2021. 11(4).

19. John R.A.B. and Ruban Kumar A., *A review on resistive-based gas sensors for the detection of volatile organic compounds using metal-oxide nanostructures*. Inorganic Chemistry Communications, 2021. 133: p. 108893.
20. Majhi S.M., Mirzaei A., Kim H.W., Kim S.S., and Kim T.W., *Recent advances in energy-saving chemiresistive gas sensors: A review*. Nano Energy, 2021. 79: p. 105369.

2 Experimental activities, Results and Discussions

2.1 Electrochemical sensing analyses

2.1.1 *Tuning the NiO Thin Film Morphology on Carbon Nanotubes; Effect of shell thickness on electrochemical detection of glucose*

Abstract. Quantification of biological or biochemical substances is critical in healthcare applications. Herein, in order to take advantage of both catalytic activity of NiO for glucose oxidation and high conductivity of CNTs, NiO films with different thicknesses were deposited on the surface of stacked-cup carbon nanotube (SCCNT) using atomic layer deposition (ALD) technique. Thanks to the synergetic effect of this composite, i.e. atomic layer deposited NiO on the surface of SCCNT (NiO/SCCNT), we prepared an electrochemical sensor with high sensitivity of $1252.3 \mu\text{A cm}^{-2} \text{mM}^{-1}$ and an ultrafast response ($<2\text{s}$) for glucose determination in alkaline solution (0.1 M, KOH). Additionally, exploiting ALD technique provided us with an opportunity to deposit NiO on the SCCNT surface with different thicknesses, which in turn, enabled us to evaluate thoroughly the effect of different thicknesses of NiO on glucose measurement.

2.1.1.1 *Introduction*

Glucose is a vital biochemical substance whose detection, quantitatively or qualitatively, is of great importance not only in clinical diagnostic tests but also in food, textile and other industries [21]. Diabetes, as a widespread metabolic disorder relevant to glucose, is being changed to a prevalent challenge for human healthcare due to change in lifestyle and environmental pollutants [22]. Evaluation of glucose can be useful as a diagnostic test for diabetes mellitus, which is a global health problem with devastating social and economic impact, as well as for cancer treatment. Therefore, many efforts have been directed to evaluate glucose using different kinds of organic and inorganic materials. Many studies have been carried out to develop non-enzymatic glucose sensors based on functionalised nanostructures of noble metals (Pt, Pd, Au) and alloys (Pt Ru, Pt Pb, Pt Au, etc.). In spite of having good electrocatalytic activity, materials based on noble metals such as Pd-SWCNT [23], Pt-CNT [24], MWCNT-RuO₂ [25], Pt Ir alloy [26] and Au Pt alloy [27] exhibit limitations due to

their high cost and vulnerability to chemisorbed intermediates and chloride ions [28]. Nowadays, transition metals (e.g. W, Mn, Zn, Fe, Co, Ni, Cu) and transition metal oxides (e.g. CuO, Mn₂O₃, Co₃O₄, NiO, WO₃, RuO₂) have received noticeable attention as cost effective electrocatalysts for electrochemical sensing [27-31]. It is important to mention that the properties (i.e., sensitivity, selectivity, response times and stability) of non-enzymatic electrochemical glucose sensors strongly depend on the electrode material and its nanostructure [32, 33]. Ni based materials, especially NiO and Ni(OH)₂, have been widely reported due to their low toxicity, low cost and high electrocatalytic activity promoted by the Ni³⁺/Ni²⁺ redox couple in basic media [34, 35]. Nonetheless, the poor stability, high charge transfer resistance and sheet resistance, which lead to insufficient electron-transfer kinetics, hinder the wide applications of Ni based materials in electrochemical sensors.

Herein, the fabrication of NiO/SCCNTs nanocomposites by ALD with different number of ALD cycles (25, 50, 100, 200, 400 and 700), as well as their morphological, structural and electrochemical characterization, and their application as the active electrode material for enzyme-free glucose detection is reported. Using ALD technology gave us this opportunity to not only prepare a sensitive and selective sensor for glucose but also to investigate the effects of thickness of nickel oxide layer on the performance of the proposed sensor for glucose determination.

2.1.1.2 Electrode preparation

Electrochemical measurements were performed using commercial screen-printed carbon electrode (SPCE), comprising of a planar substrate equipped with a carbon working electrode (4 mm in diameter, geometric area of 0.1257 cm²), a silver pseudo-reference electrode and a carbon auxiliary electrode. To modify the bare SPCEs, 1.0 mg of each NiO/SCCNTs nanostructure, i.e. SCCNT coated with NiO through 25, 50, 100, 200, 400 and 700 cycles of ALD, was ultrasonically dispersed in distilled water (1 mL). The desirable amounts of the homogenous dispersions were directly drop casted onto the surface of the carbon working electrode and left at room temperature to dry until further use. Cyclic voltammetry (CV) and amperometry (I-t) techniques were applied at DropSens μ Stat 400 Potentiostat empowered by Dropview 8400

software for data acquisition. All experiments were performed at room temperature unless otherwise stated.

2.1.1.3 Result and discussion

2.1.1.3.1 Transmission electron microscopy analyses (TEM)

The detailed structure and morphology of the as synthesized NiO/SCCNT samples was analyzed by transmission electron microscopy (TEM). Fig. 2-1 shows TEM and high-resolution TEM (HRTEM) images for samples coated through 25, 50, 100, 200, 400 and 700 cycles of NiO ALD (abbreviated as S25, S500, S100, S200, S400 and S700, respectively). The diameter of the SCCNT as found by TEM images is around 75-110 nm. To differentiate between the samples, a thorough investigation was made by taking the TEM images of individual SCCNT/NiO composites.

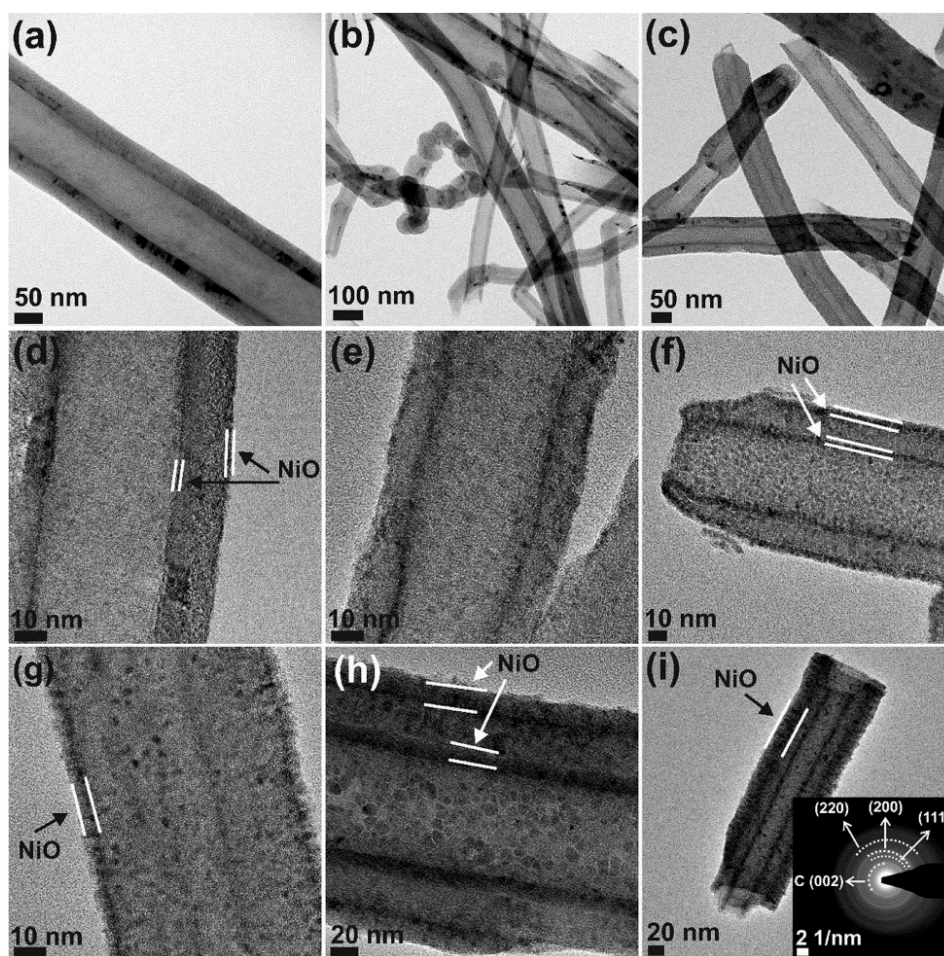


Figure 2-1. TEM images of pristine SCCNT (a, b), an overview of NiO coated SCCNTs with 100 ALD cycles (c), HRTEM images for S25 (d), S50 (e), S100 (f), S200 (g), S400 (h) and S700 (i). The inset in (i) shows the SAED pattern of S400.

It can be clearly seen that, SCCNT are equally and conformably coated from the inner and the outer surfaces with NiO nanoparticles. The polycrystalline character of the coating was confirmed by SAED (inset in Figure 2-1i) for the sample with 400 NiO ALD cycles. The main Debye-Scherrer rings correspond to the (111), (200) and (220) planes of the rock salt structure of NiO and to the (002) plane for graphitized carbon in the composites. The thickness of the NiO coating increases with the no. of ALD cycles, the average thickness calculated for samples coated with 25, 50, 100, 200, 400 and 700 cycles is 0.8 nm, 1.7 nm, 4.0 nm, 6.5 nm, 14.0 nm and 21.8 nm, respectively, figure 2-2.

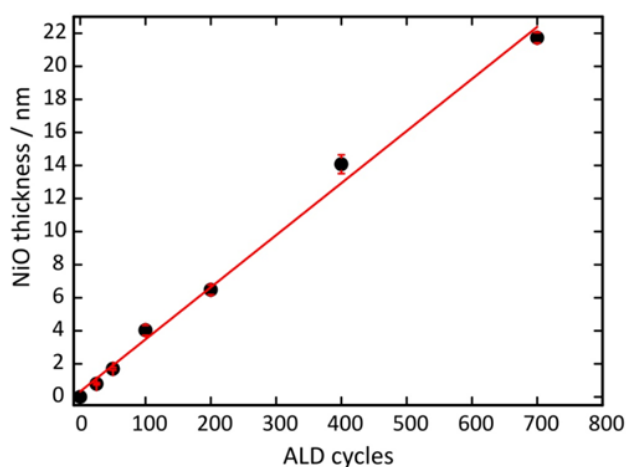


Figure 2-2. Thickness of the NiO film as a function of number of ALD cycles, under self limiting conditions. The linear fitting crosses the origin with a slope of $0.32 \text{ \AA} \text{ cycles}^{-1}$.

The layer proportionately developed with the no. of ALD cycles and the growth per cycle (GPC) is calculated as 0.032 nm from the slope of the linear fit ($R^2=0.9957$), proving the self-limiting growth behavior of the ALD process.

2.1.1.3.2 Electrochemical behavior of glucose at CNT/NiO modified electrode

In order to understand the electrochemical behavior of CNT/NiO modified electrodes, cyclic voltammetry (CV) analysis was carried out in alkaline medium (KOH solution). Regarding this, we investigated some key factors which are of great importance in both practical and theoretical aspects of glucose oxidation. Effect of different thickness of NiO on glucose oxidation, effect of alkalinity of medium as well as scan rate on electrochemical glucose oxidation, and, finally, evidences about EC' mechanism of glucose oxidation were thoroughly studied.

2.1.1.3.3 Effect of NiO thickness on glucose oxidation

Cyclic voltammetry was used for studying the interfacial redox chemistry of the nickel oxide nanostructures toward glucose oxidation. Fig. 2-3 illustrates typical CVs recorded in 0.1 M KOH with and without glucose for a CNT/NiO modified electrode (S200).

CVs for the CNT/NiO modified electrode showed a pair of well-defined anodic and cathodic peaks at about 0.530 and 0.470 V in 0.1 M KOH solution (dashed curve in fig. 2-3). These two peaks can be ascribed to Ni^{II}/Ni^{III} redox pair or Ni(OH)₂/NiOOH. Generally, electrochemical behavior of NiO toward glucose oxidation in alkaline solutions can be explained as follows: first NiO is converted to Ni(OH)₂ in alkaline medium and after that Ni(OH)₂ species generate oxyhydroxide species (NiOOH) by cycling potential, see equations 1 and 2 [36]. Afterward, NiOOH nanostructures oxidize glucose while being itself reduced back again to Ni(OH)₂. Regeneration of Ni(OH)₂ due to irreversible reduction of NiOOH by glucose increases oxidation peak current in the presence of glucose. NiOOH that is considered as active form of nickel hydroxide for catalytic oxidation of glucose, can be reproduced again via oxidation of Ni(OH)₂ at electrode surface which resulting in a catalytic cycle. Meanwhile, in the presence of glucose, cathodic peak decreases with increasing glucose concentration because NiOOH species have been already consumed by glucose and, consequently, relatively smaller current will be generated during cathodic scan, see Fig 2-3. Another interesting aspect of glucose oxidation at CNT/NiO modified electrode was positively shift of anodic peak potential with increasing glucose concentration, which has been already observed in other reports [37, 38]. Although there is not complete agreement on the reason, however, change in local pH at the electrode surface due to prolong and rapid oxidation cycle [39] and diffusion-limited process of glucose at CNT/NiO modified electrode [40] can be considered as possible reasons for this observation.



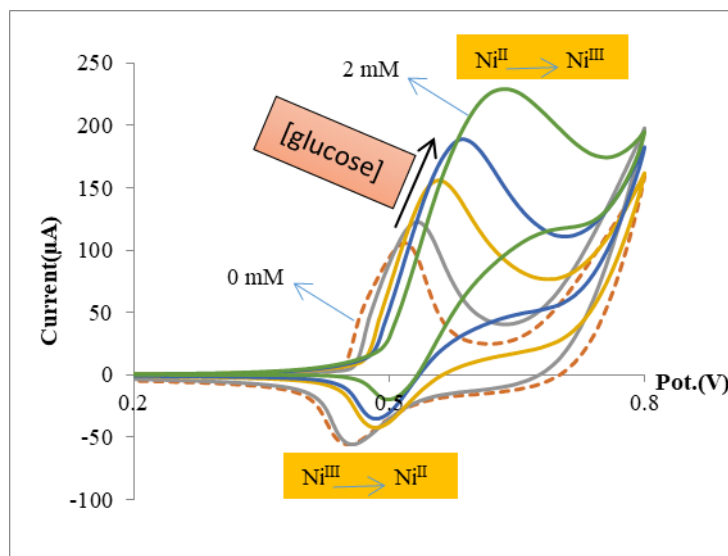


Figure 2-3. Recorded cyclic voltammograms in a 0.1 M KOH solution containing different amounts of glucose at 50 mV/s for S200 modified electrode.

Effect of different thickness of deposited NiO onto CNT toward oxidation of glucose was explored by preparing different modified electrode using S25, S50, S100, S200 and S400. Here, we put our attentions on two important figures of merit i.e. sensitivity and linear dynamic range (LDR) for glucose measurement using these modified electrodes. For achieving this, calibration curves for measurement of glucose with different modified electrodes were obtained using cyclic voltammetry and sensitivity (slope of calibration curve) and LDR were extracted from them. As can be seen in fig. 2-4, sensitivity of glucose determination increases with increasing the thickness of NiO up to S100, however, for higher thickness, i.e. S200 and S400, sensitivity decreases to some extent. This interesting observation can be explained keeping this in mind that, active sites for glucose sensing are NiO species, after converting to NiO(OH); hence, for S25 response to glucose is lowest due to the lack of NiO species for glucose oxidation. However, increasing amount of NiO species from S25 to S100 endows higher and higher sensitivity to corresponding sensors and finally for S100 sensitivity reaches the highest value because available active sites for glucose oxidation become maximum. For higher thickness, e.g., S200 and S400, increasing the thickness of NiO cannot increase the available active sites anymore, therefore, sensitivity curve reaches a plateau in this area or even declines because NiO is originally an insulant material and can increase resistance of electrode. Very sharp rising in LDR from S25 to S100 and becoming almost the same for S100, S200 and S400 can also be understood

regarding abovementioned reasons. Less NiO active sites in S25 and S50 can be saturated in lower concentrations of glucose and causes deviation of calibration curve from linearity even in low concentration of glucose. Therefore, S100 modified electrode was chosen for further studies. we also optimized amount of nanocomposites for electrode modification by dropping different amount of 1 mg/mL suspension of S100 onto the SPE, i.e. 2, 4, 6 and 8 μL , see fig. 2-4. 4 μL was chosen as the optimum volume because it gave the highest difference between i_p in the presence of glucose (2 mM) and i_p in the absence of glucose (0.1 M KOH).

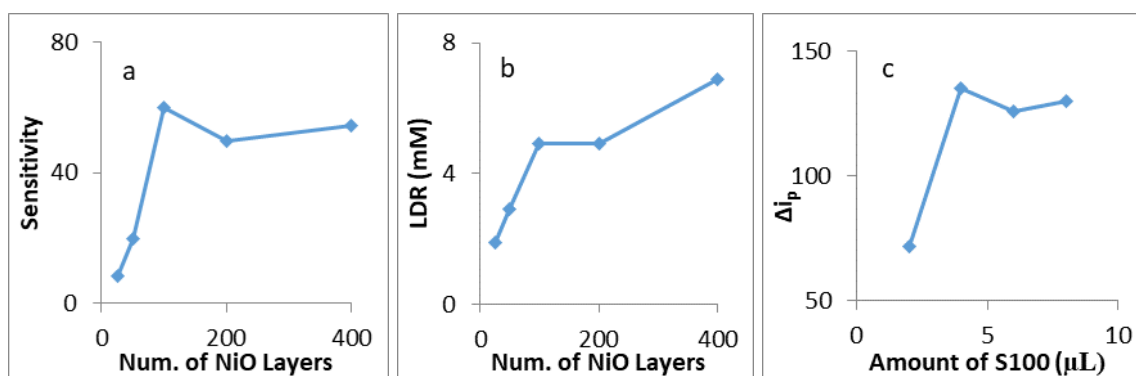


Figure 2-4. Effect of different amount of deposited NiO on (a) sensitivity and (b) LDR of glucose determination. (c) Effect of different amounts of S100 on background subtracted current (Δi_p) in glucose solution.

2.1.1.3.4 KOH effect

Further, behaviour of S100 modified electrode was thoroughly studied using different concentration of KOH from 0.01 M to 1 M in order to optimize KOH concentration and obtained results have been presented in fig. 2-5. Displayed results in fig. 2-5a depict that, in 0.01 M KOH solution anodic peak potential is appeared in a much more positive potential and peak current is considerably lower than other KOH concentrations. However, enhancing anodic peak current continues sharply from 0.01 to 0.1 M KOH concentration, maximized at 0.1 M and decreases, to some extent, from 0.2 to 1 M of KOH. These observations can be explained considering this that OH^- ions have great impact on sensing properties of CNT/NiO modified electrode toward glucose, see Eq1,2 and 3. In very low concentration of KOH, e.g. 0.01M, NiO(OH) cannot be produced enough form NiO species and, due to critical role of NiO(OH) in catalytical oxidation of glucose, peak current will be lower and peak potential occurs at higher potential. However, very high concentrations of KOH are not suitable for

performance of CNT/NiO modified electrodes since high concentrations of OH⁻ ions can block adsorption of glucose and/or causes producing undesirable intermediates during oxidation of glucose which block the surface of electrode [41] and decrease the peak current. Then, 0.1 M KOH was used for further tests.

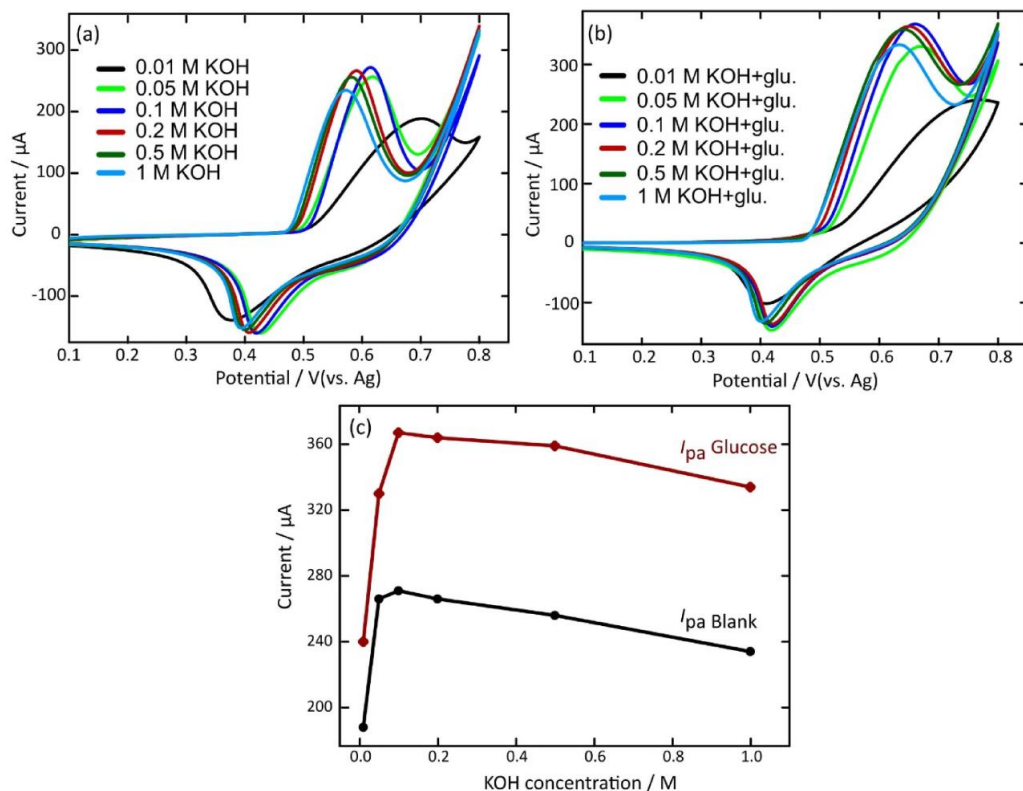


Figure 2-5. Cyclic voltammograms of the NiO/CNT modified electrode (a) in different KOH concentrations and (b) in in different KOH concentrations and a constant glucose concentration at scan rate of 50 mVs^{-1} . (c) Peak current of cyclic voltammograms in the absence (blue) and presence (red) of a constant concentration of glucose.

2.1.1.3.5 Scan rate effect

Effect of scan rate on sensing process of CNT/NiO modified electrode was studied to provide evidences about kinetic of reaction of glucose at the electrode surface. As scan rate was enhanced from 5 to 100 mV/s (fig. 2-6) both anodic and cathodic peak currents increased alongside with shift in cathodic and anodic peak potentials in negative and positive directions, respectively. Fig. 2-6 depicts both anodic and cathodic peak currents correlate with square root of scan rate with coefficient of determination (R^2) of 0.9998 and 0.9975, respectively. These data show electrochemical process of glucose determination is being controlled by slow diffusing

step(s) towards or away from electrode. Another interesting result, which can be obtained from scan rate study, is comparing recorded CVs at low scan rate with high scan rate. As it is obvious in fig. 2-6, at very low scan rate, e.g. 5mV/s, cathodic peak will be completely disappeared and just there is anodic peak. However, at higher scan rates cathodic peak gradually grows and becomes significant at higher scan rates. For explaining this phenomenon, according to Eq. 1-3, electrochemical reaction 2 is followed by chemical reaction 3 in which produced Ni^{III} in Eq.2 is consumed by glucose in Eq.3. Therefore, in slow scan rates glucose species have enough time to consume almost all produced Ni^{III} and avoiding of generation of cathodic peak in CV. However, at high scan rates, glucose species do not have enough time to consume produced Ni^{III} and these remained Ni^{III} species generate the cathodic peak. As a result, we can conclude that, electro-chemical oxidation of glucose might be occur according to Eq.1-3 in which an electrochemical reaction(Eq.2) is followed by a catalytic chemical reaction (Eq.3) that is a so-called EC' mechanism, here in this case, chemical reaction is rate-determining step (RDS).

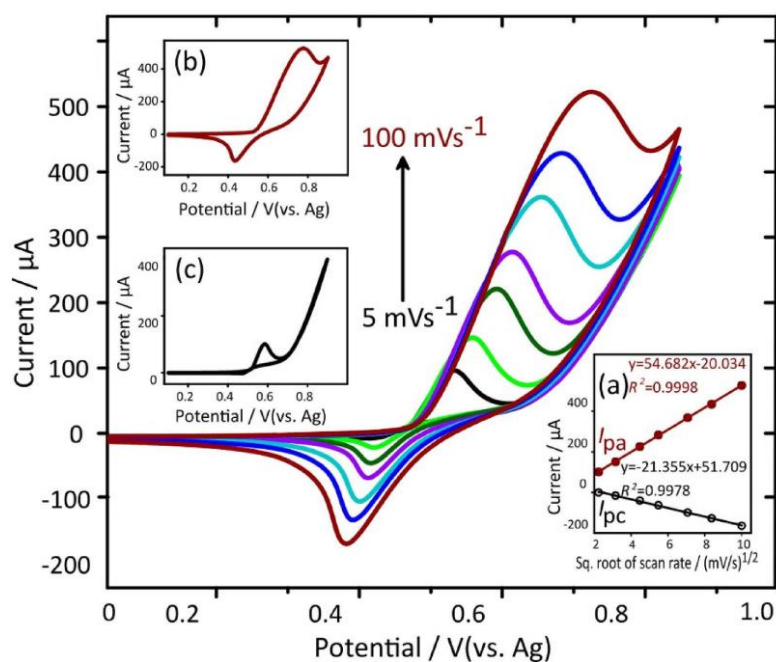


Figure 2-6. Cyclic voltammograms of the NiO/CNT modified electrode, S100, at different scan rates in the presence of glucose. Insets show (a) the plots of peak currents vs. square root of scan rate and enlarged cyclic voltammograms of NiO/CNT modified electrode at (b) 100 mVs^{-1} and (c) 5 mVs^{-1} .

2.1.1.3.6 Amperometric application of CNT/NiO modified electrode for glucose sensing

The amperometric performance of the S100 electrode was assessed by successive step-wise addition of glucose aliquots to 0.1 M KOH solution. Since the working potential has a great effect on the amperometric signals and therefore it affects the relative glucose determination, in order to enhance the analytical performance of NiO/SCCNTs sensors, comparison experiments were carried out in the range of 0.55 V to 0.75 V to optimize the applied potential (E_{app}), (Figure 2-7a). At the E_{app} of 0.55 V and 0.75 V, the responses rapidly deviated from linearity at high and low glucose concentration resulting in a narrow measurement range. The best results regarding sensitivity and linearity were obtained at $E_{app}=0.65$ V, which was selected as the optimum working potential for the subsequent amperometric analyses. Repeatability of the proposed sensor was investigated using S100 electrode prepared by dropping 4 μ L of the samples onto the surface of the SPCE. This sensor is highly stable, proven by a relative standard deviation (RSD) of 1.2 % for three successive glucose measurements, and is not poisoned by products and/or intermediate species during the glucose measurements (Figure 2-7b). This high stability of the NiO/SCCNTs sensors (by using even a very small amount of the sample, 0.0038 mg/0.1257 cm²) is due to the strong interaction of ALD deposited NiO particles onto the SCCNT substrate, which also caused to reduce the dissolution and aggregation of NiO particles in the electrolytic solution. Moreover, our group in a recent publication also reports the stability of the electrode using the same material (NiO/CNTs by ALD) for OER in similar conditions. It is noted that NiO/CNTs with 100 ALD cycles is the best electrode in both studies, which shows a remarkable stable potential profile and a well-protected core-shell structure even after the 12 hours of chronoamperometric measurements in 1 M KOH solution. Additionally, in the same report, the XRD pattern of the sample (NiO/CNTs-100) was also measured after 1 h of treatment in 1 M KOH, under similar conditions as the electrochemical experiments.

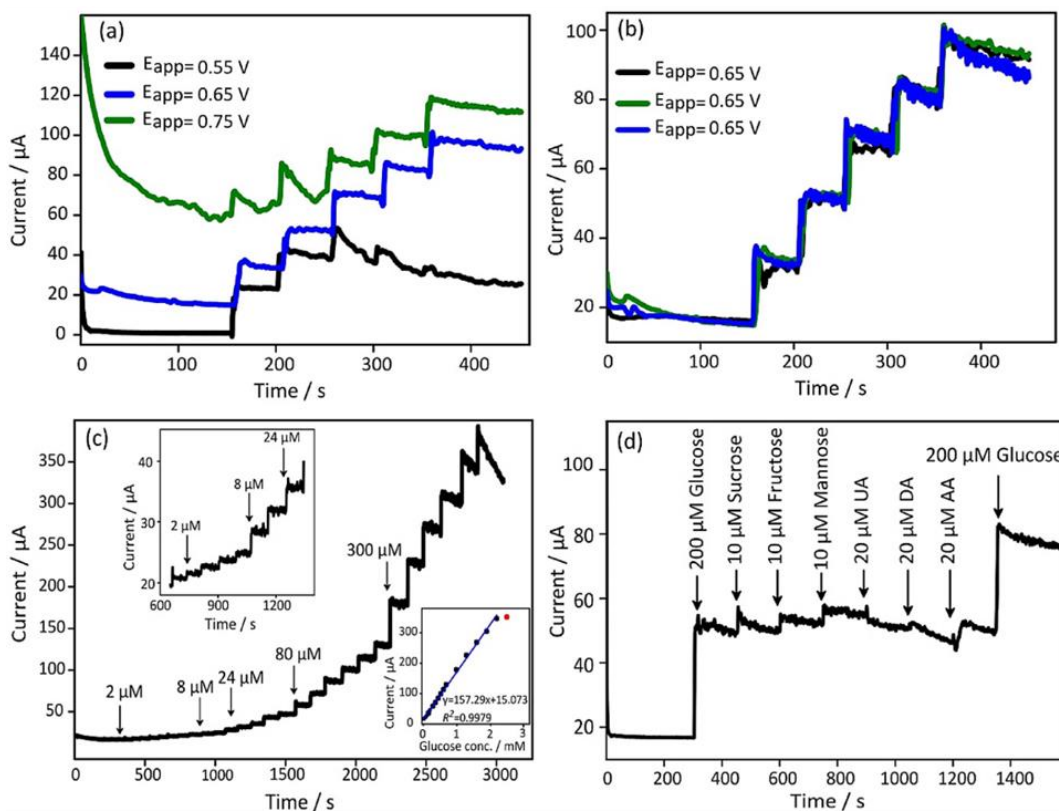


Figure 2-7. Chronoamperometric tests using S100 electrode with serial additions of glucose solutions in order to increase the total glucose concentration of the electrolyte by steps of 100 μM at different applied potentials (a) and at $E_{\text{app}}=0.65\text{ V}$ for three different measurements with the same electrode (b). Current-time responses of S100 electrode acquired in 0.1 M KOH solution and increasing concentrations of glucose at $E_{\text{app}}=0.650\text{ V}$, insets show the current-time responses in the low glucose concentration and the calibration curve for glucose determination using S100 electrode (c). Interference study to selected species on S100 electrode in 0.1 M KOH and 0.2 mM glucose (d).

However, no significant change was observed, which again proved a good stability of NiO coating for the ALD synthesized NiO/CNTs electrodes [42]. These results are also well supported by XPS characterisation for NiO/SiC nanocomposites prepared by ALD for electrochemical sensing.4 The stability of ALD synthesized NiO/CNTs is also discussed in a recent articles focused on electrochemical sensing [43]. Figure 2-7c shows that the amperometric measurements of glucose result in a well-defined steady state curve. An interesting aspect of this sensor is the fast response toward glucose oxidation. This sensor rapidly responded after addition of glucose and reached 95% of steady-state current in less than 2 seconds. The calibration curve from the amperometric measurements shows a linear dependence on the glucose concentration over a vast range of concentrations from 2 μM to 2.2 mM with a sensitivity of (extracted from the slope of calibration plot) 1252.30 $\mu\text{A cm}^{-2}\text{ mM}^{-1}$ and a

determination coefficient (R^2) of 0.9979 (inset of Figure 2-7c). The limit of detection was determined as 0.10 μM considering a signal-to-noise ratio (S/N) of 3. Some easily oxidized electrochemical active bio organic substances that usually co-exist with glucose in the human blood can interfere with the performance of non-enzymatic glucose sensors. Therefore, interference studies need to be carried out to prove the applicability of any electrochemical glucose sensor. The selectivity of our sensor was tested by amperometric detection at an applied potential of 0.65 V with S100 electrode by adding 0.2 mM of glucose in the electrolyte followed by the successive addition of 10–20 μl of sucrose (Suc), fructose (Fru), mannose (Man), uric acid (UA) dopamine (DA) and ascorbic acid (AC). Since, in physiological samples the glucose concentration is much higher (ca. 3–8 mM) compared to these interfering species (<0.5 mM) [28, 44], we selected a similar difference of concentrations for the interference study. As shown in Figure 2-7d, the corresponding oxidation current responses for a set of sugars like Suc, Fru and Man at 10 μM , and 20 μM endogenous metabolites, namely UA, DA and AC are relatively small as compared to 0.2 mM glucose. These results indicate that NiO/SCCNTs electrodes have a good selectivity towards glucose oxidation reaction in the concentration range of physiological samples and could compete with enzymatic glucose sensors.

Moreover, these figures of merit were also favourably compared with state-of-the-art sensors based on NiO in the Table 2-1.

Table 2-1 Comparative study of different modified electrode glucose sensors reported in literature

Electrode	LDR	LOD (μM)	Sensitivity ($\mu\text{A cm}^{-2} \text{mM}^{-1}$)	Response Time (s)	Ref.
Ni/MWCNTs ¹	3.2 μM –17.5 mM	0.89	67.2	< 2	[45]
NiO/GNS ²	5.0 μM –4.2 mM	5.0	666.71	5	[46]
NiO/CPE ³	1 μM –110 μM	0.16	5590	< 5	[33]
NiO QDs ⁴	1 μM –10 mM	26	13.14	---	[47]
	and 10–50 mM		7.31		
NiNPs/SMWCNT s ⁵	1 μM –1mM	0.5	1438	3	[48]
NiF ⁶	50 μM –7.35 mM	2.2	---	5	[49]
f-Ni(OH) ₂ -CNT ⁷	100 μM –1.1 mM	0.5	238.5	3	[50]
Macro- mesoporous NiO	10 μM –8.3 mM	1.0	243	< 5	[51]
NiO/CuO/PANI ⁸	20 μM –2.5 mM	2	---	5	[52]
ALD NiO/CNT ⁹	2 μM –2.2 mM	0.1	1252.3	< 2	This work

2.1.1.3.7 Conclusions

In summary, SCCNTs coated with various thicknesses of NiO by atomic layer deposition were successfully synthesized. NiO particles of a uniform morphology form a thin film, which becomes more dense with the increase of the number of ALD cycles. The electrocatalytic performance of the nanocomposites depends on the thickness of the NiO coating. The sample obtained with 100 ALD cycles (S100) shows one of the best electrochemical performance reported so far for an enzyme-free glucose sensor in alkaline media. Indeed, our sensors showed a high sensitivity of 1252.30 $\mu\text{A cm}^{-2} \text{mM}^{-1}$ over a wide linear range of concentrations (i. e., from 2 μM to 2.2 mM) and a low detection limit (0.10 μM , $S/D=3$), and a high selectivity and reproducibility. The

¹ nickel combined with multi-walled carbon nanotubes

² Nickel oxide-decorated graphene nanosheet

³ Potential scanning nano NiO modified carbon paste electrodes

⁴ nickel oxide quantum dots

⁵ nickel nanoparticles/straight multi-walled carbon nanotubes

⁶ three-dimensional porous Ni foam

⁷ Nickel hydroxide nanoflowers/carbon nano tube

⁸ Novel nickel and copper oxide nanoparticle modified polyaniline

⁹ Atomic layer deposited NiO/Carbon nano tubes

remarkable performances can be attributed to a combination of desired characteristics such as the conformal NiO coating obtained by ALD, the high specific surface area of the electrode and the good conductivity of the SCCNT substrate. These characteristics make it possible to measure with precision the glucose concentration in physiological samples.

References

21. Galant A.L., Kaufman R.C., and Wilson J.D., *Glucose: Detection and analysis*. Food Chemistry, 2015. 188: p. 149-160.
22. Ocvirk G. B.H., DuVall S.H. , *Electrochemical Glucose Biosensors for Diabetes Care*. In: Matysik F.M. (eds) *Trends in Bioelectroanalysis*. Bioanalytical Reviews. 2016.
23. Meng L., Jin J., Yang G., Lu T., Zhang H., and Cai C., *Nonenzymatic Electrochemical Detection of Glucose Based on Palladium–Single-Walled Carbon Nanotube Hybrid Nanostructures*. Analytical Chemistry, 2009. 81(17): p. 7271-7280.
24. Rong L.-Q., Yang C., Qian Q.-Y., and Xia X.-H., *Study of the nonenzymatic glucose sensor based on highly dispersed Pt nanoparticles supported on carbon nanotubes*. Talanta, 2007. 72(2): p. 819-824.
25. Tehrani R.M.A. and Ab Ghani S., *MWCNT-ruthenium oxide composite paste electrode as non-enzymatic glucose sensor*. Biosensors and Bioelectronics, 2012. 38(1): p. 278-283.
26. Holt-Hindle P., Nigro S., Asmussen M., and Chen A., *Amperometric glucose sensor based on platinum–iridium nanomaterials*. Electrochemistry Communications, 2008. 10(10): p. 1438-1441.
27. Wang X., Yang T., Feng Y., Jiao K., and Li G., *A Novel Hydrogen Peroxide Biosensor Based on the Synergistic Effect of Gold-Platinum Alloy Nanoparticles/Polyaniline Nanotube/Chitosan Nanocomposite Membrane*. Electroanalysis, 2009. 21(7): p. 819-825.
28. Zeng G., Li W., Ci S., Jia J., and Wen Z., *Highly Dispersed NiO Nanoparticles Decorating graphene Nanosheets for Non-enzymatic Glucose Sensor and Biofuel Cell*. Scientific Reports, 2016. 6(1): p. 36454.
29. Wang L., Lu X., Wen C., Xie Y., Miao L., Chen S., Li H., Li P., and Song Y., *One-step synthesis of Pt–NiO nanoplate array/reduced graphene oxide nanocomposites for nonenzymatic glucose sensing*. Journal of Materials Chemistry A, 2015. 3(2): p. 608-616.
30. Sun F., Li L., Liu P., and Lian Y., *Nonenzymatic Electrochemical Glucose Sensor Based on Novel Copper Film*. Electroanalysis, 2011. 23(2): p. 395-401.
31. Chen X.-m., Cai Z.-m., Lin Z.-j., Jia T.-t., Liu H.-z., Jiang Y.-q., and Chen X., *A novel non-enzymatic ECL sensor for glucose using palladium nanoparticles supported on functional carbon nanotubes*. Biosensors and Bioelectronics, 2009. 24(12): p. 3475-3480.
32. Prasad R. and Bhat B.R., *Multi-wall carbon nanotube–NiO nanoparticle composite as enzyme-free electrochemical glucose sensor*. Sensors and Actuators B: Chemical, 2015. 220: p. 81-90.
33. Mu Y., Jia D., He Y., Miao Y., and Wu H.-L., *Nano nickel oxide modified non-enzymatic glucose sensors with enhanced sensitivity through an electrochemical process strategy at high potential*. Biosensors and Bioelectronics, 2011. 26(6): p. 2948-2952.

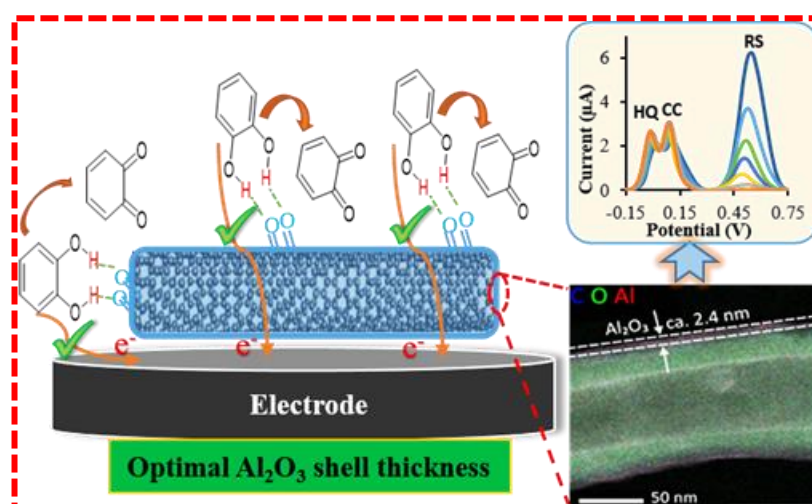
34. Luo L., Li F., Zhu L., Ding Y., Zhang Z., Deng D., and Lu B., *Nonenzymatic glucose sensor based on nickel(II)oxide/ordered mesoporous carbon modified glassy carbon electrode*. Colloids and Surfaces B: Biointerfaces, 2013. 102: p. 307-311.
35. Cao F., Guo S., Ma H., Shan D., Yang S., and Gong J., *Nickel oxide microfibers immobilized onto electrode by electrospinning and calcination for nonenzymatic glucose sensor and effect of calcination temperature on the performance*. Biosensors and Bioelectronics, 2011. 26(5): p. 2756-2760.
36. Garcia-Garcia F.J., Salazar P., Yubero F., and González-Elipse A.R., *Non-enzymatic Glucose electrochemical sensor made of porous NiO thin films prepared by reactive magnetron sputtering at oblique angles*. Electrochimica Acta, 2016. 201: p. 38-44.
37. Ci S., Huang T., Wen Z., Cui S., Mao S., Steeber D.A., and Chen J., *Nickel oxide hollow microsphere for non-enzyme glucose detection*. Biosensors and Bioelectronics, 2014. 54: p. 251-257.
38. Marini S., BenMansour N., Hjjiri M., Dhahri R., ElMir L., Espro C., Bonavita A., Galvagno S., Neri G., and Leonardi S.G., *Non-enzymatic Glucose Sensor Based on Nickel/Carbon Composite*. Electroanalysis, 2018.
39. Doyle R.L., Komarkova G., O'Brien P., and Lyons M.E.G. *Non-enzymatic glucose oxidation at electrocatalytic metal oxide films*. in *ECS Transactions*. 2013.
40. Yang J., Yu J.-H., Rudi Strickler J., Chang W.-J., and Gunasekaran S., *Nickel nanoparticle–chitosan-reduced graphene oxide-modified screen-printed electrodes for enzyme-free glucose sensing in portable microfluidic devices*. Biosensors and Bioelectronics, 2013. 47: p. 530-538.
41. Prasad R., Ganesh V., and Bhat B.R., *Nickel-oxide multiwall carbon-nanotube/reduced graphene oxide a ternary composite for enzyme-free glucose sensing*. RSC Advances, 2016. 6(67): p. 62491-62500.
42. Fan Y., Wu Y., Clavel G., Raza M.H., Amsalem P., Koch N., and Pinna N., *Optimization of the Activity of Ni-Based Nanostructures for the Oxygen Evolution Reaction*. ACS Applied Energy Materials, 2018. 1(9): p. 4554-4563.
43. Zhao L., Yu J., Yue S., Zhang L., Wang Z., Guo P., and Liu Q., *Nickel oxide/carbon nanotube nanocomposites prepared by atomic layer deposition for electrochemical sensing of hydroquinone and catechol*. Journal of Electroanalytical Chemistry, 2018. 808: p. 245-251.
44. Niu X., Lan M., Zhao H., and Chen C., *Highly Sensitive and Selective Nonenzymatic Detection of Glucose Using Three-Dimensional Porous Nickel Nanostructures*. Analytical Chemistry, 2013. 85(7): p. 3561-3569.
45. Sun A., Zheng J., and Sheng Q., *A highly sensitive non-enzymatic glucose sensor based on nickel and multi-walled carbon nanotubes nanohybrid films fabricated by one-step co-electrodeposition in ionic liquids*. Electrochimica Acta, 2012. 65: p. 64-69.
46. Zeng G., Li W., Ci S., Jia J., and Wen Z., *Highly Dispersed NiO Nanoparticles Decorating graphene Nanosheets for Non-enzymatic Glucose Sensor and Biofuel Cell*. Scientific Reports, 2016. 6.
47. Jung D.-U.-J., Ahmad R., and Hahn Y.-B., *Nonenzymatic flexible field-effect transistor based glucose sensor fabricated using NiO quantum dots modified ZnO nanorods*. Journal of Colloid and Interface Science, 2018. 512: p. 21-28.

48. Nie H., Yao Z., Zhou X., Yang Z., and Huang S., *Nonenzymatic electrochemical detection of glucose using well-distributed nickel nanoparticles on straight multi-walled carbon nanotubes*. Biosensors and Bioelectronics, 2011. 30(1): p. 28-34.
49. Lu W., Qin X., Asiri A.M., Al-Youbi A.O., and Sun X., *Ni foam: a novel three-dimensional porous sensing platform for sensitive and selective nonenzymatic glucose detection*. Analyst, 2013. 138(2): p. 417-420.
50. Yang H., Gao G., Teng F., Liu W., Chen S., and Ge Z., *Nickel hydroxide nanoflowers for a nonenzymatic electrochemical glucose sensor*. Journal of the Electrochemical Society, 2014. 161(10): p. B216-B219.
51. Fan Y., Yang Z., Cao X., Liu P., Chen S., and Cao Z., *Hierarchical Macro-Mesoporous Ni(OH)₂ for Nonenzymatic Electrochemical Sensing of Glucose*. Journal of The Electrochemical Society, 2014. 161(10): p. B201-B206.
52. Ghanbari K. and Babaei Z., *Fabrication and characterization of non-enzymatic glucose sensor based on ternary NiO/CuO/polyaniline nanocomposite*. Analytical Biochemistry, 2016. 498: p. 37-46.

2.1.2 CNT-Al₂O₃ core-shell nanostructures; effect of Al₂O₃ thickness on the electrochemical detection of dihydroxybenzene isomers

Abstract: This study aimed at analysing the effect of thickness of dielectric Al₂O₃ coatings on the conductive stacked-cup carbon nanotubes (SCCNTs) to their electrochemical properties. Atomic layer deposition (ALD) technique was used to deposit well-controlled variable thicknesses of Al₂O₃ on the SCCNTs substrates. The SCCNT/Al₂O₃ (X) modified screen printed electrodes (SPEs) were used to study their electrochemical performances towards the simultaneous determination of dihydroxybenzene isomers, namely hydroquinone (HQ) and catechol (CC). Results revealed that SCCNT/Al₂O₃ nanostructures are highly active towards dihydroxybenzene isomers and both sensitivity and selectivity of the developed electrochemical sensors are strongly dependent on the thickness of the Al₂O₃ layer. The SCCNT/Al₂O₃ heterostructures with the 9 and 19 ALD cycles (~ 2.4-3.6 nm, thickness of Al₂O₃ layer) show the best performance among other samples. The best performance was found at a shell thickness of 2.4 nm, where the peak currents increased about 10 times as compared to the non-coated CNTs modified electrode.

Graphical abstract



2.1.2.1 Introduction

Phenolic compounds such as hydroquinone (HQ, 1,4-benzenediol) and catechol (CC, 1,2-benzenediol) are distinguished members of di-hydroxybenzene family. Today, they are extensively exploited as organic intermediates in different industries including cosmetic, tanning, pharmaceutical and pesticide industries [53]. In a throughout study it was revealed that in the presence of a mixture of these two di-hydroxybenzene isomers, a synergistic genotoxic response is produced in cultured human lymphocytes. The results present further support on the hypothesis that benzene derivatives can be potentially accused for genotoxicity and leukemia in humans [54]. Besides, di-hydroxybenzenes are considered as important ecological pollutants owing to their toxicity for plants and animals and slow degradation in the nature. Considering aforementioned points, it is of great importance to develop reliable and effective techniques to monitor these two isomers. This goal has been seeking by the scientists and many analytical methods have been developed including high performance liquid chromatography with fluorescence detection [55], gas chromatography with quadrupole mass spectrometry detection [56], fluorescence spectroscopy-based methods [57], electro-chemiluminescence [58], UV-vis spectrophotometry [59] and, last but not the least, electroanalytical techniques [60, 61]. However, among all of these proposed methods, electrochemical methods have been found an elegant place thanks to the electroactive nature of these isomers. The ease of instrumentation, low cost and simplicity are spectacular features that make electroanalytical methods an appealing option over other analytical methods.

Due to the analogous composition of these phenolic di-hydroxybenzene isomers and the coexistence of other interference species, the selectivity and sensitivity of electrochemical sensors for HQ and CC remains challenging. Sensitivity and selectivity are two major factors whose improvements have been always an active field in electrochemical sensing. More sensitive and selective sensors enable us to come closer to the practical application of the sensors where, usually, low concentration of analytes and/or presence of other potentially interferences obstacle practical application of sensors.

Even though, many supported metal oxide nanoparticles with remarkable electrochemical properties have been applied to comprehend the selective and

sensitive detection of HQ and CC, however, a precise control over the size and distribution of MO_x nanoparticles onto the conductive supports remains challenging.

Atomic layer deposition (ALD) has been reported as an influential vapour-phase deposition technique with a sequential, self-saturating gas-surface reaction control behaviour. ALD shows several advantages over other methods, such as a low growth temperature, a precise atomic-scale level thickness control and the distinguished uniformity and conformality over the entire substrate.

Herein, we report the fabrication of SSCNTs/Al₂O₃ nanocomposites with different number of ALD cycles (4, 9, 19, 49 and 100), in order to control the Al₂O₃ film thicknesses. Their morphological, structural, electrochemical characterization and their application to the simultaneous detection of HQ and CC is reported. More specifically, systematic experiments were performed to reveal how the thickness of the sensing material, Al₂O₃ in present case, can bring about significant effects on performance of the electrochemical sensors.

2.1.2.2 Experimental

Reagents

Carbon nanotubes, nitric acid (67%) and argon (99.99%) were supplied from Applied Science inc., VWR chemicals and Air Liquide, respectively. Trimethylaluminum (TMA, 98%) was purchased from STREM chemicals. Dihydroxybenzene isomers and standard phosphate buffer solutions (PBS) were purchased from Sigma-Aldrich. Double-distilled water was used throughout the experimental part. All chemicals and reagents were of analytical grades and used without further purification unless otherwise stated.

Apparatus

The thickness of the Al₂O₃ deposited nanostructures was initially measured on silicon wafer (SSP) using SENpro spectroscopic ellipsometer from Sentech. The acquired data was fitted to the model using the SpectraRay 4 software. High-resolution transmission electron microscopy (HRTEM), high-angle annular dark-field scanning transmission electron microscopy (HAADF STEM) and energy dispersive X-Ray (EDX) elemental mappings were performed using a FEI Talos F200S

scanning/transmission electron microscope (S/TEM). Electrochemical measurements were performed using commercial screen-printed carbon electrode (SPCE), comprising of a planar substrate equipped with a carbon working electrode (4 mm in diameter, geometric area of 0.1257 cm²), a silver pseudo-reference electrode and a carbon auxiliary electrode. Cyclic voltammetry (CV) and square wave voltammetry techniques were performed using DropSens μ Stat 400 Potentiostat empowered by Dropview 8400 software for data acquisition.

Preparation of Al₂O₃/CNT nanostructures

Stacked-cup carbon nanotubes, SCCNTs, were pre-treated with nitric acid to functionalize and to remove the amorphous carbon as described in our report elsewhere [62]. Al₂O₃ film was deposited in a GEMSTAR-6 ALD system using Trimethylaluminum (TMA) and Millipore water (H₂O) as a metal precursor and oxygen source, respectively. Both the precursors were used at room temperatures. The temperature of the ALD chamber was set at 200 °C. One ALD cycle was adjusted as (i) 100 ms pulse/ 20 s exposure followed by a 30 s argon purge, alternatively for both the precursors. The thickness of the Al₂O₃ layer was controlled by changing the number of the ALD cycles and the samples were named as SCCNT/Al₂O₃(X), where X represents the number of Al₂O₃ ALD cycles (4-100).

Preparation of modified electrodes

Bare SPCEs were simply modified as follows; 1.0 mg of each SCCNT/Al₂O₃ nanocomposites were ultrasonically dispersed in distilled water (1 mL). The desirable amounts of the homogenous dispersions were directly drop casted onto the surface of the carbon working electrode and left at room temperature to dry until further use.

2.1.2.3 Results and discussion

2.1.2.3.1 Structural characterizations

The relative thickness of the Al₂O₃ thin film was first studied on Si-wafers with a native layer of SiO₂ using spectroscopic ellipsometry (SE), as described in our earlier report [63]. By comparing the thickness of the coated Si-wafers to the non-coated Si-wafers, fits of the SE data to the specific model (Al₂O₃/SiO₂/Si), calculated Al₂O₃ thicknesses are ca. 0.98, 2.3, 3.3, 7.7 and 15.3 nm for 4, 9, 19, 49 and 100 ALD cycles,

respectively. It gives a highly linear growth (coefficient of determination, $R^2 = 0.995$) and the growth per cycles (GPC) is calculated as 0.14 nm from the slope of the linear fit of the Al_2O_3 film thickness versus the number of ALD cycles (**Figure 2-8a**).

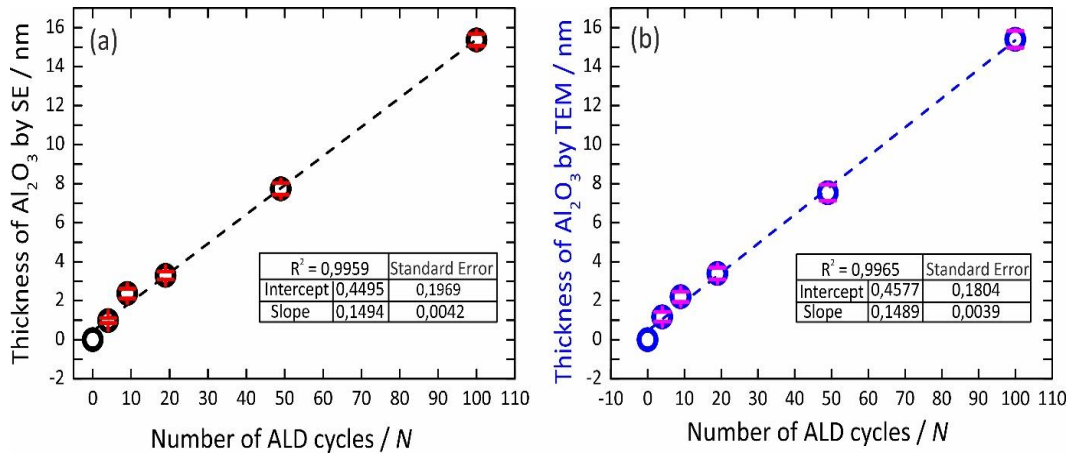


Figure 2-8. Linear fits for the Al_2O_3 thickness as a function of the number of ALD cycles as estimated, (a) on silicon wafers by spectroscopic ellipsometry (SE) and, (b) on CNTs by transmission electron microscopy (TEM). All the thicknesses were estimated from three different positions in the samples and the average values are shown in the linear fits.

The detailed structure and morphology of the $\text{CNT}/\text{Al}_2\text{O}_3(\text{X})$ heterostructures with various thicknesses of Al_2O_3 were thoroughly analysed by transmission electron microscopy (TEM). **Figure 2-9** shows bright field (BF) and HAADF-STEM micrographs for the $\text{CNT}/\text{Al}_2\text{O}_3(\text{X})$ heterostructures. It can be seen that Al_2O_3 is conformally and homogeneously deposited both onto the outer and inner surfaces of the CNTs. It starts with the deposition of small Al_2O_3 particles ($\text{CNT}/\text{Al}_2\text{O}_3(4)$, **Figure 2-9a,b** and **Figure 2-10a**) with a steady growth to a dense Al_2O_3 film (**Figure 2-9c-I** and **Figure 2-10b-d**).

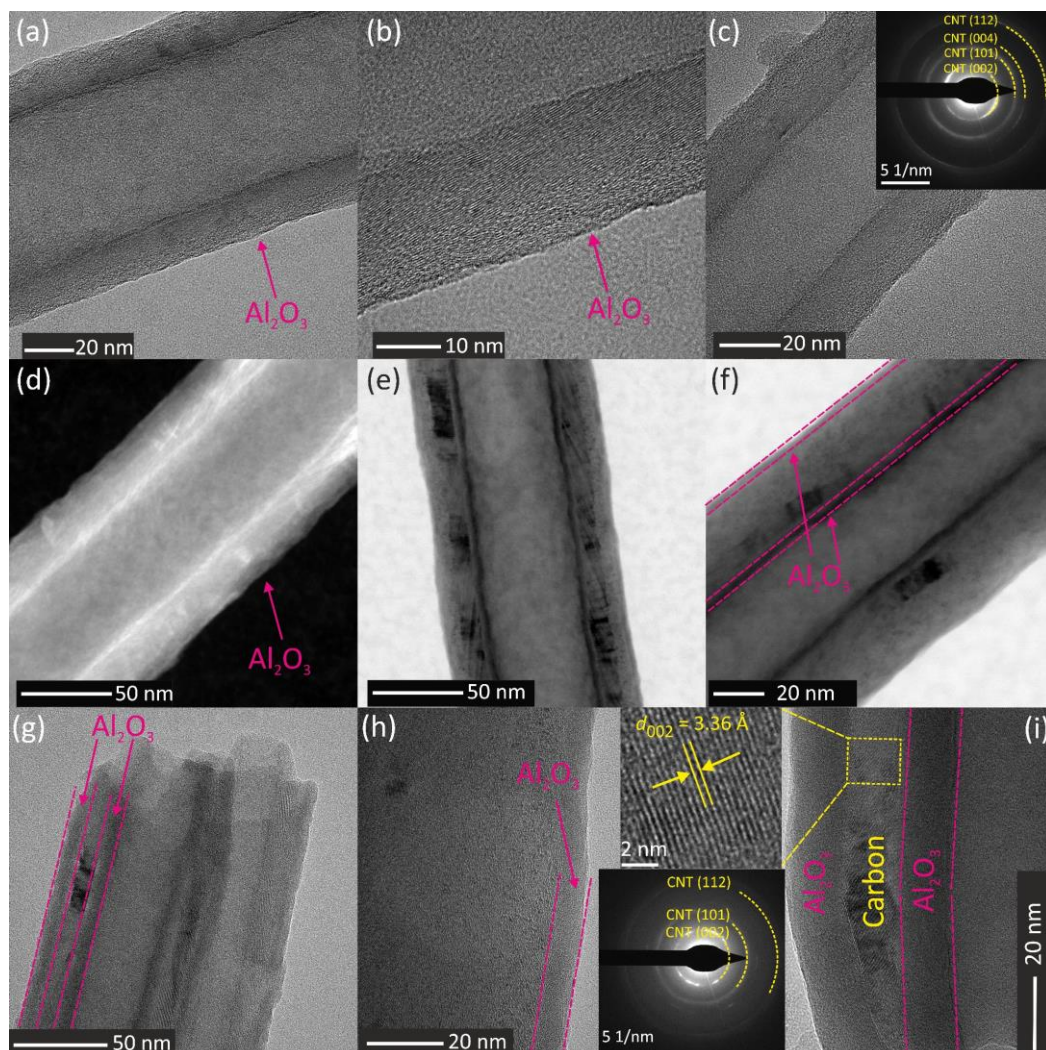


Figure 2-9. BF-HRTEM images for the (a and b) 4CNT/Al₂O₃ and (c) CNT/Al₂O₃(9) heterostructures. HAADF-STEM images for the CNT/Al₂O₃(9) heterostructures. BF-HRTEM images for the (e and f) CNT/Al₂O₃(19), (g and h) CNT/Al₂O₃(49) and (i) CNT/Al₂O₃(100) heterostructures. The insets in the (c) and (i) show the SAED patterns for the CNT/Al₂O₃(9) and CNT/Al₂O₃(100) heterostructures, respectively.

Furthermore, the micrographs demonstrate that the thickness of the Al₂O₃ film increased with the increasing of the number of ALD cycles, confirming the typical self-limiting behaviour of the ALD process. The average thickness of the Al₂O₃ thin film as estimated by the TEM images for the CNT/Al₂O₃(4), CNT/Al₂O₃(9), CNT/Al₂O₃(19), CNT/Al₂O₃(49) and CNT/Al₂O₃(100) as ca. 1.2, 2.2, 3.4, 7.5 and 15.4 nm, respectively. The linear fitting of the Al₂O₃ film thickness (estimated by TEM) as a function of the ALD cycle numbers passes through the origin with a coefficient of determination, $R^2 = 0.996$. The GPC calculated from the slope of the linear fit as 0.148 nm (**Figure 2-8b**). The insets in the **Figure 2-9 c, i** represent the

selected-area electron diffraction (SAED) patterns of the CNT/Al₂O₃(9) and 100CNT/Al₂O₃ heterostructures. The main Debye-Scherrer rings correspond to the (002), (101), (004) and (112) planes of the hexagonal graphitized carbon of the CNT substrate (ICDD 00-023-0064). The zoomed-in HRTEM from the carbon phase is shown as an inset in **Figure 2-9i**, where the lattice fringes (d-spacings) matched to the (002) plane of the hexagonal graphitised carbon of the CNTs, $d_{002} = 3.36 \text{ \AA}$. Noticeably, no reflections related to the crystalline planes of Al₂O₃ can be seen, showing that the as-deposited Al₂O₃ film by ALD is amorphous, as expected (cf. XRD patterns in our previous report) [\[64\]](#).

Figure 2-10 shows the HAADF-STEM micrographs and the corresponding EDX elemental mapping images for the CNT/Al₂O₃(4), CNT/Al₂O₃(9), CNT/Al₂O₃(19) and CNT/Al₂O₃(100) heterostructures. The Al₂O₃ phase can be identified easily by the different Z-contrast compared to the CNT. The EDX mappings nicely demonstrate the well-defined and conformal Al₂O₃ film onto the CNTs together with the confirmation of the presence and spatial distribution of Al, C and O atoms in the samples. The thickness of the Al₂O₃ film in the CNT/Al₂O₃(X) heterostructures can also be estimated easily.

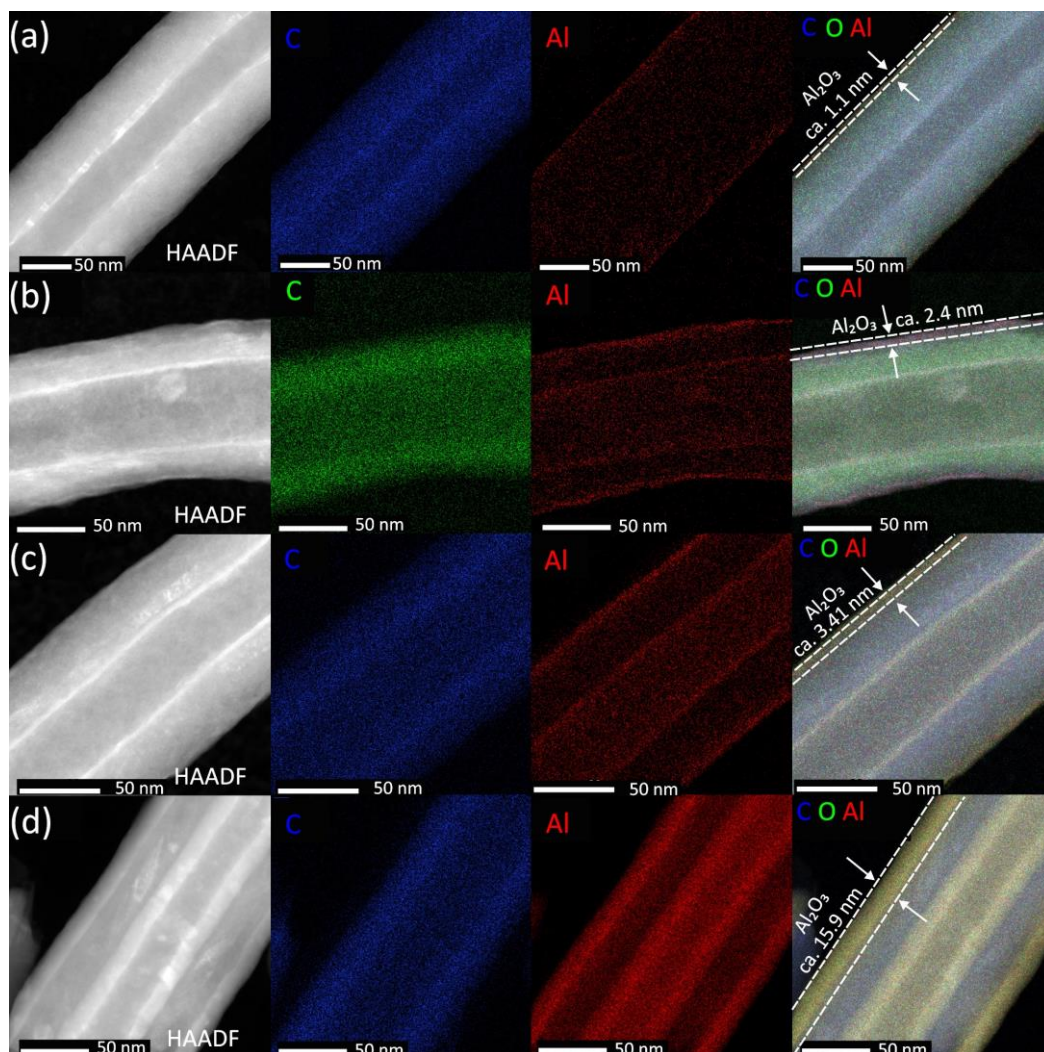


Figure 2-10. HAADF-STEM and the corresponding EDX elemental mappings images for the (a) CNT/Al₂O₃ (4), (b) CNT/Al₂O₃ (9), (c) CNT/Al₂O₃ (19) and (d) CNT/Al₂O₃ (100) heterostructures.

2.1.2.3.2 Electrochemical behavior of modified electrodes towards DHB isomers

To evaluate the electrochemical behavior of the CNT/Al₂O₃(X) nanostructures, cyclic voltammograms were recorded after placing bare SPCE and modified electrodes in the solutions containing DHB isomer(s) (**Figure 2-11**). Initial results showed that using bare SPCE as working electrode in a solution containing only HQ results in a quasi-reversible voltammogram where anodic and cathodic peaks were appeared at 0.132 and -0.142 V, respectively. Afterwards, CC was added to the above solution and cyclic voltammetry was carried out. **Figure 2-11A (Curve b)** shows that oxidation peaks of HQ and CC overlap and emerge as a single peak at 0.240 V, which makes it impossible to determine these two isomers simultaneously with bare SPCE. Additionally, as

Figure 2-11A (Curve c) depicts, SPCE shows a well-separated oxidation peak for the third isomer, RS, when it is placed in a solution containing all three isomers, 100 μ M of each. This irreversible oxidation peak of RS is far enough, i.e. 0.64 V, from the oxidation peaks of HQ and CC to be seen as a well-separated oxidation peak. Afterward, SPCE was replaced by a modified electrode, SPCE-CNT/Al₂O₃ (4), in the same solution containing all three isomers.

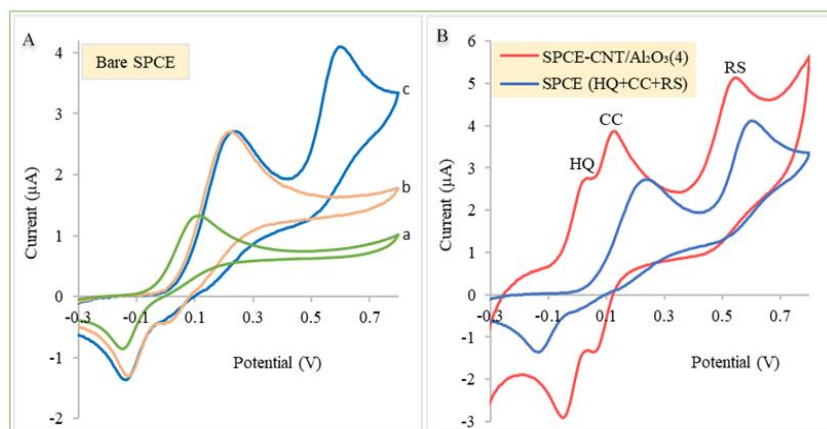


Figure 2-11. Cyclic voltammograms of (A) bare SPCE in the presence of (a) HQ, (b) HQ+CC and (c) HQ+CC+RS. (B) Comparison between the recorded CVs in a solution containing all DHB isomers (HQ+CC+RS) using bare SPCE and SPCE-CNT/Al₂O₃ (4). CVs were acquired at scan rate of 20 mV/sec. Where used, concentration of each isomer was 100 μ M in PBS pH=7.4.

First, it was observed that the single oxidation peak (overlapped) of HQ and CC at SPCE was well separated into two distinctive oxidation peaks at CNT/Al₂O₃(4) modified electrode, Figure 2-11B. This separation between HQ and CC oxidation peaks at CNT/Al₂O₃(4) modified electrode can be mainly ascribed to the different adsorption abilities of the HQ and CC on Al₂O₃ surface [65], whereas the effect of the CNT substrate on the separation of the peaks seems to be rather negligible (see Figure 2-12A inset I). Molecular dynamics simulations have already been performed to explore the interaction of phenolic compound on alumina surface in aqueous conditions and revealed that catechol molecules have the strongest adsorption ability, compared with HQ and RS, that generally acts through cooperative hydrogen bonding interactions of two neighbor hydroxyl groups of catechol with the surface oxide groups of alumina [66]. Secondly, following the peak to peak separation (ΔE_{pp}) which is typically considered as an index of electron transfer rate [67], shows that the CNT/Al₂O₃(4) modified electrode greatly decreased the ΔE_{pp} . For instance, as shown

in **Figure 2-11**, ΔE_{pp} for HQ decreased from 274 mV at SPCE to about 60 mV at CNT/Al₂O₃(4) modified electrode. Thirdly, CNT/Al₂O₃(4) modified electrode was found to enhance the oxidation peak currents and thereby improved the sensitivity of the electrochemical determination of these isomers.

Therefore, the presence of CNT/Al₂O₃(4) not only resolved the selectivity issue for electrochemical determination of DHB isomers at bare SPCE, but also, at the same time, enhanced the sensitivity of the sensor. We can ascribe this improvement in electrochemical performance of the sensor to the numerous adsorption sites provided by Al₂O₃ which can potentially modify the reaction pathway[68, 69]. Moreover, the presence of CNTs, which is known as a highly conductive material can facilitate the electron transfer between adsorbed isomers on Al₂O₃ sites and electrode, and thereby improve the electrochemical performance of the sensor [42].

To investigate the effect of Al₂O₃ on the electrochemical performance of the DHB sensors, CNT/Al₂O₃ composites with different thicknesses of the Al₂O₃ shell (ca. 1.2–15.4 nm) were used to modify the SPCE. In order to follow the variation in electrochemical characteristics more precisely, square wave voltammetry (SWV) technique was applied (**Figure 2-12A**).

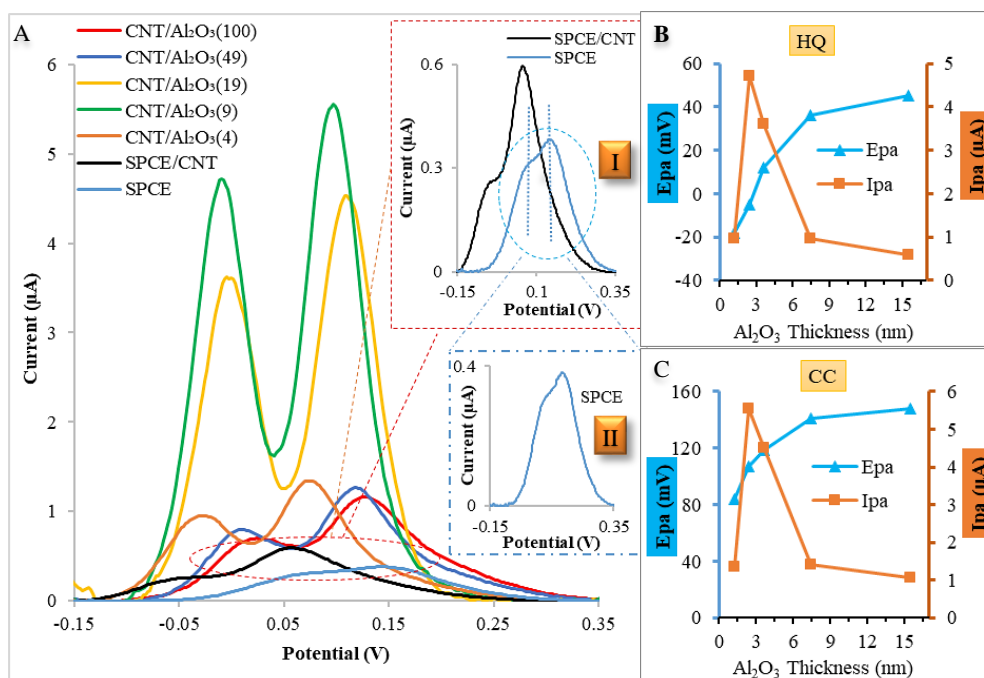


Figure 2-12. (A) Square-wave voltammograms for different electrodes (see legend A) in a solution containing 200 μM of HQ and CC in PBS pH 7.4. Graphs B (For hydroquinone) and C (for catechol) were extracted from figure A to clarify the variation of the observed anodic peak currents (I_{pa}) and anodic peak potentials (E_{pa}) versus Al₂O₃ thickness.

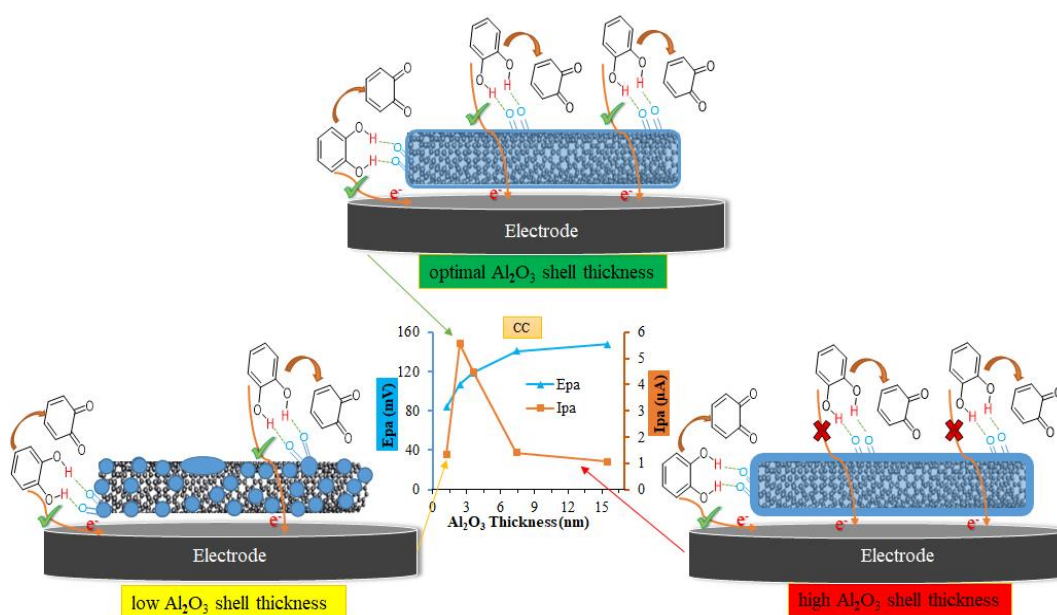
At both bare SPCE and CNT modified SPCE, the oxidation peaks of HQ and CC overlapped, though, the presence of CNT facilitates the oxidation of both isomers. This emerges in voltammograms, **Figure 2-12A inset I**, where the oxidation peak potentials at SPCE-CNT shifted negatively compared to unmodified SPCE. The presence of CNTs resulted in a relatively modest enhancement of the oxidation peak currents and, concurrently, leading to a markedly decrease in the oxidation peak potentials for both HQ and CC (**Figure 2-12A**)

However, in spite of the enhancement in the electrochemical performance of the SPCE-CNT, with respect to the bare SPCE, the peak overlapping of HQ and CC oxidation remains unsolved even at SPCE-CNT. This is attributed to the presence of CNTs, which favors the electrooxidation of both HQ and CC almost to the same extent and hence cannot differentiate their oxidation peaks. Introducing aluminum oxide brought about two contradictory impacts on the electrochemical performance of this sensor. On the one hand, as shown in **Figure 2-12B and C**, the peak currents drastically grow, up to about one order of magnitude for the CNT/Al₂O₃(9) modified electrode, decreased gently for the CNT/Al₂O₃(19) and significantly decayed for the CNT/Al₂O₃(49) and CNT/Al₂O₃(100) modified electrodes. On the other hand, with increasing the number of ALD cycles, the oxidation peak potentials for both HQ and CC shifted positively as compared to the SPCE-CNT, which means a higher electron transfer barrier for these redox systems. Considering this, it is assumed that, compared to the unmodified SPCE, the presence of CNT/Al₂O₃ plays role through providing active adsorption sites for DHB isomers and thereby facilitating the electron transfer between electrode and analytes that leads to a lower ΔE_{pp} . As we will discuss that in this electrochemical reaction, electron transfer is accompanied by proton transfer, therefore, facilitating of electron transfer can be likely ascribed to the presence of proton-acceptor functional oxide groups on the surface of the Al₂O₃ active sites that may allow this process to proceed easier. Further, these numerous adsorption sites drag more and more molecules of analyte towards the electrode to participate in the electrochemical reaction and thereby promote the peak current. However, it is not possible to assign a *direct* role to Al₂O₃ in electron transfer since Al₂O₃ is not conductive.

2.1.2.3.3 Sensing mechanism on modified electrodes

Following the above characterization and electrochemical data, here we try to explain the electrochemical behavior of the CNT/Al₂O₃ nanostructures towards DHB isomers. Previously, Compton and coll., observed the enhanced electrochemical activity towards catechol for a glassy carbon electrode whose surface was covered by alumina oxide nanoparticles and suggested that the electrocatalytic reactions would be initiated at the triple boundary formed between the isolated alumina particles, the solution, and the electrode surface [69]. In our case, a similar situation can be supposed to occur for the lower thicknesses of Al₂O₃ coating, such as for CNT/Al₂O₃(4). Indeed, even though a conformal and homogenous Al₂O₃ coating can be seen in STEM images (cf. Figure 2-10a), we can't rule out the presence of gaps/pin holes in the Al₂O₃ film at such a low-level of thickness (i.e., ≤1 nm) [64]. Anyway, this low number of ALD cycles seems to be less effective in providing enough Al₂O₃ active sites to maximize the oxidation peak currents of DHB isomers. With increasing the number of ALD cycles, the Al₂O₃ film became more continuous and effective in terms of the coverage of the CNTs surfaces, i.e., as for CNT/Al₂O₃(9) and CNT/Al₂O₃(19) nanostructures (cf. Figure 2-10b,c). With further increasing the number of ALD cycles, i.e., CNT/Al₂O₃(49) and CNT/Al₂O₃(100), the film became more dense and in parallel the highly resistive character (high- κ dielectric) of the Al₂O₃ film made it difficult to have charge transfer between adsorbed analytes onto the Al₂O₃ active sites and electrode through Al₂O₃ layer. **Scheme 1** presents a general view of the electrode reactions for catechol, as an example, where Al₂O₃ participates in reaction through its functional oxygenated groups on the surface. To have an immediate comparison, the trend of E_{pa} (anodic peak potential) and I_{pa} (anodic peak current) for catechol vs the Al₂O₃ shell thickness is also provided. At very low Al₂O₃ shell thickness, E_{pa} is minimum since uncovered CNT parts are available and facilitate electron transfer. However, there are not enough Al₂O₃ active sites to promote I_{pa}. For the modified electrode, with optimal Al₂O₃ shell thickness, i. e. CNT/Al₂O₃ (9) and CNT/Al₂O₃(19) a great enhancement in I_{pa} is observed since numerous Al₂O₃ active sites are available for electrochemical reaction to proceed. On the other hand, E_{pa} shifts positively as uncovered CNT is not available and electron transfer occurs through Al₂O₃ layer merely by electron tunneling [70]. Finally, for the modified electrode with larger Al₂O₃

shell thickness, i. e. CNT/Al₂O₃(49) and CNT/Al₂O₃(100), Epa is higher (more positive) since electron tunneling through such a thick Al₂O₃ coating becomes too difficult, if not impossible. Besides, for these thick Al₂O₃ layers, Ipa significantly decays since most of the adsorbed analyte species cannot participate in electrochemical reaction due to larger thickness and insulating character of Al₂O₃ shell. Therefore, the highest electrochemical performance for this electrochemical sensor was achieved for an Al₂O₃ layer that is enough thick to provide maximum active adsorption sites for analytes and yet, it is enough thin to allow electron transfer between adsorbed species and electrode through electron tunneling.



Scheme 1. Proposed electrochemical reaction pathway for catechol at SPCE-CNT/Al₂O₃(X) with different atomic layer deposition cycles.

In spite of higher oxidation peak potentials than SPCE-CNT, CNT/Al₂O₃(9) nanocomposite was selected as optimum sensing material for simultaneous determination of HQ and CC since it showed the highest peak currents and consequently the highest sensitivity for electrochemical measurement of HQ and CC.

2.1.2.3.4 Scan rate effect study

Figure 2-13 shows the cyclic voltammograms of 100 μM HQ (fig. 2-13A) and CC (fig. 2-13B) in PBS pH 7.0 using SPCE-CNT/ Al_2O_3 (9) over the range of scan rates 2–400 mV/s. The peak currents of both HQ and CC found to increase with increasing the potential sweep rates.

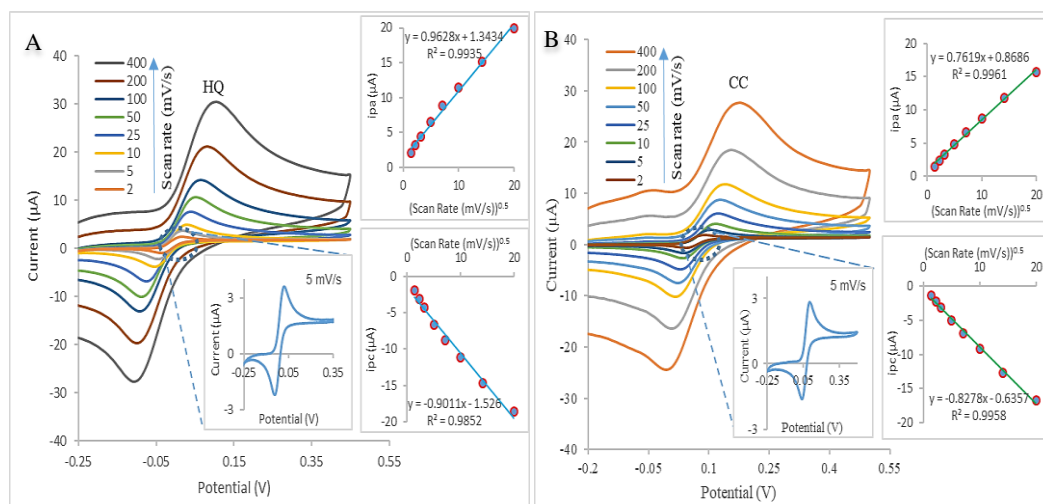


Figure 2-13. Cyclic voltammograms of CNT/ Al_2O_3 (9) modified electrode in a solution containing 100 μM (a) HQ and (b) CC in PBS pH=7.0 at scan rates from 2 to 400 mV/s. Insets depict the variation of the baseline corrected anodic peak currents (I_{pa}) and cathodic peak currents (I_{pc}) versus the square rate of scan rate.

As shown, both oxidation and reduction peak currents of HQ and CC are linearly correlated with the square root of the scan rate. This linearity implies that the bottleneck of the overall electrochemical processes at SPCE-9CNT/ Al_2O_3 should be a diffusional step where likely the adsorption step(s) are enough effective to not limit the overall electrochemical process. Moreover, increasing the potential sweep rate results in the shift of the oxidation and reduction peak potentials toward more positive and negative potentials, respectively. This shift in peak potentials with varying the scan rate reveals the quasi-reversible nature of the electrode processes.

2.1.2.3.5 Effect of the pH

Since the role of protons in the electrochemical pathway of this reaction was assumed significant, the influence of the variation in pH on the electrode responses was assessed. Solutions with different pH containing 200 μM of HQ or CC were prepared and cyclic voltammetry was performed using the SPCE-CNT/ Al_2O_3 (9). **Figure 2-14**

shows the effect of pH on both peak potentials and peak currents implying that protons are involved in the electrochemical mechanism. Both HQ and CC showed a decrease in the oxidation peak currents and peak potentials upon increasing the pH.

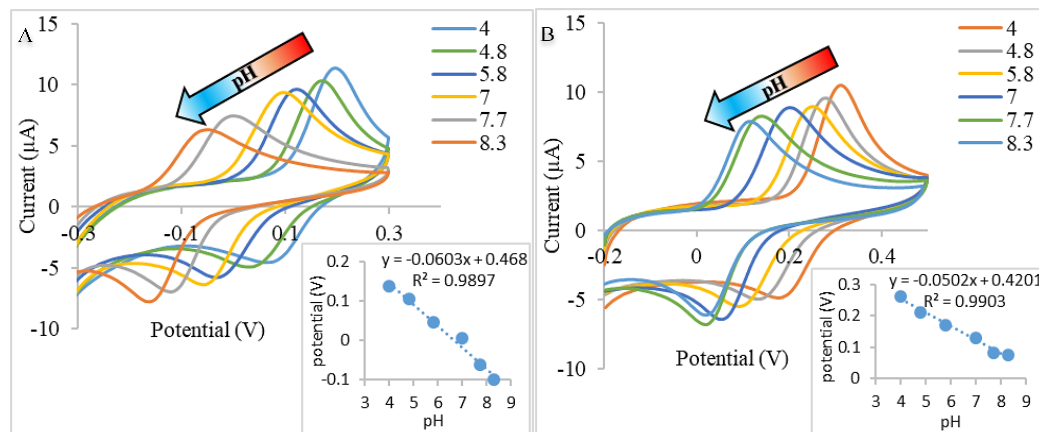


Figure 2-14. Cyclic voltammograms for a 200 μM solution of (A) HQ and (B) CC at pHs between 4 and 8.3 using SPCE-CNT/ Al_2O_3 (9). Scan rate: 20 mV/s. Insets depict the variation of the oxidation peak potentials of HQ and CC with pH.

Plotting the midpoint potential versus pH showed, for both HQ and CC, a linear shift toward negative potential with slopes of -60 mV/pH and -50 mV/pH , respectively. These slopes are in good agreement with the ideal Nernstian slope (59 mV/pH at $25 \text{ }^\circ\text{C}$) where the same number of electrons and protons participate in this proton-coupled electron transfer reaction. Considering both peak current and potential, as well as the facility of preparing buffer solution with high buffering capacity, PBS pH 7.4 was selected for further analyses.

2.1.2.3.6 Electrochemical measurement of DHB isomers

The next attention was turned towards the evaluation of the analytical figures of merit for the proposed sensor by applying square-wave voltammetry (SWV). **Figure 2-15** shows SWV curves for the successive additions of HQ, CC, and RS to a phosphate buffer solution, where SPCE-CNT/ Al_2O_3 (9) was used for electrochemical measurements. When the DHB isomers concentration rose, the corresponding oxidation peak current scaled linearly, ($R^2 \geq 0.99$). The analysis of the linear fitting model (**Table 2-2**) shows that for HQ and CC two linear segments are observed in the corresponding calibration curves while plotting the oxidation peak currents of RS against its concentration resulted in one linear part over the measured concentrations.

Table 2-2. Electroanalytical performance of SPCE-CNT/Al₂O₃ (9) and related figures of merit for DHB isomers determination.

Analyte	Linear range(s) (μM)	Least-squares fitted equation(s)	Limit of detection (μM)
HQ	2-40	$y^* = 0.0323x^{**} + 0.0887$	1.2
	50-1000	$y = 0.0136x + 2.3758$	
CC	0.5-30	$y = 0.0556x + 0.045$	0.3
	40-700	$y = 0.0177x + 1.9981$	
RS	3.5-500	$y = 0.0108x + 0.4473$	2.7

* (y) Stands for anodic peak current (i_{pa} (μA)); ** (x) Stands for analyte concentration (μM)

Low “theoretical” limit of detections were calculated by $3S_b/m$, where S_b stands for standard deviation of 12 replicate measurements of the blank solution (background) response and m refers to the slope of calibration curve (derived from the linear fitting equation at lower concentration).

The ability of the sensor for simultaneous determination of DHB isomers was also evaluated by taking into account that the cross-interference effect of HQ and CC is the most challenging issue to be addressed. The electrochemical measurements showed that the calibration curves obtained for different concentrations of HQ in the presence of a constant concentration of CC (**Figure 2-15D**) and vice versa (**Figure 2-15E**) are in accordance with the standard calibration curves (**Figure 2-15A, B**).

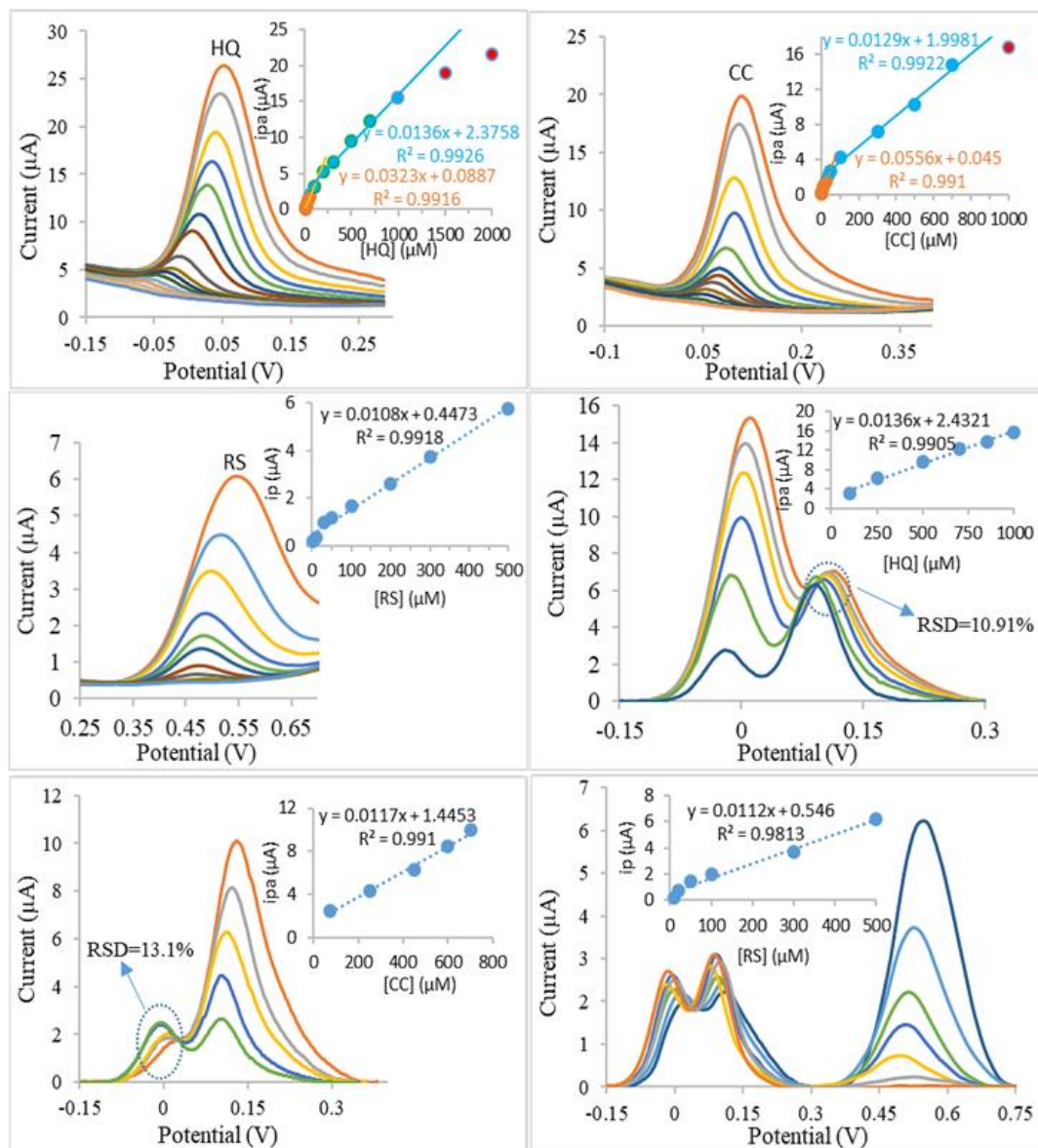


Figure 2-15. SWV responses of (A) HQ, (B) CC and (C) RS standard solutions with increasing concentrations of analytes recorded in a 0.1 M PBS pH 7.4 using SPCE-CNT/Al₂O₃ (9). Simultaneous measurement of HQ and CC in a solution containing (D) a fixed amount of CC and varying [HQ], (E) a fixed amount of HQ and varying [CC] and (F) a fixed amount of HQ and CC and varying [RS]. Inset graphs show the resulting calibration plots of the peak currents (baseline corrected) versus analytes concentrations.

This implies the absence of cross-interference effect for simultaneous determination of HQ and CC. Finally, **Figure 2-15F** clearly proves the potential of the SPCE-CNT/Al₂O₃ (9) for the simultaneous determination of all three isomers. The electroanalytical performance of the proposed sensor, SPCE-CNT/Al₂O₃ (9), for DHB isomers measurement was summarized and compared to other metal oxide based electrochemical sensors published recently, **Table 2-3**.

Table 2-3. Performance of the proposed sensor in comparison to previously reported metal oxide based electrochemical sensors for DHB isomers measurements.

Sensing material	Linear Range (μM)			LOD (μM)			Method	Real sample	Ref.
	HQ	CC	RS	HQ	CC	RS			
C₃O₄@carbon core/shell nanostructured	0.8-127.1	0.6-116.4	-	0.03	0.03	-	DPV	River water	[71]
Mesoporous carbon /CeO₂ composite	0.5-500	0.4-320	-	0.24	0.13	-	DPV	Tap water and lake water	[72]
Fe₃O₄ functionalized graphene oxide-gold nanoparticle	2-145	3-137	-	1.1	0.8	-	Amperometry	Tap water	[73]
AuNPs/RGO/WO₃ nanocomposite	0.1-10	0.1-10	-	0.036	0.020	-	DPV	River water	[74]
Carbon nanofibers-Sm₂O₃ nanocomposite	1-500	1-500	-	0.09	0.07	-	DPV	Tap water and lake water	[75]
CuO/carbon nanofragment	3-80	6-150	-	1	2	-	DPV	River water	[76]
CuO/carbon nanofragment	0.4-276.0	0.4-159.0	3.0-657	0.06	0.07	0.52	DPV	River water	[77]
NiO/CNT nanocomposite	10-500	10-400	-	2.5	2.5	-	DPV	Tap water	[43]
nitrogen-doped MWCNTs modified/nickel nanoparticles	0.3-300	0.1-300	-	0.011	0.009	-	DPV	Pond, tap and river water samples	[78]
CNT/Al₂O₃	2.0-1000	0.5-700	3.5-500	1.2	0.3	2.7	SWV	Tap water and mineral water	<i>This work</i>

Even though other metal oxides have been extensively used, to the best of our knowledge, this work is the first report on the application of aluminium oxide for simultaneous determination of DHB isomers. Comparison of the analytical figures of merit with other metal oxide-based sensor, presented in table 2-3, shows that

CNT/Al₂O₃(9) modified electrode offers comparable or even better properties for DHB isomers detection, especially with respect to linear measurement range.

2.1.2.3.7 Applicability in real sample analysis and recovery tests

The applicability of the proposed sensor was explored by spiking the DHB isomers into different media including tap water and mineral water, Nestle Vera, San Giorgio in Bosco, Padova, Italy. Before analyzing, each real sample was diluted by adding PBS pH 7.4 with ratio 1:4. The square wave voltammograms were recorded in each spiked sample and average oxidation peak currents for five replicative measurements was used to calculate the concentration of the analytes using corresponding calibration curves, see **Figure 2-15**. Acceptable range of recoveries using SPCE-CNT/Al₂O₃ (9) (**Table 2-4**) imply a negligible matrix effect of the media and, thus, promise that this sensor can be recommended for the determination of DBH isomers in the aforementioned real samples. Noteworthy, in spite of tap water analysis, which was resulted in the recoveries between 93 to 108%, for mineral water all recoveries found to be less than 100%. Therefore, although the recoveries are still acceptable, i.e. more than 91%, there is likely a negative effect of matrix on oxidation signal of DHB isomers in mineral water medium.

Table 2-4. Determination of DHB isomers in real samples, i.e. tap water and mineral water using SPE-SC CNT/Al₂O₃ (8).

Real sample	Spiked (μM)	Found (μM)	Recovery (%)	RSD (%) (n=5)
<i>Tap water</i>				
<i>HQ</i>	10	10.8	108.0	3.1
	200	187.2	93.6	4.6
<i>CC</i>	10	9.3	93.0	4.5
	200	205.2	102.6	4.1
<i>RS</i>	10	9.7	97.0	5.1
	200	210.6	105.3	5.8
<i>Mineral water</i>				
<i>HQ</i>	10	9.2	92.0	2.6
	200	183.0	91.5	3.1
<i>CC</i>	10	9.5	95.0	3.9
	200	191.0	95.5	5.6
<i>RS</i>	10	9.1	91.0	3.9
	200	189.5	94.8	4.6

2.1.2.3.8 Repeatability, reproducibility and long-term stability of modified electrodes

Since reliability of the signal is a critical aspect for a sensor, the performance of the sensor was tested with respect to inter and intra-sensor repeatability as well as effective lifetime of the proposed sensor for electrochemical measurement of DHB isomers. The repeatability of the sensor was evaluated by recording the SW voltammograms of the SPCE-CNT/Al₂O₃ (9) in solutions containing 200 μM of each analyte, i.e. HQ, CC and RS. After recording each voltammogram, for the next measurement, SPCE-CNT/Al₂O₃ (9) was just simply washed with distilled water. The relative standard variation for 10 replicative measurements was calculated to be 2.1%, 3.7% and 3.1% for HQ, CC and RS respectively. To study the reproducibility, six SPCE modified 9CNT/Al₂O₃ sensors were fabricated and their peak currents (after baseline correction) were used to estimate the reproducibility. Relative standard deviations were found to be 6.1%, 9.5% and 7.3% for HQ, CC and RS respectively. Finally, the long-term stability of the sensor was estimated by recording the SW voltammograms of the same electrode in the solutions containing 200 μM of HQ or CC or RS for one month while the electrode was stored in open air during this period. The measurements were performed every other day and for each day, five measurements for each analyte, i.e. HQ, CC and RS, were carried out and the average peak current, after baseline correction, was recorded as the signal of that day. It was observed that after 11, 19 and 30 days the sensor retained 95%, 90% and 81% of its initial signal. Noteworthy, this acceptable repeatability, reproducibility and durability of the sensor, especially up to ca. 20 days, was observed while very straightforward fabrication method was used and no common binder, e.g. Nafion or chitosan, was employed in the electrochemical sensor preparation.

2.1.2.4 Conclusions

CNT/Al₂O₃ core-shell nanostructures were prepared, the Al₂O₃ shell thickness was precisely controlled by varying the number of ALD cycles. Structural analyses demonstrated conformal deposition of Al₂O₃ onto the inner and outer carbon nanotube walls with thicknesses ranging from 1.2 to 15.4 nm. These core-shell nanostructures were used as electrochemical sensing elements for the determination of HQ, CC and RS. It is concluded that, firstly, the presence of Al₂O₃ brings about higher selectivity

by resolving the overlapped oxidation peaks of HQ and CC that can be related to the different adsorption properties of HQ and CC on aluminium oxide surface. Secondly, using the optimum thickness of the Al₂O₃ shell (ca. 2.2 nm) results in a remarkable enhancement in the peak currents for the oxidation of HQ and CC and therefore in the sensitivity of the sensor. Thirdly, the CNT core plays the important role to facilitate the electron transfer between adsorbed species on Al₂O₃ and the electrode. Therefore, in this case study, both too low and too high shell thickness resulted in a deteriorated sensitivity, almost to the same extent, due to the lack of enough active reaction sites in the former and too high electrical resistivity of a thick shell layer in the latter case. However, an optimal shell layer can provide enough active sites for electrochemical reaction to take place while electron transfer can still occur between adsorbed analytes and underlying core by electron tunnelling. In summary, insights gained from this study may turn the attention to the rather neglected role of the shell thickness in electrochemical sensing properties of core-shell nanostructures.

References

53. Hammani H., Laghrib F., Lahrach S., Farahi A., Bakasse M., Aboulkas A., and El Mhammedi M.A., *Effect of activated carbon in distinguishing the electrochemical activity of hydroquinone and catechol at carbon paste electrode*. Ionics, 2019. 25(5): p. 2285-2295.
54. Robertson M.L., Eastmond D.A., and Smith M.T., *Two benzene metabolites, catechol and hydroquinone, produce a synergistic induction of micronuclei and toxicity in cultured human lymphocytes*. Mutation Research/Fundamental and Molecular Mechanisms of Mutagenesis, 1991. 249(1): p. 201-209.
55. Luo X., Zheng H., Zhang Z., Wang M., Yang B., Huang L., and Wang M., *Cloud point extraction for simultaneous determination of 12 phenolic compounds by high performance liquid chromatography with fluorescence detection*. Microchemical Journal, 2018. 137: p. 148-154.
56. Lazzari E., Polidoro A.d.S., Onorevoli B., Schena T., Silva A.N., Scapin E., Jacques R.A., and Caramão E.B., *Production of rice husk bio-oil and comprehensive characterization (qualitative and quantitative) by HPLC/PDA and GC × GC/qMS*. Renewable Energy, 2019. 135: p. 554-565.
57. Lin Z.-Y., Kuo Y.-C., Chang C.-J., Lin Y.-S., Chiu T.-C., and Hu C.-C., *Highly sensitive sensing of hydroquinone and catechol based on β-cyclodextrin-modified carbon dots*. RSC Advances, 2018. 8(35): p. 19381-19388.
58. Lu Q., Hu H., Wu Y., Chen S., Yuan D., and Yuan R., *An electrogenerated chemiluminescence sensor based on gold nanoparticles@C60 hybrid for the determination of phenolic compounds*. Biosensors and Bioelectronics, 2014. 60: p. 325-331.
59. Sirajuddin, Bhangar M.I., Niaz A., Shah A., and Rauf A., *Ultra-trace level determination of hydroquinone in waste photographic solutions by UV-vis spectrophotometry*. Talanta, 2007. 72(2): p. 546-553.
60. Sabbaghi N. and Noroozifar M., *Nanoraspberry-like copper/ reduced graphene oxide as new modifier for simultaneous determination of benzenediols isomers and nitrite*. Analytica Chimica Acta, 2019. 1056: p. 16-25.
61. Yang H., Li S., Yu H., Zheng F., Lin L., Chen J., Li Y., and Lin Y., *In situ construction of hollow carbon spheres with N, Co, and Fe co-doping as electrochemical sensors for simultaneous determination of dihydroxybenzene isomers*. Nanoscale, 2019. 11(18): p. 8950-8958.
62. Raza M.H., Movlaee K., Wu Y., El-Refaei S.M., Karg M., Leonardi S.G., Neri G., and Pinna N., *Tuning the NiO Thin Film Morphology on Carbon Nanotubes by Atomic Layer Deposition for Enzyme-Free Glucose Sensing*. ChemElectroChem, 2019. 6(2): p. 383-392.
63. Raza M.H., Kaur N., Comini E., and Pinna N., *Toward Optimized Radial Modulation of the Space-Charge Region in One-Dimensional SnO₂-NiO Core-Shell Nanowires for Hydrogen Sensing*. ACS Applied Materials & Interfaces, 2020. 12(4): p. 4594-4606.
64. Raza M.H., Movlaee K., Leonardi S.G., Barsan N., Neri G., and Pinna N., *Gas Sensing of NiO-SCCNT Core-Shell Heterostructures: Optimization by Radial*

- Modulation of the Hole-Accumulation Layer.** *Advanced Functional Materials*, 2020. 30(6): p. 1906874.
65. Borah J.M., Sarma J., and Mahiuddin S., **Adsorption comparison at the α -alumina/water interface: 3,4-Dihydroxybenzoic acid vs. catechol.** *Colloids and Surfaces A: Physicochemical and Engineering Aspects*, 2011. 387(1-3): p. 50-56.
 66. Yeh I.-C., Lenhart J.L., and Rinderspacher B.C., **Molecular Dynamics Simulations of Adsorption of Catechol and Related Phenolic Compounds to Alumina Surfaces.** *The Journal of Physical Chemistry C*, 2015. 119(14): p. 7721-7731.
 67. Allen J. Bard and Larry R. Faulkner, **Electrochemical Methods: Fundamentals and Applications, 2nd Edition.** 2001, John Wiley: New York
 68. Poon J., Lin Q., Batchelor-Mcauley C., Salter C., Johnston C., and Compton R.G., **Altered electrochemistry at graphene-or alumina-modified electrodes: Catalysis vs electrocatalysis in multistep electrode processes.** *Journal of Physical Chemistry C*, 2015. 119(24): p. 13777-13784.
 69. Lin Q., Li Q., Batchelor-McAuley C., and Compton R.G., **Two-Electron, Two-Proton Oxidation of Catechol: Kinetics and Apparent Catalysis.** *The Journal of Physical Chemistry C*, 2015. 119(3): p. 1489-1495.
 70. McCreery R.L., **Advanced Carbon Electrode Materials for Molecular Electrochemistry.** *Chemical Reviews*, 2008. 108(7): p. 2646-2687.
 71. Zhou T., Gao W., Gao Y., and Wang Q., **Simultaneous determination of catechol and hydroquinone using non-enzymatic Co_3O_4 @carbon core/shell composites based sensor.** *Journal of the Electrochemical Society*, 2019. 166(12): p. B1069-B1078.
 72. Liu D., Li F., Yu D., Yu J., and Ding Y., **Mesoporous carbon and ceria nanoparticles composite modified electrode for the simultaneous determination of hydroquinone and catechol.** *Nanomaterials*, 2019. 9(1).
 73. Erogul S., Bas S.Z., Ozmen M., and Yildiz S., **A new electrochemical sensor based on Fe_3O_4 functionalized graphene oxide-gold nanoparticle composite film for simultaneous determination of catechol and hydroquinone.** *Electrochimica Acta*, 2015. 186: p. 302-313.
 74. Tsai M.S., Lu C.J., and Su P.G., **One-pot synthesis of AuNPs/RGO/ WO_3 nanocomposite for simultaneously sensing hydroquinone and catechol.** *Materials Chemistry and Physics*, 2018. 215: p. 293-298.
 75. He J., Qiu F., Xu Q., An J., and Qiu R., **A carbon nanofibers- Sm_2O_3 nanocomposite: A novel electrochemical platform for simultaneously detecting two isomers of dihydroxybenzene.** *Analytical Methods*, 2018. 10(16): p. 1852-1862.
 76. Alshahrani L.A., Liu L., Sathishkumar P., Nan J., and Gu F.L., **Copper oxide and carbon nano-fragments modified glassy carbon electrode as selective electrochemical sensor for simultaneous determination of catechol and hydroquinone in real-life water samples.** *Journal of Electroanalytical Chemistry*, 2018. 815: p. 68-75.
 77. Fotouhi L., Seyed Dorraji P., Sadat Seyed Keshmiri Y., and Hamtak M., **Electrochemical sensor based on nanocomposite of multi-walled carbon nanotubes/ TiO_2 nanoparticles in chitosan matrix for simultaneous and separate determination of dihydroxybenzene isomers.** *Journal of the Electrochemical Society*, 2018. 165(5): p. B202-B211.

78. Rajkumar C., Thirumalraj B., Chen S.M., Veerakumar P., and Lin K.C., *Voltammetric determination of catechol and hydroquinone using nitrogen-doped multiwalled carbon nanotubes modified with nickel nanoparticles*. *Microchimica Acta*, 2018. 185(8): p. 395.

2.1.3 One-step microwave-assisted synthesis and characterization of novel CuO nanodisks for non-enzymatic glucose sensing

Abstract

In this study, a new approach for glucose sensing emphasizing on cost-effectivity and simplicity while sensitivity of sensor remains high enough is proposed. In this respect, we prepared CuO nanodisks having an ellipsoidal form without using any template or surfactants just by using microwave irradiation for 5 minutes and used it to modify disposable commercial screen printed carbon electrodes (SPCE) without using any kind of binders like nafion. The synthesized CuO nanostructure has been thoroughly characterized using various complementary techniques (SEM, TEM, FT-IR, XRD) while the performance of proposed electrochemical sensor was investigated as for glucose sensing. Different effective parameters on performance of the electrochemical sensor, including KOH concentration, applied potential, repeatability, stability and selectivity, were investigated and discussed. The linear dynamic range, from 0.2 μM to 2.54 μM , with detection limit of 0.202 μM (at signal to noise ratio of 3) and sensitivity of 653.3 $\mu\text{A mM}^{-1} \text{cm}^{-2}$, are comparable or better than many of more sophisticated glucose sensors. Therefore, this simple and sensitive sensor can offer a cost-effective and high-performance glucose sensor with respect to previously reported copper oxide based glucose sensors.

2.1.3.1 Introduction

Glucose sensing has been largely investigated through the last decades due to its remarkable importance in many applicative fields. First of all, glucose sensing allows to monitor health status of people having diabetes, a disease characterized by elevated level of glucose in the body [79]. Diabetes can cause renal, cardiac and nervous diseases as side effects and, according the most recently report of WHO, this number is increasing at an alarming rate. Measurement of glucose is not only crucial for treating diabetes but also it is very important in different industrial activities including food processing and bio-fermentation processes.

To respond to these necessity, a vast range of methods have been developed for the quantitative determination of glucose such as fluorescence spectroscopy [80, 81], infrared spectroscopy [82, 83], chemiluminescence [84], chromatography coupled with evaporative light scattering detector or tandem mass spectrometry [85, 86] and electrochemistry [87-89]. Among aforementioned methods, electrochemical ones have found highest applications due to their high sensitivity, selectivity, simplicity and speed. Electrochemical sensors for glucose determination can be divided into two broad categories namely enzymatic and enzyme-free (non-enzymatic) sensors. Although enzymatic methods usually show higher selectivity over enzyme-free ones, the sensitivity, simplicity and low cost of enzyme-free sensors hold great promise for glucose monitoring [90].

Since common bare electrodes cannot show acceptable performance toward glucose measurements, nanostructure materials came forward to fulfil expectations. Among them, metal and metal oxides nanostructures have offered many desired properties for high performances sensors for glucose. In this respect, noble metal nanostructures such as platinum [91, 92], gold [93, 94], palladium [95, 96] and nickel [97, 98] as well as transition metal oxides like nickel oxide [99], copper oxide [100], cobalt oxide [101], manganese oxide [102] and iron oxide [103] have been exploited extensively.

As a p-type semiconductor with a narrow band gap of 1.2 eV, copper oxide has been widely exploited as a promising candidate for modification of electrode in electrochemical glucose sensors due to its high stability and electrocatalytic activity toward glucose oxidation at lower over-potentials. Regarding this, until now, many efforts have been devoted to produce different nanostructure of copper oxide such as nanowires [104], nanoparticles [105], nanorods [106], nanofibers [107], nanoneedles [108], nanospheres [109] and so on.

Among the various synthesis techniques, we have chosen microwave-assisted wet chemical techniques for the present investigation due to its unique properties of rapid heating which increased reaction rates and shortened reaction time. Indeed, as microwave energy is selectively absorbed by areas of greater moisture, microwave-assisted wet chemical technique can be used as a non-contact drying technology. This

results in more uniform temperature and moisture profiles, improved yields and enhanced product performance.

In this paper, we present the synthesis and characterization of CuO nanodisks and its excellent ability in the enzyme-free glucose sensing. CuO nanodisks having an ellipsoidal form and constituted of a network of nanorods linked together, were synthesized by an eco-friendly, simple, template and surfactant-free one-step microwave-assisted wet chemical method. Subsequently, they were used to modify screen printed carbon electrodes (SPCE). CuO modified SPCE (SPCE/CuO) electrodes exhibited excellent electro-oxidation toward glucose in alkaline media with significantly high sensitivity, which can be ascribed to peculiar CuO disk nanostructure. Results demonstrate that CuO nanodisks possess valuable electrocatalytic features and are quite attractive for the fabrication of non-enzymatic glucose sensors.

2.1.3.2 Experimental

Materials

Copper acetate, ammonia solution, potassium hydroxide (KOH), glucose, mannose, sucrose, fructose, ascorbic acid (AA), dopamine (DA) and uric acid (UA) were purchased from Sigma Aldrich (www.sigmaaldrich.com) and were used without further treatment unless otherwise stated. Solutions were prepared, in double distilled water, daily before performing tests except KOH solution, which was stable and could be used for a longer period.

Apparatus

The morphology as well as particle distribution of samples was investigated using a scanning electron microscope (FESEM Zeiss, model 1540XB) and a transmission electron microscope (TEM, model-FEI Tecnai F20 G2). The microstructure of the sample was studied using X-ray Diffraction Technique (XRD, model XPERT-PRO). The presence of functional groups on the sample surface was determined using Fourier Transform Infrared spectroscopy (FTIR-Perkin Elmer, model-spectrum 2).

Electrochemical analyses (amperometric measurements and cyclic voltammetry) were performed using commercial SPCE (DropSens C110), equipped with a 4-mm diameter

carbon working electrode, a silver pseudo-reference electrode and a carbon auxiliary electrode. DropSens μ Stat 400 Potentiostat empowered by Dropview 8400 software was exploited for data acquisition. All experiments were performed at room temperature.

Preparation of CuO nanostructure and modified electrodes

Copper acetate (5 grams) was used as precursor material and dissolved in distilled water to prepare a solution 0.1 N. The solution was neutralized with ammonia solution using drop-by-drop addition until pH of the solution reached to 9. The above solution was placed in microwave oven and microwave irradiated for 5 minutes. This irradiation time was previously optimized (data not shown) in order to obtain the desired morphological/microstructural CuO nanodisks characteristics. The radiation frequency was 2.45 GHz and its power up to 1 kW. Finally, the sample was collected and dried at 120°C in muffle furnace.

For the preparation of CuO nanodisks-modified electrodes, 1 mg of CuO nanodisk sample was dispersed in 1 mL of distilled water using ultrasonic bath. After obtaining homogeneous dispersion (2, 4, 6 and 8 μ L were tested and 4 μ L was selected as optimum volume, data not shown), the desired amount of CuO nanodisk dispersions was directly dropped onto the surface of carbon working electrode (SPCE/CuO) and left at room temperature to dry until further use.

Electrochemical tests

Electrochemical experiments were performed inside a 5 ml cell at room temperature. Potential and current were recorded by means of a DropSens μ Stat 400 potentiostat while using the same screen printed counter and reference electrodes of the commercial device. Cyclic voltammetry (CV) tests were performed at different scan rates in the potential range from 0 to 0.9 V. Tests were performed in 0.1 M KOH solution in the presence and absence of glucose. The pH effect of the analyte solution was also investigated. Amperometric measurements were carried out in stirred 0.1 M KOH solution, recording the anodic current at the optimal working potential, while drops of glucose were added sequentially.

2.1.3.3 Results and discussion

2.1.3.3.1 Structural characterizations of CuO nanodisks

The morphology, shape and size of as-prepared CuO sample was investigated by SEM and TEM analysis. SEM images reported in Fig. 2-16 (A-B), show clearly that the obtained particles were disk-shaped, with an ellipsoidal form. Measurements made on a large number of these particles allowed to draw the particle size distribution. The histogram related to size distribution of the minor and mayor axis of these particles are reported in Fig. 2-16 (C-D). Average sizes are 308 nm and 534 nm for minor axis and mayor axis, respectively. Thickness of these nanodisks is estimated to be around 31 nm.

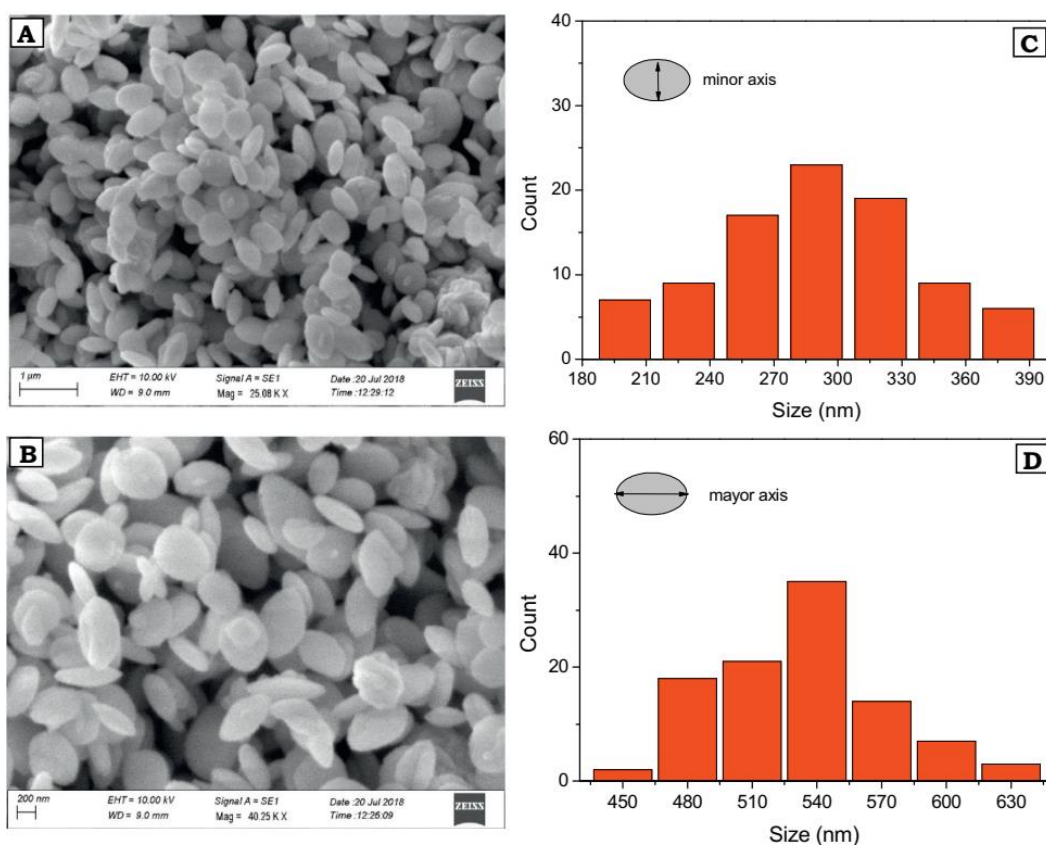


Figure 2-16. (A, B) SEM micrographs of as-prepared CuO nanostructures; (C, D) Size distribution of the minor and mayor axis of CuO elliptic particles.

TEM micrographs at growing magnification are shown in Figure 2-17(A-C). Low magnification images clearly confirm the shape and size of CuO nanodisk. Dimensional analysis also confirm size obtained by SEM analysis. At higher magnification (see Figure 2-17C), we observe that nanodisks consist of small nanorods

(about 31 nm long and 5 nm thick), linked together to form a spherical/ellipsoidal porous nanostructure. SAED pattern (Figure 2-17D) presents bright spots, which indicates their highly crystalline nature.

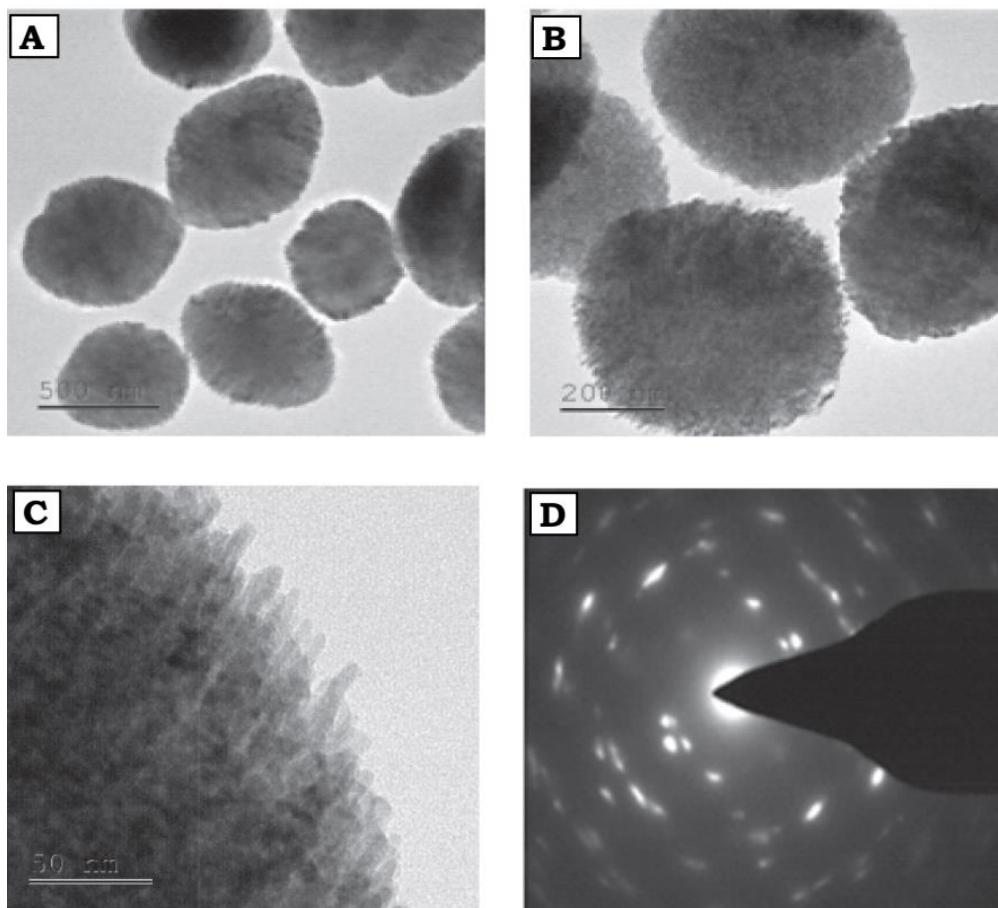


Figure 2-17. (A,B,C) TEM and (D) SAED micrographs of as-prepared CuO nanostructures.

X-ray diffraction (XRD) analysis was performed for the powder sample as-synthesized CuO in order to identify the crystalline phase (see Figure 2-18). As-synthesized CuO powder has diffraction peaks at 2θ angles of 35.66, 38.81 and 48.95 which can be associated to the $(-1\ 1\ 1)$, $(2\ 0\ 0)$ and $(-2\ 0\ 2)$ crystallographic planes of monoclinic CuO [105]. This confirms the formation of CuO crystalline phase without addition of any surfactant and post synthesis treatment in just 5 minutes of microwave irradiation.

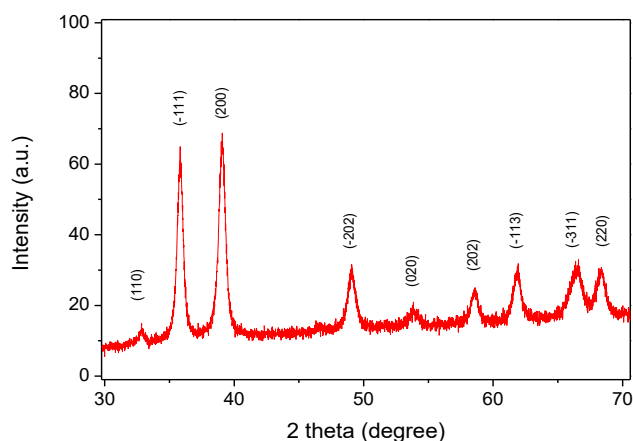


Figure 2-18. XRD pattern of as-prepared CuO nanostructure.

Fig. 2-19 reports the Fourier transform infrared spectroscopy (FTIR) spectrum of the as-prepared CuO nanostructures. The bands at around 602, and 496 cm^{-1} can be assigned to the vibrations of Cu(II)-O bonds [9, 12]. The broad absorption peak at around 3428 cm^{-1} is caused by the adsorbed water molecules [6]. The existence of peaks at 1344 cm^{-1} and 1604 cm^{-1} is attributed to the ketone group, likely coming from a little quantity of unreacted copper acetate precursor.

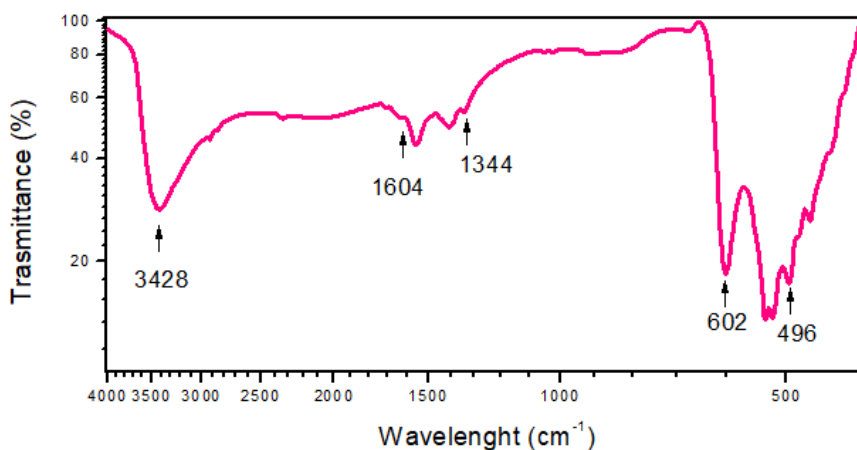


Figure 2-19. FTIR spectrum of as-prepared CuO nanostructure.

2.1.3.3.2 Electrochemical characteristics of modified CuO/SPCE

Electrochemical activity of glucose at bare SPCE and modified electrode was investigated using cyclic voltammetry (Figure 2-20a). Bare SPCE didn't show any peak neither in 0.1 M KOH solution (Fig. 2-20, curve I) nor in 1 mM glucose solution (Fig. 2-20, curve II) in the range 0 to 0.9 V at scan rate 50 mV s^{-1} .

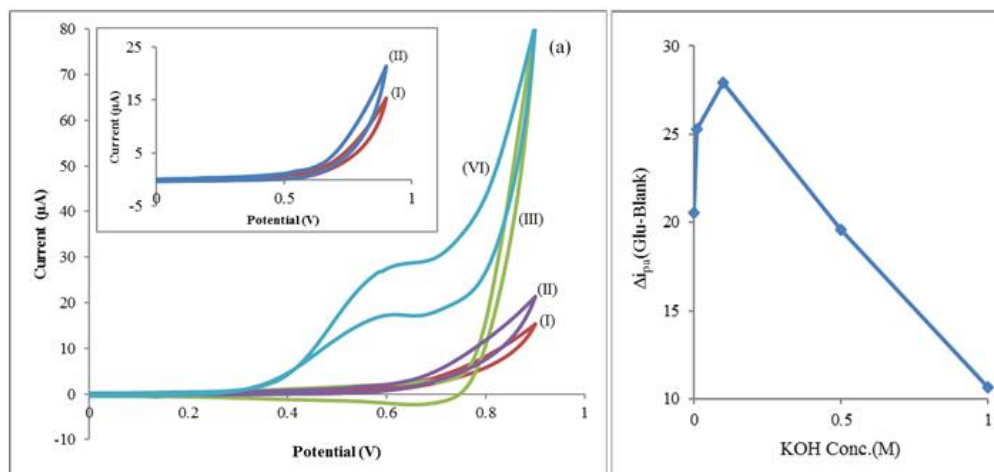
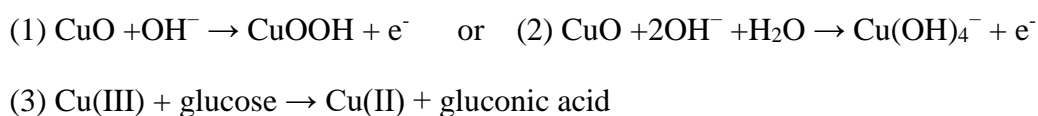


Figure 2-20. (a) Cyclic voltammograms of bare SPCE (I) and SPCE/CuO (III) in 0.1 M KOH, and bare SPCE (II) and SPCE/CuO (IV) in (1 mM glucose+0.1 M KOH) at scan rate: 50 mV s^{-1} . (b) Effect of KOH concentration on sensitivity of SPCE/CuO electrode. Net current, defined as subtraction of peak current in the presence of 1mM glucose and absence of glucose, in different concentration of KOH, i.e. 0.001, 0.01, 0.1, 0.5 and 1 mol/L.

Fig. 2-20, curve III, shows a large oxidation tail observed over +0.75 V, which is considered as the onset of water splitting at the surface of SPCE/CuO. However, a reduction peak was observed (Fig. 2-20, curve III) for SPCE modified with CuO nanodisks (SPCE/CuO) in 0.1 M KOH solution that can be attributed to the active redox couple of Cu(III)/Cu(II). The absence of oxidation peak of Cu(III)/Cu(II) in KOH solution is considered to be due to overlapping of this oxidation peak with oxidation of water, water splitting, at that high positive potential which can completely covers oxidation peak of Cu(III)/Cu(II) [110]. Moreover, for SPCE/CuO, after addition of 1 mM Glucose to KOH solution (Fig. 2-20, curve IV), a clear oxidation peak was appeared at about 550-600 mV which is corresponding to oxidation of glucose in the presence of CuO.

Although the explicit electrocatalytic mechanism of glucose oxidation in the presence of CuO in alkaline media hasn't been clarified, the most accepted mechanism suggests the production of high valence Cu (III) intermediate which can act as electron transfer medium and easily oxidizes glucose [111] according to the following paths:



Effect of KOH on electrooxidation of glucose

As mentioned above in the proposed mechanism for electrooxidation of glucose, OH⁻ ions participate in this process and investigation on their effect on performance of proposed sensor is necessary. Regarding this, different solution of KOH with concentration of 0.001, 0.01, 0.1, 0.500 and 1 mol/L were prepared and for each one cyclic voltammetry was recorded using SPCE/CuO. Afterwards, certain amount of glucose was added to each beaker to obtain 1mM of glucose and corresponding CV was acquired. In order to evaluate the effect of KOH on performance of sensor, net anodic peak currents were calculated by subtracting anodic peak current in the presence and absence of glucose ($i_{(pa)Glu} - i_{(pa)Blank}$).

Figure 2-20b clearly shows from 0.001 to 0.1 M, net current increases but in higher concentrations of KOH a fast decrease in net current was observed. We proposed that, likely, in very low concentration of KOH, e.g. 0.001M, concentration of OH⁻ ions are not enough to convert high amount CuO species into active form of CuO(OH), hence, peak current will be lower. On the other hand, in high concentrations of KOH performance of SPCE/CuO sensor was deteriorated since high concentrations of OH⁻ ions can block adsorption of glucose and/or causes producing of undesirable intermediates during oxidation of glucose which, subsequently, block the surface of electrode [41] and decrease the peak current. Accordingly, 0.1 M KOH was selected as optimum concentration for glucose monitoring at SPCE/CuO for the next analyses.

2.1.3.3.3 Effect of scan rate

In order to explore the nature of mass transfer phenomenon at SPCE/CuO, cyclic voltammograms were recorded for 0.5 mM glucose at different potential scan rate ranging from 5 to 1500 mV s⁻¹. As shown in Fig. 2-21, electrocatalytic current of oxidation peak is proportional to square root of scan rate according to equation $i_{pa}(\mu A) = 1.7037\sqrt{v} + 13.648$ with $R^2 = 0.9921$, where i_{pa} represents anodic peak current and \sqrt{v} is square root of scan rate. This observation reveals that rate-determining step is being controlled by slow diffusion of species to electrode or away from electrode surface and adsorption step is faster than diffusion.

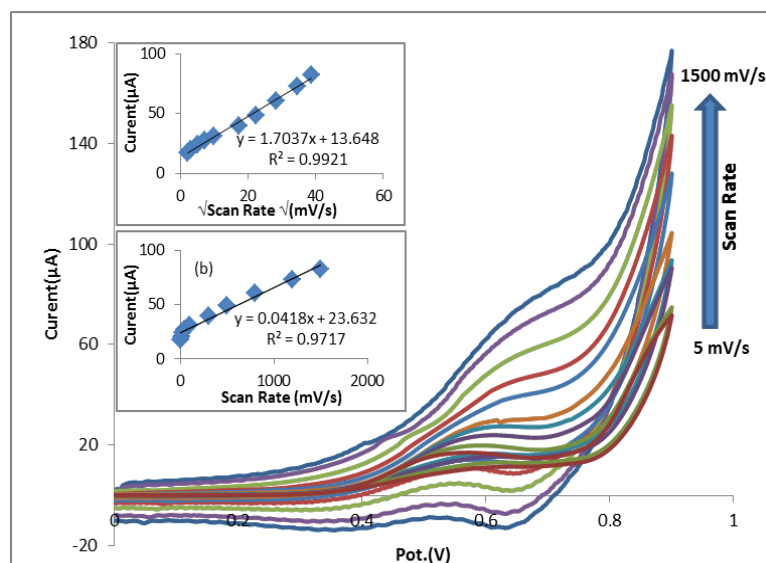


Figure 2-21. CVs of glucose oxidation at SPCE/CuO at different scan rates, i.e. 5, 10, 25, 50, 100, 300, 500, 800, 1200 and 1500 mV/s. (inset) Plots of peak current vs. square root of scan rate (a) and scan rate (b).

2.1.3.3.4 Amperometric analyses

In order to obtain the highest sensitivity for proposed sensor, amperometric technique was used for measurement of glucose. To achieve this purpose, first, effect of different applied potentials (E_{app}) on glucose sensing was investigated since E_{app} has great effect on sensitivity of this technique. The applied potentials of 0.5, 0.6 and 0.7 V were chosen, according to CV analyses to be studied. Fig. 2-22a demonstrates amperometric current time (i-t) response using SPCE/CuO after successive addition of 200 μ M glucose while solution was being stirred. Results clearly show that amperometric responses enhance increasing applied potential from 0.5 to 0.6V. However, increasing E_{app} from 0.6 to 0.7V results in lower responses.

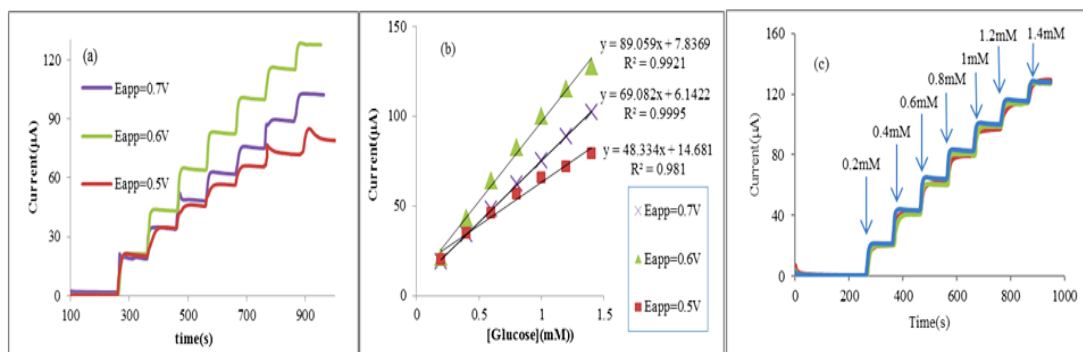


Figure 2-22. Study of SPCE/CuO sensor in 0.1 M KOH after successive addition of 200 μ M glucose (a) at different applied potential and (b) corresponding calibration curve for each potential (c).

Fig. 2-22b depicts that at applied potential of 0.6V the highest sensitivity (defined as slope of corresponding calibration curve) is observed and higher E_{app} deteriorates the sensitivity since at that high potential, other electroactive molecules and/or by-product intermediates can interfere with glucose oxidation. Therefore, applied potential of 0.6 V was selected as the optimum E_{app} for the subsequent experiments. Repeatability is another critical figure of merit for a sensor; hence, we investigated also this aspect of proposed sensor. Fig. 2-22c demonstrates clearly that for three different measurements using the same SPCE/CuO sensor we obtained very good repeatability. Noteworthy, the only procedure that was performed between different three measurements was removing the SPCE/CuO from the solution and washing it thoroughly with distilled water. After that, SPCE/CuO was ready to be used for next analysis. According to this, SPCE/CuO shows very good antifouling ability toward glucose monitoring in alkaline solution.

The capability of the proposed sensor was more investigated by attempting to obtain the calibration curve for glucose measurement (see Fig. 2-23).

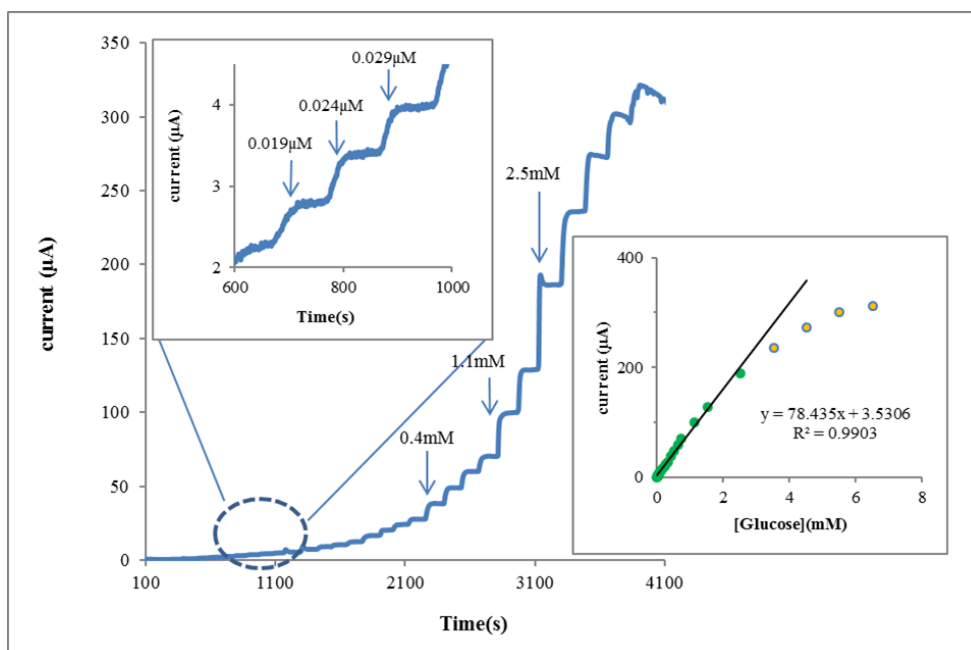


Figure 2-23. Calibration curve for proposed sensor at 0.6V and 0.1M KOH (insets show the magnification of lower concentration range and calibration curve for the glucose determination).

At optimum potential, 0.6V, there is a linear relation between current responses and glucose concentration in the range of 2 μM to 2.54 mM with sensitivity of 78.43 $\mu\text{A mM}^{-1}$ ($627.3 \mu\text{A mM}^{-1}\text{cm}^{-2}$). Limit of detection for this sensor was calculated to be 0.2 μM using calibration curve and considering formula $3\sigma/m$, where σ is standard deviation of replicative measurements of blank solution (KOH 0.1 M) and m is the slope of calibration curve.

We have also compared our results to other similar reported sensors, as listed in Table 2-5. The performance of the proposed SPCE modified CuO which had been prepared in a very simple and cost-effective way was better than most of the recently reported CuO-based enzyme-free glucose sensors.

Table 2-5. Comparison of the sensing the performance of proposed sensor to other reported CuO based sensor in the literatures.

Modifier	Potential (V)	Linearity	LOD (μM)	Sensitivity ($\mu\text{A mM}^{-1}\text{cm}^{-2}$)	Reference
CuO nanosheets	0.5	500 μM to 10 mM	0.1	520	[112]
CuO nanofibers	0.40	6 μM to 2.5 mM	0.8	431.3	[113]
CuO nanowires	0.55	-	2	648.2	[114]

CuO nanospheres	0.60	Up to 2.55 mM	1	404.53	[115]
CuO nanoparticles	0.55	0.21 μ M to 12 mM	0.21	700	[105]
CuO nanoparticles	0.60	20 μ M to 20 mM	0.06	472	[116]
CuO nanowires	0.55	5.0 μ M to 0.555 mM and 0.555 to 8.555 mM	2.86	850.7 and 446.7	[117]
CuO nanowires	0.33	0.4 μ M to 2 mM	0.049	490	[118]
CuO nanofibers	0.35	60 μ M to 3 mM	8	183.3	[119]
CuO nanodisks	0.60	2.0 μ M to 2.5 mM	0.2	627.3	This study

2.1.3.3.5 Selectivity, stability and real sample analyses

Selectivity of sensor was evaluated because, most often, selectivity determines the applicability of the sensor in real media. The higher the selectivity sensor shows, the more reliable the results will be. Usually, some other species such as sucrose (Suc), mannose (Man), fructose (Fru), uric acid (UA), dopamine (DA) and ascorbic acid (AC) co-exist with glucose in many real samples. Although normal levels of abovementioned substances are much more lower than glucose, these species potentially can interfere with electrochemical glucose measurement. Fig 2-24a demonstrates that simple sugars (Suc, Man and Fru) slightly interferewith the measurement of glucose, while UA, DA and UA show negligible interference effect. These results reveal that this sensor has a good selectivity for glucose measurement in the presence of other normal interferences.

Long-term stability of sensor was also studied. As Fig. 2-24b shows after successive measurement of glucose during 14 days, with 2-days intervals, only 9% of original signal was lost. Noteworthy, in these 14 days, the sensor was kept in open air and room temperature without any special condition. This study reveals an elegant feature of

SPCE/CuO which is high stability. This can be ascribed to high stability of copper oxide species even at ambient conditions.

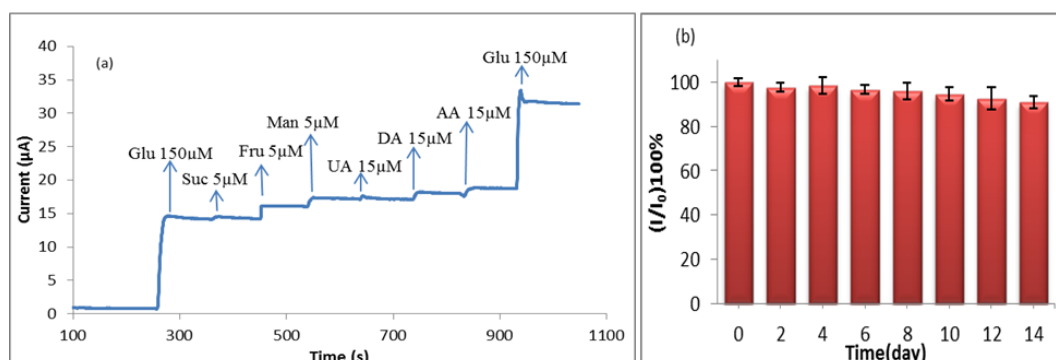


Figure 2-24. (a) Interference response of SPCE/CuO modified electrode in 0.1 M KOH at 0.6 V. (b) long-term stability of proposed sensor (each point represents 3 repetitive measurements).

To test the capability of proposed sensor for measuring glucose in urine sample, 25 µL of human urine sample was collected and diluted to 5 mL by adding 0.1 M KOH. Recoveries were calculated, after adding standard glucose solution to abovementioned urine sample at a time interval of 100 s. Results in table 2-6 imply that SPCE/CuO can be used not only in analysing glucose standard solutions but also to measure glucose in urine without suffering from matrix effect of urine sample.

Table 2-6. Results for measurement of glucose in urine sample

Added(µM)	Found(µM)	Recovery	RSD% (n=3)
200	216	108.2	7.1%
600	631	105.1	3.3%
1200	1230	102.5	5.8%

2.1.3.4 Conclusion

In conclusion, herein, a novel CuO nanostructure was synthesized using template and surfactant free microwave-assisted method. Different characterization techniques such as XDR, TEM, SAED and FTIR were used to reveal different structural properties of as-prepared CuO. XRD results confirmed the formation of CuO crystals with monoclinic structure and SEM analysis showed that CuO nanodisks consist of

nanorods linked together and thickness of the nanorod is ranging from 20 nm to 26 nm. Furthermore, this novel CuO nanodisk structure was used for the development of a very simple, cost-effective and sensitive non-enzymatic glucose sensor. The sensor offered high sensitivity of $627.3 \mu\text{A}\cdot\text{mM}^{-1}\cdot\text{cm}^{-2}$, a wide linear glucose measurement range from 2.0 μM to 2.5 mM, good selectivity, reproducibility and stability. Proposed sensor was fabricated in an extra simple way and yet kept its high sensitivity, selectivity and stability compared to many other reported CuO based glucose sensors in literature.

References

79. Maaoui H., Singh S.K., Teodorescu F., Coffinier Y., Barras A., Chtourou R., Kurungot S., Szunerits S., and Boukherroub R., *Copper oxide supported on three-dimensional ammonia-doped porous reduced graphene oxide prepared through electrophoretic deposition for non-enzymatic glucose sensing*. *Electrochimica Acta*, 2017. 224: p. 346-354.
80. Chen X., Wang J., Yang C., Ge Z., and Yang H., *Fluorescence resonance energy transfer from NaYF₄:Yb,Er to nano gold and its application for glucose determination*. *Sensors and Actuators, B: Chemical*, 2018. 255: p. 1316-1324.
81. Naaz S., Poddar S., Bayen S.P., Mondal M.K., Roy D., Mondal S.K., Chowdhury P., and Saha S.K., *Tenfold enhancement of fluorescence quantum yield of water soluble silver nanoclusters for nano-molar level glucose sensing and precise determination of blood glucose level*. *Sensors and Actuators, B: Chemical*, 2018. 255: p. 332-340.
82. Shulei W., Xueguang Y., and Yangan Z. *Non-invasive blood glucose measurement scheme based on near-infrared spectroscopy*. in *2017 Conference on Lasers and Electro-Optics Pacific Rim, CLEO-PR 2017*. 2017.
83. Simeone M.L.F., Parrella R.A.C., Schaffert R.E., Damasceno C.M.B., Leal M.C.B., and Pasquini C., *Near infrared spectroscopy determination of sucrose, glucose and fructose in sweet sorghum juice*. *Microchemical Journal*, 2017. 134: p. 125-130.
84. Khataee A., Haddad Irani-nezhad M., and Hassanzadeh J., *Improved peroxidase mimetic activity of a mixture of WS₂ nanosheets and silver nanoclusters for chemiluminescent quantification of H₂O₂ and glucose*. *Microchimica Acta*, 2018. 185(3).
85. Lindqvist D.N., Pedersen H., and Rasmussen L.H., *A novel technique for determination of the fructose, glucose and sucrose distribution in nectar from orchids by HPLC-ELSD*. *Journal of Chromatography B: Analytical Technologies in the Biomedical and Life Sciences*, 2018. 1081-1082: p. 126-130.
86. Yu L., Wen C., Li X., Fang S., Yang L., Wang T., and Hu K., *Simultaneous quantification of endogenous and exogenous plasma glucose by isotope dilution LC-MS/MS with indirect MRM of the derivative tag*. *Analytical and Bioanalytical Chemistry*, 2018. 410(7): p. 2011-2018.
87. Ampelli C., Leonardi S.G., Genovese C., Lanzafame P., Perathoner S., Centi G., and Neri G., *Monitoring of glucose in fermentation processes by using Au/TiO₂ composites as novel modified electrodes*. *Journal of Applied Electrochemistry*, 2015. 45(9): p. 943-951.
88. Leonardi S.G., Marini S., Espro C., Bonavita A., Galvagno S., and Neri G., *In-situ grown flower-like nanostructured CuO on screen printed carbon electrodes for non-enzymatic amperometric sensing of glucose*. *Microchimica Acta*, 2017. 184(7): p. 2375-2385.
89. Marini S., Ben Mansour N., Hjiri M., Dhahri R., El Mir L., Espro C., Bonavita A., Galvagno S., Neri G., and Leonardi S.G., *Non-enzymatic Glucose Sensor Based on Nickel/Carbon Composite*. *Electroanalysis*, 2018. 30(4): p. 727-733.
90. Dhara K. and Mahapatra D.R., *Electrochemical nonenzymatic sensing of glucose using advanced nanomaterials*. *Microchimica Acta*, 2017. 185(1): p. 49.

91. Unmüssig T., Weltin A., Urban S., Daubinger P., Urban G.A., and Kieninger J., *Non-enzymatic glucose sensing based on hierarchical platinum micro-/nanostructures*. Journal of Electroanalytical Chemistry, 2018. 816: p. 215-222.
92. Wang B., Yan S., Lin Z., Shi Y., Xu X., Fu L., and Jiang J., *Fabrication of graphene aerogel/platinum nanoparticle hybrids for the direct electrochemical analysis of glucose*. Journal of Nanoscience and Nanotechnology, 2016. 16(7): p. 6895-6902.
93. Jeong H., Nguyen D.M., Lee M.S., Kim H.G., Ko S.C., and Kwac L.K., *N-doped graphene-carbon nanotube hybrid networks attaching with gold nanoparticles for glucose non-enzymatic sensor*. Materials Science and Engineering C, 2018. 90: p. 38-45.
94. Núñez-Bajo E., Blanco-López M.C., Costa-García A., and Fernández-Abedul M.T., *In situ gold-nanoparticle electrogeneration on gold films deposited on paper for non-enzymatic electrochemical determination of glucose*. Talanta, 2018. 178: p. 160-165.
95. Nayak P., Nair S.P., and Ramaprabhu S., *Enzyme-less and low-potential sensing of glucose using a glassy carbon electrode modified with palladium nanoparticles deposited on graphene-wrapped carbon nanotubes*. Microchimica Acta, 2016. 183(3): p. 1055-1062.
96. Wu Q., Sheng Q., and Zheng J., *Nonenzymatic sensing of glucose using a glassy carbon electrode modified with halloysite nanotubes heavily loaded with palladium nanoparticles*. Journal of Electroanalytical Chemistry, 2016. 762: p. 51-58.
97. Ensafi A.A., Ahmadi N., and Rezaei B., *Nickel nanoparticles supported on porous silicon flour, application as a non-enzymatic electrochemical glucose sensor*. Sensors and Actuators, B: Chemical, 2017. 239: p. 807-815.
98. Ji Z., Wang Y., Yu Q., Shen X., Li N., Ma H., Yang J., and Wang J., *One-step thermal synthesis of nickel nanoparticles modified graphene sheets for enzymeless glucose detection*. Journal of Colloid and Interface Science, 2017. 506: p. 678-684.
99. Mishra S., Yogi P., Sagdeo P.R., and Kumar R., *Mesoporous Nickel Oxide (NiO) Nanopetals for Ultrasensitive Glucose Sensing*. Nanoscale Research Letters, 2018. 13.
100. Felix S., Charles X., and Grace A.N., *Non-enzymatic electrochemical detection of glucose using graphene/copper oxide nanocomposites*. Sensor Letters, 2017. 15(1): p. 60-64.
101. Heidari H. and Habibi E., *Amperometric enzyme-free glucose sensor based on the use of a reduced graphene oxide paste electrode modified with electrodeposited cobalt oxide nanoparticles*. Microchimica Acta, 2016. 183(7): p. 2259-2266.
102. Liu Y., Zhang X., He D., Ma F., Fu Q., and Hu Y., *An amperometric glucose biosensor based on a MnO₂/graphene composite modified electrode*. RSC Advances, 2016. 6(22): p. 18654-18661.
103. Mohamad Nor N., Abdul Razak K., and Lockman Z., *Physical and Electrochemical Properties of Iron Oxide Nanoparticles-modified Electrode for Amperometric Glucose Detection*. Electrochimica Acta, 2017. 248: p. 160-168.
104. Ba N., Zhu L., Zhang G., Li J., and Li H., *Facile synthesis of 3D CuO nanowire bundle and its excellent gas sensing and electrochemical sensing properties*. Sensors and Actuators, B: Chemical, 2016. 227: p. 142-148.

105. Foroughi F., Rahsepar M., Hadianfard M.J., and Kim H., *Microwave-assisted synthesis of graphene modified CuO nanoparticles for voltammetric enzyme-free sensing of glucose at biological pH values*. *Microchimica Acta*, 2018. 185(1).
106. Chen Z., Zhao B., Fu X.Z., Sun R., and Wong C.P., *CuO nanorods supported Pd nanoparticles as high performance electrocatalysts for glucose detection*. *Journal of Electroanalytical Chemistry*, 2017. 807: p. 220-227.
107. Simon I.A., Medeiros N.G., Garcia K.C., Soares R.M.D., Rosa A.T., and Silva J.A., *CuO Nanofibers Immobilized on Paraffin-Impregnated Graphite Electrode and its Application in the Amperometric Detection of Glucose*. *Journal of the Brazilian Chemical Society*, 2015. 26(8): p. 1710-1717.
108. Ye D., Liang G., Li H., Luo J., Zhang S., Chen H., and Kong J., *A novel nonenzymatic sensor based on CuO nanoneedle/graphene/carbon nanofiber modified electrode for probing glucose in saliva*. *Talanta*, 2013. 116: p. 223-230.
109. Eliot R., Wenzhao J., Michael G., Ying W., and Yu L., *CuO Nanospheres Based Nonenzymatic Glucose Sensor*. *Electroanalysis*, 2008. 20(22): p. 2482-2486.
110. Zhang J., Ma J., Zhang S., Wang W., and Chen Z., *A highly sensitive nonenzymatic glucose sensor based on CuO nanoparticles decorated carbon spheres*. *Sensors and Actuators B: Chemical*, 2015. 211: p. 385-391.
111. Zhong Y., Shi T., Liu Z., Cheng S., Huang Y., Tao X., Liao G., and Tang Z., *Ultrasensitive non-enzymatic glucose sensors based on different copper oxide nanostructures by in-situ growth*. *Sensors and Actuators B: Chemical*, 2016. 236: p. 326-333.
112. Ibupoto H.Z., Khun K., Beni V., Liu X., and Willander M., *Synthesis of Novel CuO Nanosheets and Their Non-Enzymatic Glucose Sensing Applications*. *Sensors*, 2013. 13(6).
113. Wang W., Zhang L., Tong S., Li X., and Song W., *Three-dimensional network films of electrospun copper oxide nanofibers for glucose determination*. *Biosensors and Bioelectronics*, 2009. 25(4): p. 708-714.
114. Zhang Y., Liu Y., Su L., Zhang Z., Huo D., Hou C., and Lei Y., *CuO nanowires based sensitive and selective non-enzymatic glucose detection*. *Sensors and Actuators B: Chemical*, 2014. 191: p. 86-93.
115. Reitz E., Jia W., Gentile M., Wang Y., and Lei Y., *CuO Nanospheres Based Nonenzymatic Glucose Sensor*. *Electroanalysis*, 2008. 20(22): p. 2482-2486.
116. Rahim A., Rehman Z.U., Mir S., Muhammad N., Rehman F., Nawaz M.H., Yaqub M., Siddiqi S.A., and Chaudhry A.A., *A non-enzymatic glucose sensor based on CuO-nanostructure modified carbon ceramic electrode*. *Journal of Molecular Liquids*, 2017. 248: p. 425-431.
117. He G. and Wang L., *One-step preparation of ultra-thin copper oxide nanowire arrays/copper wire electrode for non-enzymatic glucose sensor*. *Ionics*, 2018: p. 1-9.
118. Zhuang Z., Su X., Yuan H., Sun Q., Xiao D., and Choi M.M.F., *An improved sensitivity non-enzymatic glucose sensor based on a CuO nanowire modified Cu electrode*. *Analyst*, 2008. 133(1): p. 126-132.
119. Shi H.Y., Wu Y., Wang W., Song W.B., and Liu T.M., *Dopant-stimulated CuO nanofibers for electro-oxidation and determination of glucose*. *Chemical Research in Chinese Universities*, 2013. 29(5): p. 861-867.

2.2 Gas sensing analyses

2.2.1 *Evaluation of NiO-SCCNTs core-shell structure; new insight into shell thickness effect on gas sensing properties*

Abstract

Hierarchical core-shell (C-S) heterostructures composed of a NiO shell deposited onto stacked-cup carbon nanotubes (SCCNTs) were synthesized using atomic layer deposition (ALD). A controlled film of NiO particles was uniformly deposited onto the inner and outer walls of the CNTs. The NiO thickness was precisely controlled between 0.80 and 21.8 nm, by varying the number of ALD cycles from 25 to 700. The as-synthesized NiO-SCCNTs C-S heterostructures were thoroughly characterized by high-resolution transmission electron microscopy (HRTEM), energy dispersive X-ray (EDX) elemental mapping and X-ray photoelectron spectroscopy (XPS). The electrical resistance of the samples was found to increase of many orders of magnitude with the increasing of the NiO thickness. The behavior of NiO-SCCNTs sensors with various thicknesses of the NiO shell layers was investigated for low concentrations of acetone and ethanol at 200 °C. The sensing mechanism is based on the modulation of hole-accumulation region in the NiO shell layer, during the interaction of the reducing gas molecules with the adsorbed oxygen species, which account for a marked change in the resistance. The electrical conduction mechanism was further studied by developing NiO-Al₂O₃-SCCNTs heterostructures with the incorporation of Al₂O₃ dielectric layer in between the NiO and SCCNT interfaces. It suggested that the sensing mechanism is strictly related to the NiO shell layer. The remarkable performance of NiO-SCCNTs sensors towards acetone and ethanol benefits from the conformal coating by ALD, large surface area by SCCNTs and the optimized p-NiO shell layer thickness followed by the radial modulation of the space-charge region.

2.2.1.1 Introduction

Metal oxide semiconductor (MOS) gas sensors have been successfully used for the purpose of environmental monitoring, public security, sensor networks, automotive applications, domestic safety, chemical quality control and breath analysis. The development of the new sensing strategies for high sensitivity, rapid response and superior selectivity are among the major scientific ongoing challenges [120-123]. Among p-type metal oxides, NiO is one of the most frequently used candidates as active sensing material due to its wide band-gap (3.6 eV to 4.0 eV, depending upon the method of preparation and crystallinity), significant change in the electrical properties during chemical reactions on its surface, non-toxicity, high catalytic activity and low cost [124-127]. However, the low electronic conductivity of NiO limits its broad applications in chemo-resistive gas sensors [127, 128]. Nonetheless, many approaches have been introduced in the last few years to enhance the gas sensing performance of the NiO-based sensors by i) modifying the size and morphology of the sensing layers [124, 126, 129-134], ii) synthesizing NiO-based nanocomposites (e.g. with SnO₂, PdO, WO₃ and ZnO) [128, 135-137] and iii) doping NiO with e.g. Au, Fe, Pt and Zn [125, 138-141]. However, these composites may suffer from some issues during the sensing measurements, like aggregation and grain growth at high working temperatures, which cause a reduction in their durability and stability of the electrical response (i.e. baseline shift). Moreover, despite of years of work on these MO_x gas sensors, they are still facing shortcomings like high cost, low selectivity and high working temperature [142-145]. Hence, these materials are still in their infancy and state-of-the-art NiO sensors are still under active development [125, 129, 146, 147]. One of the options to overcome these problems is to employ heterostructures made of a CNTs core and a metal oxide semiconductor shell (C-S). Due to the high surface area and a lower charge recombination rate, the one-dimensional (1-D) nanostructures, such as nanowires, nanobelts and nanotubes have exhibited enhanced performances in catalysts and gas sensors as compared to other nano-sized composites [148, 149].

Carbon nanotubes (CNTs) are nanomaterials, which possess a large surface area to volume ratio; hence, they provide a direct benefit for gas sensing applications [150, 151]. However, pristine CNTs are not highly active toward gases and display slow responses and high recovery times [152]. These limitations can be appropriately

resolved by designing CNTs-MO_x heterostructures, which provide the advantages of both classes of materials without the drawbacks. Indeed, the CNTs provide a suitable conductive platform with a large surface area for metal oxides and a low operating temperature for gas sensing measurements [150, 151, 153], while NiO would provide a high response to analytes. In the recent past, many studies reported improved responses of MO_x gas sensors by preparing heterostructures between CNTs and n-type metal oxides, such as SnO₂/CNTs [154-157], hex-WO₃/MWCNTs [158], ZnO/MWCNTs [159], TiO₂/CNTs [153], V₂O₄-CNTs [160-162]. On the other hand, there are very few reports for p-type metal oxides such as NiO/CNTs heterostructures for gas sensing [152, 163]. Even though, some reports demonstrated good sensing properties, the homogeneity, conformality and a proper control over the thickness and particle size of the MO_x shell layer onto the CNT walls still remains challenging.

In addition to the nature of the sensing material, porosity and morphology, the shell thickness is also one of the most critical parameters for the design of C-S heterostructures. In particular, when the shell layer thickness is close to the Debye length (λ_D), the conduction is significantly influenced by the modulation of the space charge layer near the interface, which, consequently, leads to the enhanced gas sensing performances [127, 153, 164-167]. Unfortunately, there has not been enough reports on the design of heterostructures with optimised shell thicknesses for gas sensing applications. Generally, solution-based methods show a very limited control over the shell thickness, especially when the shell layer is in the order of few nanometers, hence, alternative methods for preparing the conformally coated nanostructures with high aspect ratio and a well-adjusted shell film thickness are needed.

Atomic layer deposition (ALD) has proven to be able to conformally coat high aspect ratio nanostructures with well-calibrated thin films. On the other hand, to the best of our knowledge, there is no report which study the role of the NiO shell thickness on gas sensing applications and try to build clear structure-property correlations.

2.2.1.2 *Experimental*

Chemicals and Reagents

Stacked-cup carbon nanotubes, SCCNTs (pyrograf III, PR24-PS) were purchased from Applied Science, inc., nitric acid (67%) was purchased from VWR chemicals.

Bis(cyclopentadienyl)nickel (Nickelocene, Ni(Cp)₂), was purchased from ABCR GmbH with a purity of 99.99%. Ozone was used as produced by using pure oxygen at a pressure of 1 bar in a BMT803N ozone delivery system. Trimethylaluminum ((CH₃)₃Al, TMA, 98%) was purchased from STREM chemicals. Argon was purchased by Air Liquide, 99.99% purity. Other gases, i.e. acetone, ethanol, H₂, NH₃, NO₂, CO₂, CO and methane were coming from certified bottles purchased from SOL company (www.solgroup.com). All other chemicals and reagents were of analytical grades and used without further purification unless otherwise stated.

Gas sensing tests

Sensors were fabricated by depositing a film of the water dispersed NiO-SCCNTs-x samples onto the platinum interdigitated area of alumina substrates (6x3 mm²) containing a Pt heater located on the backside. After that, sensors were introduced in a stainless-steel chamber for the sensing measurements. The experimental bench for the electrical characterization of the sensors allows to carry out measurements in controlled atmosphere. Gases coming from certified bottles were diluted in air at a given concentration by mass flow controllers. All the measurements were carried out at 200 °C, under a dry air total stream of 100 sccm. A multimeter data acquisition unit Agilent 34970A was used for this purpose, while a dual-channel power supplier instrument Agilent E3632A was employed to bias the built-in heater of the sensor to perform measurements at super-ambient temperature. The sensor response (S) is defined as $S = R_g / R_a$, where R_g and R_a are the electrical resistance values of the sensor in the presence and absence of target gases, respectively.

2.2.1.3 Results and discussion

2.2.1.3.1 Structural characterization

The relative thickness of the NiO ALD film was initially measured by ellipsometry. Well-cleaned Si-wafers were also coated in the ALD chamber at the same time as the SCCNTs. Ellipsometry data confirmed the successful execution of the ALD process, by comparing the thickness of the coated silicon wafer to the non-coated wafer. The growth per cycle (GPC) was consistently determined in terms of thickness of the NiO deposited layer vs. the number of ALD cycles on Si/SiO₂ wafers.

The structure and morphology of the NiO-SCCNTs samples were thoroughly analysed by transmission electron microscopy (TEM). Figure 25 shows TEM images for the samples coated by 100, 200, 400 and 700 NiO ALD cycles. Some more HRTEM images, to differentiate between the thickness of the NiO shell layer for the SCCNTs samples coated with 25, 50, 100, 200, 400 and 700 NiO ALD cycles can also be found in our recent report [62]. It can be seen that the SCCNTs are equally and conformally coated from the inner and the outer surfaces with NiO nanoparticles. It is observed that small NiO nanoparticles were deposited after 25 ALD cycles with a steady growth to a compact and dense NiO film after 700 ALD cycles. The thickness of the NiO coating increases with the number of ALD cycles. The GPC determined from the thickness of the NiO films grown on the SCCNTs for various number of ALD cycles is almost constant. The linear fitting ($R^2 = 0.993$) of the NiO thickness vs. the number of ALD cycles passes by the origin with a slope of $0.32 \text{ \AA cycles}^{-1}$ corresponding to a growth per cycle (GPC) of 0.32 \AA , as also reported recently by us [62]. The average thickness calculated for the NiO-SCCNTs samples from TEM images are similar to the values calculated from ellipsometry data (Table 2-7).

Table 2-7 Summary of the ALD deposited NiO shell layer thickness and growth per cycles (GPC) as calculated by transmission electron microscopy (TEM) on SCCNTs and ellipsometry on silicon wafers.

Number of ALD cycles	Transmission electron microscopy (TEM)			Ellipsometry		
	Thickness (nm)	GPC ($\text{\AA} / \text{cycle}$)	Slope of the linear fit (GPC)	Thickness (nm)	GPC ($\text{\AA} / \text{cycle}$)	Slope of the linear fit (GPC)
25	0.8	0.32	0.32 $\text{\AA} / \text{cycle}$	0.74	0.29	0.37 $\text{\AA} / \text{cycle}$
50	1.7	0.34		1.89	0.37	
100	4.0	0.4		3.42	0.34	
200	6.5	0.32		7.08	0.35	
400	14.0	0.35		16.04	0.4	
700	21.8	0.31		24.43	0.34	

This further proves the ALD character and the self-terminating behavior of the process under the applied conditions, indicating that thickness of the NiO shell layer can be tailored by controlling the number of ALD cycles. Further, high-resolution

transmission electron microscopy (HRTEM), high-angle annular dark-field scanning transmission electron microscopy (HAADF-STEM), bright-field (BF) and EDX mappings images are shown in Figure 25. The lattice spacing of 0.21 nm and 0.24 nm in magnified HRTEM can be assigned to the interplanar distance of the (111) and (200) lattice planes for the NiO, whereas the spacing of 0.39 nm can be assigned to the (002) plane of hexagonal graphitic carbon, respectively. The multiple concentric rings in the selected area electron diffraction pattern (SAED) obtained for NiO-SCCNT-200 confirm the polycrystalline characteristic of the sample (inset of Figure 25d). The main Debye-Scherrer rings correspond to the (200), (111) and (220) planes of the rock salt structure of NiO (ICDD 01-075-0197) and to the (002) plane for graphitized carbon (ICDD 01-075-1621). It can be seen in the HAADF-STEM and in the elemental mappings images that NiO is homogeneously distributed throughout the inner and outer walls of the SCCNT forming a smooth and conformal layer with a measurable thickness (Figure 25 e-h). The structure and phase composition of the synthesized sample were studied by X-ray diffraction (XRD). Pristine SCCNTs show the characteristic peaks of hexagonal structured graphitic carbon and ALD coated NiO-SCCNTs with 50, 100, 200 and 400 deposition cycles of NiO show the diffraction peaks corresponding to the reflections of face-centred cubic NiO. NiO-SCCNTs also show reflection coming from SCCNTs, which becomes less pronounced compared to the reflections originating from NiO, with higher number of ALD cycles. These results have been reported in our previous articles [[42](#), [62](#)].

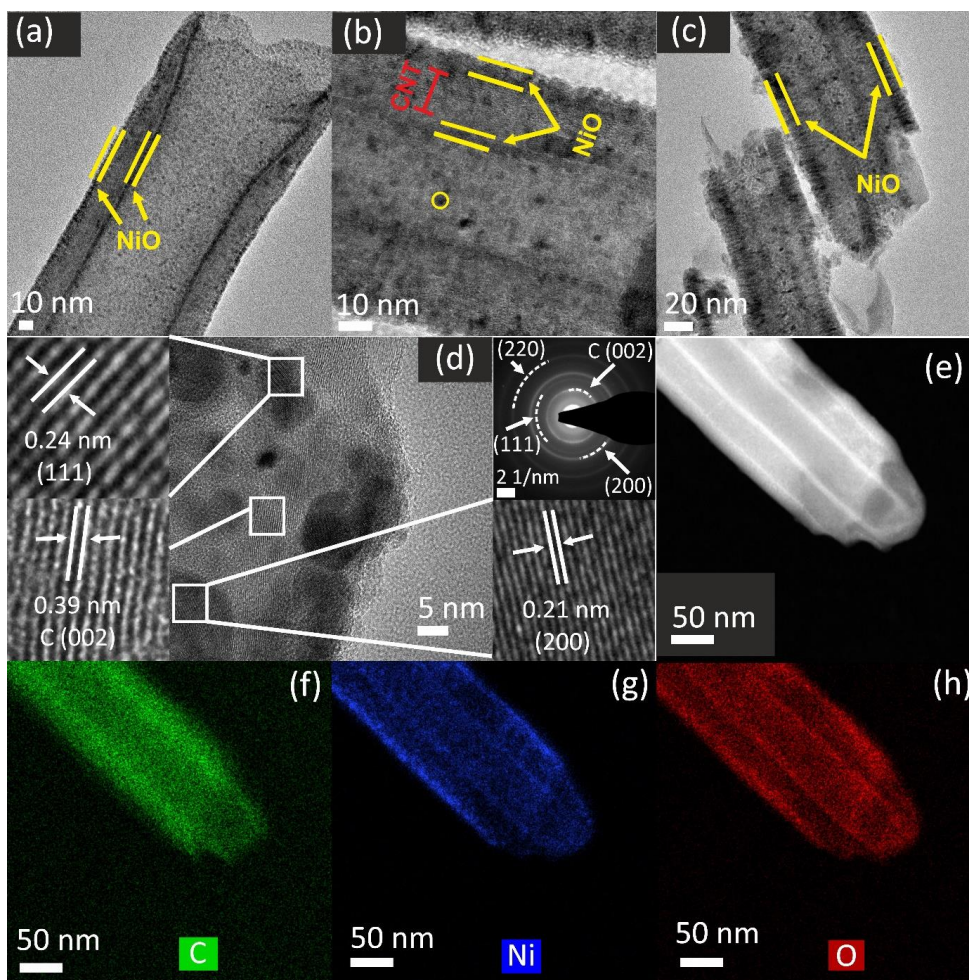


Figure 2-25. High-resolution transmission electron microscopy (HRTEM) images for (a) NiO-SCCNTs-100, (b) NiO-SCCNTs-200, (c) NiO-SCCNTs-400, (d) magnified HRTEM image for the NiO-SCCNTs-200 sample, (e) HAADF-STEM images for NiO-SCCNTs-700 and (f-h) EDX elemental mapping for carbon, nickel and oxygen, respectively.

The chemical state of the NiO film deposited on SCCNTs was examined by high-resolution X-ray photoelectron spectroscopy (XPS) [135]. Figure 26a displays the Ni $2p_{3/2}$ core level spectra for the NiO-SCCNTs samples with 100, 200 and 700 ALD cycles. The broad feature centred at 861.2 eV is mainly due to the complex multiplet splitting and to the number of possible final states due to the strong overlap of the Ni and O orbitals. More relevant is the low BE peak centred at 854.1 eV, which can be unambiguously ascribed to Ni^{2+} in the NiO_6 octahedral coordination of the cubic rock-salt NiO structure [168-172]. The remaining peak at 856.2 eV is known to be a surface component and can be attributed to surface hydroxylated NiO, similarly to Ni^{2+} in $\text{Ni}(\text{OH})_2$.

Figure 26b presents the O1s edges of NiO deposited onto SCCNTs with 100, 200 and 700 ALD cycles. The lower binding energy peak at 529.5 eV is representative of the lattice oxygen, *i.e.*, O²⁻ in NiO. At high binding energy, the small peak at 533.2 eV corresponds to residual water at the film surface. The peak at 531.5 eV can be indexed to surface hydroxyl groups [173-176]. In the present study, all deposition were executed in a moisture free highly evacuated chamber using argon as a carrier and purging gas for the precursors, so, the hydroxylated surface should be due to the short exposure in air after deposition. On the other hand, the bulk of the film still remains rock salt NiO (cf. XRD [62], TEM and SAED results above) while the surface has been hydroxylated over the top few nanometres.

It can also be further observed for both, Ni 2p and O 1s, regions that the NiO contribution became more prominent with the increasing of the number of ALD cycles. Since the thickness of NiO coating increases with the increasing of the number of ALD cycles, hence the bulk component (NiO) became more prominent than the hydroxylated surface region.

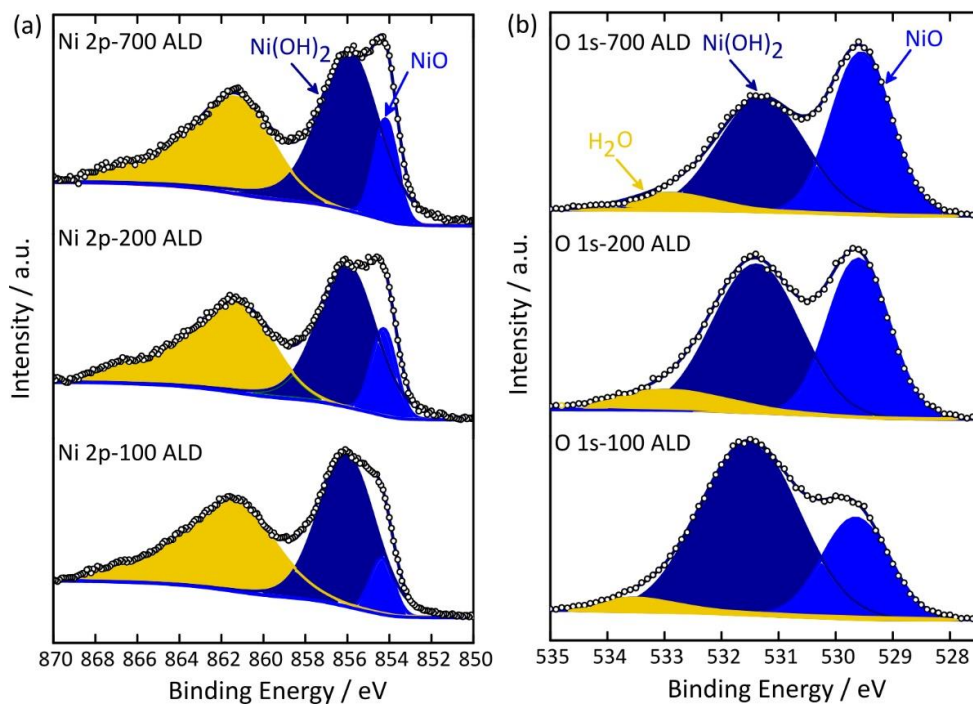


Figure 2-26. High-resolution XPS spectra for NiO-SCCNTs samples with 100, 200 and 700 ALD cycles, (a) Ni 2p and (b) O 1s scanned regions.

2.2.1.3.2 Electrical characteristics

Electrical and sensing characteristics of NiO-SCCNTs C-S heterostructures were evaluated with the planar conductometric sensor device, described in our previous reports [177]. All the samples were annealed in dry air at a temperature of 200 °C to remove any absorbed water, etc. Annealing at 200 °C did not make any change in the crystalline structure or chemical states of the samples as the NiO deposition was also originally performed at 200 °C (ALD chamber temperature). The annealed NiO-SCCNTs-X samples were deposited onto the Pt interdigitated area of the alumina substrate. First, the baseline resistance (R_a) was measured in dry air at 200 °C for the oxidised SCCNTs and all the NiO-SCCNTs-x sensors (Figure 27 a and b). The SCCNTs sensor showed a very low value of R_a *i.e.*, about 82 ohm, which is in accordance to the relatively high conductivity of the carbon nanotubes [155]. The baseline resistance (R_a) of NiO-SCCNTs-X sensors increased with the increasing of the NiO thickness (number of ALD cycles), which shows that the resistance of NiO-SCCNTs sensors largely depends on the thickness of the NiO shell layer (Figure 28a). The NiO-SCCNTs-700 sensor showed a high resistance value, approximately up-to seven-order of magnitude as compared to the oxidised SCCNTs. Hence, the resistance of the NiO-SCCNTs-X sensors is dominated by the resistive shell layer rather than the semiconducting core substrate, due to the serial connection between the highly resistive NiO shell layers and the conducting carbon nanotubes substrate.

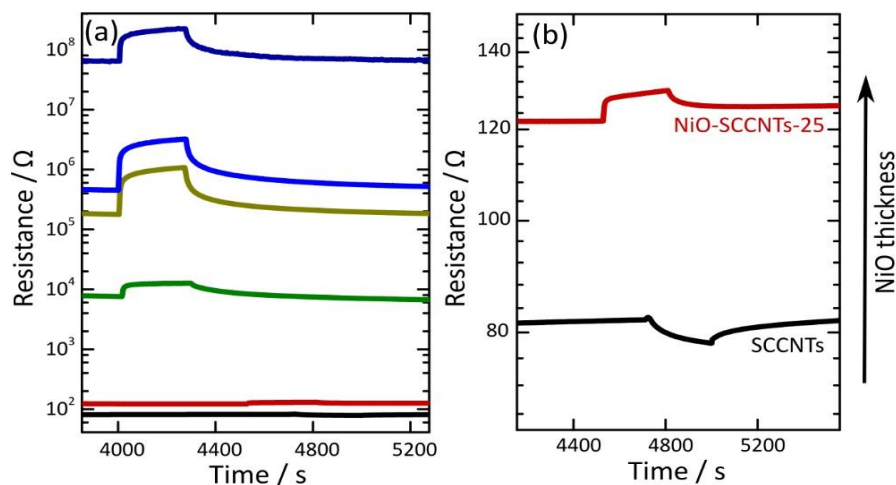


Figure 2-27. (a) Baseline resistance (R_a) variation to a 10 ppm pulse of ethanol of the oxidised SCCNTs and XNiO-SCCNTs sensors, (b) enlarged view of the SCCNTs (black) and 25NiO-SCCNTs (red) sensors.

2.2.1.3.3 Gas sensing tests

The fundamental gas sensing properties of the SCCNTs and NiO-SCCNTs-X C-S heterostructures were investigated to evaluate their applicability towards acetone and ethanol gas detections. A temperature of 200 °C was chosen for this study, which is similar to the already optimized and reported temperatures for the NiO and CNTs composites [152, 163]. The gas sensing tests were performed for acetone and ethanol with the oxidized SCCNTs and a series of NiO-SCCNTs-X sensors in an especially design sensing chamber and the variations in the resistance (R_g) were registered. Figure 28 (b-e) represent the response of all the sensors to various concentrations of acetone and ethanol at 200 °C. When acetone and ethanol were introduced in the sensing chamber, the resistance of the SCCNTs decreases and shortly reached a minimum resistance value, which indicate an n-type response of the oxidized SCCNTs (Figure 28b). Generally, CNTs are reported as a p-type semiconductor, even though, it has been reported that depending on the procedure of synthesis and pre-treatment as well as the presence of even very small amount of impurity of metal/metal oxide, this semiconducting behavior may change. Especially, the electronic properties of the CNTs are very sensitive to the chemical environment and conditions. It was demonstrated that the electrical resistance and local density of states of the CNTs are influenced by its exposure to a certain environment and these can be tuned reversibly by even small concentrations of adsorbed gases. The electronic properties of the CNTs are not only related to the diameter and chirality, but also depend on the gas history as well [178-180].

The dynamic response of the NiO-SCCNTs-X sensors towards various concentrations of acetone and ethanol (from 1 ppm to 40 ppm) as target gases is shown in the Figure 28 (c-f). It can be seen that coating of the NiO shell layer on the SCCNTs (NiO-SCCNTs, C-S heterostructures) remarkably modified the semiconducting nature of the SCCNTs. In response to acetone and ethanol, the resistance of the NiO-SCCNTs-X sensors increases and then recover promptly to the baseline value as the gases are removed from the testing chamber. The responses of the NiO-SCCNTs materials show a typical p-type behavior and a significant enhancement as compared to the non-coated SCCNTS, which can be attributed to the synergic effect of both of the materials, i.e. the good conductivity of the SCCNTs support and the significant gas response and

catalytic activity of NiO. Such a significant increase in response was already observed and well demonstrated elsewhere for other metal oxides-CNTs heterostructures [155, 163]. The gas sensing response of the NiO-SCCNTs-X sensors increased with the increasing of the concentration of the target gases (Figure 28 g and h). The linear dependence of the gas response (S) to the concentration of the target gases can be represented empirically by $S = a[C]^{b+1}$ or $\text{Log}(S-1) = b \log(C) + \log(a)$ [181]. The inset of Figure 28 g and h indicate that all the NiO-SCCNTs-X sensors have excellent linearity (determination coefficient, $R^2 > 0.98$) in logarithmic form and these NiO-SCCNTs hierarchical C-S nanostructures can be used as promising sensing materials for acetone and ethanol detection.

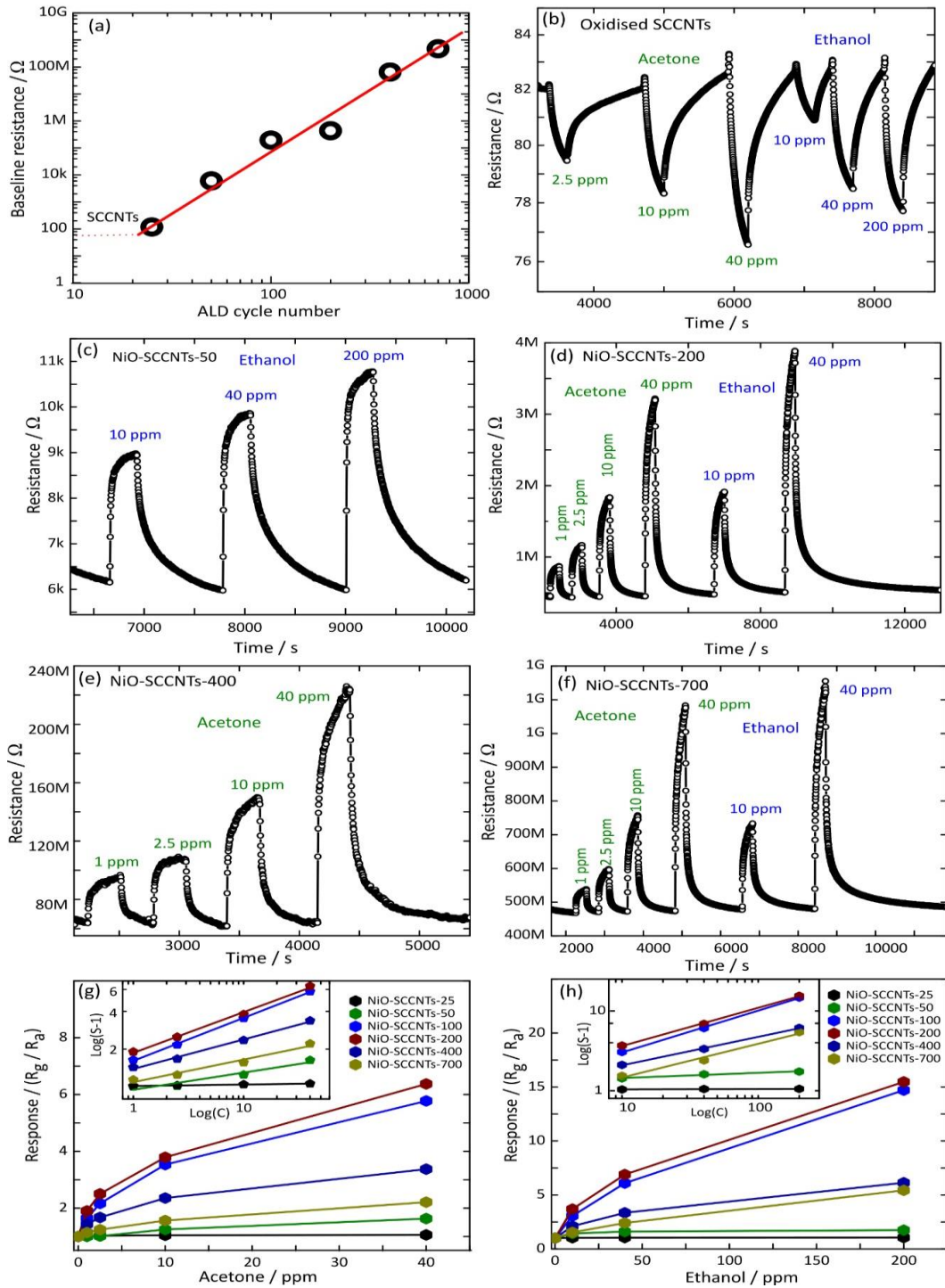


Figure 2-28. (a) The linear plot of the baseline resistance vs the number of ALD cycles (NiO shell thickness) for NiO-SCCNTs-X and SCCNTs sensors. Dynamic response towards different concentrations of acetone and ethanol at 200 °C by the fabricated sensors with, (b) oxidized SCCNTs, (c) NiO-SCCNTs-50, (d) NiO-SCCNTs-200, (e) NiO-SCCNTs-400 and (f) NiO-SCCNTs-700. The Response variations of NiO-SCCNTs-X sensors for different concentrations of target gases, (g) acetone and (h) ethanol. The insets in (g) and (h) show the linear fit for the logarithmic expression of the NiO-SCCNTs-X sensors response as a function of the target gas concentrations. All the tests were performed at 200 °C.

It is remarkable that there is a correlation between the NiO shell thickness (e.g. number of ALD cycles) of the NiO-SCCNTs-X C-S nanostructures and their gas sensing response. The response (S) initially increased as the NiO thickness increased from 0 to about 5-6.5 nm (200 ALD cycles) and then decreases progressively for the thicker films grown with 400 and 700 ALD cycles (14 and 22 nm shell thickness) (Figure 29a). As a resistive-type sensor, the gas sensing mechanism of these NiO-SCCNTs-X sensors could be explained by a change in the resistance/conductance caused by the exposure to the target gas environment. When a material is exposed to air, the oxygen molecules adsorbed on the material surface capture electrons forming negatively charged (O_2^- , O^- and O^{2-}) surface species. In case of a p-type material, the resistance of the surface decreases due to the increase of the carrier density (hole accumulation layer, HAL) and the whole layer acts as a conducting medium. On exposure to a reducing gas like acetone and ethanol, the gas molecules react with the adsorbed oxygen (oxidise to e.g. CO_2 and H_2O) leading to the release of electrons back to the surface. These electrons combine with the holes in the p-type material causing a reduction in the carrier concentration and therefore to an increase in resistance [182]. Hence, the sensing properties of the nanostructures can be enhanced by the increase of the resistance variation.

The variation of the sensing response of the NiO-SCCNTs sensors, as a function of the NiO shell thickness, presents a volcano-shaped curve (Figure 29a). It implies that the sensing property of NiO-SCCNTs nanostructures is intimately linked to the width of the depletion layer. The high sensing response of the NiO-SCCNTs-200 sensor is due to the fact that the thickness of the NiO coating is similar to the thickness of the depletion layer, *i.e.* the Debye length (λ_D) [183, 184]. At this point, the entire film is in the space-charge-region and the charge conduction in the NiO film is dominantly perturbed by the oxygen vacancies and/or acetone/ethanol chemisorbed species at the surface. It was demonstrated that for an un-doped NiO hole transport layer on ITO with thickness comparable to the Debye Length (λ_D), the performance improvement recorded was attributed to the better conductivity of thin NiO films, the higher work function and the higher hole concentration. The reported Debye length (λ_D) for a NiO film is in the range of 2-13 nm, depending upon the temperature and preparation method of the material [170, 184]. Other investigations have also observed a

correlation between the resistance variations (responsivity) and the variations in the film thicknesses of the active materials, especially for thin films. Marichy *et al.*,[\[153\]](#) Fang *et al.*,[\[127\]](#) Park *et al.*,[\[185\]](#) Katoch *et al.*,[\[183\]](#) and Qu *et al.*,[\[182\]](#) reported an optimized gas sensing performance for TiO₂-CNTs, NiO-SnO₂, In₂O₃-ZnO, SnO₂-ZnO and Fe₃O₄-Co₃O₄ heterostructures at a thickness of 5.5 nm for TiO₂ ($\lambda_D \approx 11$ nm), 5 nm for NiO ($\lambda_D \approx 2$ -13 nm), 44 nm for ZnO ($\lambda_D \approx 21.7$ nm), 20 nm for ZnO ($\lambda_D \approx 0.7$ -22 nm) and 50 nm for Co₃O₄ ($\lambda_D \approx 40$ nm), respectively. These reports of optimized gas sensing responses using different heterostructures demonstrated that the best performance is expected in the range of the Debye length. This observation also suggests that in our NiO-SCCNTs nanostructures, the electrical properties are dominated by Schottky barrier junctions across n(core)-p(shell) interfaces. Based on these results the best performing NiO-SCCNTs-200 sensor was selected for further investigations.

The dynamic response of the NiO-SCCNTs-200 sensor was measured to 10 ppm of acetone and ethanol at 200 °C (Figure 29b). It shows a good reproducibility and recovery of the signals after successive exposure to the acetone/ethanol and air. The stability of the NiO-SCCNTs-200 sensor was measured for the various concentrations of acetone and ethanol at 200 °C. Two sensors were prepared from the same samples (NiO-SCCNTs-200) and tested under similar conditions. The baseline (no drift) and good reproducibility of the signals evidenced a good stability of the fabricated sensors (Figure 29c). The selectivity of the NiO-SCCNTs-200 sensor was tested against acetone, ethanol and some interfering gases like CO₂, NO₂, NH₃, CO, methane and hydrogen. It is clear that NiO-SCCNTs-200 sensor shows a significant and clear response towards acetone and ethanol, whereas it shows lower effective signals for other gases at concentrations relevant to typical gas sensing applications (Figure 29d). Hence, the NiO-SCCNTs-200 fabricated sensor shows a good selectivity for acetone and ethanol detection at 200 °C.

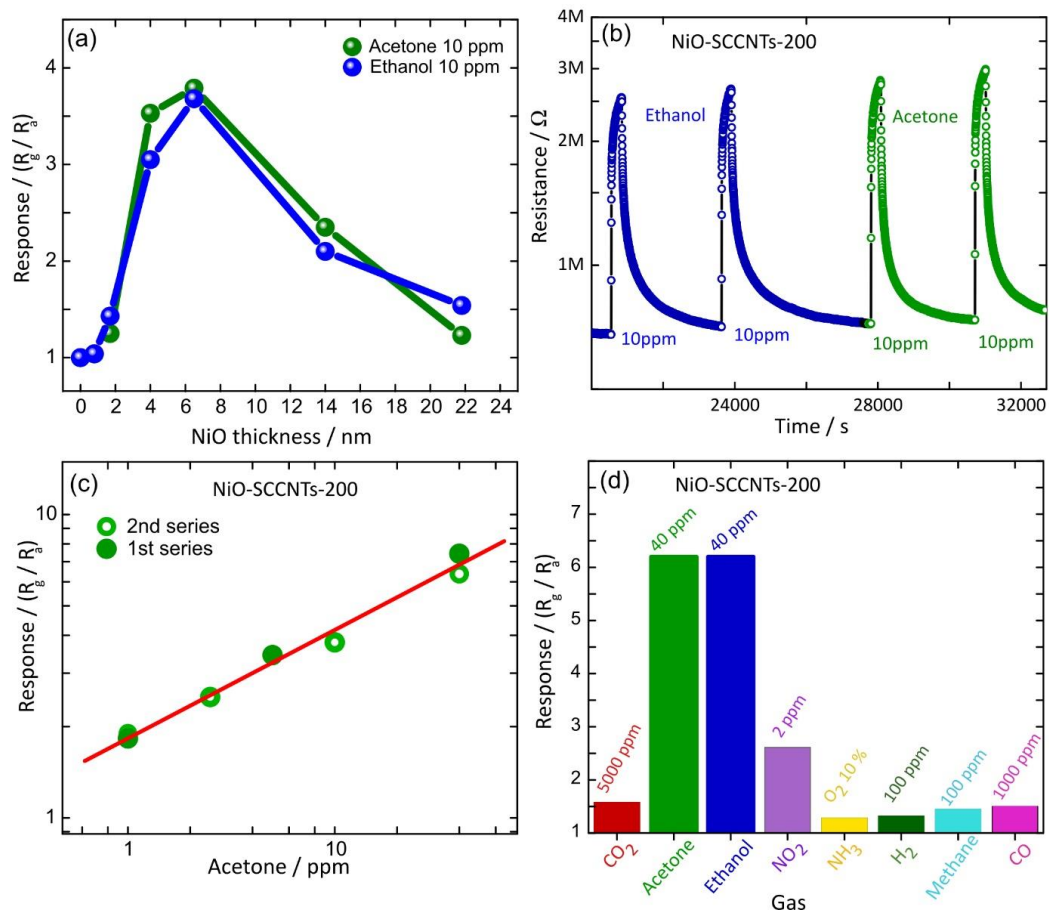


Figure 2-29. (a) NiO shell layer thickness of NiO-SCCNTs-X sensors as a function of the sensing response towards acetone and ethanol at 200 °C. (b) Successive response of NiO-SCCNTs-200 fabricated sensor to 10 ppm of ethanol and acetone at 200 °C. (c) response of two different sensors fabricated by NiO-SCCNTs-200 towards acetone at 200 °C. (d) response of NiO-SCCNTs-200 sensor to acetone, ethanol and other gases at 200 °C, which demonstrate a good selectivity towards ethanol and acetone.

2.2.1.4 Conclusion

NiO-SCCNTs core-shell (C-S) hierarchical heterostructures with a range of ultra-thin layers of NiO (from 0.80 to 21.8 nm in thickness) by ALD is reported for gas sensing applications. The SCCNTs sensor capabilities are greatly enhanced by the homogenous and conformal coating with a NiO shell layer. Both the electrical properties and the sensor response of NiO-SCCNTs C-S hierarchical heterostructures for acetone and ethanol are strongly dependent on the thickness of the NiO shell layer, proving that the sensor performances are closely related to the thickness of the electron depletion layer. NiO-SCCNTs-200 (6.5 nm NiO shell layer) sensors show the best performance among others due to the matching of the Debye length (λ_D) with the coating thickness. The NiO-SCCNTs-200 sensors also showed excellent performance in terms of

stability, reproducibility and selectivity towards acetone and ethanol. The noteworthy performance of NiO-SCCNTs-200 sensors can be attributed to the good conductivity and high surface-area of the SCCNT substrate, the conformal and homogenous NiO coating achievable by ALD and the optimized NiO thickness. All in all, we are convinced that our optimized heterostructures endow a great potential for gas sensing applications.

Reference

120. Seiyama T., Kato A., Fujiishi K., and Nagatani M., *A New Detector for Gaseous Components Using Semiconductive Thin Films*. Analytical Chemistry, 1962. 34(11): p. 1502-1503.
121. Neri G., *First Fifty Years of Chemoresistive Gas Sensors*. Chemosensors, 2015. 3(1).
122. Kim I.-D., Rothschild A., and Tuller H.L., *Advances and new directions in gas-sensing devices*. Acta Materialia, 2013. 61(3): p. 974-1000.
123. Comini E., *Metal oxide nano-crystals for gas sensing*. Analytica Chimica Acta, 2006. 568(1): p. 28-40.
124. Zeng W., Miao B., Lin L.-y., and Xie J.-y., *Facile synthesis of NiO nanowires and their gas sensing performance*. Transactions of Nonferrous Metals Society of China, 2012. 22: p. s100-s104.
125. Majhi S.M., Naik G.K., Lee H.-J., Song H.-G., Lee C.-R., Lee I.-H., and Yu Y.-T., *Au@NiO core-shell nanoparticles as a p-type gas sensor: Novel synthesis, characterization, and their gas sensing properties with sensing mechanism*. Sensors and Actuators B: Chemical, 2018. 268: p. 223-231.
126. Hotovy I., Rehacek V., Siciliano P., Capone S., and Spiess L., *Sensing characteristics of NiO thin films as NO₂ gas sensor*. Thin Solid Films, 2002. 418(1): p. 9-15.
127. Fang J., Zhu Y., Wu D., Zhang C., Xu S., Xiong D., Yang P., Wang L., and Chu P.K., *Gas sensing properties of NiO/SnO₂ heterojunction thin film*. Sensors and Actuators B: Chemical, 2017. 252: p. 1163-1168.
128. Xu L., Zheng R., Liu S., Song J., Chen J., Dong B., and Song H., *NiO@ZnO Heterostructured Nanotubes: Coelectrospinning Fabrication, Characterization, and Highly Enhanced Gas Sensing Properties*. Inorganic Chemistry, 2012. 51(14): p. 7733-7740.
129. Liu B., Yang H., Zhao H., An L., Zhang L., Shi R., Wang L., Bao L., and Chen Y., *Synthesis and enhanced gas-sensing properties of ultralong NiO nanowires assembled with NiO nanocrystals*. Sensors and Actuators B: Chemical, 2011. 156(1): p. 251-262.
130. Wang J., Yang P., Wei X., and Zhou Z., *Preparation of NiO two-dimensional grainy films and their high-performance gas sensors for ammonia detection*. Nanoscale research letters, 2015. 10: p. 119-119.
131. Ren Y., Chim W.K., Chiam S.Y., Huang J.Q., Pi C., and Pan J.S., *Formation of Nickel Oxide Nanotubes with Uniform Wall Thickness by Low-Temperature Thermal Oxidation Through Understanding the Limiting Effect of Vacancy Diffusion and the Kirkendall Phenomenon*. Advanced Functional Materials, 2010. 20(19): p. 3336-3342.
132. Zhu G., Xi C., Xu H., Zheng D., Liu Y., Xu X., and Shen X., *Hierarchical NiO hollow microspheres assembled from nanosheet-stacked nanoparticles and their application in a gas sensor*. RSC Advances, 2012. 2(10): p. 4236-4241.
133. Hoa N.D. and El-Safty S.A., *Synthesis of Mesoporous NiO Nanosheets for the Detection of Toxic NO₂ Gas*. Chemistry – A European Journal, 2011. 17(46): p. 12896-12901.
134. Cho N.G., Woo H.-S., Lee J.-H., and Kim I.-D., *Thin-walled NiO tubes functionalized with catalytic Pt for highly selective C₂H₅OH sensors using*

- electrospun fibers as a sacrificial template*. Chemical Communications, 2011. 47(40): p. 11300-11302.
135. Wang L., Lou Z., Wang R., Fei T., and Zhang T., ***Ring-like PdO–NiO with lamellar structure for gas sensor application***. Journal of Materials Chemistry, 2012. 22(25): p. 12453-12456.
 136. Wang L., Deng J., Fei T., and Zhang T., ***Template-free synthesized hollow NiO–SnO₂ nanospheres with high gas-sensing performance***. Sensors and Actuators B: Chemical, 2012. 164(1): p. 90-95.
 137. Wang Y., Maity A., Sui X., Pu H., Mao S., Singh N.K., and Chen J., ***In Operando Impedance Spectroscopic Analysis on NiO–WO₃ Nanorod Heterojunction Random Networks for Room-Temperature H₂S Detection***. ACS Omega, 2018. 3(12): p. 18685-18693.
 138. Kim H.-J., Choi K.-I., Kim K.-M., Na C.W., and Lee J.-H., ***Highly sensitive C₂H₅OH sensors using Fe-doped NiO hollow spheres***. Sensors and Actuators B: Chemical, 2012. 171-172: p. 1029-1037.
 139. Mattei G., Mazzoldi P., Post M.L., Buso D., Guglielmi M., and Martucci A., ***Cookie-like Au/NiO Nanoparticles with Optical Gas-Sensing Properties***. Advanced Materials, 2007. 19(4): p. 561-564.
 140. ul Haq M., Wen Z., Zhang Z., Khan S., Lou Z., Ye Z., and Zhu L., ***A two-step synthesis of nanosheet-covered fibers based on α -Fe₂O₃/NiO composites towards enhanced acetone sensing***. Scientific Reports, 2018. 8(1): p. 1705.
 141. Wang J., Wei L., Zhang L., Zhang J., Wei H., Jiang C., and Zhang Y., ***Zinc-doped nickel oxide dendritic crystals with fast response and self-recovery for ammonia detection at room temperature***. Journal of Materials Chemistry, 2012. 22(37): p. 20038-20047.
 142. Wetchakun K., Samerjai T., Tamaekong N., Liewhiran C., Siriwong C., Kruefu V., Wisitorsaat A., Tuantranont A., and Phanichphant S., ***Semiconducting metal oxides as sensors for environmentally hazardous gases***. Sensors and Actuators B: Chemical, 2011. 160(1): p. 580-591.
 143. Wang S., Kang Y., Wang L., Zhang H., Wang Y., and Wang Y., ***Organic/inorganic hybrid sensors: A review***. Sensors and Actuators B: Chemical, 2013. 182: p. 467-481.
 144. Shin J., Choi S.-J., Lee I., Youn D.-Y., Park C.O., Lee J.-H., Tuller H.L., and Kim I.-D., ***Thin-Wall Assembled SnO₂ Fibers Functionalized by Catalytic Pt Nanoparticles and their Superior Exhaled-Breath-Sensing Properties for the Diagnosis of Diabetes***. Advanced Functional Materials, 2013. 23(19): p. 2357-2367.
 145. Liu X., Ma T., Pinna N., and Zhang J., ***Two-Dimensional Nanostructured Materials for Gas Sensing***. Advanced Functional Materials, 2017. 27(37): p. 1702168.
 146. Arnal P.M., Comotti M., and Schüth F., ***High-Temperature-Stable Catalysts by Hollow Sphere Encapsulation***. Angewandte Chemie International Edition, 2006. 45(48): p. 8224-8227.
 147. Pinna N., Neri G., Antonietti M., and Niederberger M., ***Nonaqueous Synthesis of Nanocrystalline Semiconducting Metal Oxides for Gas Sensing***. Angewandte Chemie International Edition, 2004. 43(33): p. 4345-4349.
 148. Yujin C., Chunling Z., and Taihong W., ***The enhanced ethanol sensing properties of multi-walled carbon nanotubes / SnO₂ core/shell nanostructures***. Nanotechnology, 2006. 17(12): p. 3012.

149. Li T., Zeng W., and Wang Z., *Quasi-one-dimensional metal-oxide-based heterostructural gas-sensing materials: A review*. Sensors and Actuators B: Chemical, 2015. 221: p. 1570-1585.
150. Chandrasekhar P., *CNT Applications in Sensors and Actuators*, in *Conducting Polymers, Fundamentals and Applications: Including Carbon Nanotubes and Graphene*, P. Chandrasekhar, Editor. 2018, Springer International Publishing: Cham. p. 53-60.
151. Jennifer S.-O., Hung-Ta W., Byoung S.K., Zhuangchun W., Fan R., Andrew G.R., and Stephen J.P., *Carbon nanotube films for room temperature hydrogen sensing*. Nanotechnology, 2005. 16(10): p. 2218.
152. Chen N., Li Q., Li Y., Deng D., Xiao X., and Wang Y., *Facile synthesis and gas sensing performances based on nickel oxide nanoparticles/multi-wall carbon nanotube composite*. Journal of Materials Science: Materials in Electronics, 2015. 26(10): p. 8240-8248.
153. Catherine M., Nicola D., Mariangela L., Marc Georg W., Jean-Philippe T., Giovanni N., and Nicola P., *Gas sensing properties and p-type response of ALD TiO₂ coated carbon nanotubes*. Nanotechnology, 2015. 26(2): p. 024004.
154. Lu G., Ocola L.E., and Chen J., *Room-Temperature Gas Sensing Based on Electron Transfer between Discrete Tin Oxide Nanocrystals and Multiwalled Carbon Nanotubes*. Advanced Materials, 2009. 21(24): p. 2487-2491.
155. Marichy C., Russo P.A., Latino M., Tessonnier J.-P., Willinger M.-G., Donato N., Neri G., and Pinna N., *Tin Dioxide–Carbon Heterostructures Applied to Gas Sensing: Structure-Dependent Properties and General Sensing Mechanism*. The Journal of Physical Chemistry C, 2013. 117(38): p. 19729-19739.
156. Van Hieu N., Thuy L.T.B., and Chien N.D., *Highly sensitive thin film NH₃ gas sensor operating at room temperature based on SnO₂/MWCNTs composite*. Sensors and Actuators B: Chemical, 2008. 129(2): p. 888-895.
157. Duc Hoa N., Van Quy N., Suk Cho Y., and Kim D., *Nanocomposite of SWNTs and SnO₂ fabricated by soldering process for ammonia gas sensor application*. physica status solidi (a), 2007. 204(6): p. 1820-1824.
158. Balázsi C., Sedláčková K., Llobet E., and Ionescu R., *Novel hexagonal WO₃ nanopowder with metal decorated carbon nanotubes as NO₂ gas sensor*. Sensors and Actuators B: Chemical, 2008. 133(1): p. 151-155.
159. Tulliani J.-M., Cavalieri A., Musso S., Sardella E., and Geobaldo F., *Room temperature ammonia sensors based on zinc oxide and functionalized graphite and multi-walled carbon nanotubes*. Sensors and Actuators B: Chemical, 2011. 152(2): p. 144-154.
160. Willinger M.-G., Neri G., Bonavita A., Micali G., Rauwel E., Herntrich T., and Pinna N., *The controlled deposition of metal oxides onto carbon nanotubes by atomic layer deposition: examples and a case study on the application of V₂O₄ coated nanotubes in gas sensing*. Physical Chemistry Chemical Physics, 2009. 11(19): p. 3615-3622.
161. Santangelo S., Messina G., Faggio G., Willinger M.G., Pinna N., Donato A., Arena A., Donato N., and Neri G., *Micro-Raman investigation of vanadium-oxide coated tubular carbon nanofibers for gas-sensing applications*. Diamond and Related Materials, 2010. 19(5): p. 590-594.

162. Willinger M.-G., Neri G., Rauwel E., Bonavita A., Micali G., and Pinna N., *Vanadium Oxide Sensing Layer Grown on Carbon Nanotubes by a New Atomic Layer Deposition Process*. Nano Letters, 2008. 8(12): p. 4201-4204.
163. Jung D., Han M., and Lee G.S., *Gas-sensing properties of multi-walled carbon-nanotube sheet coated with NiO*. Carbon, 2014. 78: p. 156-163.
164. Sysoev V.V., Strelcov E., Kar S., and Kolmakov A., *The electrical characterization of a multi-electrode odor detection sensor array based on the single SnO₂ nanowire*. Thin Solid Films, 2011. 520(3): p. 898-903.
165. Mirzaei A., Kim J.-H., Kim H.W., and Kim S.S., *How shell thickness can affect the gas sensing properties of nanostructured materials: Survey of literature*. Sensors and Actuators B: Chemical, 2018. 258: p. 270-294.
166. Marichy C. and Pinna N., *Atomic Layer Deposition to Materials for Gas Sensing Applications*. Advanced Materials Interfaces, 2016. 3(21): p. 1600335.
167. Xu Z., Hou Y., and Sun S., *Magnetic Core/Shell Fe₃O₄/Au and Fe₃O₄/Au/Ag Nanoparticles with Tunable Plasmonic Properties*. Journal of the American Chemical Society, 2007. 129(28): p. 8698-8699.
168. Alders D., Voogt F.C., Hibma T., and Sawatzky G.A., *Nonlocal screening effects in 2p x-ray photoemission spectroscopy of NiO (100)*. Physical Review B, 1996. 54(11): p. 7716-7719.
169. Jiang Y., Yu S., Li J., Jia L., and Wang C., *Improvement of sensitive Ni(OH)₂ nonenzymatic glucose sensor based on carbon nanotube/polyimide membrane*. Carbon, 2013. 63: p. 367-375.
170. Seo S., Park I.J., Kim M., Lee S., Bae C., Jung H.S., Park N.-G., Kim J.Y., and Shin H., *An ultra-thin, un-doped NiO hole transporting layer of highly efficient (16.4%) organic-inorganic hybrid perovskite solar cells*. Nanoscale, 2016. 8(22): p. 11403-11412.
171. Soriano L., Preda I., Gutiérrez A., Palacín S., Abbate M., and Vollmer A., *Surface effects in the Ni 2p x-ray photoemission spectra of NiO*. Physical Review B, 2007. 75(23): p. 233417.
172. Marrani A.G., Novelli V., Sheehan S., Dowling D.P., and Dini D., *Probing the redox states at the surface of electroactive nanoporous NiO thin films*. ACS Appl Mater Interfaces, 2014. 6.
173. Awais M., Dowling D.P., Decker F., and Dini D., *Electrochemical characterization of nanoporous nickel oxide thin films spray-deposited onto indium-doped tin oxide for solar conversion scopes*. Adv Cond Matter Phys, 2015. 2015.
174. Diaz-Morales O., Ferrus-Suspedra D., and Koper M.T.M., *The importance of nickel oxyhydroxide deprotonation on its activity towards electrochemical water oxidation*. Chemical Science, 2016. 7(4): p. 2639-2645.
175. Manders J.R., Tsang S.-W., Hartel M.J., Lai T.-H., Chen S., Amb C.M., Reynolds J.R., and So F., *Solution-Processed Nickel Oxide Hole Transport Layers in High Efficiency Polymer Photovoltaic Cells*. Advanced Functional Materials, 2013. 23(23): p. 2993-3001.
176. Novelli V., Awais M., Dowling D.P., and Dini D., *Electrochemical characterization of rapid discharge sintering (RDS) NiO cathodes for dye-sensitized solar cells of p-type*. Am J Anal Chem, 2015. 6.

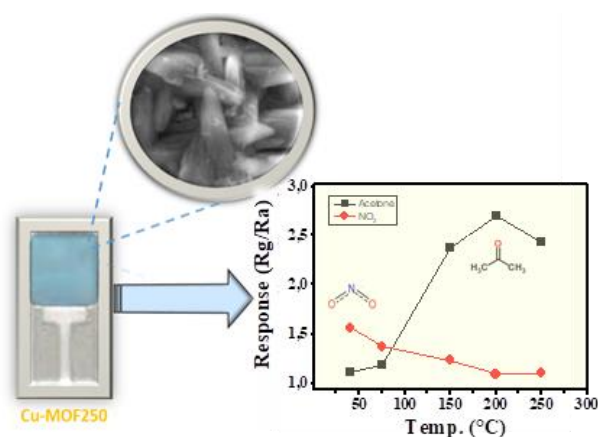
177. Marichy C., Donato N., Willinger M.-G., Latino M., Karpinsky D., Yu S.-H., Neri G., and Pinna N., *Tin Dioxide Sensing Layer Grown on Tubular Nanostructures by a Non-Aqueous Atomic Layer Deposition Process*. *Advanced Functional Materials*, 2011. 21(4): p. 658-666.
178. Collins P.G., Bradley K., Ishigami M., and Zettl A., *Extreme Oxygen Sensitivity of Electronic Properties of Carbon Nanotubes*. *Science*, 2000. 287(5459): p. 1801.
179. Sumanasekera G.U., Adu C.K.W., Fang S., and Eklund P.C., *Effects of Gas Adsorption and Collisions on Electrical Transport in Single-Walled Carbon Nanotubes*. *Physical Review Letters*, 2000. 85(5): p. 1096-1099.
180. Wang Y. and Yeow J.T.W., *A Review of Carbon Nanotubes-Based Gas Sensors*. *Journal of Sensors*, 2009. 2009: p. 24.
181. Wang J., Zheng Z., An D., Tong X., and Zhou Q., *Highly selective n-butanol gas sensor based on porous In₂O₃ nanoparticles prepared by solvothermal treatment*. *Materials Science in Semiconductor Processing*, 2018. 83: p. 139-143.
182. Qu F., Liu J., Wang Y., Wen S., Chen Y., Li X., and Ruan S., *Hierarchical Fe₃O₄@Co₃O₄ core-shell microspheres: Preparation and acetone sensing properties*. *Sensors and Actuators B: Chemical*, 2014. 199: p. 346-353.
183. Katoch A., Choi S.-W., Sun G.-J., and Kim S.S., *An approach to detecting a reducing gas by radial modulation of electron-depleted shells in core-shell nanofibers*. *Journal of Materials Chemistry A*, 2013. 1(43): p. 13588-13596.
184. Xu Q., Zhang Z., Song X., Yuan S., Qiu Z., Xu H., and Cao B., *Improving the triethylamine sensing performance based on debye length: A case study on α -Fe₂O₃@NiO(CuO) core-shell nanorods sensor working at near room-temperature*. *Sensors and Actuators B: Chemical*, 2017. 245: p. 375-385.
185. Park S., Ko H., Kim S., and Lee C., *Role of the Interfaces in Multiple Networked One-Dimensional Core-Shell Nanostructured Gas Sensors*. *ACS Applied Materials & Interfaces*, 2014. 6(12): p. 9595-9600.

2.2.2 Modulation of gas selectivity towards acetone and NO₂ using Cu-MOF based gas sensor

Abstract

Acetone and NO₂ are gaseous species harmful to the human body even at very low concentrations. Thus, highly sensitive and selective sensors for both gases are required from biomedical and environmental sectors. Here, we report on the use of metal-organic frameworks (Cu-MOF)-based conductometric sensors for the simple sensing of these gases. Copper linked benzene-1,2,4,5-tetracarboxylate metal-organic frameworks (Cu-MOF) was synthesized by a hydrothermal method and its detailed morphological and structural properties have been investigated by XRD, TG-DTA, FE-SEM, HR-TEM and EDS studies. Gas sensing devices were fabricated by printing thick film of Cu-MOF powder on conductometric ceramic platform provided with Pt interdigitated electrode and integrated heater. On the basis of physical characterization and in-situ electrical studies, two sensors have been fabricated using Cu-MOFs heat treated at 250°C and 400°C in air, and named as Cu-MOF250 and Cu-MOF400, respectively. The Cu-MOF400 based electrodes exhibit promising sensing ability towards the detection of acetone at operating temperature of 250°C, whereas Cu-MOF250 has the better sensing ability towards NO₂ gas at 40°C. It has been successfully demonstrated that the Cu-MOF250 sensor has dual sensing capability, able to detect selectively acetone at the operating temperature of 200°C, and NO₂ at near ambient temperature (40°C).

Graphical Abstract



1. Introduction

During the past few years, research in the field of metal organic frameworks (MOFs) has attracted vast attention due to its potential for designable architectures interlinking organic and inorganic chemistry [1] for various applications such as catalysis, sensors, separation, purification, drug storage and delivery, gas storage, and energy [2-3]. MOFs, as porous crystalline materials, feature characteristics of high surface area, high compatibility with both organic and aqueous mediums, highly designable structures, controllable porosity due to metal organic art and can be considered as low-cost materials depending on the metal source employed for their preparation.

Involving and utilizing MOFs in the field of chemical sensors is increasing gradually due to the interlinking and interaction of gases and biomolecules with the functional groups in the organic ligand of MOFs through hydrogen bonding, hydrophobic (π stacking) interactions, electron donor/acceptor interactions, or the formation of a dative covalent bonding [4-6]. MOFs show good selectivity which arises from the interaction of the gas with the organic linker or the structural metal [7]. On the other hand, heating of MOFs in air atmosphere gives rise to porous metal oxides/composites with varied shape and porosity, and large surface area. These MOFs-derived porous transition metal oxides have properties comparable or even better properties than the corresponding metal oxides synthesized by other traditional practices such as hydrothermal, chemical precipitation, and solid state reaction method [8-9]. Thus, MOF-based or MOF-derived sensors are acquiring growing interest for the sensing of a variety of vapour and gases. Here, we focused our attention on acetone and NO_2 , which are gaseous species harmful to the human body at very low concentration. Thus, highly sensitive and selective sensors for both gases are required from biomedical and environmental sectors.

Acetone, the simplest ketone, is one of the widely used organic solvents in industries, hospitals, and research laboratories. High level of acetone inhalation for short period of time may cause nose, throat, lung and eye irritation and continued exposure leads to severe headache and narcosis. It is also a prominent volatile organic compound (VOC) found in the exhaled human breath, and therefore, used as a biomarker for

diabetes; indeed, the exhaled breath concentration of acetone in excess of 1.8 ppm is generally found among diabetic patients [10]. The modern health care industry is focussing on diabetic patient monitoring through glucose measurement by non-invasive method both during hospitalisation and in-house care. In this endeavour, exhaled human breath analysis using high performing acetone gas sensor is undoubtedly more comfortable and most sought after diagnostic device.

NO₂ gas is very harmful to the environment as it is main source of nitric acid aerosol leading to the smog and acid rains and it has negative effect on human health [11]. Respiratory patients' inhaled breath of NO₂ should be below 53 ppb at ambient air, according to U.S Environmental Protection Agency's quality standard for NO₂ [12]. Therefore, there is a great need to develop highly sensitive, selective, cost effective, rapid and reliable non-invasive techniques for monitoring acetone and NO₂ [13-14].

In the present work, we have synthesised copper linked benzene-1,2,4,5-tetracarboxylate metal-organic frameworks (Cu-MOF) and investigated the influence of thermal treatment on the conductometric sensing ability of the thermally functionalized Cu-MOF for the detection of acetone and NO₂ gases with high accuracy and selectivity.

2.2.2.1 *Experimental*

Materials synthesis

Pyromellitic acid (1,2,4,5-Benzene tetracarboxylic acid (C₁₀H₆O₈)) and copper acetate monohydrate [Cu(CO₂CH₃)₂.H₂O] were purchased from Alfa Aesar. N,N-dimethylformamide [(CH₃)₂NC(O)H] was purchased from Spectrochem. Private Ltd. Mumbai and ethanol was purchased from Changsheng Fine Chem. Co. Ltd. Synthesis of Cu-MOF was carried out by the modified hydrothermal method [15]. In this process, one equivalent of copper acetate monohydrate and two equivalent of benzene-1,2,4,5-tetracarboxylic acid were initially dissolved in 90 mL of ethanol-water mixture (1:1) and solution was stirred for 1 hr.

After obtaining homogenous condition, the reaction mixture was poured and placed into teflon coated autoclave (100 ml) reaction vessel with fully sealed condition. The

reaction mixture was continuously oven-heated for 24 hrs at 120°C in ambient atmosphere. Afterwards, the reaction mixture was gradually cooled and filtered through filter paper. Then, as-prepared material was gently washed with de-ionised water until all unreacted materials are removed from the product. The filtered material was dried at 120°C for 10 hrs and it was activated at 200°C for 2 hrs [16].

Characterization studies

Crystalline structure and morphology of the samples were characterized by using X-ray powder diffraction (Bruker D8 Advance Diffractometer; $\text{CuK}\alpha_1 = 1.5405 \text{ \AA}$) and field emission scanning electron microscopy (Quanta FEG-250) and high-resolution transmission electron microscopy (JEOL-2100), and selected area electron diffraction (SAED) with an energy dispersive X-ray detection (EDS). Thermal stability of the sample was analysed by using a thermo gravimetric and differential scanning calorimeter analyser (TG-DSC Netzsch-Model STA 409PC). The individual chemical environment of the sample was analysed by X-ray photo electron spectroscopy (PHI-VERSAPROBE III).

Gas sensing studies

Electrodes for gas sensing studies were made by printing thick films ($\sim 20 \mu\text{m}$) of Cu-MOF powder dispersed in demineralised water in order to form a slurry, on alumina substrates ($6 \times 3 \text{ mm}^2$) provided with Pt interdigitated electrodes and a Pt heater placed on the backside. Before sensing tests, the devices have been subjected to a low (250 °C) and high (400°C) temperature thermal treatment, in order to obtain two different sensors.

Sensing experiments were carried out by inserting the sensors in a stainless-steel gas chamber, where the atmosphere can be controlled, in the temperature ranging from room temperature (RT) to 400°C, under a dry synthetic air (20% O_2 , 80% N_2) which constantly flowed through the test chamber. Duly certified gases in cylinders could further be diluted to required concentration level by using mass flow controllers. A multimeter data acquisition unit Agilent 34970A was used for acquiring the sensor signal, while a power supplier Agilent E3632A was employed to bias the built-in heater of the sensor to perform measurements at high temperatures. The sensor response, S , was defined as $S = R/R_0$ where R_0 is the baseline resistance in air and R

is the electrical resistance of the sensor in the presence of gases tested. The response time is defined as the time required to reach 90% of the saturation value after a test gas is introduced, and the recovery time is the time necessary for the sensor to return to 10% above the origin value in air after releasing the test gas.

2.2.2.2 Results and discussion

2.2.2.2.1 TG-DTA analysis

In order to verify the thermal stability and to identify possible phase transition(s) of Cu-MOF, TG-DTA analyses was carried out for as-prepared sample from room temperature up to 600°C in air atmosphere. A typical thermogravimetric (TG) result (red curve) shown in Fig. 30 indicates a gradual weight loss from room temperature till 300°C due to the removal of water and other organic molecules. A major and sharp weight loss is observed between 300 to 340°C, which could be ascribed to the breakage of metal organic frameworks due to the decomposition of organic linker (pyromellitic acid) from the MOF. When temperature rises from 340 to 600°C, there is no significant change of weight loss which suggests the formation of stable inorganic phase(s). The weight loss corresponds well with the differential thermogravimetric analysis (DTA) by the appearance of an exothermic peak (blue curve) at around 330°C which confirms the stability of the Cu-MOF till 300°C [17-18].

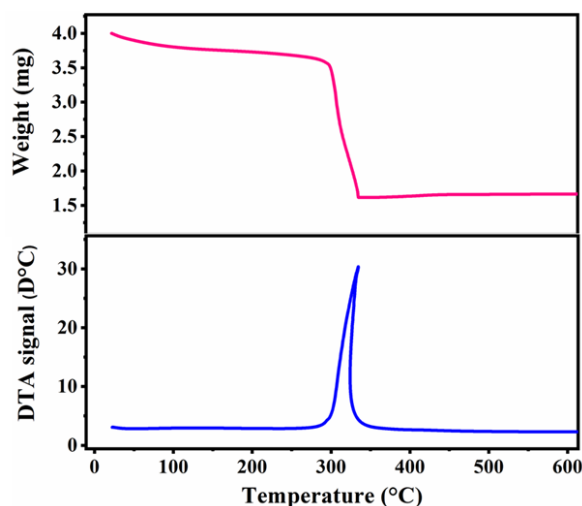


Figure 2-30. Thermogravimetric (TG) and differential thermal analyses (DTA) of as-prepared Cu-MOF carried out under air.

2.2.2.2.2 SEM and TEM studies

To have an indication about the morphological changes induced by thermal treatment on Cu-MOF, the as synthesized sample was treated at different temperatures. FE-SEM images of as prepared Cu-MOF and Cu-MOF250 are first shown in Fig. 31a,b respectively. In both the cases, Cu-MOF crystallized in the form of fish trunk-like shapes with sharp-edged surfaces. This observation indicates then there was no significant change in the morphology due to calcination at 250°C. Surface of the crystallites appears to be relatively clean due to the removal of water and other volatile organic compounds.

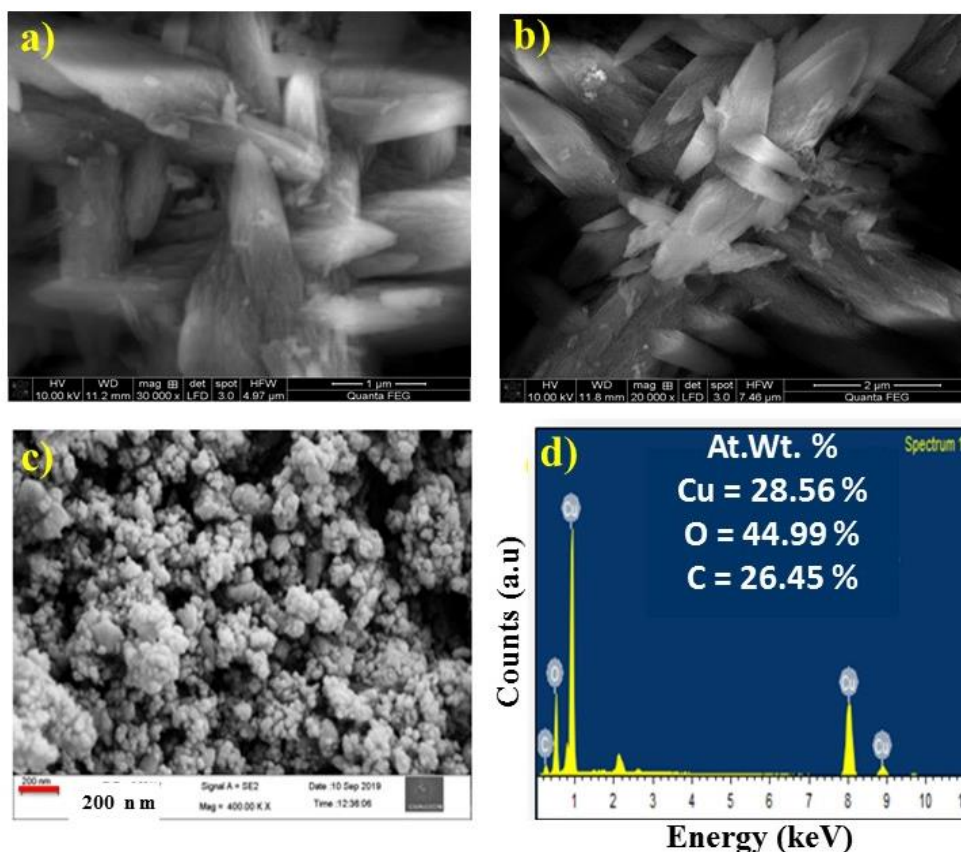


Figure 2-31. FE-SEM images of Cu-MOF (a) as prepared, calcined at (b) 250°C, (c) 400°C and (d) a typical electron diffraction X-ray spectrum (Elemental composition represented in %)

On the other hand, FE-SEM image (Fig. 31c) of Cu-MOF400 indicates the disintegration of large fish-trunk like structure into small near spherical particles [15]. Fig. 31d represents a typical EDS spectrum demonstrating the presence of Cu, along with C and O. Compared to EDS data on the as synthesized and Cu-MOF250 samples

(not shown), EDS data on Cu-MOF400 indicate a lower C content (26.4 at. % vs. 36.3 at. %) and a higher oxygen content (34. at.7% vs. 45.0 at.%). These findings confirm that the MOF got disintegrated leading to the formation Cu or its oxide phases (CuO/Cu₂O).

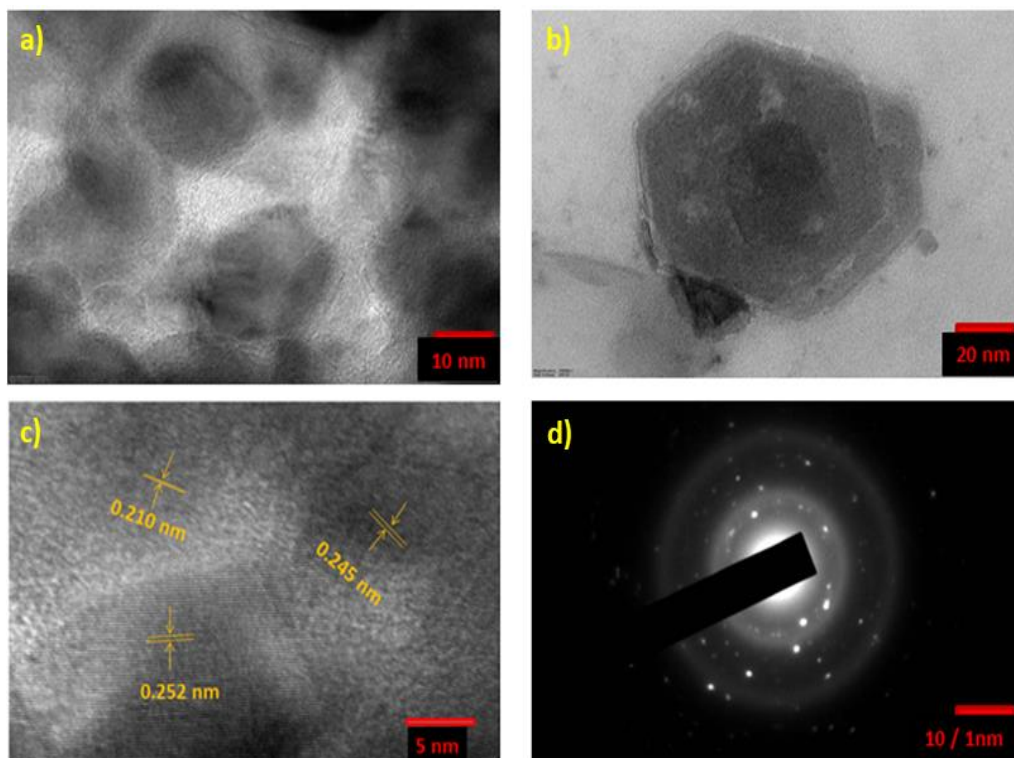


Figure 2-32. HR-TEM images (a-c) and (d) SAED pattern of Cu-MOF400.

High resolution TEM studies on Cu-MOF400 sample confirm the formation of hexagonal structures, characteristic of CuO/Cu₂O, having sizes in the range of 150 to 180 nm (Fig. 32a, b). TEM picture shown in Fig. 32c highlights the lattice fringes corresponding to Cu, Cu₂O and CuO phase. The observed interlayer distances of 2.10 Å, 2.45 Å and 2.51 Å corresponds to (111) plane of Cu and CuO and (002) plane of Cu₂O respectively [19]. SAED pattern in Fig. 32d confirms the crystalline nature of this sample.

2.2.2.2.3 Powder XRD analysis

Powder XRD analysis was performed to investigate the phase formation and crystal structure. Fig. 33 shows the XRD pattern of the pristine Cu-MOF, which is identical with the reported XRD pattern (JCPDS card No.006-2674) [15]. The sample calcined

at 250°C did not show any significant change in the XRD pattern which, in agreement with the TGA results, confirm that the Cu-MOF is stable and intact up to 250°C.

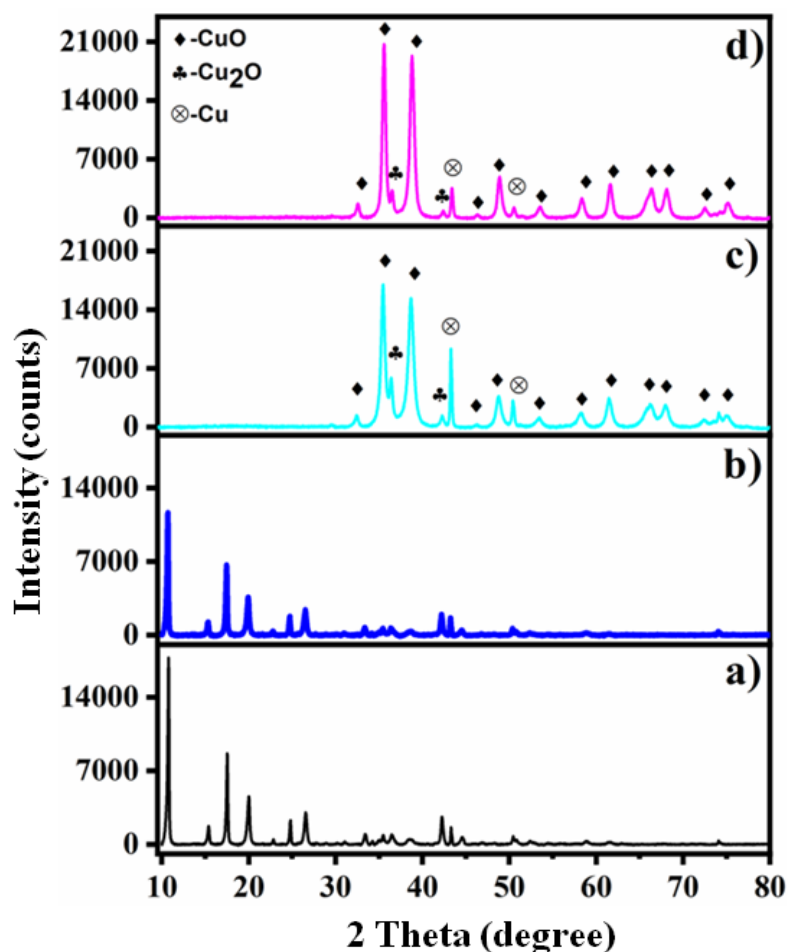


Figure 2-33. Powder XRD patterns of Cu-MOF; (a) as-prepared, and calcined at (b) 250°C, (c) 300°C and (d) 400°C.

The XRD pattern of Cu-MOF calcined at 300°C confirms that there is a phase transition leading to the formation of mainly CuO and the secondary phases being Cu₂O and Cu as indicated in the Fig. 33c. The observed diffraction peaks at 2 theta values of 32.43, 35.44, 38.62, 46.20, 48.71, 53.44, 58.27, 61.45, 66.18, 68.99, 72.40 and 75.12° correspond to CuO phase in agreement with the JCPDS data (card No.045-0937). The minor peaks observed at 29.52, 36.37, 42.26, 61.45 and 74.10° could be assigned to Cu₂O phase (JCPDS card No. 005-0667) and additional minor diffraction peaks at 43.25, and 50.40° correspond well with the Cu phase (JCPDS card No. 004-0836) respectively. Similarly, XRD pattern of sample calcined at 400°C indicate the presence of major CuO phase. On the other hand, the intensities of Cu peaks got

reduced indicating the possible conversion of Cu into CuO at higher temperature [20,21].

2.2.2.2.4 XPS analysis

The Cu-MOF400 was further investigated by XPS to examine the chemical state of Cu atom after thermal treatment. Survey spectrum (Fig. 34a) indicates the main elements (Cu, O, C) present in the end product. Fig. 34b shows O1s spectra in CuO exhibiting peaks at 534.4 eV and a broad peak at 529.82 eV, which was assigned to the O1s of Cu₂O. Another three peaks at 528.03, 531.13 and 533.13 eV are attributed to the other oxygen components such as –OH, H₂O and the species of carbonate on the surface [20,21]. Fig. 34c shows peaks corresponding to binding energies of Cu 2p_{3/2} and Cu 2p_{1/2} peaks at 932.2 and 952.0 eV respectively.

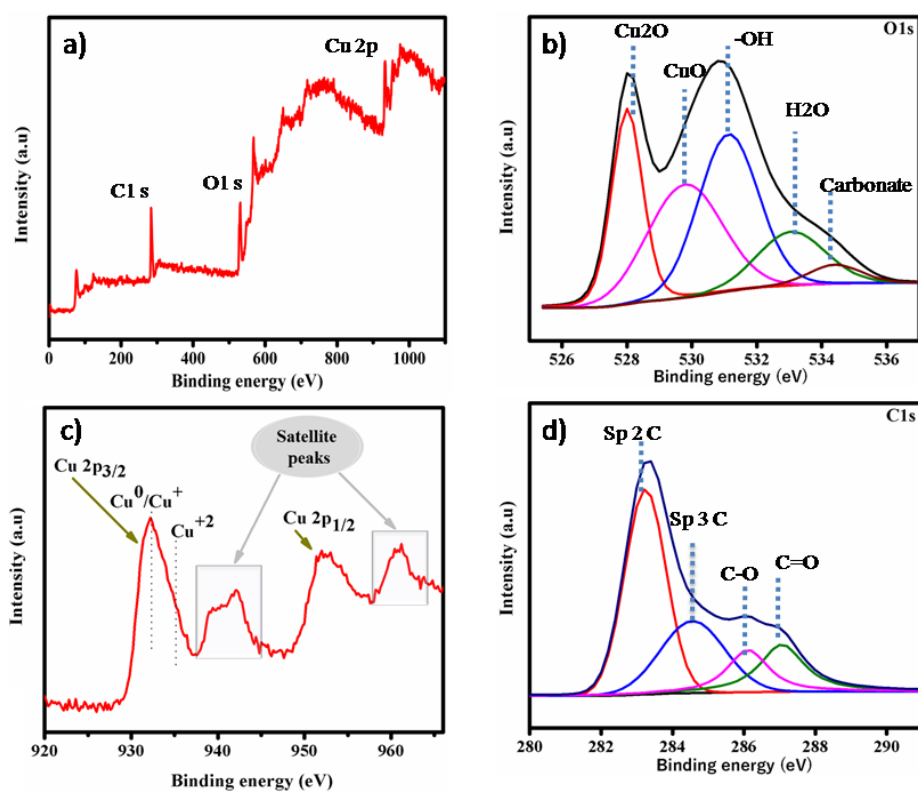


Figure 2-34. XPS spectra of Cu-MOF400: survey (a), Cu 2P_{3/2} (b), C1s (c), O1s (d).

Fig. 34d shows XPS scan in the carbon region, which shows that the carbon exists in different chemical state in the material. The deconvoluted C1s spectrum exhibit peaks at 283.17, 284.57, 286.11 and 288.03 eV which can be attributed to the graphite carbon

(sp²), diamond-like carbon(sp³), C-O and C=O carbon present in the CuO-Cu₂O-Cu/400°C [22,23].

2.2.2.2.5 Electrical tests

A detailed electrical characterization of the Cu-MOF sample was performed by measuring the resistance of the Cu-MOF based sensor in air from room temperature to 400°C (Fig. 35a). Initially, the resistance is very high and remains out of measurement range of our instrument until 200°C. At this temperature, we noted a sharp decrease of the resistance by many orders of magnitude. By comparing this behaviour with TGA and DTA analyses, it appears that the strong decrease of electrical resistance observed is related to decomposition of Cu-MOF into volatile organic impurities and Cu-CuO-Cu₂O composite. It is noteworthy that the electrical resistance variation occurs at lower temperature compared to weight change in the thermogram, and this is expected because the variation of the electrical properties are due to modifications/reconstruction processes occurring at the surface during the initial stages of oxidation.

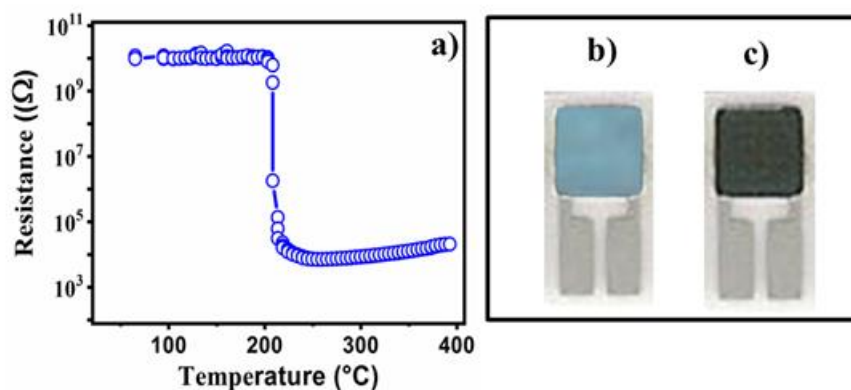


Figure 2-35. (a) Electrical resistance of Cu-MOF sensor from room temperature to 400°C. (c) Cu-MOF 250 sensor, (d) Cu-MOF 400 sensor

The above results indicate that the structure of the Cu-MOF sensing film can be easily modulated by a proper thermal treatment. This peculiarity is very interesting and has been exploited here for preparing two different sensors derived from Cu-MOF, by heat treating in situ the sensing film of as-prepared Cu-MOF at the temperatures of 250°C and 400°C, respectively (see Fig. 35c,d).

Regarding Cu-MOF250 sensing film, thermo-gravimetric studies and its characteristic light blue colour indicate that the bulk structure of Cu-MOF is retained even after heating at 250°C. The electrical resistance assume a low value due to large drop related to the surface reorganization even if this bulk structure is not still modified at all. On the other hand, Cu-MOF400 sensor, show a colour change from the characteristic blue for Cu-MOF to black of CuO. On the basis of TGA and DTA results, it can be concluded that the total destruction of Cu-MOF structure occurs at this higher temperature leading to the formation of a new CuO-based structure [24].

2.2.2.2.6 Acetone sensing tests

The sensing properties of Cu-MOF250 and Cu-MOF400 sensors towards acetone were first investigated. To find the best operating conditions, the sensors were preliminarily exposed to 20 ppm of acetone at different temperatures. As an example, the variation of resistance at the introduction of acetone for the Cu-MOF400 sensor at the temperature of 400, 350 and 300°C, is reported in Fig. 36a.

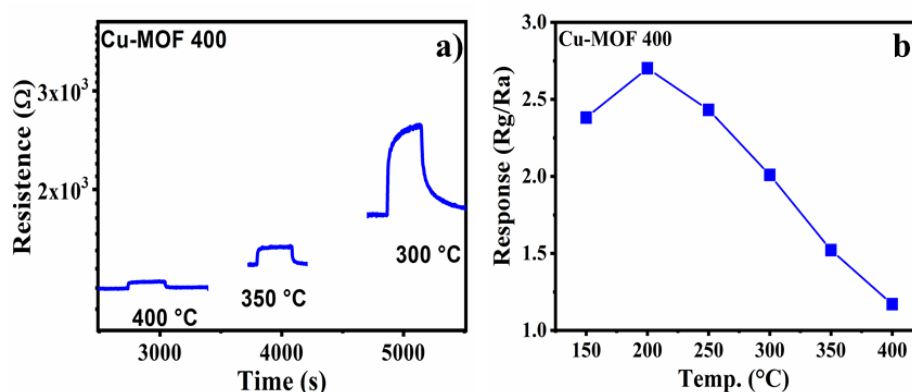


Figure 2-36. a) Variation of resistance at the introduction of acetone for the Cu-MOF400 sensor at the working temperature of 400, 350 and 300°C. b) Response of Cu-MOF400 sensor to acetone as a function of temperature.

At high temperature, the response of the fabricated sensor increases quickly upon the injection of acetone, and then decreases rapidly and returns to its initial value after acetone is released from the chamber, indicating the rapid and reversible response and recovery behaviour of the sensor. The sensor shows an increasing response to acetone with the decreasing of the temperature (Fig. 36b). However, with decreasing temperature, it has been noted that both response and recovery times become longer. At temperatures lower than 150°C, the recovery takes too longer and hence the sensor

is not suitable for practical applications. Thus, the optimal temperature, with the right balance between higher response and faster dynamics, is set at 250 °C. Fig.37a shows the transient response of Cu-MOF400 sensor to different concentrations of acetone at this optimal temperature of 250°C. The same tests have been performed with the sensor Cu-MOF250 (Fig. 37b). It can be clearly observed that the sensor Cu-MOF400 is more sensitive to acetone when compared to Cu-MOF250 (Fig. 37c).

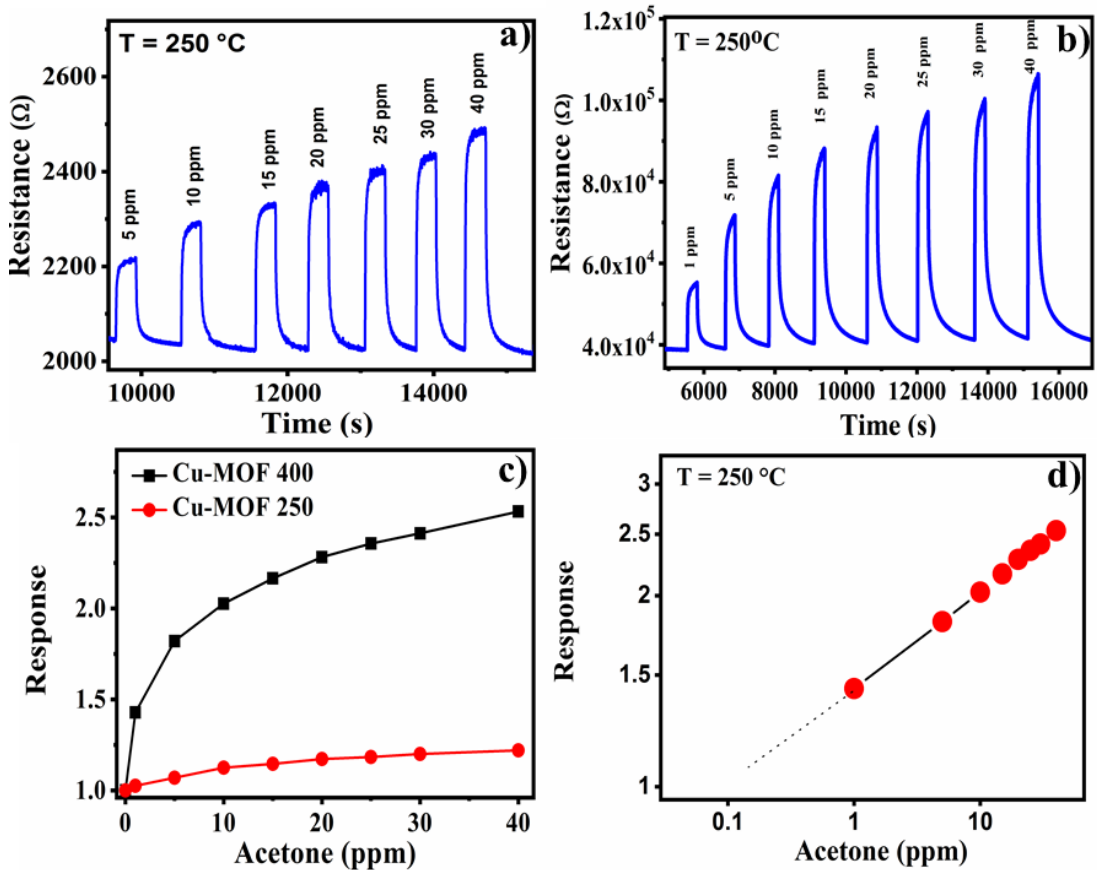


Figure 2-37 a) Transient response of Cu-MOF400 sensor to different concentrations of acetone at the optimal temperature of 250°C; b) Transient response of Cu-MOF250 sensor to different concentrations of acetone at the optimal temperature of 250°C; c) Calibration curves; d) Calibration curve in log-scale for Cu-MOF400 sensor.

The response of both sensors increases with the increase of acetone gas concentration which could be attributed to the fact that more acetone molecules participate in the surface sensing reaction, leading to the enhancement of the sensing signal. The detection limit, evaluated at $S/N = 3$, as extrapolated by Fig. 37d, is around 200 ppb, which indicates that it can be used as promising material for monitoring sub ppm concentrations of acetone.

In order to investigate the stability of sensor, the sensing response of the Cu-MOF400 sensor was measured in the presence of 5 ppm acetone gas at the working temperature of 200°C (Fig. 38a). The results clearly indicate that the response remains almost constant with slight fluctuations during the test, indicating a good stability of the Cu-MOF based sensors and excellent reproducibility. The response time is about 180 s and the recovery time is 250 s for 20 ppm acetone gas at 200°C.

In order to further validate the performance of the Cu-MOF sensor, the selectivity towards different gases was investigated at the operating temperature of 250°C. Fig.38b shows the sensor responses to test gases at various concentrations. It is clear that the sensor response to acetone is much higher than that to NO₂, H₂, CO, CO₂, CH₄ and NH₃ implying that it displays good selectivity to acetone.

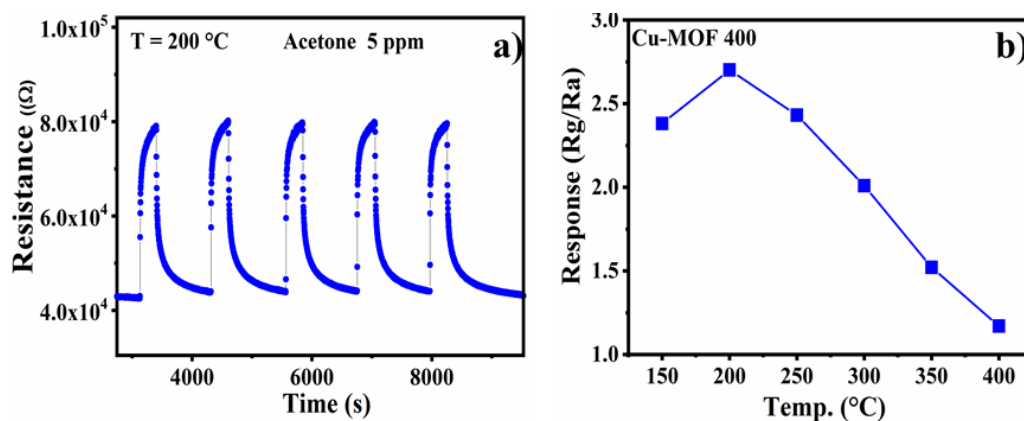


Figure 2-38. a) Response of the Cu-MOF400 sensor in the presence of 5 ppm acetone gas at the working temperature of 200 °C; b) Response of the Cu-MOF400 sensor against a number of gases at various concentrations. Tests were carried out at the operating temperature 250 °C.

In view of these results, it can be concluded that the Cu-MOF400 has promising characteristics and compare very well with previously developed CuO [25] and Fe₂O₃/NiFe₂O₄ bimetallic oxides [26] derived from metal–organic frameworks based sensors for acetone monitoring.

2.2.2.2.7 NO₂ sensing tests

The Cu-MOF250 and Cu-MOF400 sensors were subsequently investigated toward nitrogen dioxide sensing, exposing them to 2 ppm of NO₂ at different temperatures. Initially, measurements have been carried out at operating temperatures above 200°C and the response of both sensors were found to be very small, then NO₂ sensing tests

were carried in a lower temperature range, from 200 to 40°C. In this operating temperature range, the performances for NO₂ sensing of the two sensors are very similar. The variation of resistance at the introduction of NO₂ for the Cu-MOF250 sensor, is reported in Fig. 39.

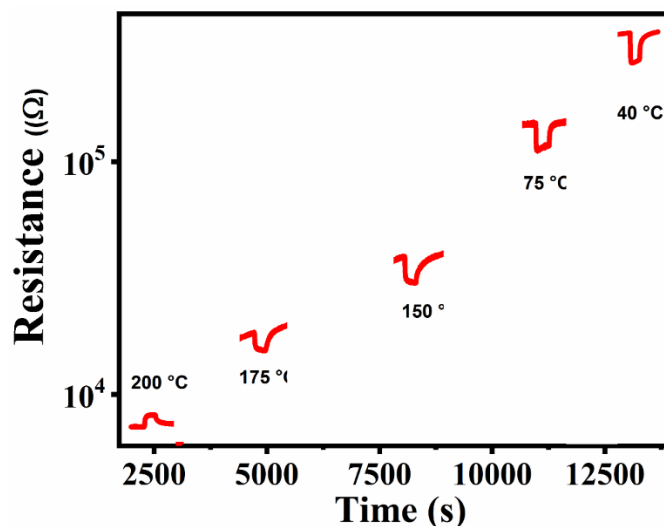


Figure 2-39. Effect of operating temperature on the sensing characteristics of Cu-MOF250 toward 20 ppm of NO₂ in the temperature range 200° to 40°C.

Interestingly, with the decreasing temperature, the recovery time remain faster. So, for NO₂ sensing, the optimal balance between higher response and faster dynamics can be set at near room temperature, i. e. 40°C. The transient response to different concentrations of NO₂ target gas at this temperature is reported in Fig. 40a. Calibration curve demonstrated the ability to detect very low concentration of NO₂ (Fig. 40b). The stability and selectivity of Cu-MOF250 sensor was also evaluated in the presence of 2 ppm NO₂ at the working temperature of 40°C and other interferent gases (Fig. 40c and 11d). Both characteristics are also satisfied for this sensor which can be proposed as high performance sensor for NO₂ gas at room temperature [27].

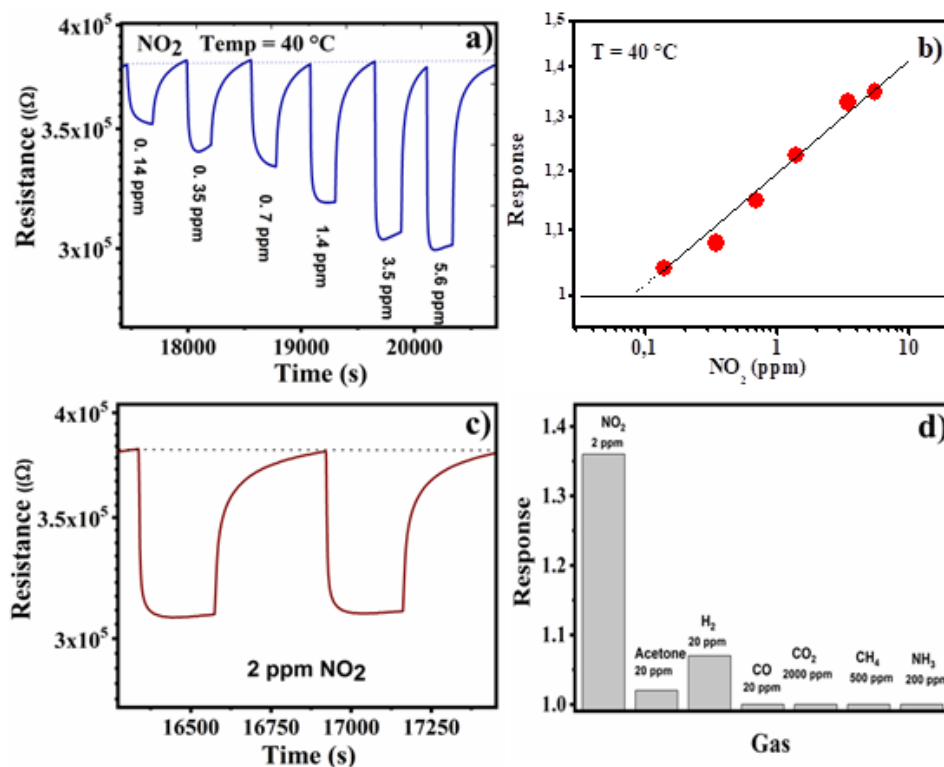


Figure 2-40. a) Transient response of Cu-MOF 250 sensor to different concentrations of NO_2 at the optimal temperature of 40°C ; b) Calibration curve in log-scale for Cu-MOF 250 sensor; c) Reproducibility response to NO_2 ; d) Response of the Cu-MOF 250 sensor against a number of gases at various concentrations. Tests were carried out at the operating temperature of 40°C .

Humidity is an important factor to take into account for the practical use of conductometric sensors because it could give place at strong interferences with the target gas, modifying the sensing behavior. Therefore, the performances of Cu-MOF 250 sensor towards 2 ppm NO_2 were also investigated at 50% of relative humidity (RH). It can be observed that the baseline resistance change very little when the surrounding atmosphere was changed from dry to humid gas (Fig. 41a). Interestingly, this behavior is very different from that observed by Koo and collaborators on the $\text{Cu}_3(\text{HHTP})_2$ MOF system [28]. These authors noted that the baseline resistance of their MOF sensor continuously increased in humid atmospheres, likely due high adsorption of water molecules on the open Cu sites. $\text{Cu}_3(\text{HHTP})_2$ system has a 2 nm channel opening whereas for Cu-MOF is only 0.9 nm and this could explain the different behavior. The Cu-MOF 250 sensor showed also stable NO_2 signal in the wet carrier gas. The increase of the baseline resistance of the sensor in humid air and the decrease during NO_2 pulses, indicate that the majority current

carriers are holes. It appears also that there was no noticeable degradation of performances on successive pulses of NO_2 .

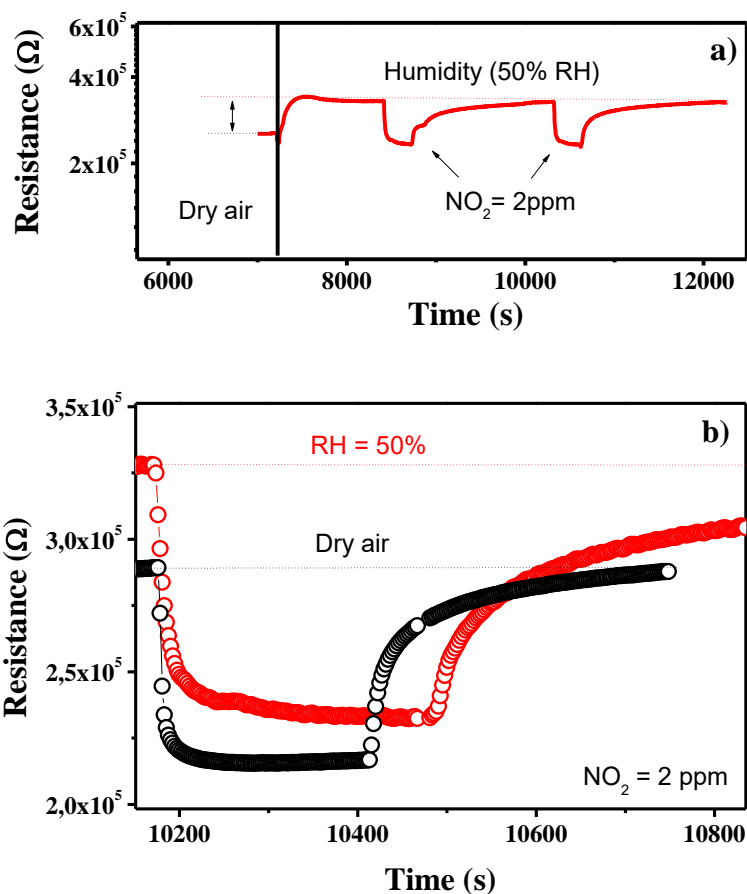


Figure 2-41. a) Response of Cu-MOF250 sensor to NO_2 pulses at 40°C at 40% of RH. b) Comparison between the transient response of Cu-MOF 250 sensor to 2 ppm of NO_2 at the temperature of 40°C in dry air and under humid conditions

The comparison between the response in dry and humid conditions shows clearly almost no difference, whereas the response and recovery times are longer in humid atmosphere (Fig. 41b). Thus, in humid conditions, the resistance baseline is not reached within the probed time frame. This behavior could be explained assuming that water hindered the approach of nitrogen dioxide to the surface occupying part of it (for example forming surface $-\text{OH}$ species) and, at the same time, reduce the NO_2 desorption due to stronger bonding formed between these surface species.

2.2.2.2.8 Temperature-dependent dual selectivity for detecting acetone and NO₂

The results above reported demonstrated that the Cu-MOF400 sensor can effectively detect acetone at 250°C and Cu-MOF250 sensor detects NO₂ at lower operating temperature of 40°C. However, an important challenge is the detection of more gaseous species with the same sensor. This is due to demand for continuous miniaturization and power consumption reduction, which drive the research towards the reduction of the number of sensors, increasing performance, reducing package size and cost for practical applications. For example, reducing the number of sensors in an array is of utmost importance for developing portable analyzers. The temperature modulation technique, i.e. to give a cyclic temperature profile to sensor in order to operate at different temperatures, is a very effective method for obtaining dual selective sensors.

On the basis of these considerations, we tried to detect both the target gases here using the Cu-MOF250 sensor. As shown in Fig. 42a, response of the sensor for NO₂ and acetone at fixed temperatures has been measured. It was noted that the device is very sensitive to acetone at the operating temperature of 250°C when compared to NO₂, while the opposite occurs at lower temperature.

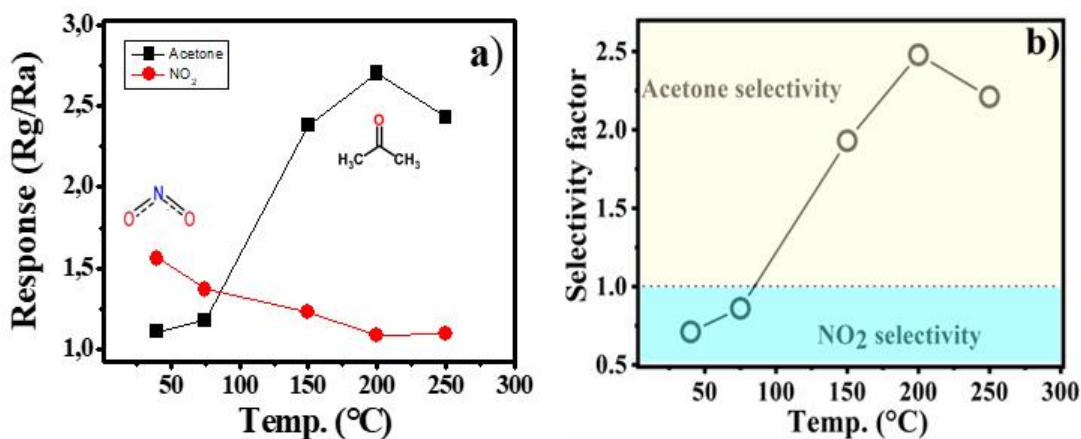


Figure 2-42. a) Response of Cu-MOF250 sensor to acetone and NO₂ as a function of temperature. b) Selectivity factor for the Cu-MOF 250 sensor.

Then, the selectivity factor (determined as $S_{\text{acetone}}/S_{\text{NO}_2}$) was evaluated (Fig. 42b). Data confirm the ability of Cu-MOF250 sensor to detect selectively acetone at the operating temperature of 200°C, whereas NO₂ can be detected at near room temperature.

2.2.2.3 Conclusions

In summary, in this study, the synthesis and characterization of Cu-MOF is reported. Results obtained from characterization studies revealed that the morphological and structural characteristics of Cu-MOF do not vary significantly with thermal treatment in air up to 300°C. Above this temperature, Cu-MOF has been converted to mainly CuO phase with traces of Cu and Cu₂O. These studies, in combination with *in-situ* and real time measurement of electrical resistance during controlled thermal treatments, permitted to select two temperatures, 250 and 400°C, for obtaining Cu-MOF based sensors with the designed microstructural and electrical characteristics. The obtained results demonstrate that these sensors could find promising use for acetone and NO₂ sensing. In addition, the dual selectivity of Cu-MOF250 sensor towards acetone and NO₂ at two different temperatures was demonstrated.

References

- [1] F.A. Almeida Paz, J. Klinowski, S.M.F. Vilela, J.P.C. Tomé, J.A.S. Cavaleiro, J. Rocha, Ligand design for functional metal-organic frameworks, *Chem. Soc. Rev.* (2012). <https://doi.org/10.1039/c1cs15055c>.
- [2] A. Chidambaram, K.C. Stylianou, Electronic metal-organic framework sensors, *Inorg. Chem. Front.* (2018). <https://doi.org/10.1039/c7qi00815e>.
- [3] N.S. Bobbitt, M.L. Mendonca, A.J. Howarth, T. Islamoglu, J.T. Hupp, O.K. Farha, R.Q. Snurr, Metal-organic frameworks for the removal of toxic industrial chemicals and chemical warfare agents, *Chem. Soc. Rev.* (2017). <https://doi.org/10.1039/c7cs00108h>.
- [4] S. Carrasco, Metal-organic frameworks for the development of biosensors: A current overview, *Biosensors.* (2018). <https://doi.org/10.3390/bios8040092>.
- [5] J. V. Alegre-Requena, E. Marqués-López, R.P. Herrera, D.D. Díaz, Metal-organic frameworks (MOFs) bring new life to hydrogen-bonding organocatalysts in confined spaces, *CrystEngComm.* (2016). <https://doi.org/10.1039/c5ce02526e>.
- [6] A. Karmakar, P. Samanta, A. V. Desai, S.K. Ghosh, Guest-Responsive Metal-Organic Frameworks as Scaffolds for Separation and Sensing Applications, *Acc. Chem. Res.* (2017). <https://doi.org/10.1021/acs.accounts.7b00151>.
- [7] B. Yan, Photofunctional MOF-based hybrid materials for the chemical sensing of biomarkers, *J. Mater. Chem. C.* (2019). <https://doi.org/10.1039/c9tc01477b>.
- [8] V. Stavila, A.A. Talin, M.D. Allendorf, MOF-based electronic and opto-electronic devices, *Chem. Soc. Rev.* (2014). <https://doi.org/10.1039/c4cs00096j>.
- [9] R.R. Salunkhe, Y. V. Kaneti, Y. Yamauchi, Metal-Organic Framework-Derived Nanoporous Metal Oxides toward Supercapacitor Applications: Progress and Prospects, *ACS Nano.* (2017). <https://doi.org/10.1021/acsnano.7b02796>.
- [10] M. Karmaoui, S.G. Leonardi, M. Latino, D.M. Tobaldi, N. Donato, R.C. Pullar, M.P. Seabra, J.A. Labrincha, G. Neri, Pt-decorated In₂O₃ nanoparticles and their ability as a highly sensitive (<10 ppb) acetone sensor for biomedical applications, *Sensors Actuators, B Chem.* (2016). <https://doi.org/10.1016/j.snb.2016.02.100>.
- [11] A. Faustini, R. Rapp, F. Forastiere, Nitrogen dioxide and mortality: Review and meta-analysis of long-term studies, *Eur. Respir. J.* (2014). <https://doi.org/10.1183/09031936.00114713>.
- [12] Primary national ambient air quality standard for nitrogen dioxide, *Fed. Regist.* (2009).
- [13] W. Liu, L. Xu, K. Sheng, X. Zhou, B. Dong, G. Lu, H. Song, A highly sensitive and moisture-resistant gas sensor for diabetes diagnosis with Pt@In₂O₃ nanowires and a molecular sieve for protection, *NPG Asia Mater.* (2018). <https://doi.org/10.1038/s41427-018-0029-2>.
- [14] C.T. Quy, N.X. Thai, N.D. Hoa, D.T. Thanh Le, C.M. Hung, N. Van Duy, N. Van Hieu,

- C₂H₅OH and NO₂ sensing properties of ZnO nanostructures: Correlation between crystal size, defect level and sensing performance, *RSC Adv.* (2018). <https://doi.org/10.1039/c7ra13702h>.
- [15] Synthesis, Morphology and Lead Ion Adsorption Properties of Metal Organic Frameworks of Copper and Cobalt, *Chem. Sci. J.* (2016). <https://doi.org/10.4172/2150-3494.1000113>.
- [16] R. Senthil Kumar, S. Senthil Kumar, M. Anbu Kulandainathan, Efficient electrosynthesis of highly active Cu₃(BTC)₂-MOF and its catalytic application to chemical reduction, *Microporous Mesoporous Mater.* (2013). <https://doi.org/10.1016/j.micromeso.2012.09.028>.
- [17] C.R. Rawool, A.K. Srivastava, A dual template imprinted polymer modified electrochemical sensor based on Cu metal organic framework/mesoporous carbon for highly sensitive and selective recognition of rifampicin and isoniazid, *Sensors Actuators, B Chem.* (2019). <https://doi.org/10.1016/j.snb.2019.03.032>.
- [18] T. Wang, X. Li, W. Dai, Y. Fang, H. Huang, Enhanced adsorption of dibenzothiophene with zinc/copper-based metal-organic frameworks, *J. Mater. Chem. A.* (2015). <https://doi.org/10.1039/c5ta05204a>.
- [19] A.K. Kar, R. Srivastava, Selective synthesis of Cu-Cu₂/C and CuO-Cu₂O/C catalysts for Pd-free C-C, C-N coupling and oxidation reactions, *Inorg. Chem. Front.* (2019). <https://doi.org/10.1039/c8qi01198b>.
- [20] R. Zhang, L. Hu, S. Bao, R. Li, L. Gao, R. Li, Q. Chen, Surface polarization enhancement: High catalytic performance of Cu/CuOX/C nanocomposites derived from Cu-BTC for CO oxidation, *J. Mater. Chem. A.* (2016). <https://doi.org/10.1039/c6ta01199c>.
- [21] W. Jia, E. Reitz, H. Sun, B. Li, H. Zhang, Y. Lei, From Cu₂(OH)₃Cl to nanostructured sisal-like Cu (OH)₂ and CuO: Synthesis and characterization, *J. Appl. Phys.* (2009). <https://doi.org/10.1063/1.3097286>.
- [22] T. Ghodselahi, M.A. Vesaghi, A. Shafiekhani, A. Baghizadeh, M. Lameii, XPS study of the Cu@Cu₂O core-shell nanoparticles, *Appl. Surf. Sci.* (2008). <https://doi.org/10.1016/j.apsusc.2008.08.110>.
- [23] A.A. Dubale, A.G. Tamirat, H.M. Chen, T.A. Berhe, C.J. Pan, W.N. Su, B.J. Hwang, A highly stable CuS and CuS-Pt modified Cu₂O/CuO heterostructure as an efficient photocathode for the hydrogen evolution reaction, *J. Mater. Chem. A.* (2016). <https://doi.org/10.1039/c5ta09464j>.
- [24] Y. Wang, Y. Lü, W. Zhan, Z. Xie, Q. Kuang, L. Zheng, Synthesis of porous Cu₂O/CuO cages using Cu-based metal-organic frameworks as templates and their gas-sensing properties, *J. Mater. Chem. A.* (2015). <https://doi.org/10.1039/c5ta01108f>.
- [25] L.J. Zhou, Y.C. Zou, J. Zhao, P.P. Wang, L.L. Feng, L.W. Sun, D.J. Wang, G.D. Li, Facile synthesis of highly stable and porous Cu₂O/CuO cubes with enhanced gas sensing properties, *Sensors Actuators, B Chem.* (2013). <https://doi.org/10.1016/j.snb.2013.07.059>.

- [26] T. Zhou, R. Zhang, Y. Wang, T. Zhang, MOF-Derived 1D α - $\text{Fe}_2\text{O}_3/\text{NiFe}_2\text{O}_4$ heterojunction as efficient sensing materials of acetone vapors, *Sensors Actuators, B Chem.* (2019). <https://doi.org/10.1016/j.snb.2018.10.124>.
- [27] D. Ding, Q. Xue, W. Lu, Y. Xiong, J. Zhang, X. Pan, B. Tao, Chemically functionalized 3D reticular graphene oxide frameworks decorated with MOF-derived Co_3O_4 : Towards highly sensitive and selective detection to acetone, *Sensors Actuators, B Chem.* (2018).
- [28] W.-Tae Koo, S.-Joon Kim, J.-Soo Jang, D.-Ha Kim, I.-Doo Kim, Catalytic Metal Nanoparticles Embedded in Conductive Metal–Organic Frameworks for Chemiresistors: Highly Active and Conductive Porous Materials, *Advanced Science* (2019), <https://doi.org/10.1002/advs.201900250>

2.2.3 H₂ detection mechanism in chemoresistive sensor based on low-cost synthesized WO₃ nanorods

Nanostructured WO₃ represents a promising material for fast and reliable molecular hydrogen detection through chemo-resistive effect. Here, an extended experimental investigation of WO₃-H₂ interaction is presented and modeled. A powder of WO₃ nanorods (400 nm long, 50 nm large) is produced by hydrothermal technique and drop casted on Pt interdigitated electrode. H₂ sensing tests at different concentrations (2000–50,000 ppm) and temperatures (250–400 °C) are reported. Scanning Electron Microscopy (SEM), X-ray Diffraction analysis (XRD), and electrical measurements were performed. The response and recovery kinetics of H₂ sensing are carefully described by using a two-isotherms Langmuir model, and kinetics barriers for WO₃-H₂ interaction are evaluated. Two microscopic processes lead to gas detection. A fast process (shorter than 4 s) is attributed to H₂ interaction with adsorbed oxygen at WO₃ nanorods surface. A slow process (20–1000 s), with activation energy of 0.46 eV, is attributed to oxygen vacancy generation in WO₃. H intercalation in WO₃ is ruled out. The recovery of WO₃ after H₂ exposure is also modeled. The chemo-resistive effect leading to H₂ sensing by WO₃ is explained through the above processes, whose kinetic barriers have been quantified. These data open the route for the development of fast, sensitive, and low-temperature operating H₂ sensors based on WO₃.

2.2.3.1 Introduction

In recent years the scientific community is devoting a large interest to hydrogen as a source of energy, since it is an excellent candidate to replace fossil fuels for many applications, such as chemical industry, power generation, medical treatment, and many others [1], [2], [3]. Soon, hydrogen production, transportation, and storage will become key issues for sustainable development. However, H₂ is a colorless, tasteless, and odorless gas which becomes inflammable and explosive when the concentration exceeds 4%. Therefore, fast and very sensitive sensors are necessary where H₂ is produced, stored, and transported to promptly find any leakage. Typically, fast H₂ sensors work at high temperatures (250–400 °C), increasing the explosion danger [4], [5]. The progress in H₂ application cannot proceed without a parallel development of safe, fast, and reliable H₂ sensors. To this aim, a proper investigation is needed to unveil the interaction between H₂ and the sensing material leading to reliable detection.

One of the most promising materials for H₂ sensing is WO₃, an *n*-type metal oxide semiconductor with an indirect bandgap ranging between 2.6 and 3.2 eV [6]. It has been widely studied for its reversible chromogenic ability under external stimuli such as electrical bias (electrochromism) or reducing ambient (gaschromism) [7], for its ability to detect many gases such H₂S, NH₃, NO₂, and H₂ [8], [9], [10], [11] and for its properties in electrochemical storage application [12], [13]. Nanostructured WO₃ shows better performances thanks to a larger surface-to-volume ratio, higher specific surface area, and crystal faceting with marked surface reactivity [14], [15], [16]. Further, improvement of performances is obtained by surface decoration with noble monometallic, or bimetallic nanoparticles, such as Pt [17], Pd [18], Au [19] or proper combination of these [20], [21] leading to synergistic effects [22].

The affinity of WO₃ for reducing gases makes it an excellent candidate for optical and chemoresistive H₂ sensor realization since low concentrations can be detected also below 250 °C. Zhang et al. [11] synthesized urchin-like hexagonal WO₃ and tested them at 250 °C for H₂ sensing at concentrations ranging between 10 and 80 ppm. Wu et al. [18] synthesized Pd loaded mesoporous WO₃ for H₂ sensing test. They compared bare WO₃, mesoporous WO₃, and Pd-loaded mesoporous WO₃, showing that the latter is the best one in terms of response efficiency at room temperature at 5000 ppm of H₂. Chang et al. [23] studied the gas sensing performances of Pt-loaded WO₃ thin-film at 200 °C under different concentrations of H₂ (between 1 and 10,000 ppm). Mattoni et al. [17] synthesized a single-crystal Pt-decorated WO₃ thin film and tested it at room temperature under sub-ppm concentration of hydrogen. In 2017, using a density functional theory approach, Tian et al. [24] proposed a model for the interaction between H₂ and hexagonal WO₃, according to which the H₂ sensing mechanism

proceeds through H₂O molecules formation after interaction of H₂ with oxygen ions adsorbed onto noble metal nanoparticles, if any. Experimental works by Wu and Chang claimed Tian's model. On the other hand, Mattoni et al. proposed a different model based on adsorption of H₂ on Pt nanoparticles, H₂ dissociation and intercalation of H⁺ ions inside the lattice of WO₃. A comprehensive understanding of WO₃-H₂ interaction is still missing, univocal experimental evidence of chemical reactions or energy barriers do not result from literature and a detailed description of temperature-activated kinetics is however required. A basic comprehension of actual processes underlying the WO₃-H₂ interaction could promote a step forward in H₂ sensing by WO₃.

In this paper, we synthesized by hydrothermal technique hexagonal WO₃ nanorods, and we studied the interaction with H₂ molecules at different temperatures and concentrations. The experimental kinetic curves of the material response and recovery were satisfactorily modeled by using two thermally activated processes leading to chemo-resistive effect. A comprehensive description of the WO₃-H₂ interaction is discussed.

2.2.3.2 *Material and methods*

Synthesis

Hydrothermal synthesis of hexagonal WO₃ nanorods is employed by using (Na₂WO₄), sodium chloride (NaCl), and HCl [25]. The experimental procedure is detailed here: 0.825 g of Na₂WO₄ is added to 19 ml of deionized water. After stirring for 10 min, a certain quantity of HCl is added to solution to get a 2.4 pH. The solution is then put in a stainless-steel autoclave (25 ml). Before closing, 0.5 g of NaCl is added as a capping agent which leads to hexagonal nanorods morphology [26]. The sealed autoclave is put in an oven at 180 °C for 3 h. The autoclave is cooled down naturally, the obtained powder is separated (by centrifugation at 6000 rpm for 10 min) and washed with water and ethanol several times, finally dried on a hot plate for 1 h.

For the electrode realization, WO₃ nanorods powder is dissolved in 5 ml of deionized water and sonicated for 20 min. Several drops are then dipped on an interdigitated Pt electrode until all the fingers are fully coated.

Characterization

The morphological analyses were carried out by a scanning electron microscope (SEM) Gemini Field Emission SEM Carl Zeiss SUPRATM 25 (FEG-SEM, Carl Zeiss Microscopy GmbH, Jena, Germany). X-ray diffraction (XRD) patterns were acquired through a Bruker-AXSD5005θ-diffractometer, using a Göbel mirror to parallel the Cu Kα radiation operating

at 40 kV and 30 mA. The transmittance spectra were obtained by using a UV–VIS–NIR spectrophotometer Varian Cary 500. Gas sensing measurements were performed in a stainless-steel test chamber which allowed measurements in a controlled atmosphere. Gases coming from certified bottles were used and diluted in synthetic dry air at a given concentration by using mass flow controllers. The sensor was heated from room temperature (~ 20 °C) up to 400 °C under a dry air (RH < 3%) total stream of 100 sccm by using a dual-channel power supplier instrument Agilent E3632A to bias the built-in heater. The response to different gases was evaluated by recording the resistance at an applied voltage of 1.0 V through a Keithley 6487 picometer with a time sensitivity of about 2.5 s. A detailed description of the sensor platform and the setup for H₂ sensing tests are reported in a previous paper [27].

2.2.3.3 Results and discussion

2.2.3.3.1 Structural and electrical properties of WO₃ nanorods

Fig. 43a shows low and high (inset) magnification SEM images of obtained powder on interdigitated electrode, confirming the nanorods morphology. An aspect ratio of about 8 is determined by SEM images (nanorods average length and diameter of 400 and 50 nm, respectively). All interdigitated fingers were covered to maximize the response during gas sensing measurements. Some drops of WO₃ nanorods solution (powder well dissolved in deionized water) were drop casted on a corner glass and XRD analyses were performed to identify the crystal structure of our nanostructures. From the powder diffraction pattern shown in Fig. 43b, the typical peaks of hexagonal WO₃ (PDF card 00 075 2187) can be observed, with the corresponding Miller Indexes reported. This result confirms the hexagonal structure of WO₃ nanorods. We investigated the electrical resistance R in dry air at different temperatures T (Fig. 43c). By increasing the temperature from 250° to 400 °C, the electrical conductance $G (=I/R)$ of WO₃ nanorods increases by almost three orders of magnitude, following an exponential behavior with an activation energy E_b of 0.53 eV. In an n -type semiconductor, as the WO₃, the conductivity depends on electron concentration in conduction band and on electron mobility. Disregarding the thermal dependence of electron mobility, the measured activation energy for conductance could account for the energy position (0.53 eV) below the conduction band of the intrinsic donor-like defects of undoped WO₃, in agreement with Kalanur et al. [28].

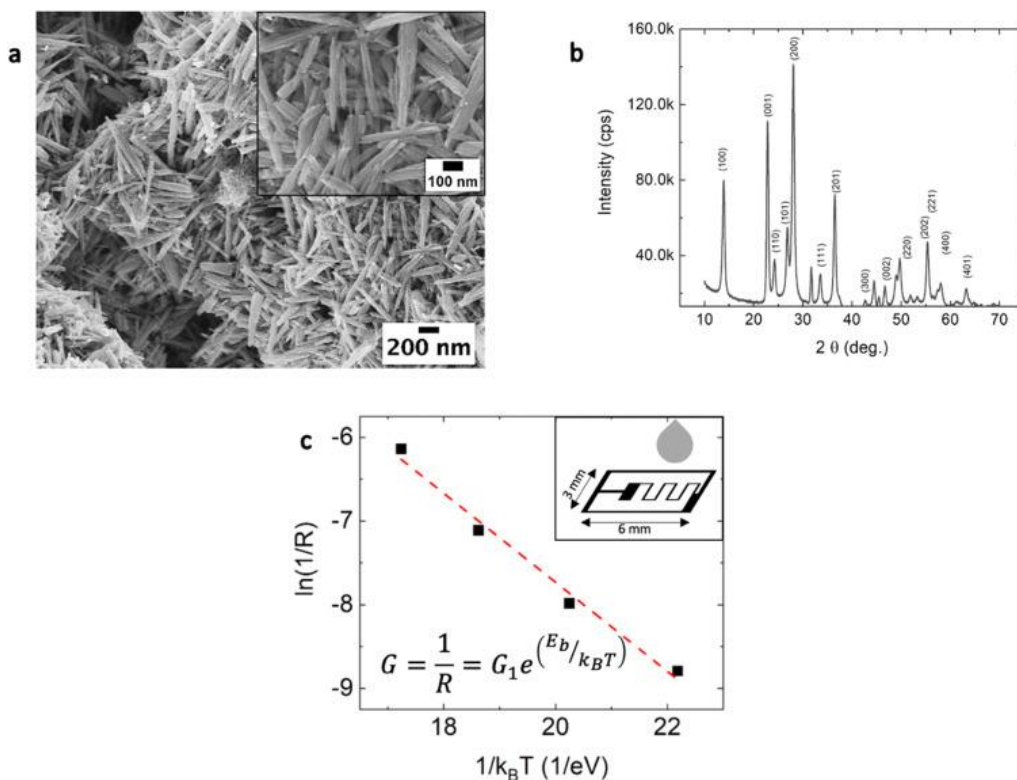


Figure 2-43. (a) low and (inset) high magnification SEM image of WO₃ nanorods deposited on the interdigitated substrate, (b) XRD pattern, and (c) Arrhenius plot of inverse of measured resistance (R); inset in (c): schematic of interdigitated substrate drop coated.

2.2.3.3.2 H₂ sensing results

Experimental H₂ sensing curves are obtained by measuring resistance variations as a function of time while a mixture of H₂ and dry air (response phase) or dry air only (recovery phase) are fluxed in the chamber. To investigate the WO₃-H₂ interaction, we tested different concentrations (2000–50,000 ppm) and different temperatures (250–400 °C). Fig. 44 shows resistance variations (black curve) at 350 °C under different H₂ concentrations (red curve), confirming a strong dependence of resistance on H₂ concentration. Resistance decreases when H₂ is fluxed in the test chamber (gas in arrow), while increases when H₂ flux is stopped (gas out arrow).

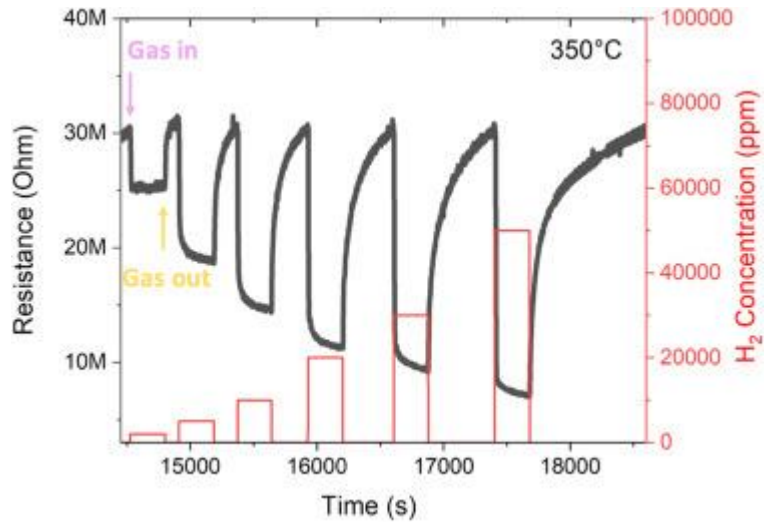


Figure 2-44. Dynamic resistance variation of WO_3 -based sensor (black curve) at $350\text{ }^\circ\text{C}$ under different H_2 concentrations (red curve). Arrows indicate when H_2 is fluxed in the chamber (named “gas in”) or it is stopped (named “gas out”)

From experimental curves of resistance variation, a sensor response S (%) can be defined. Since WO_3 is an *n-type* semiconductor and H_2 is a reducing gas, S (%) is determined as follows: $S\% = (R_a - R_g) / R_a \times 100$ in which R_g and R_a are the measured resistances in presence and absence of H_2 gas, respectively. To understand WO_3 - H_2 interaction, S (%) is defined for each tested temperature and concentration. Fig. 45 shows sensor response curves obtained at each temperature (250 – $400\text{ }^\circ\text{C}$) as a function of elapsed time during the “response” (pink background in panel b) and “recovery” (yellow background in the panel b) phase, respectively.

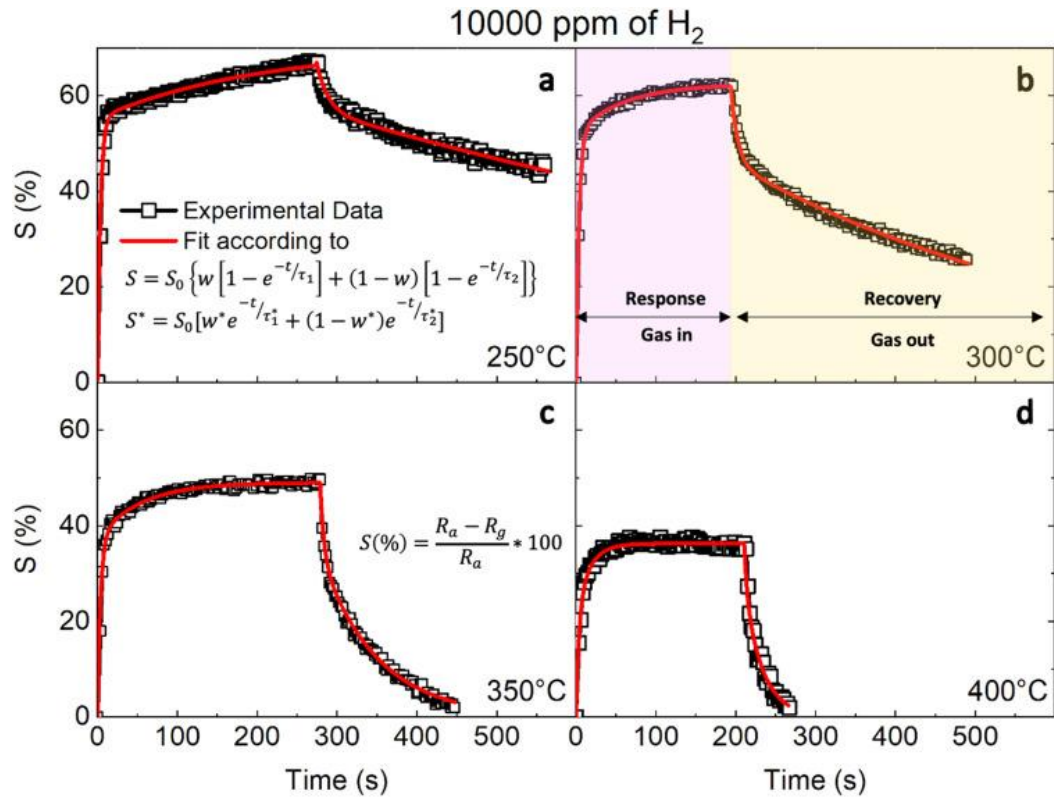


Figure 2-45. Dynamic responses of WO₃-based sensor (squared symbols) and fit (red lines) obtained at (a) 250 °C, (b) 300 °C, (c) 350 °C, and (d) 400 °C under 10,000 ppm of H₂ as a function of elapsed time starting when H₂ is fluxed in chamber

In each case of Fig. 45, the response curve increases rapidly when H₂ is fluxed into the chamber, while it tends to saturate after about 20 s. When H₂ flux is stopped, the recovery mechanism starts, and the curves decrease in a temperature dependent way.

H₂ concentration tests are carried out at 350 °C and Fig. 46 shows response and recovery curves obtained under (a) 2000 ppm, (b) 5000 ppm, (c) 10,000 ppm, (d) 20,000 ppm, (e) 30,000 ppm, and (f) 50,000 ppm fluxes of H₂.

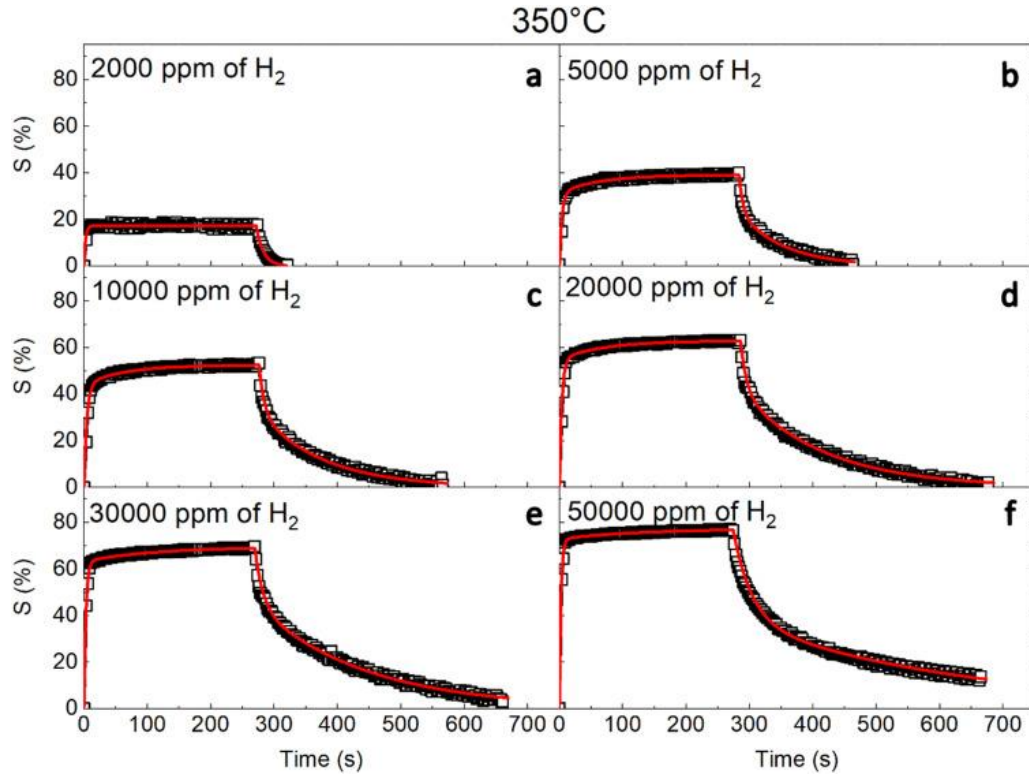


Figure 2-46. Dynamic responses of WO_3 -based sensor (squared symbols) and fit (red lines) obtained at 350 °C under (a) 2000 ppm, (b) 5000 ppm, (c) 10,000 ppm, (d) 20,000 ppm, (e) 30,000 ppm and (f) 50,000 ppm fluxes of H_2 as a function of elapsed time

Response curves increase rapidly when H_2 gas is fluxed in chamber. After about 20 s the curves tend to saturation and when H_2 flux is stopped the recovery mechanism starts, with the curves decreasing rapidly at first but then slowly tending to the initial value.

2.2.3.3.3 H_2 sensing kinetics

In order to determine H_2 sensing kinetics, all experimental curves were fitted by considering the Langmuir absorption theory with two isotherms in such a way that two processes are assumed to play an independent role. According to Langmuir, resistance variation during response phase, S , and during recovery phase, S^* , can be fitted as follows:

$$S = S_0 \left\{ w \left[1 - e^{-t/\tau_1} \right] + (1 - w) \left[1 - e^{-t/\tau_2} \right] \right\} \quad (3.3.1)$$

$$S^* = S_0 \left[w^* e^{-t/\tau_1^*} + (1 - w^*) e^{-t/\tau_2^*} \right] \quad (3.3.2)$$

in which S_0 is the maximum value of resistance change (the same value was fixed for response and recovery phases), τ_n and τ_n^* (n stands for 1 or 2) are lifetimes associated to the two isotherms during response and recovery phases, respectively; w and w^* are weights attributed to process 1 during response and recovery phases, respectively.

The fitting curves (red lines) shown in Figure 44 are in excellent agreement with experimental data (black squares), supporting the hypothesis of a fast (P1) and a slow (P2) process, independent and concomitant. Fitting parameters are listed in Table 2-8.

The maximum response value (S_0) changes with temperature: it is maximum (70%) at 250°C, as expected given the very high resistance at this temperature. P1 is characterized by times of few seconds (roughly the time resolution of experimental set-up), both in response and in recovery phases and regardless of temperature, while P2 is characterized by long times (10-200 s) in response and (20-1100 s) in recovery phases. In both cases, τ_2 and τ_2^* are clearly dependant on temperature, since they decrease when temperature increases. Concerning the weight w : P1 is predominant (w around 60-84%) during response phase while it is minority during recovery phase. Such a result could suggest different mechanisms occurring during response and recovery phases.

Table 2-8. Results of the fitting procedure to response and recovery transients at various temperatures and at fixed concentration of H₂ (10,000 ppm) based on (3.3.1), (3.3.2).

Temperature (°C)	S_0 (%)	τ_1 (s)	τ_2 (s)	w (%)	τ^*_1 (s)	τ^*_2 (s)	w^* (%)
250	70	4	200	78	14	1137	15
300	63	4	61	83	8	483	29
350	49	4	54	76	5	71	32
400	36	4	16	60	3	23	25

The maximum response value (S_0) changes with temperature: it is maximum (70 %) at 250 °C, as expected given the very high resistance at this temperature. P1 is characterized by times of few seconds (roughly the time resolution of experimental set-up), both in response and in recovery phases and regardless of temperature, while P2 is characterized by long times (10–200 s) in response and (20–1100 s) in recovery phases. In both cases, τ_2 and τ_2^* are clearly dependent on temperature, since they decrease when temperature increases. Concerning the weight, w , P1 is predominant (w around 60–84%) during the response phase while it is minority during the recovery

phase. Such a result could suggest different mechanisms occurring during response and recovery phases.

We performed an analogous analysis when tests were carried out at fixed temperature by varying H_2 concentration. For all these cases shown in Fig. 46, except at 2000 ppm, (3.3.1), (3.3.2) can be used to fit experimental curves by obtaining good agreement. In the case of the lowest concentration (Fig. 46(a)) only one process (P1) is identified both during the response and the recovery phase, and so, w is maximum. Table 2-9 reports all parameters obtained from fitted curves. The maximum response values depend on concentration since the highest value (77%) is obtained at a higher concentration (50,000 ppm).

Table 2-9. Results of the fitting procedure to response and recovery transients at various concentrations of H_2 at a temperature of 350 °C, based on (3.3.1), (3.3.2).

Concentration 10^3 (ppm)	S_0 (%)	τ_1 (s)	τ_2 (s)	w (%)	τ^*_1 (s)	τ^*_2 (s)	w^* (%)
2	17	3	–	100	11	–	100
5	39	4	63	80	6	71	42
10	53	5	65	84	8	102	40
20	63	4	70	87	10	132	34
30	69	3	111	91	12	174	36
50	77	3	126	94	29	359	50

Both in response and recovery phases, P1 is characterized by short lifetimes, regardless of concentration, while P2 has increasing lifetimes with increasing concentration. P1 is predominant in the response phase since w is around 80–95%, but not during the recovery phase. Also, in this case, this can be due to different mechanisms occurring during response and recovery phases. It should be noted that, within the Langmuir theory, the surface coverage θ_m by the adsorbed gas molecules [30] is expected to increase similarly. This evidence suggests that process P1 is related to a surface coverage by H_2 .

The Langmuir adsorption model with two isotherms very well describes our experimental data, pointing out that the WO_3 - H_2 interaction proceeds through at least two ways. Indeed, the thermal dependence of τ is highly significant as it will unveil the energy barrier for concurring processes. Fig. 47 reports the inverse of lifetimes for the two processes, both in response (a) and in recovery (b) phases in an Arrhenius plot, by clearly showing linear behaviors for the four cases. It should be noted that in the

response phase the fast process is too close to the time resolution which hinders us to resolve high frequency (orange box in Fig. 47) so that the linear trend can be meaningful only for this process. The inverse of a lifetime gives the probability rate, which is thermally activated, as follows:

$$\frac{1}{\tau} = \exp\left(-\frac{E_a}{k_B T}\right)$$

where k_B is Boltzmann constant, T is temperature and E_a is activation energy (E_a' for response phase and E_a'' for recovery phase). The physical meaning of these activation energies is depicted in Fig. 47c, as kinetic energy barriers in the interaction potential V between the WO_3 surface and the approaching H_2 molecule. By analyzing the meaningful Arrhenius plots reported in Fig. 47 for P1 (black spheres) and P2 (red spheres) involved during (a) response phase and (b) recovery phase, we can extract E_a values for each involved process (dotted lines). The result of such an exercise gives E_a of 461 meV in the response phase for P2; 295 meV and 821 meV in the recovery phase for P1 and P2, respectively. The experimental determination of these activation energies is a key point to reach a solid description of the WO_3 - H_2 interaction leading to H_2 sensing.

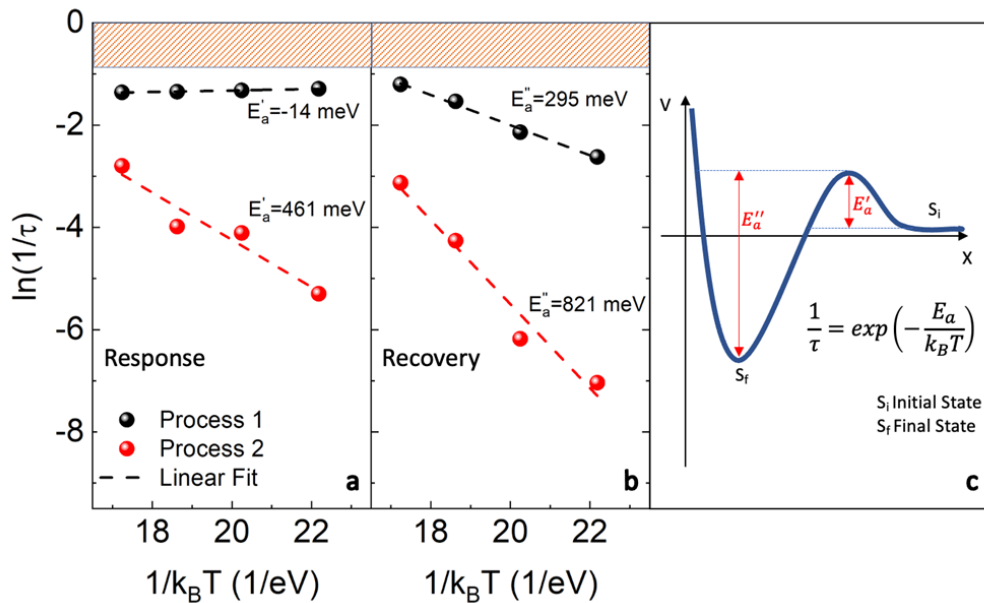


Figure 2-47. Arrhenius plot of inverse of lifetime τ of P1 (black sphere) and P2 (red sphere) during (a) response and (b) recovery phase. Dotted lines are linear fit to each set of data. The evidenced region indicates the time resolution of experimental set-up. (c) schematic representation of energy barriers for the sensing processes.

2.2.3.3.4 Modelling of WO_3 - H_2 interaction

It is well assessed that H intercalation occurs in hexagonal WO_3 , especially during the electrochromic process [31]. H_2 intercalation causes internal changes of WO_3 structure also reflected by a significant change of optical transmittance. Mattoni et al., proposed that WO_3 - H_2 interaction leads to H_2 intercalation in WO_3 crystals [17], while for other models such a process is not required. It is essential now to prove if H_2 intercalation occurs or not in our samples. To this aim, several drops of WO_3 nanorods solution were dropped on corning glass substrates, realizing a very thin film. Two WO_3 coated glasses were annealed at 350 °C for 30 min in forming gas (FG, gas mixture of $N_2:H_2 = 95:5$) or in N_2 . Annealing in FG simulates the exposure of WO_3 nanorods to H_2 gas during the sensing test at 350 °C. Transmittance spectra acquired just after annealing of WO_3 coated glasses are shown in Fig. 48. The annealing in inert ambient does not significantly modify the transmittance curve of the sample. FG annealing induces a barely appreciable reduction of transmittance, far away from the expected chromism induced by intercalating H_2 . Moreover, the H_2 intercalation typically produces an enhancement in measured resistance according to Mirzaei et al. [32] as following reaction consequence: $xH^+ + xe^- + WO_3 \rightarrow H_xWO_3$

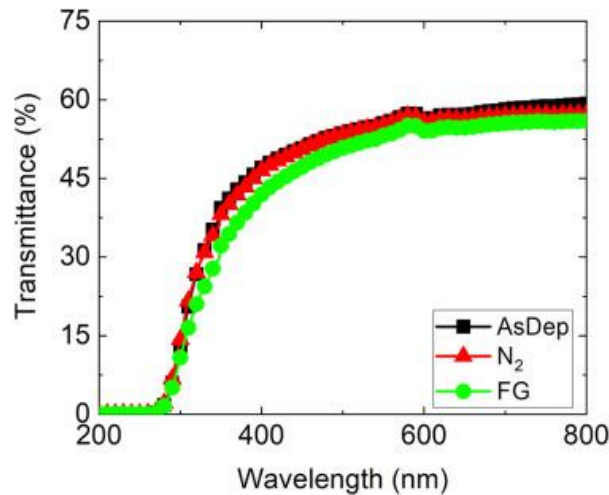


Figure 2-48. transmittance spectra of AsDep (black line + squares), N_2 (red line + triangles), and FG (green line + circles) samples.

On the contrary, after H_2 exposure, our samples reveal a marked decreased resistance at any temperature and any H_2 concentration. Such evidence, together with transmittance spectra, tell us that during H_2 exposure H intercalation in WO_3 nanorods, if any, is not a key process and can be ruled out in modeling the WO_3 - H_2 interaction.

To model the $\text{WO}_3\text{-H}_2$ interaction, we now need to discuss the P1 and P2 occurring in response and recovery phase. Firstly, it must be specified that during the response phase the interaction will involve H_2 , while during the recovery phase, only residual H_2 , if any, can be considered. Experimental results give us much information about active processes. The evidence can be summarized as follows: (i) P1 is faster than P2, both in response and in recovery phases. τ_1 is around 4 s, regardless of temperature and concentration, while τ_1^* slightly depends on temperature and concentration; (ii) P1 is more probable than P2, both in response and recovery phases, and at any temperature and any concentration; (iii) the H_2 concentration dependence of w suggests a surface process for P1; (iv) Arrhenius plots hint that P1 is a very fast process in response phase, while it is thermally activated ($E''_a=295$ meV) at recovery phase when the temperature is ranging between 250 °C and 400 °C. P2 needs high activation energy both in response (461 meV) and recovery phases (821 meV) in the same temperature range; (v) at very low H_2 concentration (below 5000 ppm), only one process is active.

2.2.3.4 Conclusion

We investigated $\text{WO}_3\text{-H}_2$ interaction by testing WO_3 nanorods exposed to H_2 (2000–50,000 ppm) fluxes at different temperatures (250–400 °C). The Langmuir adsorption theory was successfully used to model experimental data of sensing kinetics, evidencing that two processes occur both in response and in recovery phases, regardless of the temperature, for concentrations larger than 5000 ppm. The fast process (lifetimes of few seconds) is attributed to H_2 interaction with adsorbed O at WO_3 surface, in the response phase, and to O adsorption (barrier of 0.29 eV), in the recovery phase. Since a high concentration of H_2 consumes all adsorbed oxygen leaving WO_3 uncovered, the slow process (lifetimes of hundreds of seconds) is attributed to generation (barrier of 0.46 eV) and recombination (barrier of 0.82 eV) of oxygen vacancies in WO_3 nanorods. No H intercalation in WO_3 bulk is observed. At low H_2 concentrations, only fast processes are evidenced, which are linked to surface processes. Our data and modeling show that WO_3 nanorods are a promising material for H_2 sensing and, to improve the sensitivity at low hydrogen concentrations, increasing the exposed surface of WO_3 nanorods is beneficial for fast detection.

References

- [1] J. Yang, A. Sudik, C. Wolverton, D.J. Siegel, High capacity hydrogen storage materials: attributes for automotive applications and techniques for materials discovery, *Chem. Soc. Rev.* 39 (2) (2010) 656–675
- [2] H. Zhao, D. Lu, J. Wang, W. Tu, D. Wu, S.W. Koh, P. Gao, Z.J. Xu, S. Deng, Y. Zhou, B. You, H. Li, Raw biomass electroreforming coupled to green hydrogen generation, *Nat. Commun.* 12 (2021) 1–10
- [3] Ohsawa, M. Ishikawa, K. Takahashi, M. Watanabe, K. Nishimaki, K. Yamagata, K. I. Katsura, Y. Katayama, S. Asoh, S. Ohta, Hydrogen acts as a therapeutic antioxidant by selectively reducing cytotoxic oxygen radicals, *Nat. Med.* 13 (2007) 688–694
- [4] T. Hübert, L. Boon-Brett, G. Black, U. Banach, Hydrogen sensors—A review, *Sens. Actuators, B Chem.* 157 (2011) 329–352
- [5] Y. Luo, C. Zhang, B. Zheng, X. Geng, M. Debligny, Hydrogen sensors based on noble metal doped metal-oxide semiconductor: a review, *Int. J. Hydrog. Energy* 42 (2017) 20386–20397
- [6] H. Zheng, J.Z. Ou, M.S. Strano, R.B. Kaner, A. Mitchell, K. Kalantar-Zadeh, Nanostructured tungsten oxide - properties, synthesis, and applications, *Adv. Funct. Mater.* 21 (2011) 2175–2196
- [7] S.K. Deb, Opportunities and challenges in science and technology of WO₃ for electrochromic and related applications, *Sol. Energy Mater. Sol. Cells* 92 (2008) 245–258
- [8] J. Shi, Z. Cheng, L. Gao, Y. Zhang, J. Xu, H. Zhao, Facile synthesis of reduced graphene oxide/hexagonal WO₃ nanosheets composites with enhanced H₂S sensing properties, *Sens. Actuators, B Chem.* 230 (2016) 736–745
- [9] H. Ji, W. Zeng, Y. Xu, Y. Li, Nanosheet-assembled hierarchical WO₃ flower-like nanostructures: hydrothermal synthesis and NH₃-sensing properties, *Mater. Lett.* 250 (2019) 155–158
- [10] Z. Hua, C. Tian, Z. Qiu, Y. Li, X. Tian, M. Wang, E. Li, An investigation on NO₂ sensing mechanism and shielding behavior of WO₃ nanosheets, *Sens. Actuators, B Chem.* 259 (2018) 250–257
- [11] Y. Zhang, W. Zeng, Y. Li, NO₂ and H₂ sensing properties for urchin-like hexagonal WO₃ based on experimental and first-principle investigations, *Ceram. Int.* 45 (2019) 6043–6050
- [12] F. Zheng, C. Xi, J. Xu, Y. Yu, W. Yang, P. Hu, Y. Li, Q. Zhen, S. Bashir, J.L. Liu, Facile preparation of WO₃ nano-fibers with super large aspect ratio for high performance supercapacitor, *J. Alloy. Compd.* 772 (2019) 933–942

- [13] P.A. Shinde, A.C. Lokhande, A.M. Patil, C.D. Lokhande, Facile synthesis of self-assembled WO₃ nanorods for high-performance electrochemical capacitor, *J. Alloy. Compd.* 770 (2019) 1130–1137
- [14] J. Zhang, X. Liu, G. Neri, N. Pinna, Nanostructured materials for room-temperature gas sensors, *Adv. Mater.* 28 (2016) 795–831
- [15] P.S. Kolhe, P. Mutadak, N. Maiti, K.M. Sonawane, Synthesis of WO₃ nanoflakes by hydrothermal route and its gas sensing application, *Sens. Actuators A: Phys.* 304 (2020), 111877
- [16] S.H. Lee, R. Deshpande, P.A. Parilla, K.M. Jones, B. To, A.H. Mahan, A.C. Dillon, Crystalline WO₃ nanoparticles for highly improved electrochromic applications, *Adv. Mater.* 18 (2006) 763–766
- [17] G. Mattoni, B. De Jong, N. Manca, M. Tomellini, A.D. Caviglia, Single-crystal Pt-decorated WO₃ ultrathin films: a platform for sub-ppm hydrogen sensing at room temperature, *ACS Appl. Nano Mater.* 1 (2018) 3446–3452
- [18] C.H. Wu, Z. Zhu, S.Y. Huang, R.J. Wu, Preparation of palladium-doped mesoporous WO₃ for hydrogen gas sensors, *J. Alloy. Compd.* 776 (2019) 965–973
- [19] S. Zeb, G. Sun, Y. Nie, Y. Cui, X. Jiang, Synthesis of highly oriented WO₃ nanowire bundles decorated with Au for gas sensing application, *Sens. Actuators B: Chem.* 321 (2020), 128439
- [20] F. Zheng, L. Zhang, Y.Y. Li, Q. Liu, Z. Li, H.C. Yao, Bimetallic AuPd alloy nanoparticles decorated on macroporous WO₃ supports for selective detection of acetone, *ACS Appl. Nano Mater.* (2021) 4–11
- [21] S. Kim, S. Park, S. Park, C. Lee, Acetone sensing of Au and Pd-decorated WO₃ nanorod sensors, *Sens. Actuators, B Chem.* 209 (2015) 180–185
- [22] Zaleska-Medynska, M. Marchelek, M. Diak, E. Grabowska, Noble metal-based bimetallic nanoparticles: the effect of the structure on the optical, catalytic and photocatalytic properties, *Adv. Colloid Interface Sci.* 229 (2016) 80–107
- [23] C.H. Chang, T.C. Chou, W.C. Chen, J.S. Niu, K.W. Lin, S.Y. Cheng, J.H. Tsai, W. C. Liu, Study of a WO₃ thin film based hydrogen gas sensor decorated with platinum nanoparticles, *Sens. Actuators B: Chem.* 317 (2020), 128145
- [24] F.H. Tian, C. Gong, Y. Peng, X. Xue, H₂ sensing mechanism under different oxygen concentration on the hexagonal WO₃ (001) surface: a density functional theory study, *Sens. Actuators, B Chem.* 244 (2017) 655–663

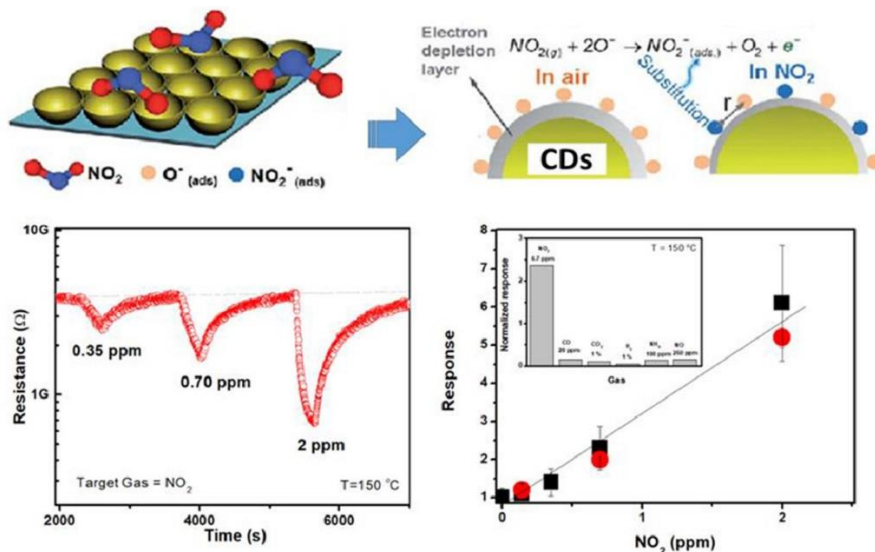
- [25] J. Wang, E. Khoo, P.S. Lee, J. Ma, Controlled synthesis of WO₃ nanorods and their electrochromic properties in H₂SO₄ electrolyte, *J. Phys. Chem. C* 113 (2009) 9655–9658
- [26] T. Peng, D. Ke, J. Xiao, L. Wang, J. Hu, L. Zan, Hexagonal phase WO₃ nanorods: hydrothermal preparation, formation mechanism and its photocatalytic O₂ production under visible-light irradiation, *J. Solid State Chem.* 194 (2012) 250–256,
- [27] Gullino, M. Parvis, L. Lombardo, S. Grassini, N. Donato, K. Moulae, G. Neri, Employment of Nb₂O₅ thin-films for ethanol sensing, in *Proc. IEEE International Instrumentation and Measurement Technology Conference (I2MTC)*, 2020 1–6
- [28] S.S. Kalanur, Structural, optical, band edge and enhanced photoelectrochemical water splitting properties of Tin-doped WO₃, *Catalysts* 9 (2019) 456
- [29] M. Urso, S.G. Leonardi, G. Neri, S. Petralia, S. Conoci, F. Priolo, S. Mirabella, Room temperature detection and modelling of sub-ppm NO₂ by low-cost nanoporous NiO film, *Sens. Actuators B: Chem.* 305 (2020), 127481
- [30] K. Mukherjee, S.B. Majumder, Analyses of response and recovery kinetics of zinc ferrite as hydrogen gas sensor, *J. Appl. Phys.* 106 (2009), 064912,
- [31] K. Bange, Colouration of tungsten oxide films: a model for optically active coatings, *Sol. Energy Mater. Sol. Cells* 58 (1) (1999) 1–131.
- [32] A. Mirzaei, J.H. Kim, H.W. Kim, S.S. Kim, Gasochromic WO₃ nanostructures for the detection of hydrogen gas: an overview, *Appl. Sci.* 9 (2019) 1775
- [33] A. Georg, W. Graf, R. Neumann, V. Wittwer, Mechanism of the gasochromic coloration of porous WO₃ films, *Solid State Ion.* 127 (2000) 319–328

2.2.4 Carbon-dots conductometric sensor for high performance gas sensing

Abstract

In this paper the first example of using C-dots (CDs) as sensing nanomaterial for monitoring low concentrations of NO₂ in ambient air is reported. In the logic to support a green circular economy, CDs were prepared from a natural low cost precursor consisting in olive solid waste (OSW) by a simple pyrolysis process combined with chemical oxidation. Characterization data showed the formation of spherical CDs with dimensions in the narrow size range from 0.5 to 5 nm and charged with functional groups (COO⁻ (carboxylate), C-O-C (epoxide) and C-OH (hydroxyl) imprinting excellent water colloidal dispersion. The nanomaterial was used to fabricate and test a conductometric gas sensor (CDs-sensor) that was found to exhibit excellent performances in terms of high and selective response to sub-ppm concentration of NO₂ at low temperature (150 °C), low limit of detection (LOD) of 50 ppb, good reproducibility and stability over use and aging. To the best of our knowledge, this is the first example reported in the literature of CDs high performances gas sensing material. Results here presented pave the way for a new class of a carbon nanomaterial for gas sensing to be applied in the field of environmental monitoring.

Graphical abstract



2.2.4.1 Introduction

Carbon dots (CDs) represent one of the most promising nanomaterial for many advanced applications due to their multifunctional properties deriving from their unique quantum confinement and edge effects [1,2]. They also exhibit high chemical stability and good conductivity which, coupled with the very high surface area, can address effectively the use of CDs for sensing applications. In a recent review paper, the use of CDs for sensing towards several class of both organic and inorganic analytes has been extensively described [3]. However, most of the studies address sensing applications focusing on both CDs fluorescence and electrochemical properties as transduction detection method. Target analytes were mostly metal ions (Fe^{+3} , Cu^{2+} , Hg^{2+} , etc.) and electroactive (bio)molecules (H_2O_2 , dopamine, glucose, etc.) [3].

Surprisingly, no particular attention has been given to CDs as material for gas sensing that is one of the most important applicative sector for environmental sustainability. Limited study appeared only very recently. In one paper, a CDs-based quartz crystal microbalance sensor was used for the detection of gaseous formaldehyde [4]. In another work, Shauloff et al. fabricated an artificial nose based on CDs as the principle capacitance sensing determinant [5]. However, conductometric (resistive) sensors, which represents the most suitable, practical and cheaper gas sensing technology for monitoring a wide variety of gases [6], based on CDs are not reported so far.

In the environmental pollution, one of the most dangerous gas is nitrogen dioxide (NO_2) representing a relevant source of atmospheric pollution being a product of burning fossil fuel in industry, power plants, houses heating, and car engines. It relevantly contributes to particulate matter, photochemical smog and acid rain and it is very toxic for human health even at very low concentrations [7-10]. Therefore, sensitive, selective and easy to use sensors for NO_2 monitoring in both industrial and urban areas are strongly required and today no satisfactory solutions are present [11]. In this respect, only one study has been reported for optical detection (fluorescence) of NO_2 gas using a hybrid carbon nanodot functionalized aerogel (CDs/ SiO_2 ,) tested in a pure nitrogen atmosphere [12]. Also for the electrical detection, a single example describing a conductometric sensors uses a hybrid reduced graphene oxide-carbon dots (rGO-CD) sensing material has been described so far [13, 14]. However, both above

mentioned studies have practical limitations. Actually, CDs/SiO₂ fluorescence material has been demonstrated to work only in N₂ atmosphere, displaying a detection of limit of 250 ppb, which rule out its use for the low concentrations of NO₂ to be monitored in ambient air. In this respect, the Environmental Protection Agency (EPA) has settled one-hour exposure to NO₂ at the level of 100 ppb. Further, these work are based on sensing layer obtained by complex and multi-step synthetic procedures for the preparation.

In this work we present the first example of pure CDs sensing nanomaterial exhibiting excellent performances towards NO₂ monitoring in conductometric sensor architecture with selective and sensitive response up to sub-ppm concentrations of NO₂ in air.

The CDs here used were obtained from olive solid wastes (OSWs) raw material, an agricultural waste from the olive oil industry, highly appealing from an economical point of view due to its abundance and low cost [15]. Actually, OSWs are produced in massive quantities during olive oil production and represent a waste with high pollution potential. Therefore, providing to its re-use is within the logic of the circular economy. The transformation of OSWs in CDs here described leads to carbon nanoparticles having very small particle size, which implies an extremely large surface-to-volume ratio and hence an elevated proportion of highly reactive sites. These features make these materials very appealing candidates for gas sensors material with high performance. Further, the easy processability of CDs enables the use of a facile integration on a variety of sensing platforms made in plastics, ceramics, or silicon, so offering different possibility for various practical applications. Finally, due the lack of investigation on CDs for gas sensing, this study can also represent a stimulus for further investigations on these nanomaterials in the environmental sensor field.

2.2.4.2 *Experimental Section*

Synthesis of carbon dots (CDs): The CDs were prepared according to the method reported in [15]. Briefly, olive solid w. astes OSWs (collected from Puglia – Italy) were purified from impurities by means of Soxhlet extractor using water as a solvent. The purified OSWs then were pyrolyzed for 1 hour at 600 °C to obtain a carbon-based material named as pyrolyzed olive solid wastes (POSWs). 0.1 g of POSWs was

dispersed in 10 ml of 0.45 wt% H₂O₂ aqueous solution and sonicated for 10 min. The mixture was then refluxed for 90 min. When cooled down to room temperature, the brownish supernatant obtained after centrifugation (9900 rcf for 20 min) was filtered through 0.2µm microfilter and then dialyzed against MilliQ-water through a dialysis membrane (500-1000 Da cutoff).

Cyclic Voltammetry: Cyclic voltammetry (CV) was carried to estimate the HOMO and LUMO energy levels of the CDs and the band gap. The electrochemical measurement was performed by the electrochemical workstation Autolab MSTAT204 Potentiostat/Galvanostat using a three-electrode electrochemical cell with a glassy carbon (3 mm Dia.) working electrode, a Ag/AgCl reference electrode, and a platinum counter electrode (Pt wire) in a 20 mL acetonitrile solution containing 0.1 M tetrabutylammonium hexafluorophosphate (TBAPF₆) as the supporting electrolyte and 1 mL of 1 mg/ml CDs solution. Cyclic voltammetry of the sample was run at a scan rate of 50 mV/s at room temperature.

Sensing tests: Devices for the sensing tests were fabricated by printing thick films of the C-dots powders dispersed in water on alumina substrates (6 mm × 3 mm) and provided by Pt interdigitated electrodes and a Pt heater located on the backside [8]. For the sensing tests, the sensors were introduced in a stainless-steel test chamber and after an initial time of stabilization at the fixed working temperature in flowing synthetic dry air (20% O₂ in nitrogen), exposed to pulses of gas mixtures of selected composition.

Electrical measurements were collected through a data acquisition unit Agilent 34970A, while a dual channel power supplier instrument Agilent E3632A was employed to bias the built-in heater of the sensor. The concentration of NO₂ was varied from 140 ppb to 2.8 ppm. The gas response, S , is defined as $S = R/R_0$ for NO₂, where R is the electrical resistance of the sensor at different NO₂ concentrations and R_0 is the baseline resistance in dry synthetic air. Dynamic characteristics, such as response time, τ_{res} , defined as the time required for the sensor resistance to reach 90% of the equilibrium value after the target gas is injected and recovery time, τ_{rec} , taken as the time necessary for the sensor resistance to reach 90% of the baseline value in air, were also evaluated.

2.2.4.3 Results and discussion

2.2.4.3.1 Structural characterization

CDs was produced by using OSWs as starting material (see Scheme 1). First, the pyrolysis of OSWs at 600°C for one hour has been carried to produce carbonized olive solid wastes (COSWs). The chemical oxidation of this intermediate material was employed to obtain CDs using H₂O₂ as an oxidizing agent. Optimization of H₂O₂ concentration (0.45 wt%) led to CDs of low diameter with a production yield of 10%. H₂O₂ is beneficial for breaking down the carbonaceous particles and extracting CDs with surfaces rich of oxygenated groups [15]



Scheme 1: Schematization of the synthesis process of CDs.

The morphology of the CNDs obtained from OSWs has been investigated by TEM and AFM. The TEM micrographs show well dispersed nanoparticles with good contrast and narrow size dispersion ranging from 1 to 4.5 nm as shown by the size

distribution histogram drawn from TEM images and an average size of 2.8 ± 0.6 nm (Figure 49a and b).

Similar dimensions have been obtained by AFM for the height of the CNDs with a range of 0.5 to 5 nm having an average of 2.8 ± 0.9 nm, demonstrating that the particles have quasi-spherical morphology (Figure 49c-d)

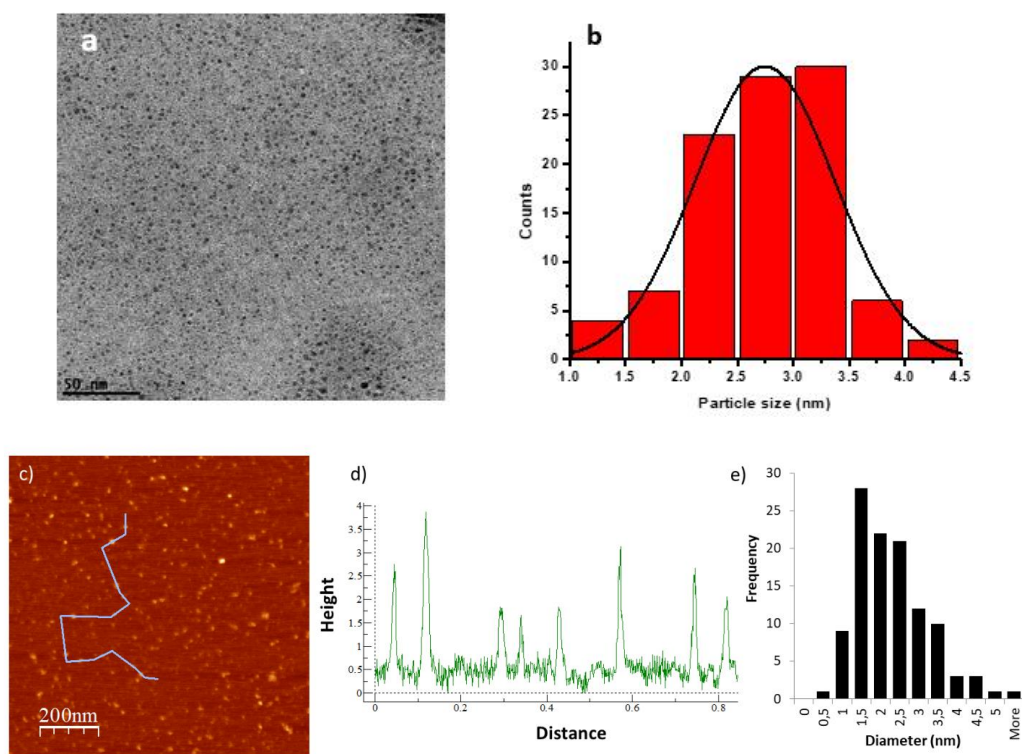


Figure 2-49. Morphological characterization of CNDs: a) TEM micrograph, b) TEM size distribution histogram, c) AFM height micrograph, d) AFM height profile and e) AFM height distribution histogram

The functional surface groups were investigated using FTIR spectroscopy (Figure 50). The peaks shown at 3424, 3236, 2923/2850, 1656, 1412, 1320 and 1116 and 1096 cm^{-1} are assigned to $-\text{OH}$, N-H , C-H , C=O (carbonyl), COO^- (carboxylate), C-OH (hydroxyl) and C-O-C (epoxide) [16,17] groups respectively. The presence of such functional groups implies that the synthesized CNDs have excellent water-soluble colloidal dispersion [18]. It was also found that these dots are negatively charged with ξ -potentials = -32 mV in 10 mM PBS, the negative charge could be ascribed to the existence of oxygenated functional groups [19-21].

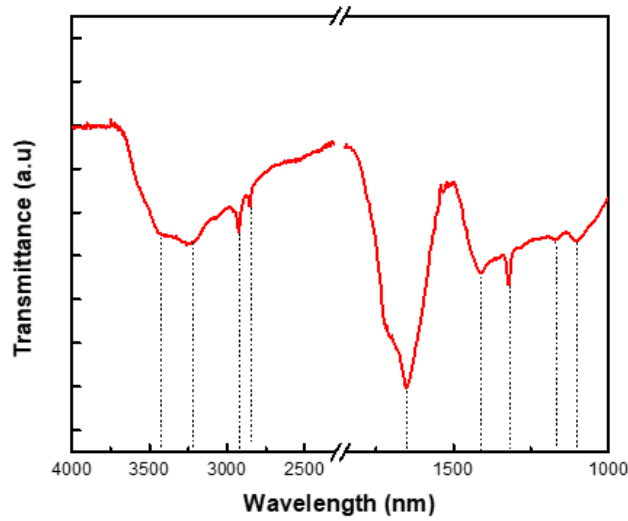


Figure 2-50. FT-IR spectrum of synthesized CDs

In terms of conduction properties, the synthesized CDs evidence a semiconductor behavior with a band gap of 1.55 eV, estimated from the difference between LUMO (-4.24 eV) and HOMO (-5.79 eV) energy levels [22]. The HOMO – LUMO levels were calculated from oxidation and reduction onset resulted from the cyclic voltammogram (see Figure 51a) using the equations (1) and (2):

$$HOMO = -[E_{onset,ox} + 4.66 \text{ eV}] \quad (1)$$

$$LUMO = -[E_{onset,red} + 4.66 \text{ eV}] \quad (2)$$

where $E_{onset,ox}$ and $E_{onset,red}$ are the onset of the oxidation and reduction potentials respectively [23-24].

The semiconductor behavior has been confirmed by analyzing the electrical resistance of thick films (around 10 μm) at different temperatures. The electrical measurements have been performed on the same platform used for the conductometric sensing tests (Figure 51b), with the aim to acquire also direct information on the behavior of CDs as a sensing layer in the practical device. In the inset of this Figure 51b is noted CDs deposited as thick films by printing on the conductometric transduction device having a pair of interdigitated Pt electrodes on the ceramic substrate.

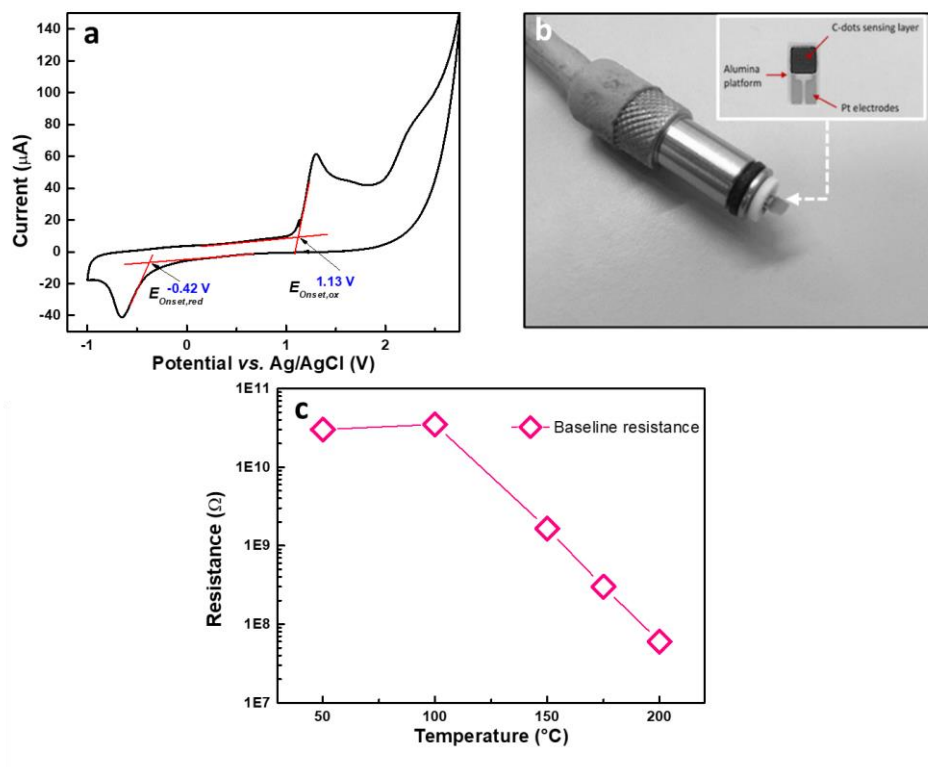


Figure 2-51. a) Cyclic voltammogram versus Ag/AgCl reference electrode of synthesized CDs; b) picture of the conductometric sensor probe; in the inset is shown the sensor head; c) Baseline resistance vs. operating temperature trend.

2.2.4.3.2 Electrical and gas sensing properties

The range of temperature investigated was between 50 °C and 200 °C due to both the restrictions imposed by the very high resistance registered below 50 °C and the unstable and large baseline drift observed at temperatures higher than 200 °C. The trend of baseline resistance in this temperature range is reported in Figure 51c. At near room temperature, the resistance is out of the range of measurement with our instrumentation. Increasing the temperature, the resistance decreases, as expected by a semiconductor material. This behavior can be explained as follows: at low temperature, free electrons are trapped by O_2 molecules as ionized species (O^- or O^{2-}), generating a depletion layer (Schottky potential barrier); further, the grain boundaries at the contact between the very small CDs might create additional potential barriers, increasing the electrical resistance. Increasing the operating temperature, thermally generated electrons give the main contribution to the resistance decrease. However, as an additional process due to the adsorbed O_2 molecules desorption from the CDTs

surface upon increasing of the temperature, releases the trapped electrons and decreases the resistance.

On the basis of above described electrical characteristics that make CDs to be full compatibles for their use in conductometric platform for gas sensing, we have tested its performances in the monitoring of low NO₂ concentration in air. First, we evaluated the effect of operating temperature on the sensor response. Figure 52a reports the variation of resistance for the CDs sensor subjected to pulses of NO₂ at the concentration of 2 ppm in dry air.

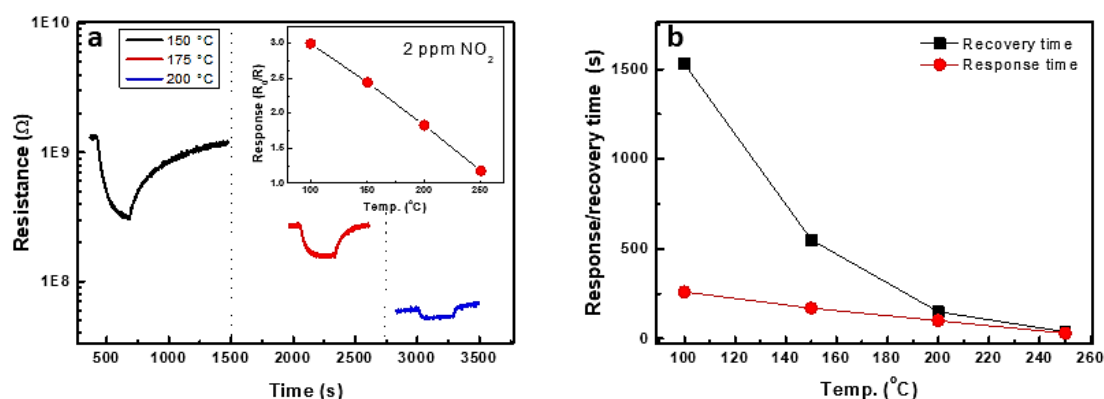


Figure 2-52. a) Resistance variation at different temperatures of CDs sensor subjected to pulses NO₂ at the concentration of 2 ppm. Inset shows the trend of sensor response with temperature; b) Response/recovery time at different temperatures of the CDs sensor.

From the above reported data, it clearly appears that the CDs-based sensor is very sensitive to NO₂ gas exposure exhibiting a tendency to a response enhancement with the temperature decrease. However, by reducing the temperature, the recovery time becomes longer (see Figure 52b) and this limits the practical application of the sensor. Therefore, the best balance between high response and faster dynamics can be settled at 150 °C. Figure 53a reports the resistance variation for the CDs sensor, at the optimal temperature of 150 °C, subjected to pulses of NO₂ at different concentration (from 140 ppb to 2 ppm) in dry air. The interaction among NO₂ molecules and CDs leads to a linear variation of the resistance with the nitrogen dioxide in the investigated concentration range, as highlighted in the calibration curve graph reported in Figure 53b. It is noteworthy the good reproducibility of the two reported calibration curves, registered by two diverse sensors fabricated by using the same CDs. The resistance variations observed are well reversible; the response and recovery times are in the order of about 150 sec. and 315 sec., respectively.

The interaction between the NO₂ molecule and CDs leads to a decrease of the resistance at all temperatures and NO₂ concentrations investigated, indicating that the CDs sensor has a p-type behaviour. This finding can be attributed to presence of electron withdrawing oxygen functional groups on the surface of CDs, as also suggested by some authors for other colloidal quantum dots [25].

The sensing mechanism can be described into the framework of general theory of p-type semiconducting gas sensors functioning [26]. However, the true sensing mechanism of NO₂ on carbon materials is still not fully understood and only hypotheses could be formulated taking into account examples coming from CNTs and graphene as previous carbon nanostructures-based sensing material for NO₂ [27-29]. Here, we can suppose that the resistance of sensing layer decreases after adsorption of NO₂ gas molecule due to the direct adsorption/chemisorption of NO₂ on the CDs surface, which is covered of adsorbed O⁻ oxygen ions, the main surface oxygen species present at the operating temperature of 150 °C. NO₂ interacts with the chemisorbed oxygen ions on the surface and extracts electrons. Indeed, NO₂ as an electron acceptor consume electrons, resulting in the increase of hole concentration. The depletion layer becomes thinner (low electrical resistance, see Figure 53c) and therefore, electrical resistance decreases, as experimentally observed.

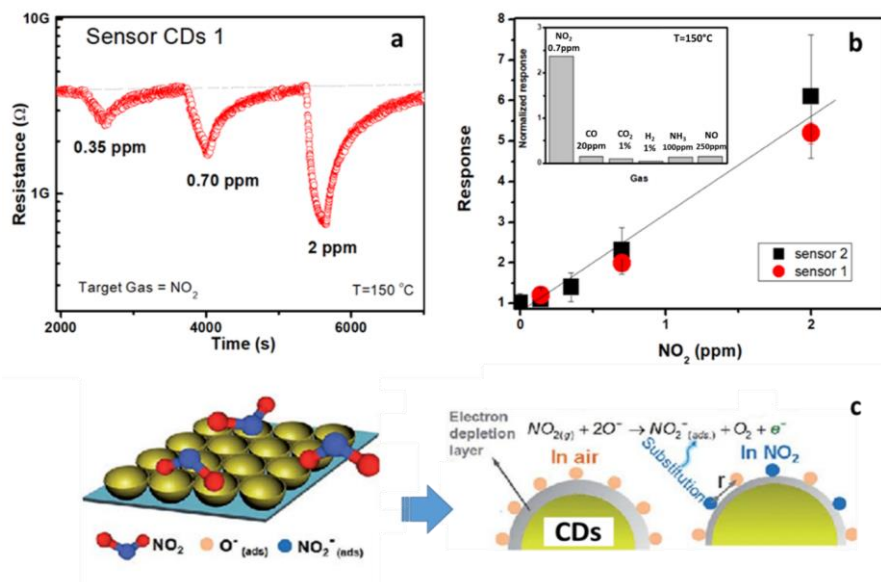


Figure 2-53. a) Transient response towards different NO₂ concentrations for the CDs sensor; b) calibration curve towards NO₂, whereas the inset shows the response to different gases; c) schematization of the NO₂ proposed sensing mechanism on CDs-based conductometric sensor.

Above explanation is in accordance with data reported for other carbon nanostructures, such as CNTs, where Schottky barrier modulation is the main detection mechanism postulated for gas sensing [30]. However, other sensing mechanisms cannot be excluded and can be concurrently present, depending on many factors linked mainly to size of carbon nanostructures. Indeed, carrier transport through the electrode-carbon particles is influenced by the particle size and the width of the depletion region. In air, oxygen is adsorbed at the active carbon sites, accepting electrons from the conduction band and causing, depending on the size, a partial to fully depleted region devoided of mobile charge carriers. The conduction mechanism is then governed by Schottky barriers at the grain boundaries, and grain control mechanism, respectively.

For our CDs-based conductometric sensor, the sensing mechanism can be supposed to be related to limited charge transport across Schottky barriers. The conduction across Schottky barriers is regulated by thermoionic emission carrier transport, or less usually, by tunneling. Relevant to gas sensing is however that the activation energy for conductance is a function of the barrier height, which is directly affected by the charge and fractional coverage of the surface species and, hence, a function of the composition of the gas surrounding the sensor.

Selectivity to target gas, response reproducibility and stability are also important parameters of a sensor for the practical use. From inset reported in Figure. 53b is noted a very low response toward reducing gases (CO , NH_3 , CO_2 , CH_4), which implies that the sensor is also highly selective towards NO_2 . Experimental results have also demonstrated a good signal reproducibility. Figure 54a shows the reproducibility test when the sensor was exposed to pulses of 2 ppm of NO_2 at 175 °C. A fairly stable response was observed for a period of approximately three months (see Fig. 54b).

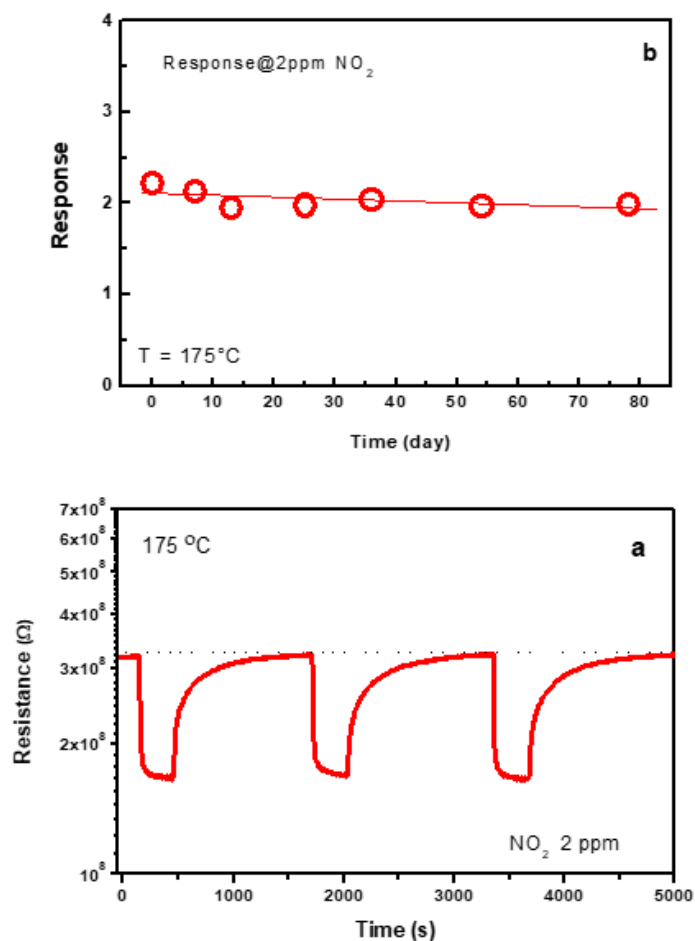


Figure 2-54. a) Response of the sensor to consecutive pulses of 2 ppm of NO₂; b) Sensor response evaluated for a period of approximately 3 months.

The good sensing properties (sensitivity, selectivity, stability) of the sensor towards NO₂ can be then explained with the characteristics of CDs synthesized. First, the large specific surface area of the very small CDs provides many unsaturated sites with high reactivity, maximizing the interaction with the target gas. As regarding the excellent selectivity towards NO₂, it is associated to the surface state of CDs. Indeed, other than addressing the semiconducting behaviour, the chemical structure of the surface has the noticeable function to interact with the gases surrounding the sensor. In this way, depending on the chemical nature on the CDs surface and gaseous specie, the interaction will have a different strength and charge transfer. It seems then that the presence of the various organic groups on the CDs surface as indicated by FT-IR and XPS investigation can be relevant for NO₂ gas. In this perspective, it is interesting to note that it is possible to modulate the surface chemistry of the C-dots by introducing new ligands. These modifications can change the interaction of CDs with the gas

molecules, modulating then the selectivity of the sensor versus different gases. At last, the long term stability of the sensor can be related to mild temperature (150 °C) chosen for sensing tests. This aspect is fundamental in order to avoid thermal stress to sensing layer in general, and in particular in the case of CDs sensing layer, this mild temperature avoids to modify/degrade the labile surface groups on the surface of CDs.

Finally, the sensing performances of the developed CDS-based sensor were also compared with previously reported conductometric sensors based on other carbon nanomaterials (see Table 2-10).

Table 2-10. Comparison of the NO₂ sensing performances of carbon conductometric sensors.

Sensing material	Limit of Detection [ppb]	Response ¹ /concentration	Operating temperature	Measurement range [ppm]	UV light	Ref.
SWCNTs ²	86	100/0.1 ppm	50 °C	0.1-10	no	[30]
Graphene oxide	0.21	10/1 ppm	150 °C	1-9	no	[31]
Aligned SWCNTs	-	7/0.5 ppm	RT ³	0.5-10	yes	[32]
S-doped graphene	-	0.2/500 ppt	RT	0.5-100	no	[33]
3D rGO ⁴	186	0.1/1 ppm	22 °C	1-8	no	[34]
rGO	-	37/5 ppm	RT	5-100	no	[35]
CVD Graphene	4	3/1 ppm	RT	1-20	yes	[36]
C-dots	50	140/0.7 ppm	150 °C	0.14-2	no	This work

¹ Response (*R*) is defined as $R = 100 * |R_g - R_a| / R_a$ where *R_a* and *R_g* are, respectively, the recorded signal in the absence and presence of NO₂ at the indicated concentration. ² Single-wall carbon nanotube; ³ Room temperature. ⁴ Reduced Graphene Oxide.

From this comparison, it is worthy to mention the outstanding sensitivity (3rd column in Table 2-10) of our nanomaterials. Further, this remarkable sensitivity and full and fast response/recovery of the signal is reached without the use of UV light. Once again, these comparative data confirm that the suitable carbon nanostructure obtained improve the performance of conductometric device for monitoring NO₂ at part-per-

billion levels. However, we plan to further improve the performances of our materials by investigating in future studies both the effect of possible surface functionalization of C-dots and also the optimization of film structure and morphology.

2.2.4.4 Conclusion

In summary, CDs here reported were produced by a simple pyrolysis process combined with chemical oxidation from olive solid wastes, a cheap and readily available natural precursor. Morphological and microstructural characterization indicated that these nanometer CDs have a spherical shape with dimension ranging from 0.5 to 5 nm. Further, the presence of charged functional groups (COO- (carboxylate), C-O-C (epoxide) and C-OH (hydroxyl), which imprint excellent water colloidal dispersion properties, has been also highlighted. NO₂ sensing properties of CDs has been investigated showing excellent performances in terms of sensitivity, selectivity, full recovery after exposure and stability. Noteworthy, this study represents the first evidence of using CDs sensing material for conductometric gas sensor. Therefore, we expect that this study will pay the way for a large family of CDs produced by different natural sources to be employed as highly sensitive sensors.

References

- [1]. S. Anwar, H. Ding, M. Xu, X. Hu, Z. Li, J. Wang, L. Liu, L. Jiang, D. Wang, C. Dong, M. Yan, Q. Wang and H. Bi, Recent Advances in Synthesis, Optical Properties, and Biomedical Applications of Carbon Dots, *ACS Applied Bio Materials*, 2, (2019) 2317-2338.
- [2]. H. Li, Z. Kang, Y. Liu and S.-T. Lee, Carbon nanodots: synthesis, properties and applications, *Journal of Materials Chemistry*, 22, (2012) 24230-24253.
- [3]. M. Li, T. Chen, J. J. Gooding and J. Liu, Review of Carbon and Graphene Quantum Dots for Sensing, *ACS Sensors*, 4, (2019), 1732-1748.
- [4]. W.A. Amer, A.F.Rehab, M.E. Abdelghafar, N.L. Torad, A.S. Atlam, M.M. Ayad, Green synthesis of carbon quantum dots from purslane leaves for the detection of formaldehyde using quartz crystal microbalance, *Carbon* 2021, 179, 159-171.
- [5]. N. Shauloff, A. Morag, K. Yaniv, S. Singh, R. Malishev, O. Paz-Tal, L. Rokach, R. Jelinek, Sniffing Bacteria with a Carbon-Dot Artificial Nose, *Nano-Micro Letters* 13(2021), 112.
- [6]. J. Zhang, X. Liu, G. Neri and N. Pinna, Nanostructured Materials for Room-Temperature Gas Sensors, *Advanced Materials*, 28, (2016),795-831.
- [7]. T. W. Hesterberg, W. B. Bunn, R. O. McClellan, A. K. Hamade, C. M. Long and P. A. Valberg, Critical review of the human data on short-term nitrogen dioxide (NO₂) exposures: Evidence for NO₂ no-effect levels, *Critical Reviews in Toxicology*, 39, (2009) 743-781.
- [8]. R. Rella, A. Serra, P. Siciliano, A. Tepore, L. Valli and A. Zocco, NO₂ gas detection by Langmuir-Blodgett films of copper phthalocyanine multilayer structures, *Supramolecular Science*, 4, (1997), 461-464.
- [9]. R. Rella, A. Serra, P. Siciliano, A. Tepore, L. Valli and A. Zocco, Effects of NO₂ oxidizing gas on a novel phthalocyanine Langmuir-Blodgett thin film, *Thin Solid Films*, 286, (1996), 256-258.
- [10]. R. Rella, A. Rizzo, A. Licciulli, P. Siciliano, L. Troisi and L. Valli, Tests in controlled atmosphere on new optical gas sensing layers based on TiO₂/metal-phthalocyanines hybrid system, *Materials Science and Engineering: C*, 22 (2002), 439-443.
- [11]. M.Urso, S.G Leonardi, G. Neri, Petralia, S. Conoci, F. Priolo, S. Mirabella, Room temperature detection and modelling of sub-ppm NO₂ by low-cost nanoporous NiO film, *Sensor and Actuators, B: Chemical*, 305, (2020), 127481

- [12]. R. Wang, G. Li, Y. Dong, Y. Chi and G. Chen, Carbon Quantum Dot-Functionalized Aerogels for NO₂ Gas Sensing, *Analytical Chemistry*, 85, (2013), 8065-8069.
- [13]. J. Hu, C. Zou, Y. Su, M. Li, N. Hu, H. Ni, Z. Yang and Y. Zhang, Enhanced NO₂ sensing performance of reduced graphene oxide by in situ anchoring carbon dots, *Journal of Materials Chemistry C*, 5, (2017), 6862-6871.
- [14]. Q. R. Liu, J. J. Zhang, H. He, G. X. Huang, B. L. Xing, J. B. Jia and C. X. Zhang, Green preparation of high yield fluorescent graphene quantum dots from coal-tar-pitch by mild oxidation, *Nanomaterials*, 8, (2018), 844-853.
- [15]. S. Sawalha, A. Silvestri, A. Criado, S. Bettini, M. Prato and L. Valli, Tailoring the sensing abilities of carbon nanodots obtained from olive solid wastes, *Carbon*, 167, (2020) 696-708.
- [16]. V. Nguyen, L. Yan, J. Si and X. Hou, Femtosecond laser-induced size reduction of carbon nanodots in solution: Effect of laser fluence, spot size, and irradiation time, *Journal of Applied Physics*, 117, (2015), 084304.
- [17]. P. Das, M. Bose, S. Ganguly, S. Mondal, A. K. Das, S. Banerjee and N. C. Das, Green approach to photoluminescent carbon dots for imaging of gram-negative bacteria *Escherichia coli*, *Nanotechnology*, 28, (2017), 195501.
- [18]. K. Radhakrishnan, P. Panneerselvam and M. Marieeswaran, A green synthetic route for the surface-passivation of carbon dots as an effective multifunctional fluorescent sensor for the recognition and detection of toxic metal ions from aqueous solution, *Anal Methods*, 11, (2019), 490-506.
- [19]. M. Y. Xue, Z. H. Zhan, M. B. Zou, L. L. Zhang and S. L. Zhao, Green synthesis of stable and biocompatible fluorescent carbon dots from peanut shells for multicolor living cell imaging, *New J Chem*, 40, (2016), 1698-1703.
- [20]. R. Bandi, B. R. Gangapuram, R. Dadigala, R. Eslavath, S. S. Singh and V. Guttena, Facile and green synthesis of fluorescent carbon dots from onion waste and their potential applications as sensor and multicolour imaging agents, *RSC Adv*, 6, (2016), 28633-28639.
- [21]. S. Bettini, S. Sawalha, L. Carbone, G. Giancane, M. Prato and L. Valli, Carbon nanodot-based heterostructures for improving the charge separation and the photocurrent generation, *Nanoscale*, 11, (2019), 7414-7423.
- [22]. J. Chen, J. Liu, J. Li, L. Xu and Y. Qiao, One-pot synthesis of nitrogen and sulfur co-doped carbon dots and its application for sensor and multicolor cellular imaging, *Journal of Colloid and Interface Science*, 485, (2017), 167-174.

- [23]. J. Choi, N. Kim, J.-W. Oh and F. S. Kim, Bandgap engineering of nanosized carbon dots through electron-accepting functionalization, *Journal of Industrial and Engineering Chemistry*, 65, (2018), 104-111.
- [24]. Z. Zeng, W. Zhang, D. M. Arvapalli, B. Bloom, A. Sheardy, T. Mabe, Y. Liu, Z. Ji, H. Chevva, D. H. Waldeck and J. Wei, A fluorescence-electrochemical study of carbon nanodots (CNDs) in bio- and photoelectronic applications and energy gap investigation, *Phys Chem Chem Phys*, 19, (2017), 20101-20109.
- [25]. P. Litvin, I. V. Martynenko, F. Purcell-Milton, A. V. Baranov, A. V. Fedorov and Y. K. Gun'ko, Colloidal quantum dots for optoelectronics, *Journal of Materials Chemistry A*, 5, (2017), 13252-13275.
- [26]. H.-J. Kim and J.-H. Lee, Highly sensitive and selective gas sensors using p-type oxide semiconductors: Overview, *Sensors and Actuators B: Chemical*, 192, (2014) 607-627.
- [27]. S. Mao, G. Lu and J. Chen, Nanocarbon-based gas sensors: progress and challenges, *Journal of Materials Chemistry A*, 2, (2014), 5573-5579.
- [28]. V. Schroeder, S. Savagatrup, M. He, S. Lin and T. M. Swager, Carbon nanotube chemical sensors, *Chem Rev*, 119, (2018), 599-663.
- [29]. L. Huang, Z. Wang, J. Zhang, J. Pu, Y. Lin, S. Xu, L. Shen, Q. Chen and W. Shi, Ultrasensitive and selective nitrogen dioxide sensor based on self-assembled graphene/polymer composite nanofibers, *ACS Applied Materials & Interfaces*, 6, (2014), 7426-7433.
- [30]. L. Sacco, S. Forel, I. Florea, and C.-S. Cojocaru, Ultra-sensitive NO₂ gas sensors based on single-wall carbon nanotube field effect transistors: Monitoring from ppm to ppb level, *Carbon*, 157, (2020), 631-639.
- [31]. J. Park, Y. Kim, S.Y. Park, S.J. Sung, H.W. Jang, and C.R. Park, Band gap engineering of graphene oxide for ultrasensitive NO₂ gas sensing, *Carbon*, 159, (2020), 175-184.
- [32]. S. S. Chauhan, D. Kumar, P. Chaturvedi, and M.R. Rahman, Highly Sensitive and Stable NO₂ Gas Sensors Based on SWNTs With Exceptional Recovery Time, *IEEE Sensors Journal*, 19, (2019), 11775-11783.
- [33]. L. Guo, and T. Li, Sub-ppb and ultra selective nitrogen dioxide sensor based on sulfur doped graphene, *Sens. Actuators B*, 255, (2018), 2258-2263.
- [34]. J. Wu, K. Tao, J. Miao, and L.K. Norford, Carbon nanocoil-based fast-response and flexible humidity sensor for multifunctional applications, *ACS Applied Materials & Interfaces*, 7, (2015), 27502-27510.

- [35]. T. Han, S. Gao, Z. Wang, T. Fei, S. Liu, and T. Zhang, Investigation of the effect of oxygen-containing groups on reduced graphene oxide-based room-temperature NO₂ sensor, *J. Alloys and Compounds*, 801, (2019), 142-150.
- [36]. X. Yan, Y. Wu, R. Li, C. Shi, R. Moro, Y. Ma, and L. Ma, High-Performance UV-Assisted NO₂ Sensor Based on Chemical Vapor Deposition Graphene at Room Temperature, *ACS Omega*, 4, (2019), 14179-14187.

3 Final remarks and outlooks

Detection and monitoring various substances in both gas and aqueous phase have been an ever-growing subject in different fields ranging from healthcare purposes to industrial requirements. In order to address the need to design and develop more reliable sensors, it is necessary to deepen the knowledge we possess concerning the sensing materials and the reaction mechanisms that govern their behavior. This Ph.D. thesis, therefore, is a devoted attempt to illustrate a series of results that are in line with the aforementioned aims. The results obtained here, for both gas sensing and electrochemical sensing studies, were remarkable as compared with similar reports not only due to the introduction of new sensing materials but also because of presenting mechanistic data concerning the sensing procedures. As examples, in the research activities presented in sections 2.1.1, 2.1.2, 2.2.1, 2.2.2, and 2.2.3, the quantitative results regarding the performance of these sensors are interpreted and discussed in detail from a mechanistic point of view as well. This approach was of great importance, as getting a deeper knowledge of sensing mechanisms will consequently pave the way for further improvement of sensing strategies in the future. To briefly highlight the most important issues and opportunities presented in this thesis, following points are worthy of note;

1. In some studies, the sensing materials were chosen to be *suitable for mechanistic studies*, for example, a base CNT covered by different thicknesses of the shell layers (NiO or Al₂O₃) was used to follow the effect of shell thickness/type on the sensing performance.
2. In some other studies, where the main goal was solely improving the sensing performance, *low-cost and straight forward synthesised* sensing materials were utilized, e.g. CuO (section 2.1.3), WO₃ (section 2.2.3) and carbon dots (2.2.4).
3. In this thesis, whenever our knowledge/data allowed us, *quantitative* results were supported and interpreted in a *qualitative* (from mechanistic point of view) manner as well.

4. In some cases, e.g. section 2.2.1 and 2.1.2, the *novel sensing mechanisms* proposed in this thesis are clearly in contrast with many former reports found in the literature.

Looking backward, although an acceptable attempt has been made in this thesis to present and discuss new sensing materials and sensing mechanisms, in order to have more reliable sensors, further advances are still needed. Looking forward, I hope scientific attempts that I have made in this thesis, together with other research activities by researchers all over the world lead us to a better understanding of the function of proposed sensors and finally improve their performance in the upcoming years.

4 Appendixes

4.1 Appendix A: List of tables

Table 2-1 Comparative study of different modified electrode glucose sensors reported in literature.....	33
Table 2-2. Electroanalytical performance of SPCE-CNT/Al ₂ O ₃ (9) and related figures of merit for DHB isomers determination.....	53
Table 2-3. Performance of the proposed sensor in comparison to previously reported metal oxide based electrochemical sensors for DHB isomers measurements..	55
Table 2-4. Determination of DHB isomers in real samples, i.e. tap water and mineral water using SPE-SC CNT/Al ₂ O ₃ (8).	56
Table 2-5. Comparison of the sensing the performance of proposed sensor to other reported CuO based sensor in the literatures.	73
Table 2-6. Results for measurement of glucose in urine sample.....	75
Table 2-7 Summary of the ALD deposited NiO shell layer thickness and growth per cycles (GPC) as calculated by transmission electron microscopy (TEM) on SCCNTs and ellipsometry on silicon wafers.....	84
Table 2-8. Results of the fitting procedure to response and recovery transients at various temperatures and at fixed concentration of H ₂ (10,000 ppm) based on (3.3.1), (3.3.2).	130
Table 2-9. Results of the fitting procedure to response and recovery transients at various concentrations of H ₂ at a temperature of 350 °C, based on (3.3.1), (3.3.2).	131
Table 2-10. Comparison of the NO ₂ sensing performances of carbon conductometric sensors.....	150

4.2 Appendix B: List of figures

Figure 1-1. Schematic view of common interfacial electrochemical methods.....	2
Figure 1-2. Schematic view of a two-electrode (a) and three-electrode (b) system: Here Aux. Auxiliary electrode, Ref. Reference electrode and Work are work electrodes.....	3
Figure 1-3. a) potential-time change diagram, b) concentration section changes with time and c) corresponding current-time response.....	6
Figure 1-4. Potential-time excitation profile in a cyclic voltammetry analysis (a) and the resulting voltammogram for a reversible electrochemical reaction (b).....	10
Figure 1-5. Differential pulse voltammetry. (a) The profile of potential waveform applied to the electrode over time and (b) the resulting voltammogram.....	11
Figure 1-6. Square wave voltammetric analysis. Profile of potential waveform applied to the electrode over time (a) Current profile obtained over time (b) and normalized acquired voltammogram (c)	13
Figure 1-7. A typical thick film gas sensor preparation procedure by drop casting method using a gas sensing substrate with platinum interdigitated electrodes onto the front side and platinum heater part onto the backside.	15
Figure 1-8. Schematic view of our in-house built gas sensing setup.....	16
Figure 2-1. TEM images of pristine SCCNT (a, b), an overview of NiO coated SCCNTs with 100 ALD cycles (c), HRTEM images for S25 (d), S50 (e), S100 (f), S200 (g), S400 (h) and S700 (i). The inset in (i) shows the SAED pattern of S400.....	23
Figure 2-2. Thickness of the NiO film as a function of number of ALD cycles, under self limiting conditions. The linear fitting crosses the origin with a slope of $0.32 \text{ \AA cycles}^{-1}$	24
Figure 2-3. Recorded cyclic voltammograms in a 0.1 M KOH solution containing different amounts of glucose at 50 mV/s for S200 modified electrode.....	26

Figure 2-4. Effect of different amount of deposited NiO on (a) sensitivity and (b) LDR of glucose determination. (c) Effect of different amounts of S100 on background subtracted current (Δi_p) in glucose solution..... 27

Figure 2-5. Cyclic voltammograms of the NiO/CNT modified electrode (a) in different KOH concentrations and (b) in in different KOH concentrations and a constant glucose concentration at scan rate of 50 mVs^{-1} . (c) Peak current of cyclic voltammograms in the absence (blue) and presence (red) of a constant concentration of glucose. 28

Figure 2-6. Cyclic voltammograms of the NiO/CNT modified electrode, S100, at different scan rates in the presence of glucose. Insets show (a) the plots of peak currents vs. square root of scan rate and enlarged cyclic voltammograms of NiO/CNT modified electrode at (b) 100 mV s^{-1} and (c) 5 mV s^{-1} 29

Figure 2-7. Chronoamperometric tests using S100 electrode with serial additions of glucose solutions in order to increase the total glucose concentration of the electrolyte by steps of $100 \mu\text{M}$ at different applied potentials (a) and at $E_{app}=0.65 \text{ V}$ for three different measurements with the same electrode (b). Currenttime responses of S100 electrode acquired in 0.1 M KOH solution and increasing concentrations of glucose at $E_{app}=0.650 \text{ V}$, insets show the current-time responses in the low glucose concentration and the calibration curve for glucose determination using S100 electrode (c). Interference study to selected species on S100 electrode in 0.1 M KOH and 0.2 mM glucose (d). 31

Figure 2-8. Linear fits for the Al_2O_3 thickness as a function of the number of ALD cycles as estimated, (a) on silicon wafers by spectroscopic ellipsometry (SE) and, (b) on CNTs by transmission electron microscopy (TEM). All the thicknesses were estimated from three different positions in the samples and the average values are shown in the linear fits..... 42

Figure 2-9. BF-HRTEM images for the (a and b) $4\text{CNT}/\text{Al}_2\text{O}_3$ and (c) $\text{CNT}/\text{Al}_2\text{O}_3(9)$ heterostructures. HAADF-STEM images for the $\text{CNT}/\text{Al}_2\text{O}_3(9)$ heterostructures. BF-HRTEM images for the (e and f) $\text{CNT}/\text{Al}_2\text{O}_3(19)$, (g and h) $\text{CNT}/\text{Al}_2\text{O}_3(49)$ and (i) $\text{CNT}/\text{Al}_2\text{O}_3(100)$ heterostructures. The insets in the

(c) and (i) show the SAED patterns for the CNT/Al ₂ O ₃ (9) and CNT/Al ₂ O ₃ (100) heterostructures, respectively.	43
Figure 2-10. HAADF-STEM and the corresponding EDX elemental mappings images for the (a) CNT/Al ₂ O ₃ (4), (b) CNT/Al ₂ O ₃ (9), (c) CNT/Al ₂ O ₃ (19) and (d) CNT/Al ₂ O ₃ (100) heterostructures.....	45
Figure 2-11. Cyclic voltammograms of (A) bare SPCE in the presence of (a) HQ, (b) HQ+CC and (c) HQ+CC+RS. (B) Comparison between the recorded CVs in a solution containing all DHB isomers (HQ+CC+RS) using bare SPCE and SPCE-CNT/Al ₂ O ₃ (4). CVs were acquired at scan rate of 20 mV/sec. Where used, concentration of each isomer was 100μM in PBS pH=7.4.....	46
Figure 2-12. (A) Square-wave voltammograms for different electrodes (see legend A) in a solution containing 200 μM of HQ and CC in PBS pH 7.4. Graphs B (For hydroquinone) and C (for catechol) were extracted from figure A to clarify the variation of the observed anodic peak currents (I _{pa}) and anodic peak potentials (E _{pa}) versus Al ₂ O ₃ thickness.....	47
Figure 2-13. Cyclic voltammograms of CNT/Al ₂ O ₃ (9) modified electrode in a solution containing 100 μM (a) HQ and (b) CC in PBS pH=7.0 at scan rates from 2 to 400 mV/s. Insets depict the variation of the baseline corrected anodic peak currents (I _{pa}) and cathodic peak currents (I _{pc}) versus the square rate of scan rate.	51
Figure 2-14. Cyclic voltammograms for a 200 μM solution of (A) HQ and (B) CC at pHs between 4 and 8.3 using SPCE-CNT/Al ₂ O ₃ (9). Scan rate: 20 mV/s. Insets depict the variation of the oxidation peak potentials of HQ and CC with pH..	52
Figure 2-15. SWV responses of (A) HQ, (B) CC and (C) RS standard solutions with increasing concentrations of analytes recorded in a 0.1 M PBS pH 7.4 using SPCE-CNT/Al ₂ O ₃ (9). Simultaneous measurement of HQ and CC in a solution containing (D) a fixed amount of CC and varying [HQ], (E) a fixed amount of HQ and varying [CC] and (F) a fixed amount of HQ and CC and varying [RS]. Inset graphs show the resulting calibration plots of the peak currents (baseline corrected) versus analytes concentrations.	54

Figure 2-16. (A, B) SEM micrographs of as-prepared CuO nanostructures; (C, D) Size distribution of the minor and mayor axis of CuO elliptic particles.	66
Figure 2-17. (A,B,C) TEM and (D) SAED micrographs of as-prepared CuO nanostructures.	67
Figure 2-18. XRD pattern of as-prepared CuO nanostructure.	68
Figure 2-19. FTIR spectrum of as-prepared CuO nanostructure.	68
Figure 2-20. (a) Cyclic voltammograms of bare SPCE (I) and SPCE/CuO (III) in 0.1 M KOH, and bare SPCE (II) and SPCE/CuO (IV) in (1 mM glucose+0.1 M KOH) at scan rate: 50 mV s ⁻¹ . (b) Effect of KOH concentration on sensitivity of SPCE/CuO electrode. Net current, defined as subtraction of peak current in the presence of 1mM glucose and absence of glucose, in different concentration of KOH, i.e. 0.001, 0.01, 0.1, 0.5 and 1 mol/L.	69
Figure 2-21. CVs of glucose oxidation at SPCE/CuO at different scan rates, i.e. 5, 10, 25, 50, 100, 300, 500, 800, 1200 and 1500 mV/s. (inset) Plots of peak current vs. square root of scan rate (a) and scan rate (b).	71
Figure 2-22. Study of SPCE/CuO sensor in 0.1 M KOH after successive addition of 200µM glucose (a) at different applied potential and (b) corresponding calibration curve for each potential (c).	72
Figure 2-23. Calibration curve for proposed sensor at 0.6V and 0.1M KOH (insets show the magnification of lower concentration range and calibration curve for the glucose determination).	73
Figure 2-24. (a) Interference response of SPCE/CuO modified electrode in 0.1 M KOH at 0.6 V. (b) long-term stability of proposed sensor (each point represents 3 repetitive measurements).	75
Figure 2-25. High-resolution transmission electron microscopy (HRTEM) images for (a) NiO-SCCNTs-100, (b) NiO-SCCNTs-200, (c) NiO-SCCNTs-400, (d) magnified HRTEM image for the NiO-SCCNTs-200 sample, (e) HAADF-STEM images for NiO-SCCNTs-700 and (f-h) EDX elemental mapping for carbon, nickel and oxygen, respectively.	86

Figure 2-26. High-resolution XPS spectra for NiO-SCCNTs samples with 100, 200 and 700 ALD cycles, (a) Ni 2p and (b) O 1s scanned regions.	87
Figure 2-27. (a) Baseline resistance (R_a) variation to a 10 ppm pulse of ethanol of the oxidised SCCNTs and XNiO-SCCNTs sensors, (b) enlarged view of the SCCNTs (black) and 25NiO-SCCNTs (red) sensors.....	88
Figure 2-28. (a) The linear plot of the baseline resistance vs the number of ALD cycles (NiO shell thickness) for NiO-SCCNTs-X and SCCNTs sensors. Dynamic response towards different concentrations of acetone and ethanol at 200 °C by the fabricated sensors with, (b) oxidized SCCNTs, (c) NiO-SCCNTs-50, (d) NiO-SCCNTs-200, (e)NiO-SCCNTs-400 and (f) NiO-SCCNTs-700. The Response variations of NiO-SCCNTs-X sensors for different concentrations of target gases, (g) acetone and (h) ethanol. The insets in (g) and (h) show the linear fit for the logarithmic expression of the NiO-SCCNTs-X sensors response as a function of the target gas concentrations. All the tests were performed at 200 °C.	91
Figure 2-29. (a) NiO shell layer thickness of NiO-SCCNTs-X sensors as a function of the sensing response towards acetone and ethanol at 200 °C. (b) Successive response of NiO-SCCNTs-200 fabricated sensor to 10 ppm of ethanol and acetone at 200 °C. (c) response of two different sensors fabricated by NiO-SCCNTs-200 towards acetone at 200 °C. (d) response of NiO-SCCNTs-200 sensor to acetone, ethanol and other gases at 200 °C, which demonstrate a good selectivity towards ethanol and acetone.	94
Figure 2-30. Thermogravimetric (TG) and differential thermal analyses (DTA) of as-prepared Cu-MOF carried out under air.	105
Figure 2-31. FE-SEM images of Cu-MOF (a) as prepared, calcined at (b) 250°C, (c) 400°C and (d) a typical electron diffraction X-ray spectrum (Elemental composition represented in %)	106
Figure 2-32. HR-TEM images (a-c) and (d) SAED pattern of Cu-MOF400.....	107
Figure 2-33. Powder XRD patterns of Cu-MOF; (a) as-prepared, and calcined at (b) 250°C, (c) 300°C and (d) 400°C.....	108

Figure 2-34. XPS spectra of Cu-MOF400: survey (a), Cu 2P3/2 (b), C1s (c), O1s (d).	109
Figure 2-35. (a) Electrical resistance of Cu-MOF sensor from room temperature to 400°C. (c) Cu-MOF 250 sensor, (d) Cu-MOF 400 sensor	110
Figure 2-36. a) Variation of resistance at the introduction of acetone for the Cu- MOF400 sensor at the working temperature of 400, 350 and 300°C. b) Response of Cu-MOF400 sensor to acetone as a function of temperature.....	111
Figure 2-37 a) Transient response of Cu-MOF400 sensor to different concentrations of acetone at the optimal temperature of 250°C; b) Transient response of Cu- MOF250 sensor to different concentrations of acetone at the optimal temperature of 250°C; c) Calibration curves; d) Calibration curve in log-scale for Cu-MOF 400 sensor.....	112
Figure 2-38. a) Response of the Cu-MOF400 sensor in the presence of 5 ppm acetone gas at the working temperature of 200 °C; b) Response of the Cu-MOF400 sensor against a number of gases at various concentrations. Tests were carried out at the operating temperature 250 °C.	113
Figure 2-39. Effect of operating temperature on the sensing characteristics of Cu- MOF250 toward 20 ppm of NO ₂ in the temperature range 200° to 40°C.....	114
Figure 2-40. a) Transient response of Cu-MOF 250 sensor to different concentrations of NO ₂ at the optimal temperature of 40°C; b) Calibration curve in log-scale for Cu-MOF 250 sensor; c) Reproducibility response to NO ₂ ; d) Response of the Cu-MOF 250 sensor against a number of gases at various concentrations. Tests were carried out at the operating temperature of 40 °C.....	115
Figure 2-41. a) Response of Cu-MOF250 sensor to NO ₂ pulses at 40 °C at 40% of RH. b) Comparison between the transient response of Cu-MOF 250 sensor to 2 ppm of NO ₂ at the temperature of 40°C in dry air and under humid conditions....	116
Figure 2-42. a) Response of Cu-MOF250 sensor to acetone and NO ₂ as a function of temperature. b) Selectivity factor for the Cu-MOF 250 sensor.....	117
Figure 2-43. (a) low and (inset) high magnification SEM image of WO ₃ nanorods deposited on the interdigitated substrate, (b) XRD pattern, and	

(c) Arrhenius plot of inverse of measured resistance (R); inset in (c): schematic of interdigitated substrate drop coated.....	126
Figure 2-44. Dynamic resistance variation of WO ₃ -based sensor (black curve) at 350 °C under different H ₂ concentrations (red curve). Arrows indicate when H ₂ is fluxed in the chamber (named “gas in”) or it is stopped (named “gas out”)	127
Figure 2-45. Dynamic responses of WO ₃ -based sensor (squared symbols) and fit (red lines) obtained at (a) 250 °C, (b) 300 °C, (d) 350 °C, and (d) 400 °C under 10,000 ppm of H ₂ as a function of elapsed time starting when H ₂ is fluxed in chamber.....	128
Figure 2-46. Dynamic responses of WO ₃ -based sensor (squared symbols) and fit (red lines) obtained at 350 °C under (a) 2000 ppm, (b) 5000 ppm, (c) 10,000 ppm, (d) 20,000 ppm, (e) 30,000 ppm and (f) 50,000 ppm fluxes of H ₂ as a function of elapsed time	129
Figure 2-47. Arrhenius plot of inverse of lifetime τ of P1 (black sphere) and P2 (red sphere) during (a) response and (b) recovery phase. Dotted lines are linear fit to each set of data. The evidenced region indicates the time resolution of experimental set-up. (c) schematic representation of energy barriers for the sensing processes.	132
Figure 2-48. transmittance spectra of AsDep (black line + squares), N ₂ (red line + triangles), and FG (green line + circles) samples.	133
Figure 2-49. Morphological characterization of CDs: a) TEM micrograph, b) TEM size distribution histogram, c) AFM height micrograph, d) AFM height profile and e) AFM height distribution histogram	143
Figure 2-50. FT-IR spectrum of synthesized CDs	144
Figure 2-51. a) Cyclic voltammogram versus Ag/AgCl reference electrode of synthesized CDs; b) picture of the conductometric sensor probe; in the inset is shown the sensor head; c) Baseline resistance vs. operating temperature trend.	145

Figure 2-52. a) Resistance variation at different temperatures of CDs sensor subjected to pulses NO_2 at the concentration of 2 ppm. Inset shows the trend of sensor response with temperature; b) Response/recovery time at different temperatures of the CDs sensor..... 146

Figure 2-53. a) Transient response towards different NO_2 concentrations for the CDs sensor; b) calibration curve towards NO_2 , whereas the inset shows the response to different gases; c) schematization of the NO_2 proposed sensing mechanism on CDs-based conductometric sensor..... 147

Figure 2-54. a) Response of the sensor to consecutive pulses of 2 ppm of NO_2 ; b) Sensor response evaluated for a period of approximatively 3 months. 149

4.3 Appendix C: list of publications and conference presentations

Publications

- 1) Moulæe, Kaveh and Neri, Giovanni; "Electrochemical sensing of Amino Acid; A Review on Challenges and Achievements", **2021**, Biosensors, (Accepted) (IF: 5.52)
- 2) Sawalha, S.; Moulæe, K.; Nocito, G.; Silvestri, A.; Petralia, S.; Prato, M.; Bettini, S.; Valli, L.; Conoci, S.; Neri, G. Carbon-dots conductometric sensor for high performance gas sensing. *Carbon Trends* **2021**, 5, 100105 (IF: NA)
- 3) Moulæe, K.; Raza, M. H.; Pinna, N.; Donato, N.; Neri, G. CNT/Al₂O₃ core-shell nanostructures by atomic layer deposition; effect of Al₂O₃ thickness on the electrochemical detection of dihydroxybenzene isomers. *Physical Chemistry Chemical Physics* **2021**, (IF: 3.68)
- 4) Mineo, G.; Moulæe, K.; Neri, G.; Mirabella, S.; Bruno, E. H₂ detection mechanism in chemoresistive sensor based on low-cost synthesized WO₃ nanorods. *Sensors and Actuators B: Chemical* **2021**, 348, 130704 (IF: 7.34)
- 5) Arul, C.; Moulæe, K.; Donato, N.; Iannazzo, D.; Lavanya, N.; Neri, G.; Sekar, C. Temperature modulated Cu-MOF based gas sensor with dual selectivity to acetone and NO₂ at low operating temperatures. *Sensors and Actuators B: Chemical* **2021**, 329, 129053 (IF: 7.34)
- 6) Raza, M. H.; Moulæe, K.; Leonardi, S. G.; Barsan, N.; Neri, G.; Pinna, N. Gas Sensing of NiO-SCCNT Core-Shell Heterostructures: Optimization by Radial Modulation of the Hole-Accumulation Layer. *Advanced Functional Materials* **2020**, 30, 1906874 (IF: 18.81)
- 7) Raza, M. H.; Moulæe, K.; Wu, Y.; El-Refaei, S. M.; Karg, M.; Leonardi, S. G.; Neri, G.; Pinna, N. Tuning the NiO thin film morphology on carbon nanotubes by atomic layer deposition for enzyme-free glucose sensing. *ChemElectroChem* **2019**, 6, 383-392 (IF: 4.15)
- 8) Murugesan, D.; Moulæe, K.; Neri, G.; Ponpandian, N.; Viswanathan, C. α -MoO₃ nanostructure on carbon cloth substrate for dopamine detection. *Nanotechnology* **2019**, 30, 265501 (IF: 3.55)

- 9) Jagadeesan, M.; Movlaee, K.; Krishnakumar, T.; Leonardi, S.; Neri, G. One-step microwave-assisted synthesis and characterization of novel CuO nanodisks for non-enzymatic glucose sensing. *Journal of Electroanalytical Chemistry* **2019**, 835, 161-168 (IF: 3.82)
- 10) Movlaee, K.; Periasamy, P.; Krishnakumar, T.; Ganjali, M.; Leonardi, S.; Neri, G.; Chavali, M.; Siril, P. F.; Devarajan, V. Microwave-assisted synthesis and characterization of WO_x nanostructures for gas sensor application. *Journal of Alloys and Compounds* **2018**, 762, 745-753 (IF: 4.18)

Presentations

Montreal, Canada (2019)

- Speaker, IEEE sensors, Palais des congres de montreal, 2019, montreal, Canada

Lipari, Italy (2019)

- Speaker, Associazione Italiana di chimica per ingegneria (AICING), 2019, Lipari, Italy

Napoli, Italy (2019)

- Speaker, Associazione Italiana Sensori e Microsistemi (AISEM), 2019, Napoli, Italy

Catania, Italy (2018)

- Speaker, Convegno Nazionale Sensori (CNS), 2018, Catania, Italy

Tehran University, Tehran, Iran